Utilization of Meteorological Satellite Data in Cloud Analysis

2024

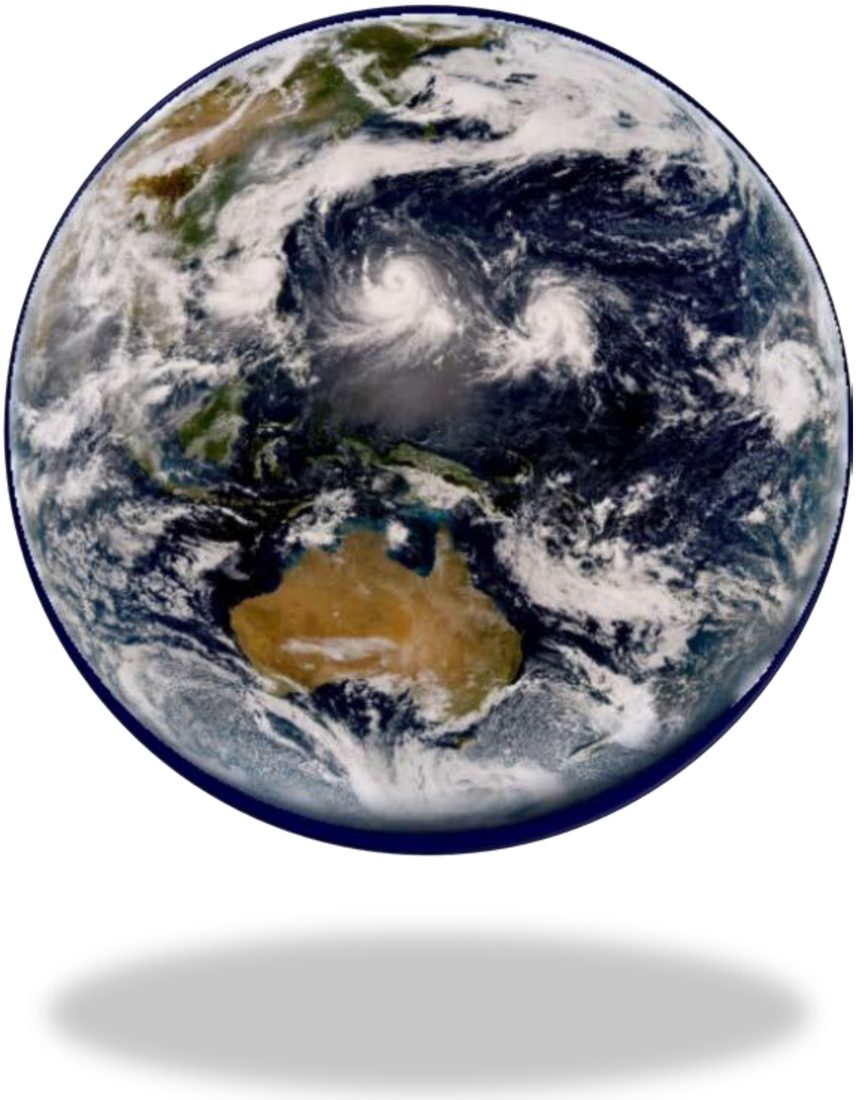

METEOROLOGICAL SATELLITE CENTER

JAPAN METEOROLOGICAL AGENCY

MARCH 2024

1. Outline of Meteorological Satellite Observation

1.1. Observation by Meteorological Satellites

An advantage of meteorological satellite-based observation is the capacity for consistent worldwide monitoring with high spatial resolution. It enables monitoring of short-term atmospheric phenomena such as the development of cumulonimbus masses, cloud areas in lows/typhoons, and climate change.

1.1.1. Satellite Orbit

The major satellite orbits used in meteorological observation are geostationary and polar sun-synchronous. Geostationary satellites follow the earth's rotation over the equator, making them appear stationary from the earth. These include JMA's Himawari-8/9 units orbiting at 140.7°E at altitudes of approximately 35,800 km, with observation of the area from the North Pole to the South Pole at intervals of around 10 minutes for monitoring of weather disturbances and climate change. Polar-orbiting satellites observe 2,000 – 3,000 km widths across the orbit in latitudinal circulation at relatively low altitudes in short cycles (e.g., around 850 km high with 100 minutes per cycle in the NOAA series). Low-orbit observation provides higher-resolution imagery than that of geostationary satellites, but covers the same position in the sky only twice a day.

1.1.2. Observation by Himawari-8/9

Himawari-8/9 observe using a moving internal mirror that scans the earth longitudinally from the north in a stepwise fashion (Bessho et al. 2016). The figure below illustrates Himawari-8/9's complete full-disk observation (i.e., covering the entire earth as seen from the satellite) and five area observations. Himawari-8/9 observation is based on observation timeline with a basic interval of 10 minutes. The figure shows the observation areas and frequencies on a timeline of 10 minutes.

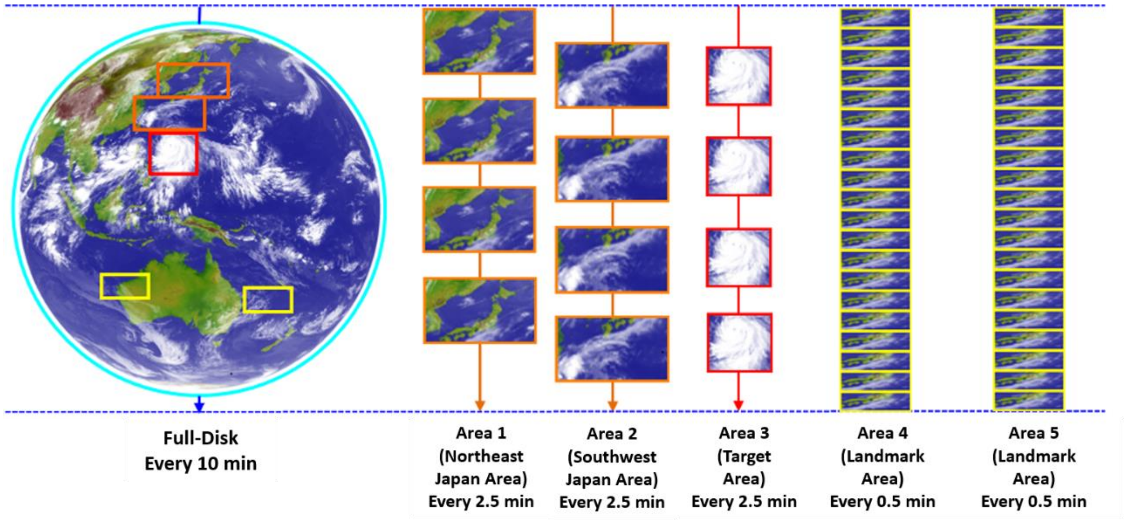

Fig. 1-1-1. Himawari-8/9 observation areas and frequencies on a timeline of 10 minutes

Himawari-8/9 perform a full-disk observation and five area observations on the timeline of 10 minutes. Two observations (i.e., 2,000-km longitudinal and 1,000-km latitudinal, as per the orange rectangles in Fig. 1-1-1) are made every 2.5 minutes over the area around Japan. These two areas are fixed, while the area in the red rectangle for typhoon monitoring (1,000-km longitudinal and latitudinal) can be changed every 2.5 minutes for specific focus on typhoons, cyclones and volcanic eruptions. In two other areas (1,000-km longitudinal, 500-km latitudinal), locations for observation can be changed every 30 seconds. This produces imagery relating to coastline characteristics as landmarks to enable correction of satellite attitude parameters based on positional differences between landmarks and predictions. The 30-second frequency of imagery capture allows monitoring of rapidly developing cumulonimbus areas that may cause extreme phenomena.

Wavelength (µm)	Himawari-8/9				Himawari-6/7		Example usages
	Band no.	Horizontal resolution (km)	Central wavelength (µm)		Channel	Horizontal resolution (km)	
			Himawari-8	Himawari-9			
0.47	1	1	0.47	0.47		-	Color composite imagery, aerosols
0.51	2	1	0.51	0.51	-	-	Color composite imagery, aerosols
0.64	3	0.5	0.64	0.64	VIS	1	Color composite imagery, low cloud/fog
0.86	4	1	0.86	0.86			Vegetation, aerosols
1.6	5	2	1.61	1.61			Discrimination of cloud phases
2.3	6	2	2.26	2.26			Cloud particle radius variation
3.9	7	2	3.89	3.83	IR4	4	Low cloud/fog, natural fires
6.2	8	2	6.24	6.25	IR3	4	Upper-layer water vapor concentration
6.9	9	2	6.94	6.96			Middle-layer water vapor concentration
7,3	10	2	7.35	7.34			Middle-layer water vapor concentration
8.6	11	2	8.59	8.59			Discrimination of cloud phases, SO_2
9.6	12	2	9.64	9.63			Ozone total volume
10.4	13	2	10.41	10.41	IR1	4	Cloud imagery, cloud-top information
11.2	14	2	11.24	11.21			Cloud imagery, sea surface temperature
12.4	15	2	12.38	12.36	IR2	4	Cloud imagery, sea surface temperature
13.3	16	2	13.28	13.31			Cloud-top height

Table 1. Comparison of Himawari-8/9 and Himawari-6/7 bands. Spatial resolutions are as defined at the subsatellite point.

1.1.1. Advanced Himawari Imagers on board Himawari-8/9

The Advanced Himawari Imager (AHI) units on board the Himawari-8/9 satellites feature 16 bands (3 visible, 3 near-infrared and 10 infrared). Table 1 compares these bands with those on the previous Himawari-6/7 units, with the rightmost column showing example usages of observation data for each band. The characteristics of each band are detailed in the next section.

References:

- Bessho et al., 2016: An introduction to Himawari-8/9 - Japan's new-generation geostationary meteorological satellites. J. Meteor. Soc. Japan, 94, 151-183. https://doi.org/10.1007/978-3-642-14791-3

1.2. Himawari-8/9 AHI Band Characteristics

As described previously, the Advanced Himawari Imagers (AHIs) on Himawari-8/9 have 16 bands in the visible, near-infrared and infrared ranges, as opposed to the 5 bands of the Himawari-6 and 7 imagers. Difference imagery is also created with focus on solar reflectance and brightness temperature for each corresponding pixel. This section describes these bands along with difference imagery used in cloud analysis and RGB composite imagery.

1.2.1. Visible Imagery

(1) Introduction of Visible Imagery

Visible imagery shows solar reflectance (usually not corrected for solar zenith angle) in the wavelength range of visible light (roughly from 0.4 to 0.8 μm). Areas with strong solar reflection are rendered with bright pixels, highlighting dense clouds and snow. Sea surfaces have weak solar reflection, making them appear dark. Targets appear differently depending on solar elevation. As reflection energy is lower with incident energy per unit area, high-latitude regions appear darker than low-latitude regions, and images in the morning and evening are darker than those at noon. Some cloud areas are also darker due to the shade of vertically developed cumulonimbus. Figure 1-2-1 shows a lower cloud that became harder to see due to cumulonimbus shade. Areas without sunlight at night appear pitch black.

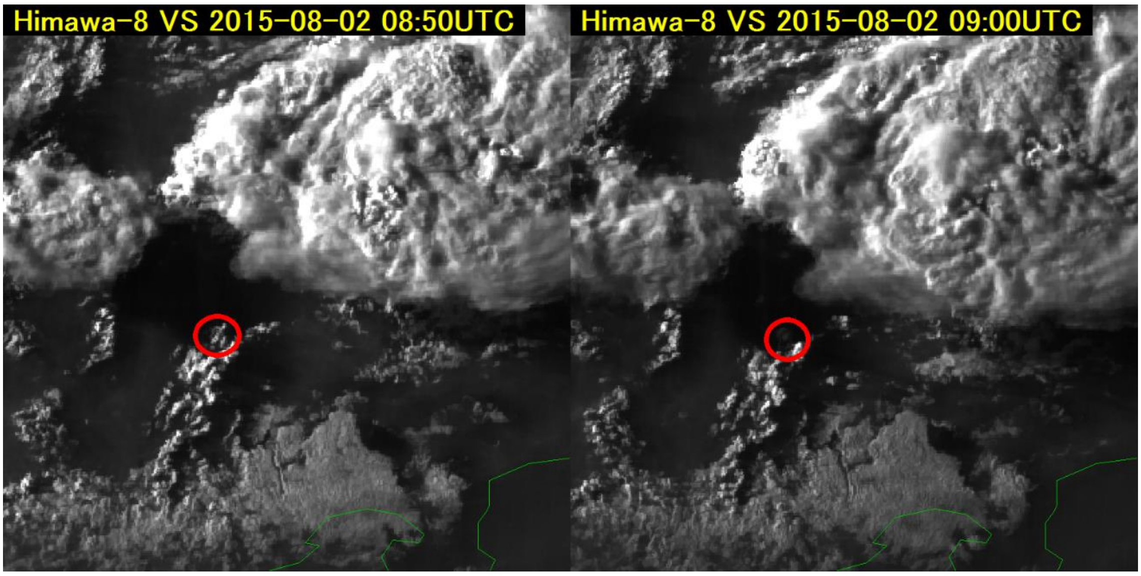

Fig. 1-2-1 Lower cloud entering the cumulonimbus shade

Himawari-6 and 7 had only a single band with a central wavelength of around 0.68 μm, while Himawari-8/9 have three bands with central wavelengths of around 0.47, 0.51 and 0.64 μm, corresponding to blue, green and red in human vision. These colors form True Color RGB composite imagery resembling the earth as viewed by the human eye from outer space.

Figure 1-2-2 shows solar reflection characteristics in visible and near-infrared ranges. Even within the visible range, these depend on wavelength (see Section 1.2.5).

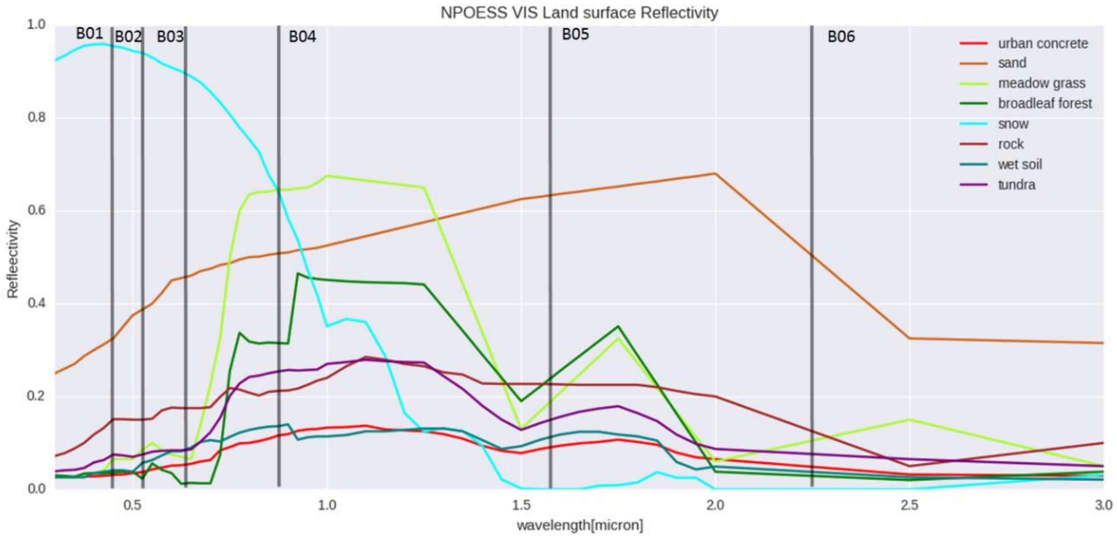

Fig. 1-2-2 Solar reflectance of land surface types in the Community Radiative Transfer Model (CRTM) in the visible and near-infrared ranges. The black lines indicate the central wavelengths of Himawari-8 AHI Bands 1 - 6.

(2) Visible Imagery Usage

A) Distinction between Thick and Thin Clouds

The solar reflectance of clouds depends on their density of particles, with lower clouds typically containing more particles and appearing brighter. Vertically developed thick clouds such as cumulonimbus also have a high particle count, making them appear bright. Thin upper clouds may be transparent, revealing the state of lower clouds and land/sea surfaces below.

B) Distinction between Convective and Stratiform Clouds

The top surfaces of stratiform clouds are smooth and uniform, while those of convective clouds are rough and uneven. These textures are highlighted when sunlight hits at an angle.

C) Cloud Top Height Comparison

When sunlight hits at an angle, clouds with a higher top may form shadows over those below. This allows comparison of top heights.

D) Land Surface Identification

Figure 1-2-3 shows solar reflectance for individual land conditions in the visible range (from the same source as Fig. 1-2-2). Within the wavelengths of AHI Bands 1 – 3 in particular, snow shows the largest reflectance, then sand, then vegetation (much smaller).

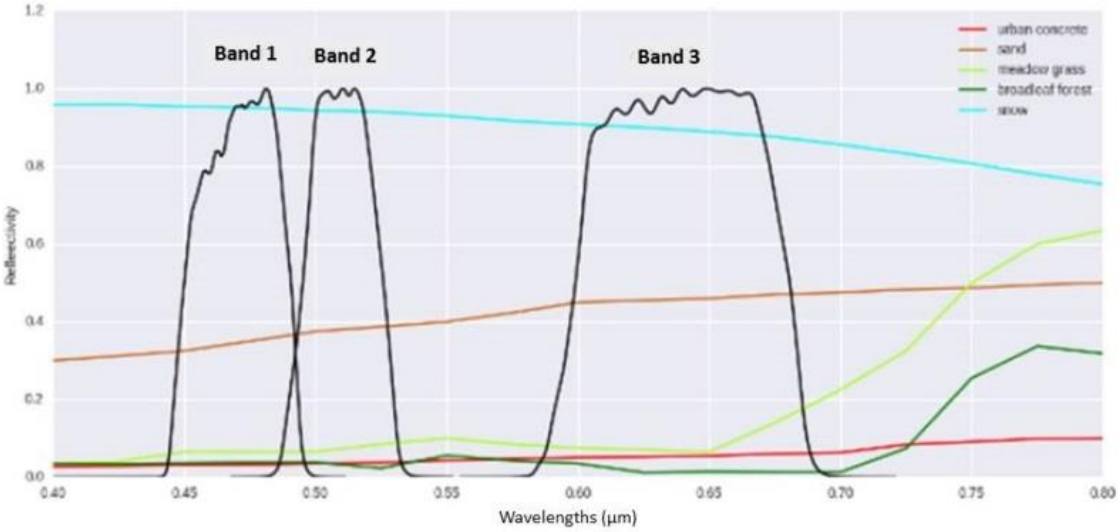

Fig. 1-2-3 Solar reflectance of land surface types in the CRTM in the visible range. Black lines indicate response functions of Himawari-8 AHI Bands 1 – 3.

As an example, the True Color RGB composite image in Fig. 1-2-4 shows desert areas in Australia. These appear reddish-brown because Bands 1 (blue) and 2 (green) contribute less than Band 3 (red), as shown by the sand characteristics in Fig. 1-2-3. Green is unrecognizable even in vegetation areas such as tropical rainforests.

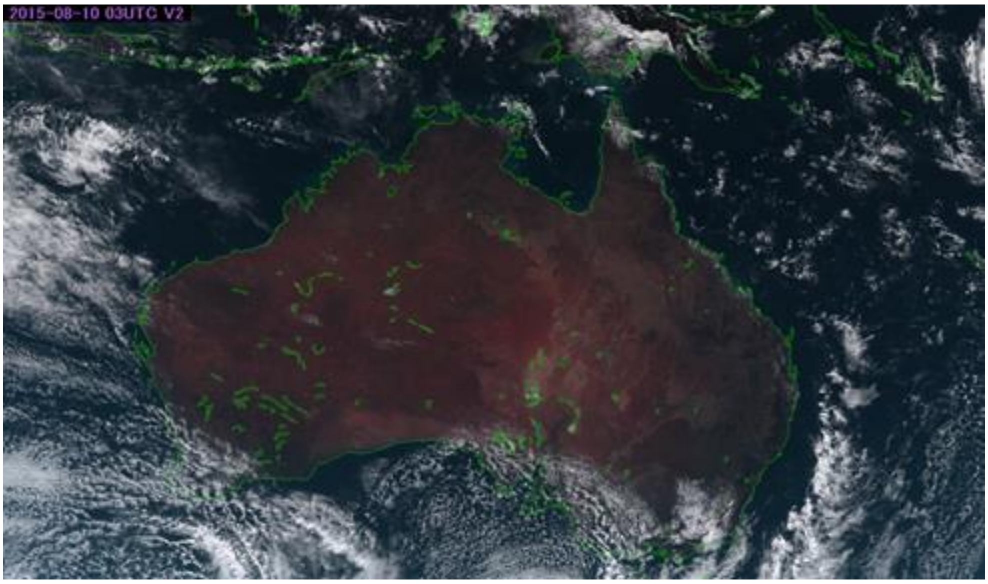

Fig. 1-2-4 True Color RGB composite image of Australia

E) Aerosol Identification

In Band 1, aerosol masses such as smoke and dust are clearly visible due to Mie scattering when the size of the scattering particles is comparable to the wavelength of the light. Figure 1-2-5 shows continental wildfire smoke over the Sea of Japan. This is clearer in Band 1 image (with a shorter central wavelength) than in Band 3 image.

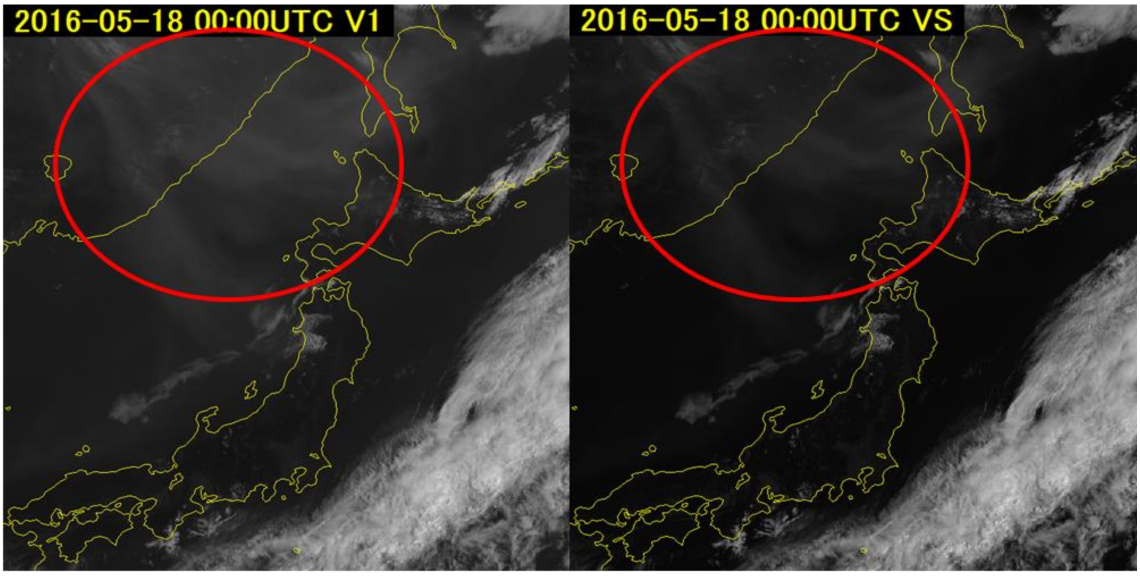

Fig. 1-2-5 Continental wildfire smoke over the Sea of Japan; more apparent in Band 1 (left) than in Band 3 (right)

1.2.2. Near-infrared Imagery

(1) Introduction

Himawari-8 is the first satellite in the Himawari series to have near-infrared bands, which are toward the longer-wavelength side of the visible range. Although invisible to the human eye, the range is widely used in everyday items such as optical fibers and remote controls.

Observed radiance in such imagery consists mostly of reflected sunlight, and radiation from the Earth in this can largely be ignored (as in visible imagery). Accordingly, the medium applies only to daytime conditions. However, it can reveal characteristic reflections that differ from those of visible bands, especially for land surfaces and ice clouds (Fig. 1-2-2).

(2) Usage

A) Land Surface Determination (All Bands)

As per Fig. 1-2-6, Band 4 shows large solar reflectances for vegetation such as grassland and broadleaf forest areas. It can also be used to identify burnt areas (which show smaller solar reflectance than healthy vegetation; Fig. 1-2-7), and renders coastlines more clearly than Band 3 (Fig. 1-2-8). Band 5 can be used to distinguish between lower-level water clouds and snow/ice-covered land because it shows much smaller solar reflectance values than Bands 1 to 4 (Fig. 1-2-2).

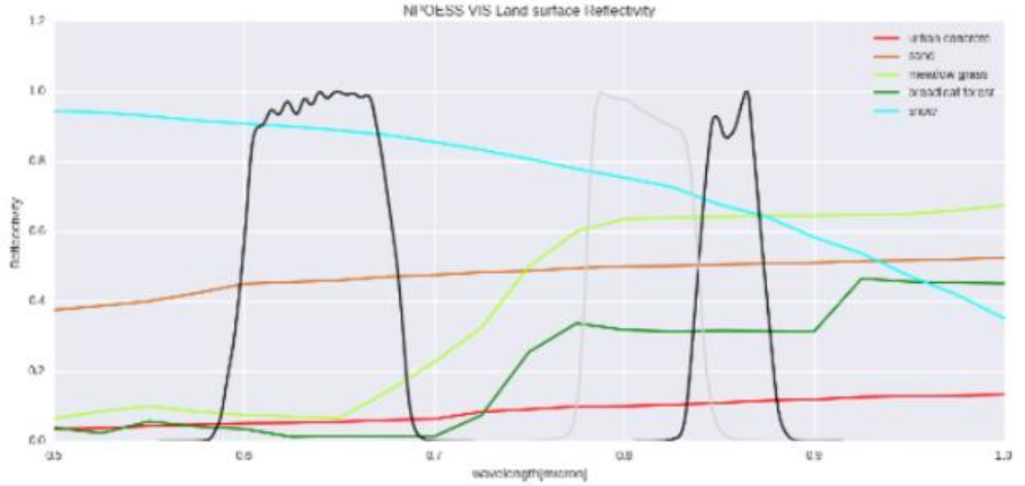

Fig. 1-2-6 Solar reflectances from 0.5 to 1.0 µm corresponding to land surfaces in CRTM (Delst and Han, 2008), with response functions of Himawari-8 AHI Bands 3 and 4 in black and MSG SEVIRI VIS0.8 in grey.

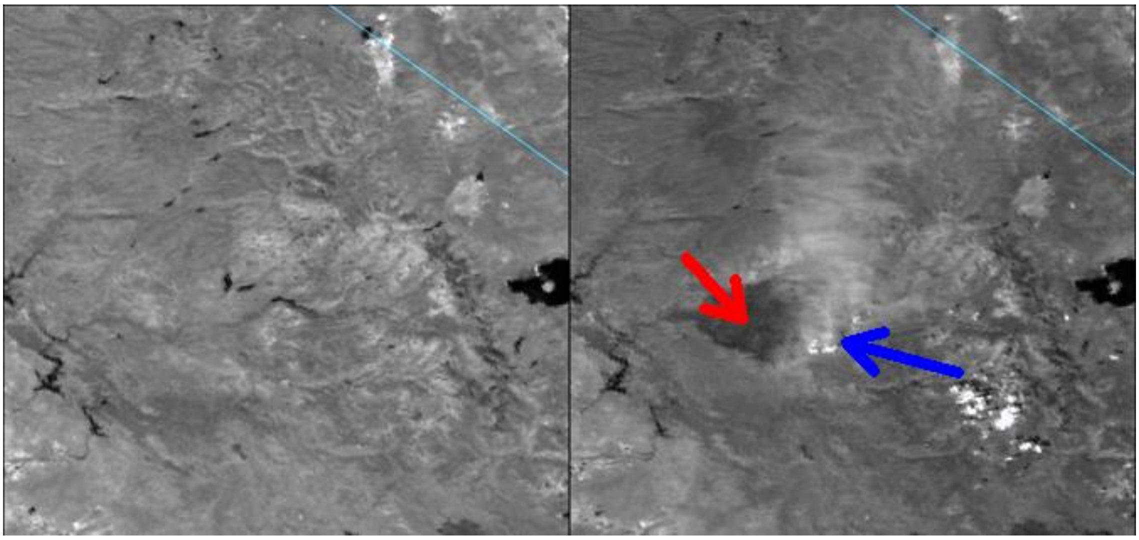

Fig. 1-2-7 M7 band image (0.865 μm) on S-NPP/VIIRS before (left) and after (right) a California wildfire. Red arrow: burnt area and smoke; blue arrow: thick pyro-cumulus associated with fire and volcanic activity (GOES-R Program Office, 2015).

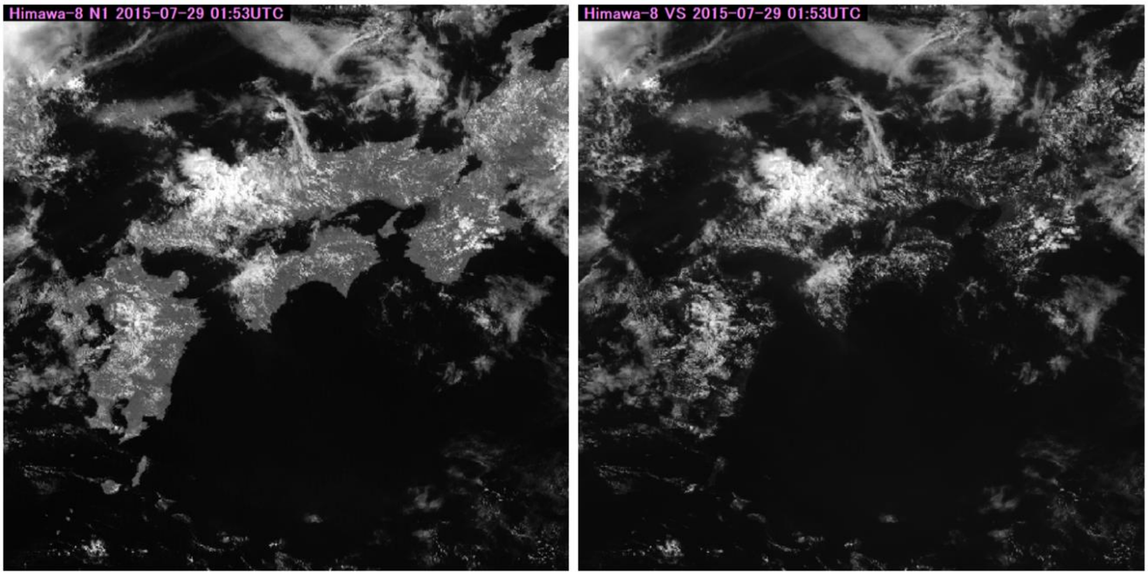

Fig. 1-2-8 Band 4 (left) and Band 3 (right) images. The coastlines in Band 4 are obviously clearer.

B) Cloud Particle Phase/Size Determination (Bands 5 and 6)

Solar reflectances in both bands vary by particle phase (i.e., water or ice) at the cloud top. When sunlight is perpendicularly incident from a medium with a refractive index n_1 to one with n_2, reflectance R is expressed by:

$$R = \left(\frac{n_1 - n_2}{n_1 + n_2}\right)^2$$

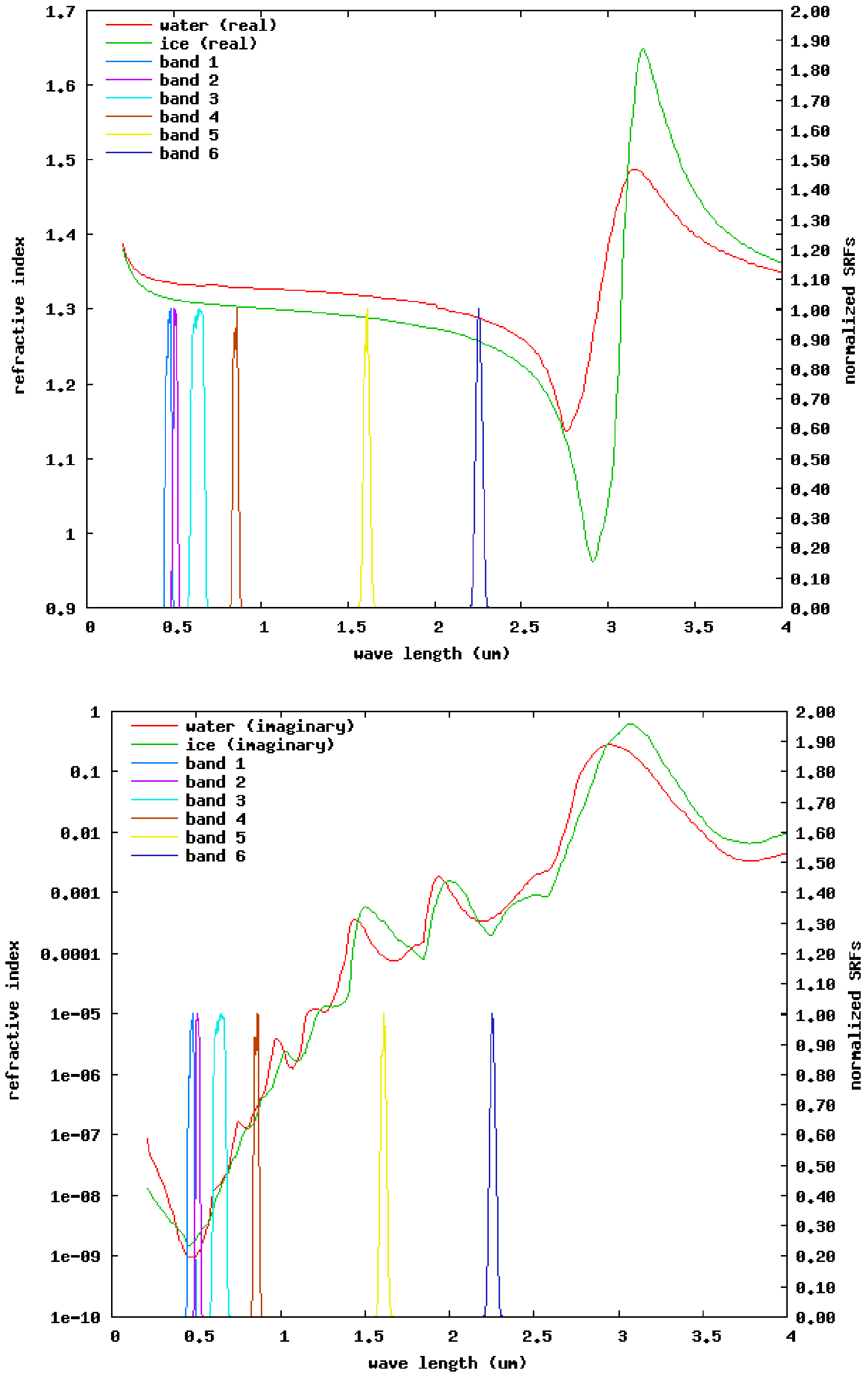

Fig. 1-2-9 Complex refractive index values in visible and near-infrared ranges, and response functions of Himawari-8 AHI Bands 1 to 6. Top: real part (refractive index); bottom: imaginary part (absorption coefficient).

Reflectance differences related to particle phases in Bands 5 and 6 are accounted for by the complex refractive index (Fig. 1-2-9). The real part of this is simply called refractive index, and the imaginary part is the absorption coefficient, where ice has larger values in Band 5 (yellow) and water is larger in Band 6 (blue).

In Band 5 (Fig. 1-2-10), mid- and lower-level water clouds appear bright, as in Bands 1 to 4.

However, upper-level ice clouds (in red) are relatively dark since their absorption coefficient (green in Fig. 1-2-9) is larger than that of water (in red), which facilitates related identification. Band 6 is also affected by particle phases, while Band 5 generally makes phase determination easier.

Cloud solar reflectance also depends on particle size, especially in Band 6. As per Fig. 1-2-11, greater optical thickness equates to larger solar reflectance in both Bands 3 and 6, and a greater cloud effective radius is associated with a smaller solar reflectance in Band 6 (darker area in red, Fig. 1-2-12). This suggests upper-level ice clouds potentially containing relatively large particles.

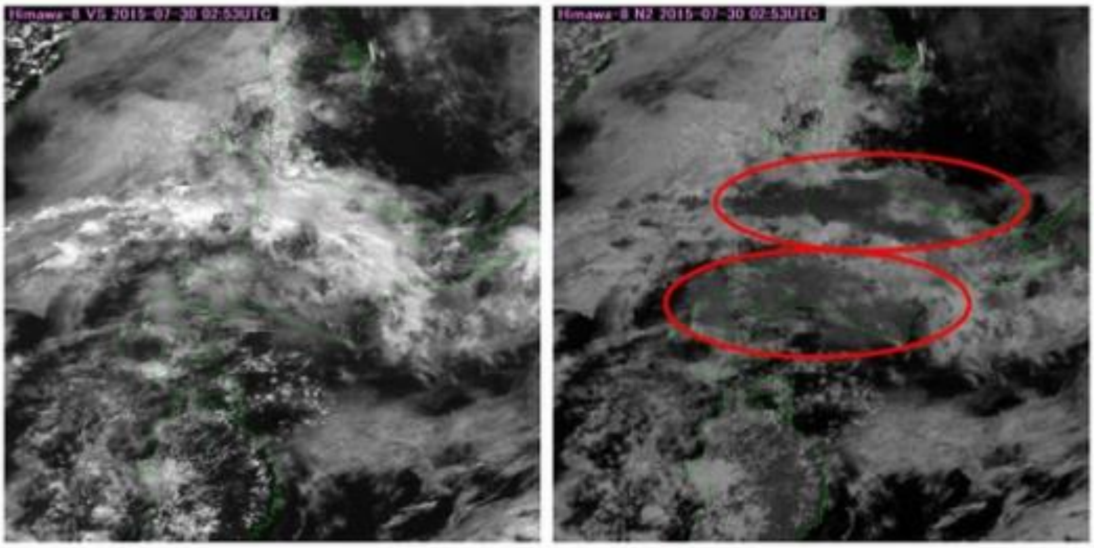

Fig. 1-2-10 Cloud reflection differences associated with cloud particle phases. Left: Band 3; right: Band 5; red: upper-level clouds.

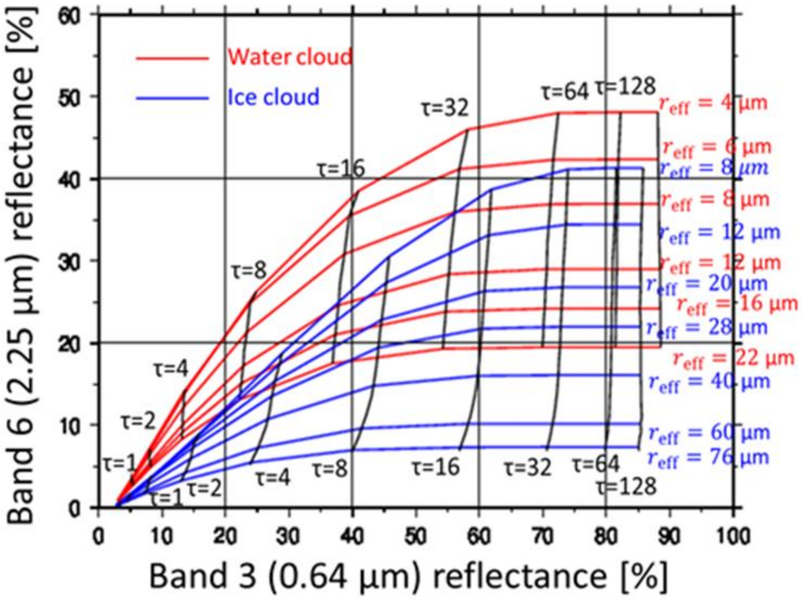

Fig. 1-2-11 Solar reflectance of water/ice clouds in Bands 3 and 6 depending on optical thickness (τ) and effective radius (r_{eff}) via radiative transfer calculation (Hayashi, 2018)

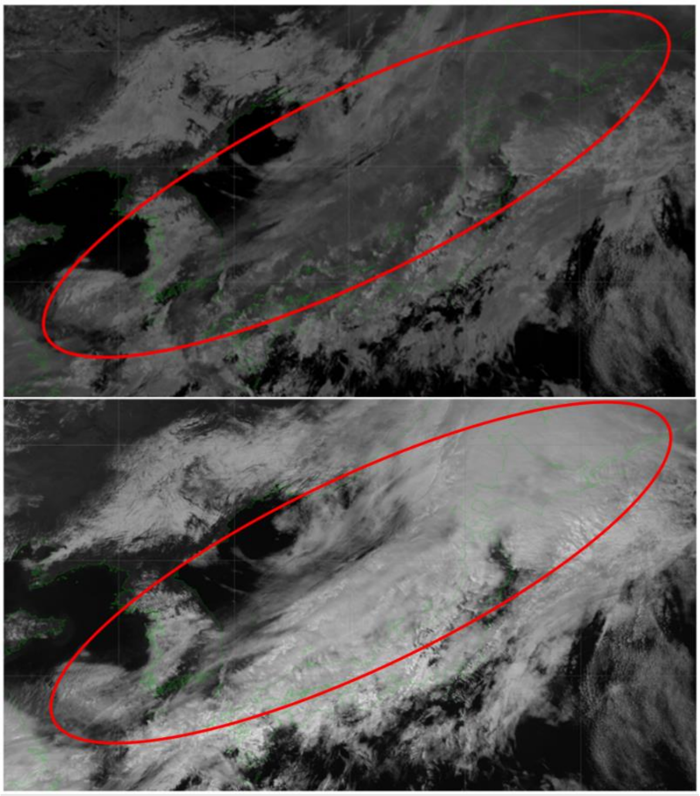

Fig. 1-2-12 Upper-level clouds in Bands 6 (top) and 3 (bottom). Red: upper-level ice clouds.

C) Hotspot Detection (Bands 5 and 6)

Bands 5 and 6 are responsive to the Earth's radiation only when temperatures are very high, which can be used to detect bright hotspots such as wildfires and volcanoes (Fig. 1-2-13). Hotspots can also be seen using Band 7 (see Section 1.2.3 Infrared Imagery).

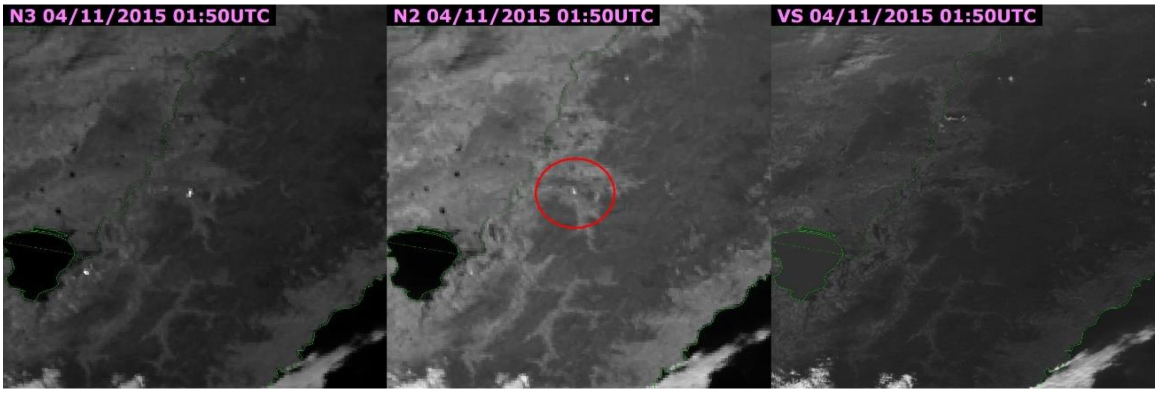

Fig. 1-2-13 Images from Bands 6 (left), 5 (middle) and 3 (right). A wildfire (red; middle) appears in Bands 6 and 5, but not in Band 3.

(3) Near-Infrared Band Characteristics

- Band 4 (0.86 μm)

  - Useful for identifying vegetation, burnt forest areas and other land surface types
- Band 5 (1.6 µm)
  - Useful for identifying water phases and differences between lower-level water clouds and upper-level ice clouds or snow/ice-covered land
  - Responsive to hotspots
- Band 6 (2.3 µm)
  - Responsive to cloud particle sizes
  - Responsive to hotspots

1.2.3. Infrared Imagery

(1) Introduction

Observed radiance in Himawari-8/9 AHI infrared bands 7 – 16 consists mostly of Earth's radiation, and reflected sunlight can largely be ignored (except in Band 7, which consists of both during daytime). Observed radiance in infrared bands is converted to brightness temperature using Planck's Law with the assumption of blackbody radiation. Infrared imagery is generally rendered so that areas with lower brightness temperatures appear brighter, with clouds appearing bright and sea surfaces appearing dark. Unlike visible and near-infrared bands, infrared bands can be used both day and night, making them suitable for 24-hour observation of clouds and surface temperatures.

As per Fig. 1-2-14, infrared bands are often affected by atmospheric molecule absorption. Bands 8 – 10 are known in particular for relatively strong water vapor absorption, with 10 and 11 being slightly affected by relatively low levels of sulfur dioxide from volcanic and industrial activity. Bands 12 and 16 are affected by ozone and carbon dioxide absorption, respectively, while 7, 11, 13, 14 and 15 ("window bands") exhibit relatively low absorption. As above, Band 7 is affected by solar reflection in the daytime, and has characteristics differing from those of other infrared bands.

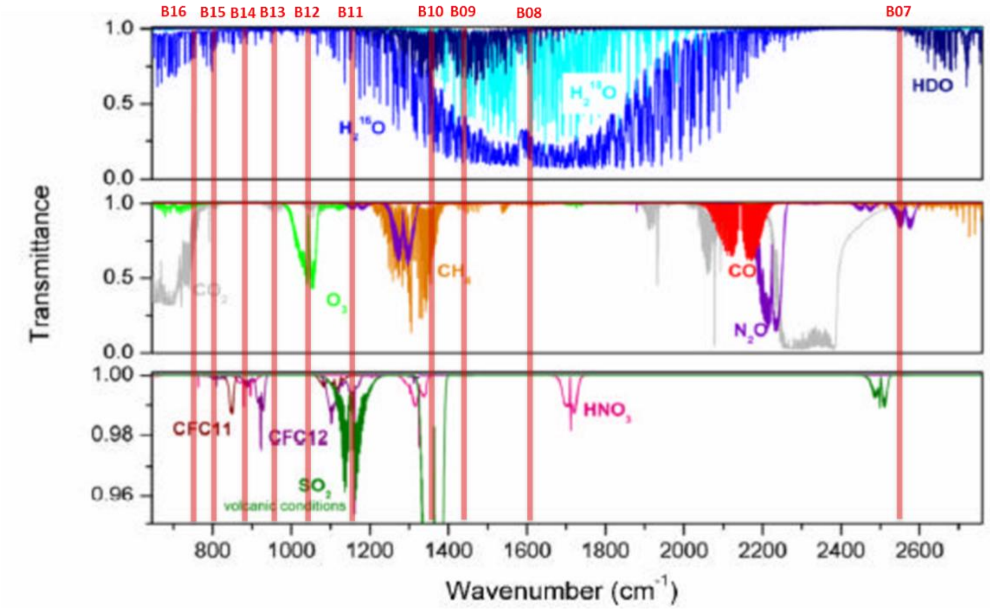

Fig. 1-2-14 Transmittance of major atmospheric molecules in the infrared range. The x-axis represents wavenumbers rather than wavelengths. Red lines indicate the central wavelengths of Himawari-8 AHI Bands 7 – 16 (Clerbaux *et al.*, 2011; amended with additional text).

(2) Window Bands

The window bands 7, 11, 13, 14 and 15 have weighting functions with peaks at the surface

(Fig. 1-2-15), reflecting their provision of information on the ground surface and in the lower atmosphere.

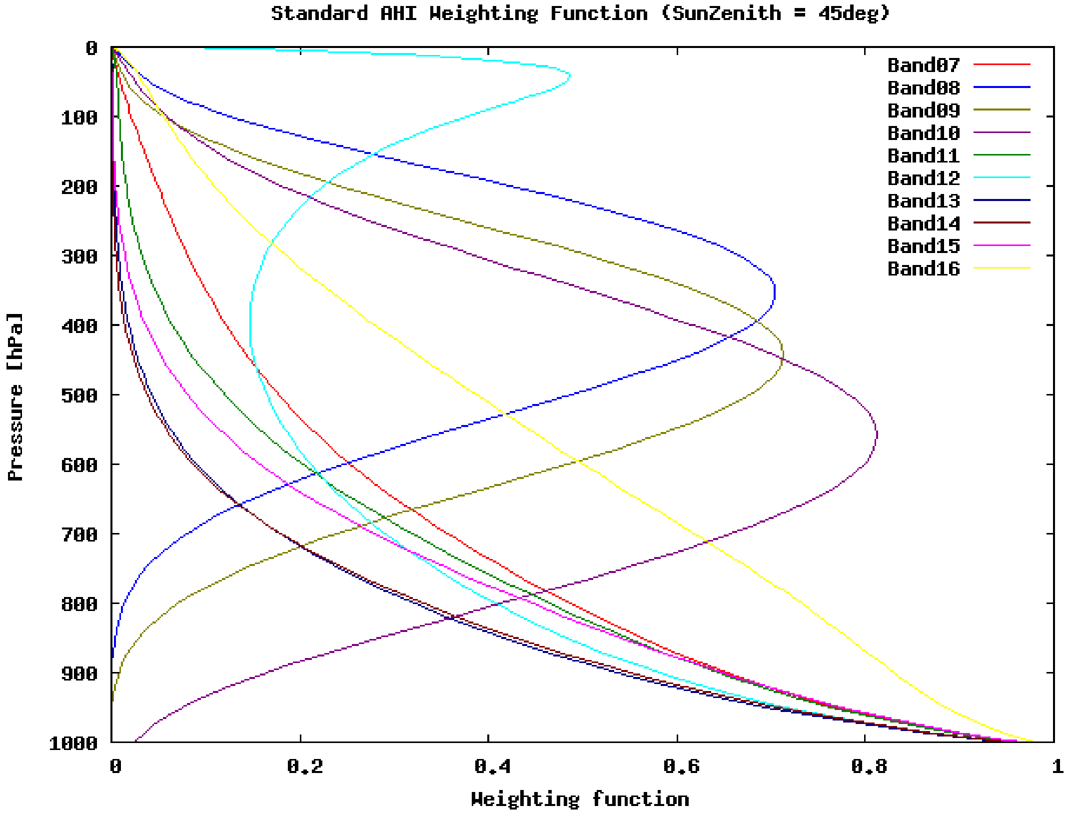

Fig. 1-2-15 Weighting functions of Himawari-8 AHI Bands 7 - 16

Band 7 is called the shortwave window band. Band 7 can be used as one of the window bands only in the nighttime because daytime radiance contains reflected sunlight. The relationship between brightness temperature and radiance here differs from those of other window bands, with Fig. 1-2-16 showing this (left) against Band 13 (right). The latter shows practical linearity for 220 to 300 K, while Band 7 exhibits nonlinearity. Accordingly, small changes in low radiance values can cause large changes in brightness temperature in Band 7, resulting in reduced resolution below 230 K in particular. As a result, cumulonimbus and thick upper clouds may exhibit dot noise in Band 7 and related difference imagery (Fig. 1-2-17).

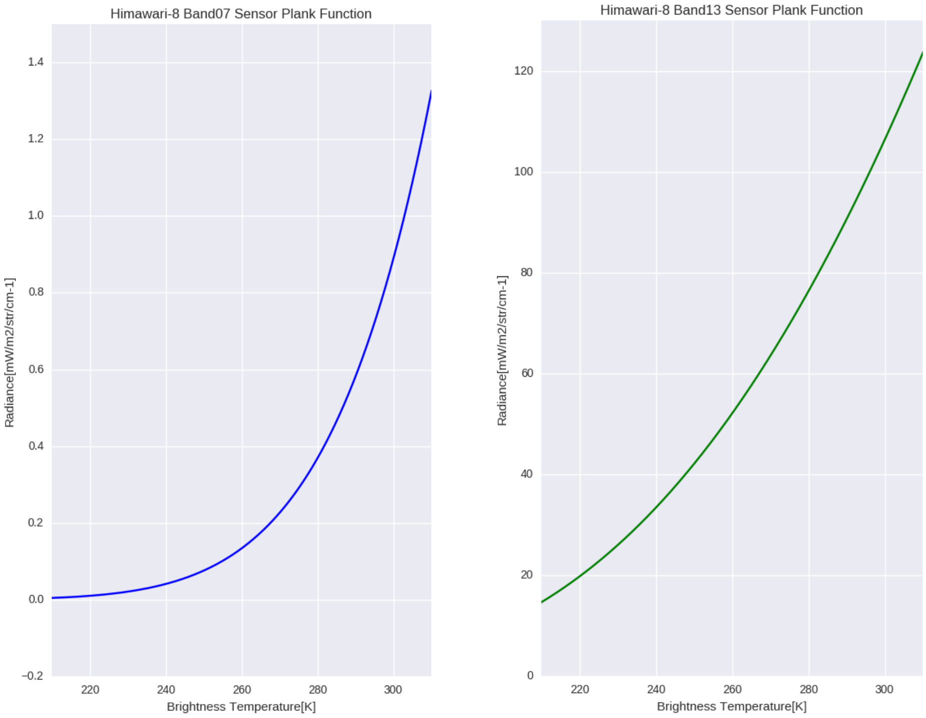

Fig. 1-2-16 Brightness temperature vs. radiance in Bands 7 (left) and 13 (right)

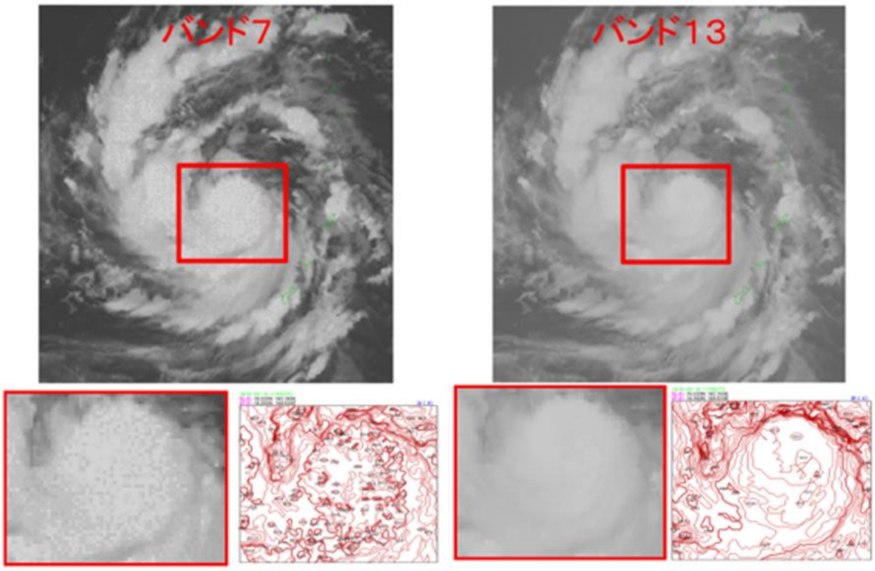

Fig. 1-2-17 Noise in Band 7 (left) in a low brightness temperature area around the center of Typhoon Goni in 2015, and Band 13 image (right)

Bands 11, 13, 14 and 15 are called the longwave window bands, with Band 11 being more affected by water vapor absorption and sulfur dioxide. This band is useful for distinguishing cloud particle phases (as described later), and bands on other sensors with similar central wavelengths are sometimes called “cloud-top phase bands”. Figure 1-2-14 indicates that the central wavelength of Band 13 has a transmittance closer to 1 than Bands 14 and 15, making it suitable for subjective cloud analysis. Thus, Band 13 is sometimes called a “clean” window band. Imagery showing differences between Band 13 and others can also be revealing, while Band 15 is more known as a “dirty” window band for its lower transmittance than 13 and 14, which have similar central wavelengths to 13 (Fig. 1-2-18) and provide comparable imagery. However, differences in absorption coefficients (Fig. 1-2-19), surface emissivity (Fig. 1-2-20) and atmospheric transmittance (Fig. 1-2-14) are seen, as per the upper clouds with lower brightness temperatures in Fig. 1-2-21.

Bands 13 and 15 will replace IR1 and IR2 on MTSAT-2, respectively, due to their higher correlations than adjacent bands, while IR4 on MTSAT-2 will be replaced by Band 7 (Murata et al., 2015).

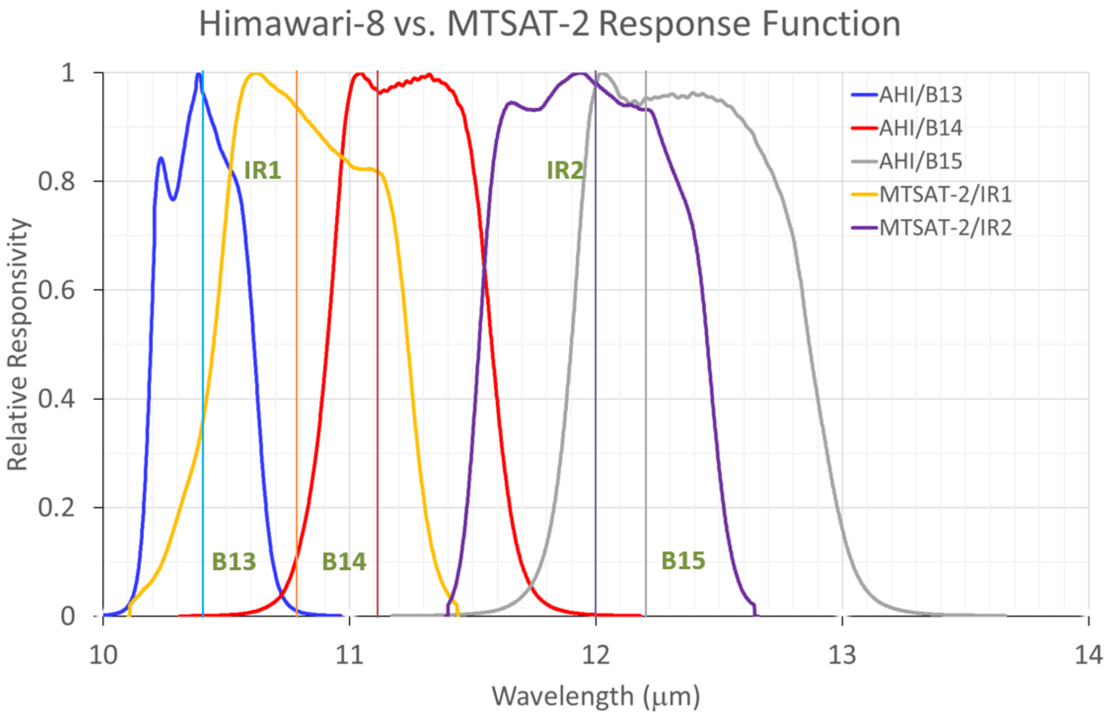

Fig. 1-2-18 Response functions of bands 13 (blue) 14 (red) and 15 (gray) on Himawari-8 and IR1 (yellow) and IR2 (purple) on MTSAT-2. Vertical lines are centre wavelengths.

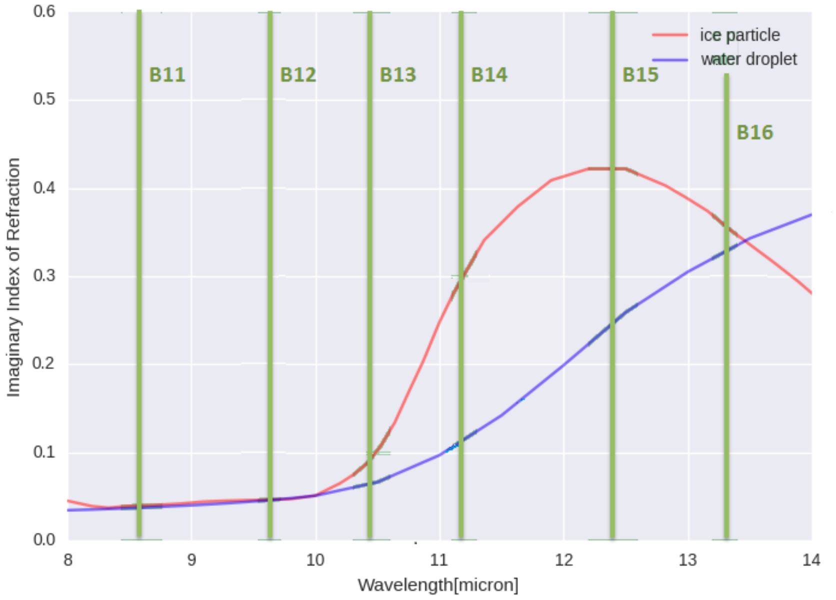

Fig. 1-2-19 Imaginary part of complex refractive index (i.e., absorption coefficients) for water and ice between 8 and 14 µm (Hale and Querry, 1973 for water; Warren, 1984 for ice). Vertical lines: central wavelengths of Himawari-8 AHI bands 11 to 16.

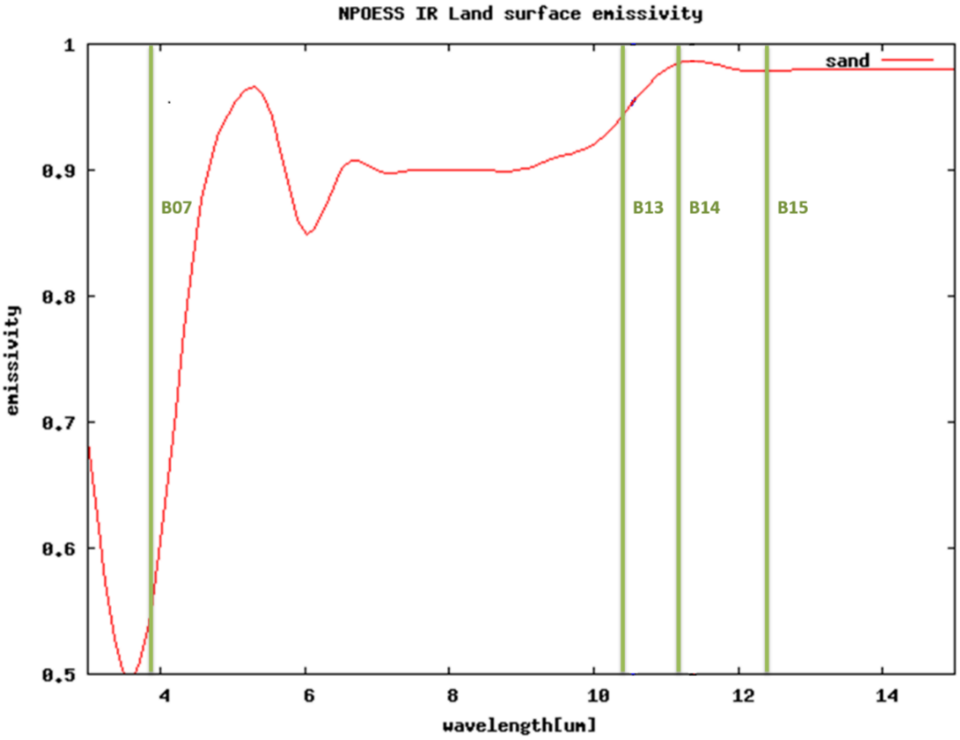

Fig. 1-2-20 Sand emissivity between 3 and 15 µm in CRTM. Vertical lines: central wavelengths of Himawari-8 AHI bands 7, 13, 14 and 15.

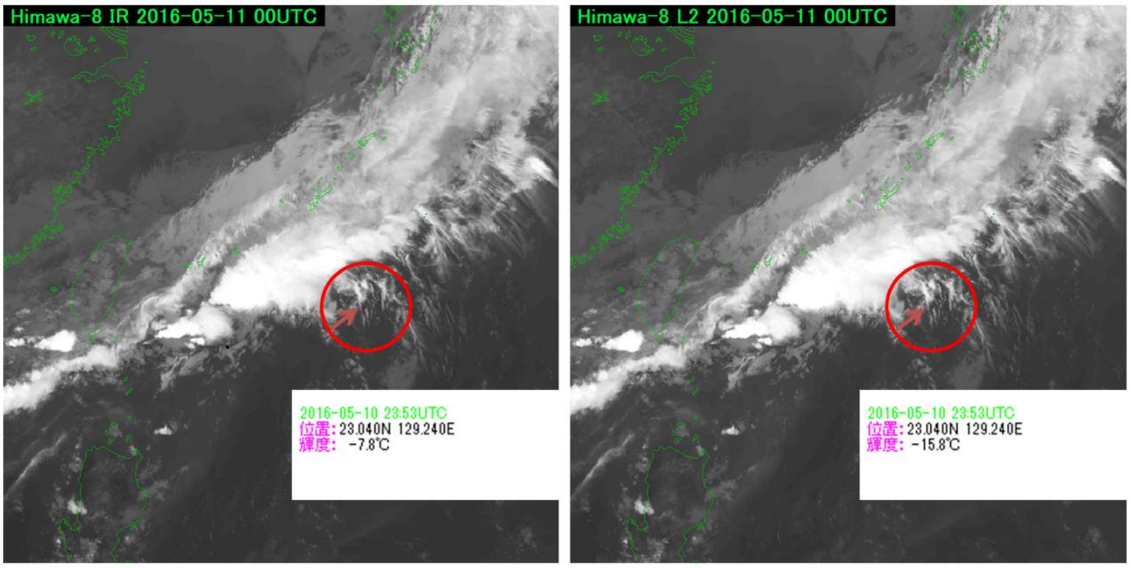

Fig. 1-2-21 Band 13 (left) and 14 (right) images indicating brightness temperatures of –7.8 and –15.8°C, respectively.

(3) Water Vapor Bands

Bands 8, 9, and 10 are called water vapor bands. Water vapor imagery corresponds to the amount of water vapor between the upper and middle troposphere because it is affected by a relatively strong absorption of water vapor. The weighting functions in Fig. 1-2-15 show that each water vapor band has a different peak altitude, suggesting that the observed water vapor altitudes are different. However, it should be noted that these bands do not represent only water vapor at a peak altitude of a weighting function, but rather a distribution with some depth (Kumabe, 2006).

As can be seen from the weighting functions (Fig. 1-2-15), Band 8 has a peak around 300 to 400 hPa in the standard atmosphere. This altitude corresponds to the upper troposphere, and it is the highest among the water vapor bands. Band 9 has a peak around 400 to 500 hPa, which corresponds to the upper and middle troposphere. Band 10 has a peak around 500 to 600 hPa, which corresponds to the middle troposphere, and it is the lowest among the water vapor bands. Also, according to Fig. 1-2-14, Band 8 has the smallest water vapor transmittance, followed by Bands 9 and 10. Comparing the overall brightness of Bands 8, 9, and 10 in Fig. 1-2-22, Band 8 is the brightest (i.e., the highest brightness temperature) as it is the most affected by the water vapor in the upper layer.

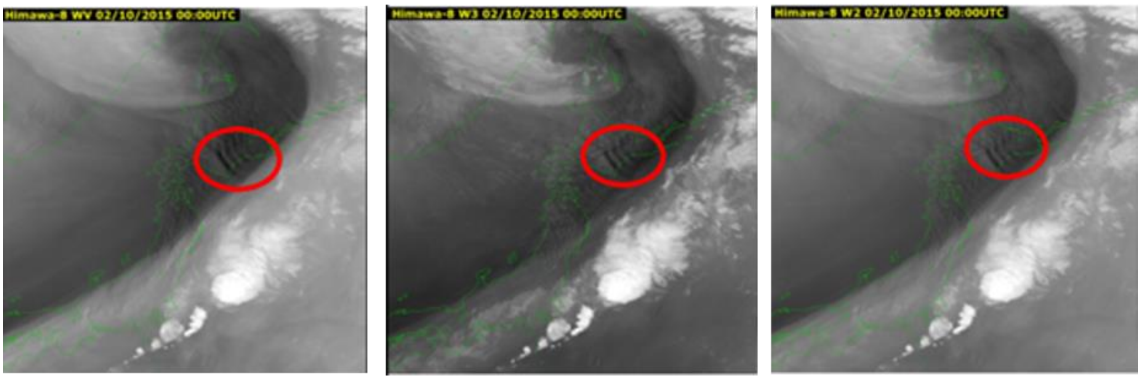

Fig. 1-2-22 Wave patterns corresponding to mountain lee waves in water vapor imagery (red oval). Bands 8, 9 and 10 from left to right.

By using Bands 8, 9, and 10 together, it is possible to understand the three-dimensional distribution of water vapor to some extent.

Taking Band 8 which mainly corresponds to water vapor in the upper troposphere as an example, the standard atmosphere is simplified into three layers: upper, middle, and lower, and the amount of infrared absorption and emission is schematically shown (Fig. 1-2-23). From near the ground surface to the lower layers of the atmosphere, the air is hot and contains a lot of water vapor, so a large amount of infrared radiation is emitted. However, at the same time, most of it is absorbed by water vapor, and only a small amount of infrared radiation reaches the satellite. As altitude increases, both the temperature and the amount of water vapor decrease, so less infrared radiation is emitted, but absorption by water vapor is also reduced. In the upper layers, both the temperature and the amount of water vapor are even lower, so the amount of emitted infrared radiation is small, but it reaches the satellite almost without being absorbed.

Dry areas with little water vapor in the upper and middle layers show high brightness temperatures and appear dark because a large amount of radiation from the lower layers reaches a satellite almost unabsorbed. Humid areas with a lot of water vapor in the upper and lower layers show low brightness temperatures and appear bright because radiation from clouds and water vapor in the upper and middle layers is dominant. Figure 1-2-24 shows the characteristics of water vapor imagery related to atmospheric phenomena.

From the perspective of radiative characteristics, JMA has chosen Band 8 as a successor to IR3 on MTSAT-2 (Murata et al., 2015).

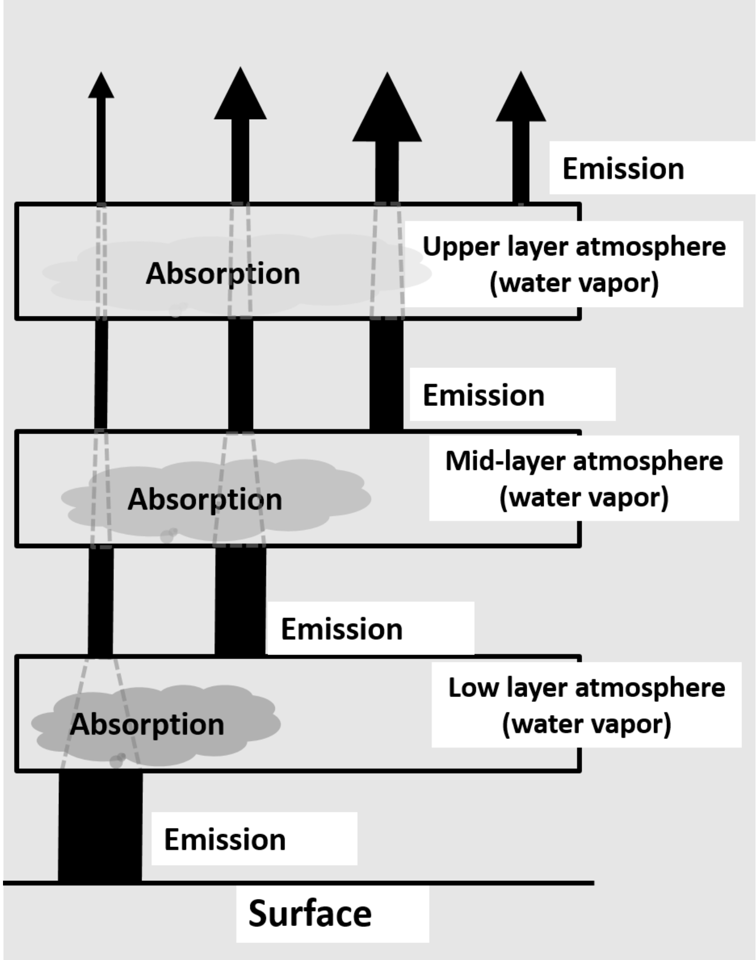

Fig. 1-2-23 Conceptual diagram of radiation in water vapor imagery (Kishimoto, 1997)

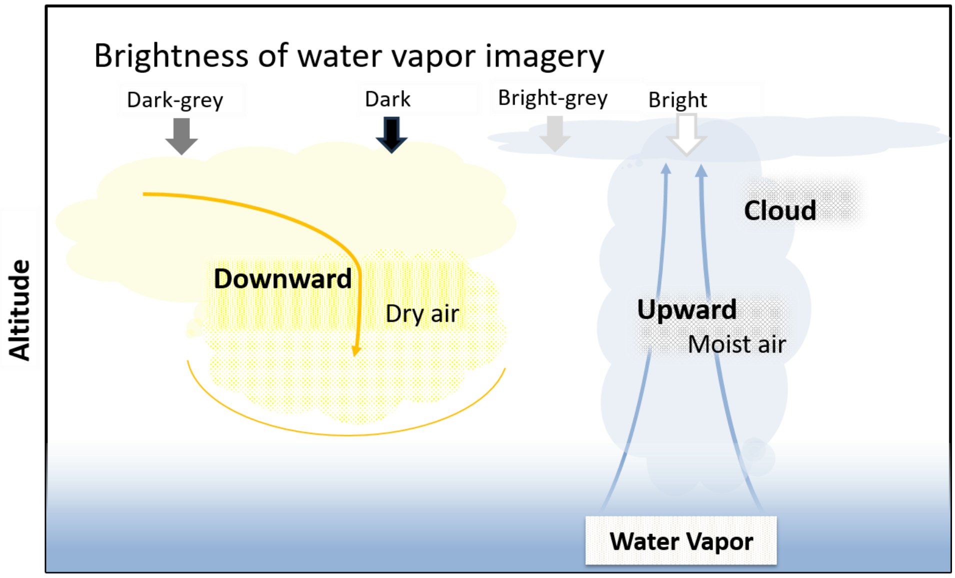

Fig. 1-2-24 Schematic relationship between atmospheric phenomena and appearance in water vapor imagery

(4) Infrared Imagery Usage

A) 24-hour Observation (All Bands)

As mentioned above, infrared bands are available both day and night. Moreover, we can consider that observed radiance in Bands 8-16 contains only Earth's emission and is not affected by solar reflection. This makes it easier to use these bands for 24-hour observation.

B) Cloud Top Height Estimation (Window Bands)

Normally, satellite observations of clouds reveal only their tops, and brightness temperatures of clouds in infrared window band imagery can be considered as temperatures of their tops. Cloud top temperatures can be converted to cloud top heights by combining them with vertical temperature profiles obtained from objective analysis and numerical weather prediction. In the troposphere, except for inversion layers, temperatures are generally lower in the upper layer, suggesting that clouds with lower cloud top temperatures have higher cloud top heights. Vertical development of clouds can be detected by monitoring changes in cloud top temperature. Note that it may be difficult to apply this estimation to some clouds, such as vertically developed cumulonimbus clouds seen from an angle and thin cirrus clouds.

C) Land/Sea Surface Temperature Estimation (Window Bands)

Land and sea surface temperature can also be estimated from infrared window band imagery only when not covered by clouds. Sea surface temperature in the open ocean derived by satellite observation is particularly valuable information because there are few in-situ observations.

D) Reflected Sunlight Component (Band 7, Only in the Daytime)

The wavelength around 3.9 μm is largely affected by sunlight reflection. For this reason, an observed radiance of Band 7 contains both reflected sunlight and Earth's radiation in the daytime.

Generally, according to Fig. 1-2-25, 3.9 μm reflectance of clouds is larger when the particle size is smaller, and water clouds show larger reflectance than ice clouds. Among the water clouds, those over the sea surface usually have larger particle sizes and show smaller reflectance than those over the land. This feature can be used to distinguish the cloud particle size and phase. However, contamination of Earth's radiation makes it harder to distinguish them by only Band 7 imagery. To solve this problem, the method for extracting the reflected sunlight component of 3.9 μm by using the other window band around 10 μm has been devised (Rosenfeld, 2004). JMA applies this method for Band 7 using Band 13 as a 10 μm band. As shown in the Band 7 image in Fig. 1-2-26, the upper clouds (red arrow) consisting of ice appear brighter mainly because of their lower temperatures and smaller reflectance, and the lower clouds (blue arrow) appear darker. The reflected sunlight component image reveals that the upper clouds reflect less sunlight, and the lower clouds reflect more. The reflected sunlight component of Band 7 is also utilized in RGB imagery.

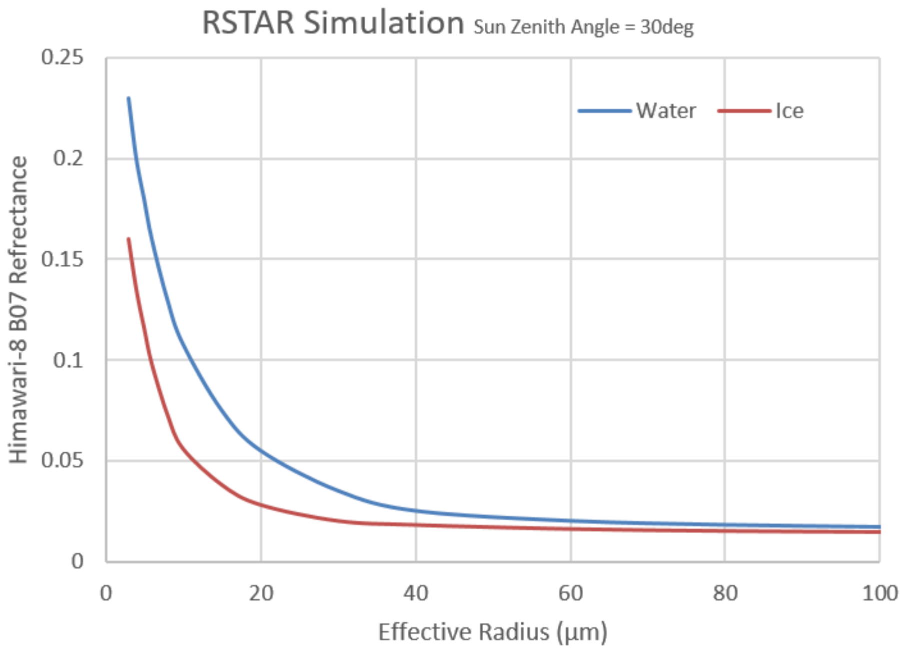

Fig. 1-2-25 3.9 μm reflectance of clouds depending on phase (water and ice) and effective radius simulated by the radiative transfer model RSTAR (Nakajima and Tanaka, 1986, 1988; Stamnes *et al.*, 1988)

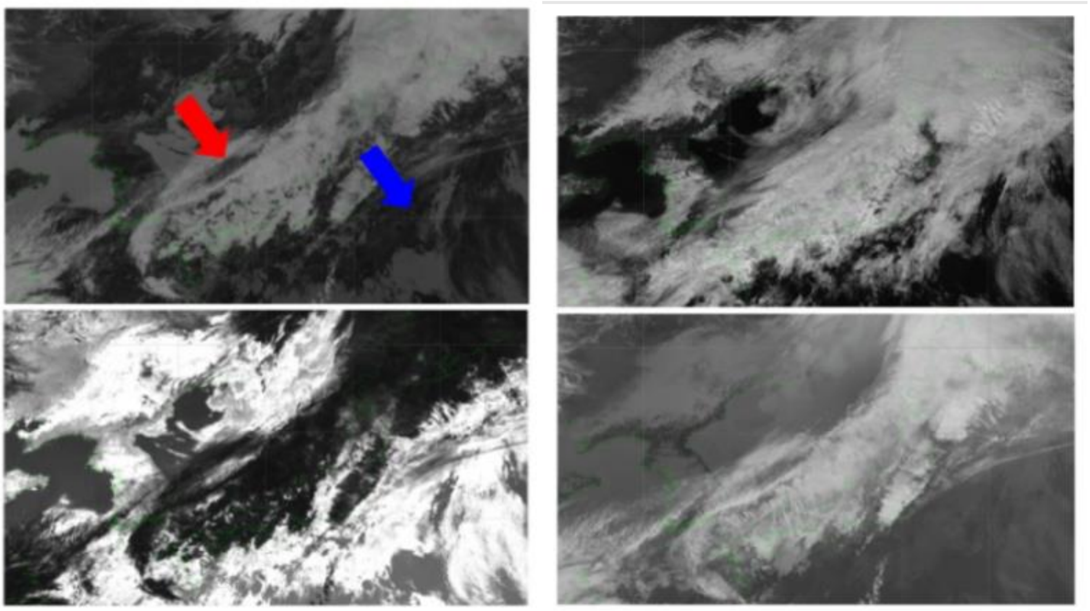

Fig. 1-2-26 Example of Band 7 (upper left) image and an image acquired by the method from Rosenfeld (2004) (lower left). Images of Band 3 (top right) and Band 13 (bottom right) at the

same time. Note that the lower left image has been rendered so that areas with larger reflectance are brighter, which is the same way as visible and near-infrared imagery.

E) Hotspot Detection (Band 7)

High-temperature heat sources such as wildfires, volcanoes, and industrial areas may appear as tiny dark areas in Band 7 (and tiny bright areas in Bands 5 and 6).

As shown in Fig. 1-2-27, radiance in Band 7 exponentially rises as blackbody temperature increases, while radiance in Band 13 gradually rises. In other words, if the target is hot enough, observed radiance in Band 7 will be highly sensitive to its temperature change. Assuming an area corresponding to one pixel of satellite observation, if a temperature of half of it is 300 K and the other half is 500 K, the brightness temperature of the entire pixel is not the arithmetic mean of them (400 K) but is approx. 420 K in Band 13 and approx. 460 K in Band 7 (Fig. 1-2-28). According to the above, hotspots appear even if heat sources are smaller than a pixel. In the example (Fig. 1-2-29), hotspots can be seen as tiny dark areas.

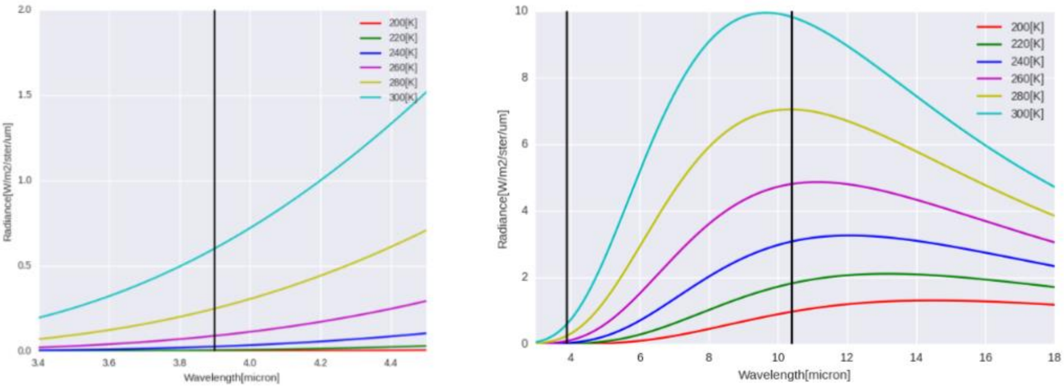

Fig. 1-2-27 Radiance of blackbodies at various temperatures in the spectral range from 3.4 to 4.5 μm (right panel) and from 3 to 18 μm (left panel), obtained from Planck's law. Black lines indicate central wavelengths of Himawari-8 AHI Band 7 in right panel, Band 13 in left panel, respectively.

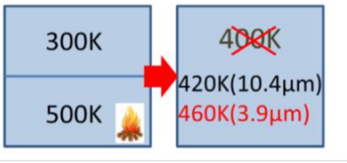

Fig. 1-2-28 Schematic diagram of satellite observation in Bands 7 (3.9 μm) and 13 (10.4 μm) of a pixel that half of it is 300 K and the other half is 500 K

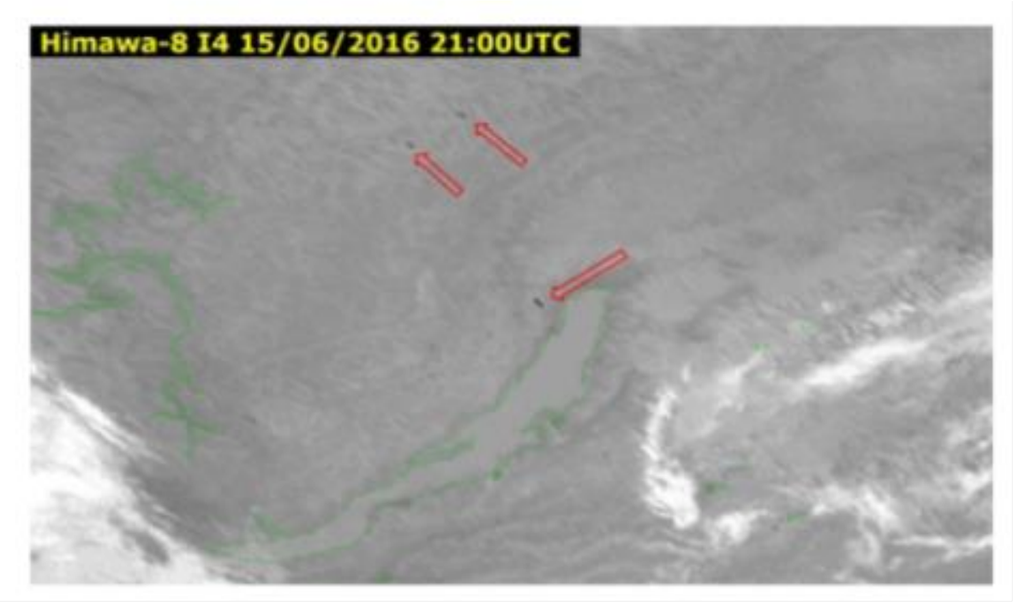

Fig. 1-2-29 Example of hotspots (wildfire near Lake Baikal) in Band 7

F) Fog Detection (Difference between Bands 7 and 13, Only in the Nighttime)

According to Fig. 1-2-30, the emissivity of stratocumulus/fog is smaller in 3.8 µm (equivalent to Band 7) than in 11 µm (equivalent to Bands 13 or 14), resulting in the observed brightness temperature being lower in Band 7 in the nighttime than in Band 13. Generally, difference imagery between Bands 7 and 13 is made by subtracting the brightness temperatures of Band 13 from Band 7, and areas with negative values are rendered as bright areas. Therefore, difference imagery between Bands 7 and 13 reveals potential stratocumulus/fog areas as bright areas, and it can be used for fog monitoring.

Figure 1-2-31 shows a case of fog or the lower clouds spread over the Seto Inland Sea. Though fog was observed in the surface observation around the Seto Inland Sea, it is difficult to identify fog areas by a Band 13 image. On the other hand, a difference image between Bands 7 and 13 shows bright areas with distinct edges corresponding to areas with fog/mist observation.

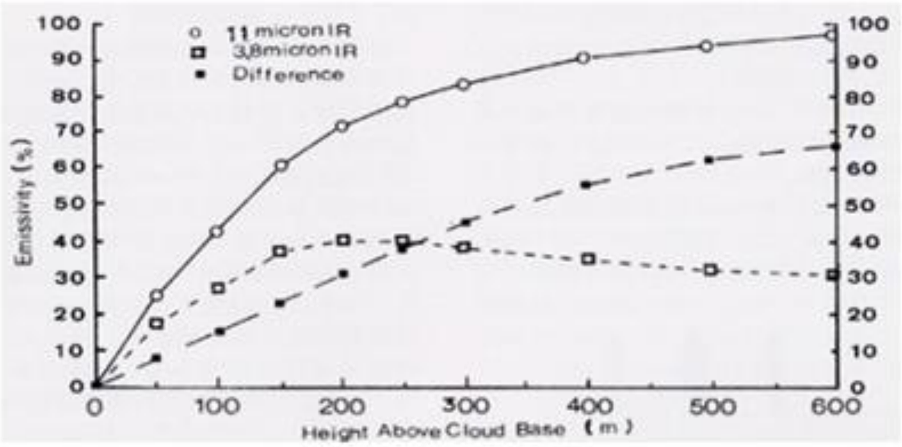

Fig. 1-2-30 Relationship between height above cloud base (i.e., cloud thickness) of stratocumulus of cloud water content 0.1 gm^{-3} and the emissivity (Ellrod, 1995)

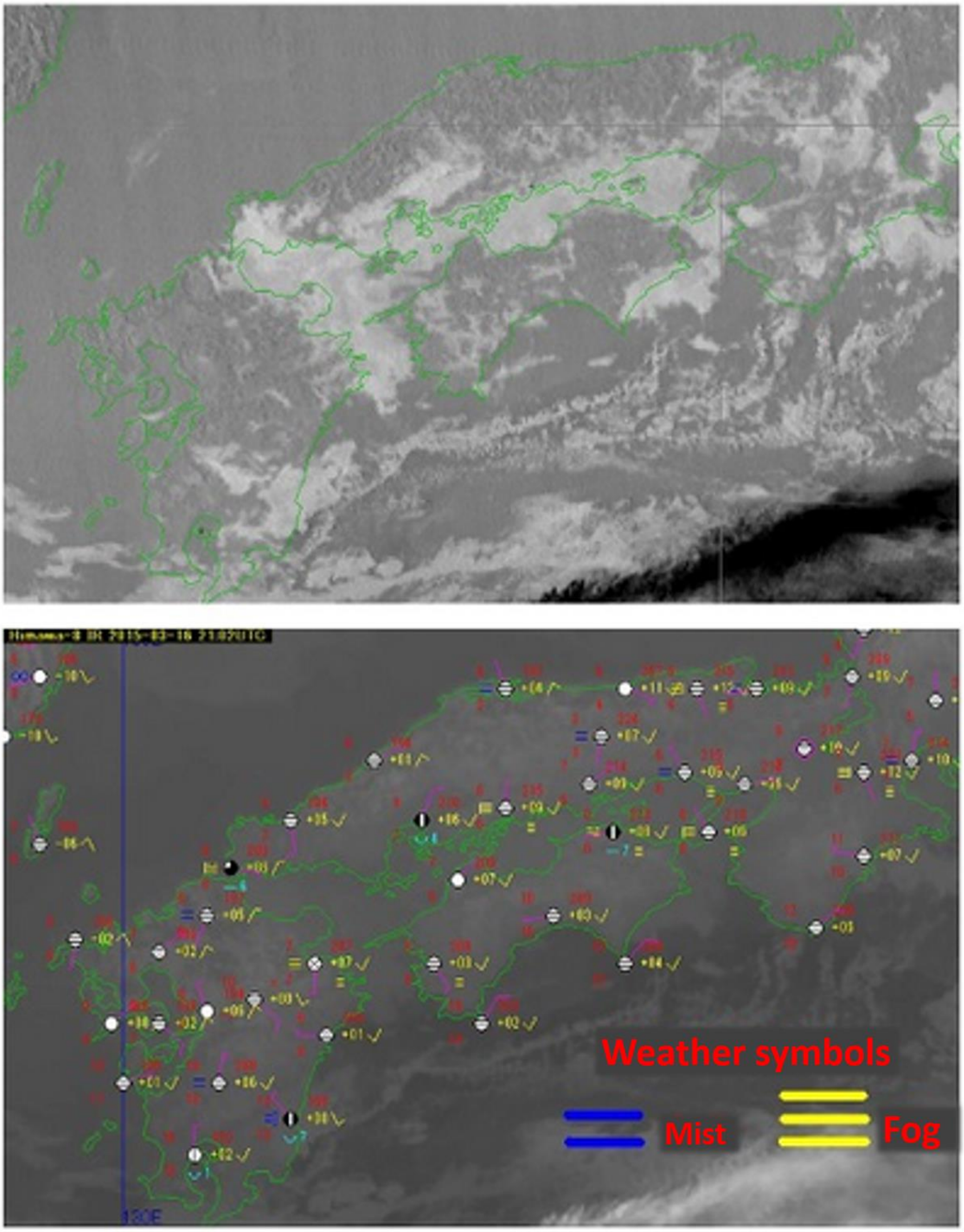

Fig. 1-2-31 Fog around the Seto Inland Sea. Top: a difference image between Bands 7 and 13; bottom: Band 13 with surface observation data.

G) Upper-cloud Distinction between Bands 7 and 13; Nighttime

At night, radiation from the relatively high-temperature earth surface penetrates thin higher clouds, adding to radiation from the cloud top. Accordingly, the cloud top temperature in Band 7 is higher than the actual value. As the transmission effect is larger for Band 7 than for Band 13, the cloud top temperature is higher than the infrared temperature, and the related difference is positive. In difference imagery, upper clouds appear differently mainly depending on their thickness. Thin upper clouds transmit radiation from below and appear to have a brightness temperature higher than the actual cloud top temperature (Fig. 1-2-32, MSC, 2005). It is possible to distinguish between cumulonimbus, which brings rainfall, and anvil cirrus, which does not.

Thick upper clouds do not transmit significant radiation from below, and brightness temperature is as low as cloud top temperature, resulting in dot noise as described previously.

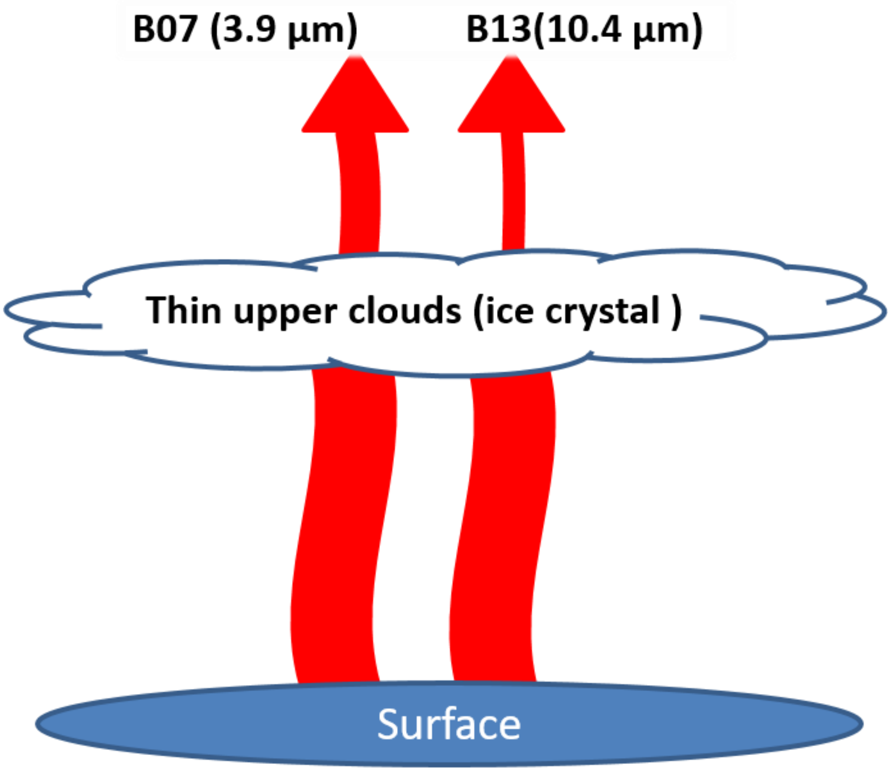

Fig. 1-2-32 Radiation through thin upper clouds in Bands 7 and 13 (MSC, 2005)

H) Land Surface Distinction between Bands 7 and 13; Nighttime

In this difference imagery, land surfaces may display certain characteristics because of emissivity differences between Bands 7 and 13. For example, the emissivity of sand is lower in Band 7 (Fig. 1-2-20), resulting in desert areas appearing bright as per Fig. 1-2-33.

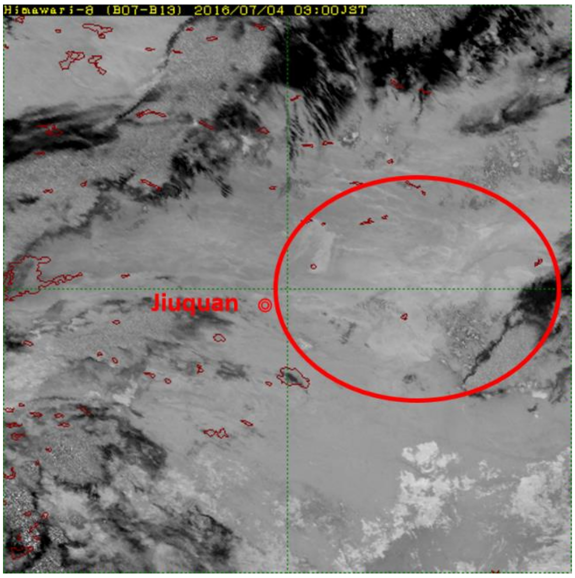

Fig. 1-2-33 Difference image between Bands 7 and 13 around the Gobi Desert at night. The desert area (red circle) appears brighter.

I) Atmospheric Characteristics in Upper/Middle Layers (Water Vapor Bands)

Atmospheric currents can be visualized in water vapor imagery using water vapor as a tracer, with bright and dark areas indicating upper to middle-level troughs, ridges, vortices and jet streams. Temporal changes in these areas enable estimation of trough deepening in upper to middle layers and the strength of subsidence in dry regions.

J) Observation of Wave Patterns (Water Vapor Bands)

The spatial resolution of infrared imagery at the sub-satellite point from Himawari-8/9 has been enhanced from the previous 4 km to 2 km, making phenomena easier to identify. As per Fig. 1-2-22, wave patterns (in red) are often found in water vapor imagery in correspondence with mountain lee waves, which provide important information for aircraft operations (MSC, 2002).

K) Sulfur Dioxide Monitoring (Bands 10 and 11)

As per Fig. 1-2-14, Bands 10 and 11 are sensitive to absorption by sulfur dioxide molecules. Figure 1-2-34 shows a volcanic eruption, with plume appearance being clearer in Bands 10 and 11 than in Band 8. The appearance is also distinctive in Bands 13 and 15, indicating potential other plume content such as water vapor and volcanic ash (due to the continuous water vapor absorption zone around the central wavelength of Band 13). Bands 11 and 13 show that the eastern part of the plume appears darker than the western part, suggesting more sulfur dioxide in the former.

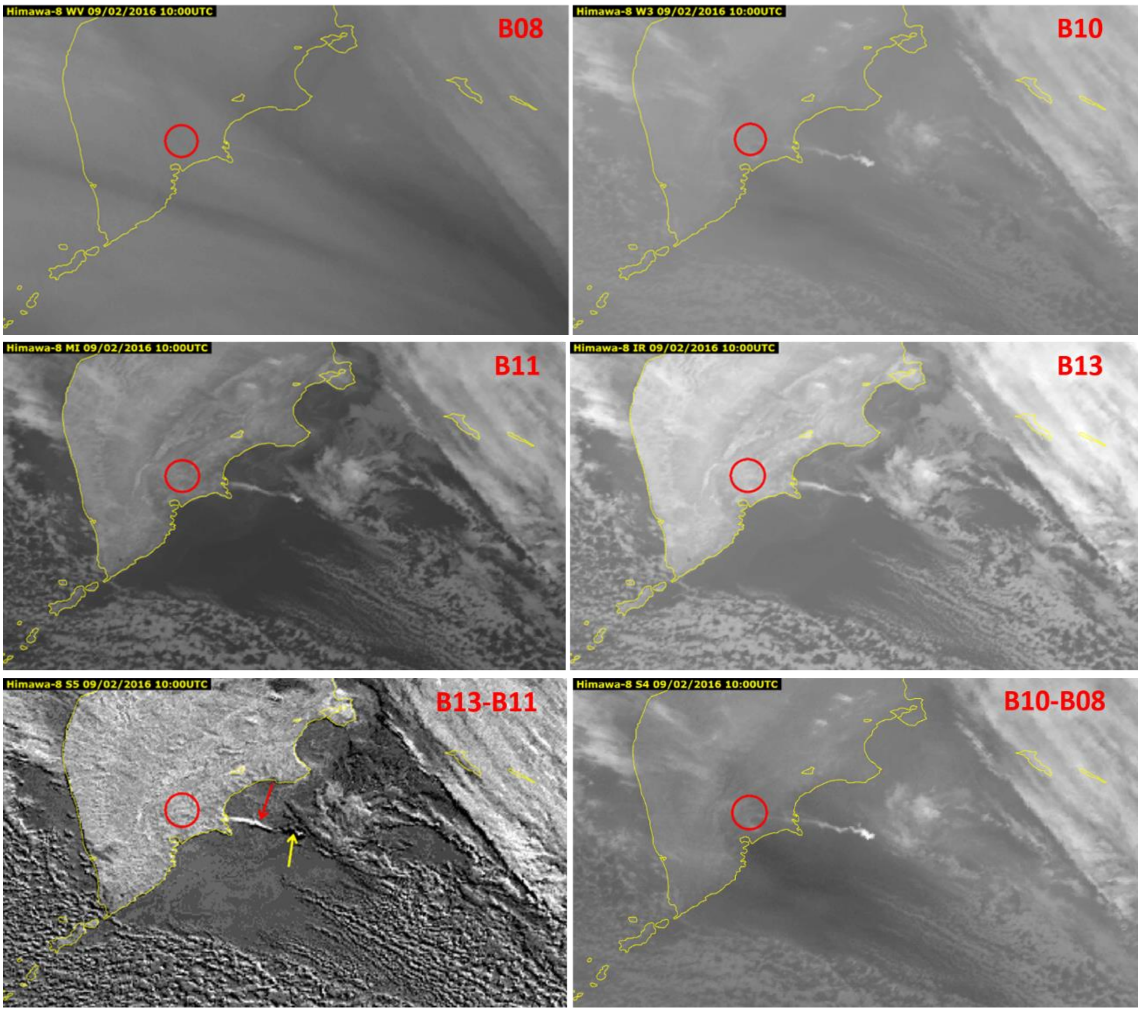

Fig. 1-2-34 Zhupanovsky eruption (red) on the Kamchatka Peninsula

L) Cloud Phase Distinction (Bands 11 and 15)

Band 11 imagery is more useful for estimating cloud particle phases than other window bands (e.g., Bands 13 and 14). As per Fig. 1-2-35, brightness temperature difference using Band 11 shows a much more noticeable difference between cloud particle phases than that of Band 15. Band 11 shows higher emissivity than Band 14 (Fig. 1-2-36) for upper ice clouds, resulting in a higher brightness temperature. Lower water clouds and sea surfaces exhibit lower brightness temperatures in Band 11 due to lower water vapor absorption and differences in emissivity, which supports cloud phase distinguishment. Accordingly, JMA/MSC uses Band 11 to obtain cloud particle phase information for cloud products.

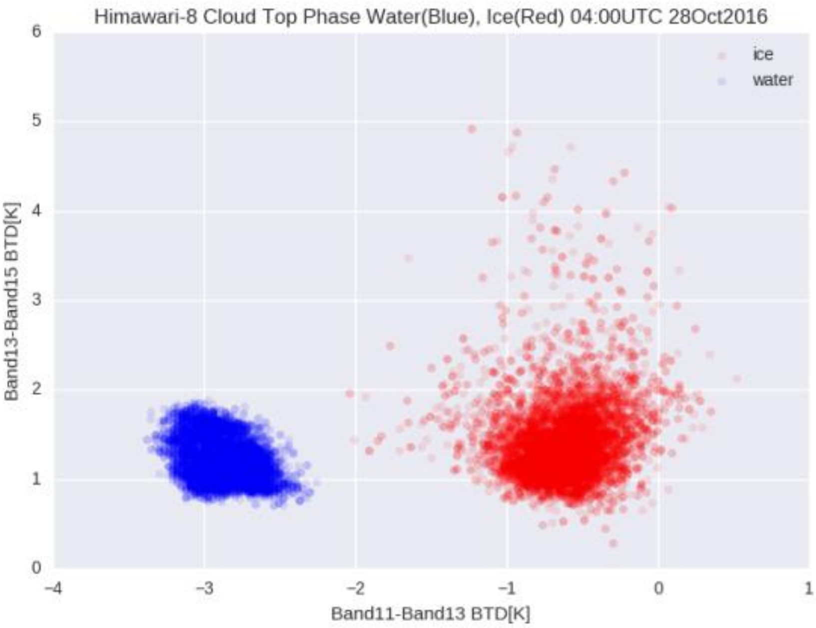

Fig. 1-2-35 Brightness temperature differences for tops of clouds consisting of ice (red) and water (blue). X-axis: Bands 11 – 13; Y-axis: Bands 13 – 15.

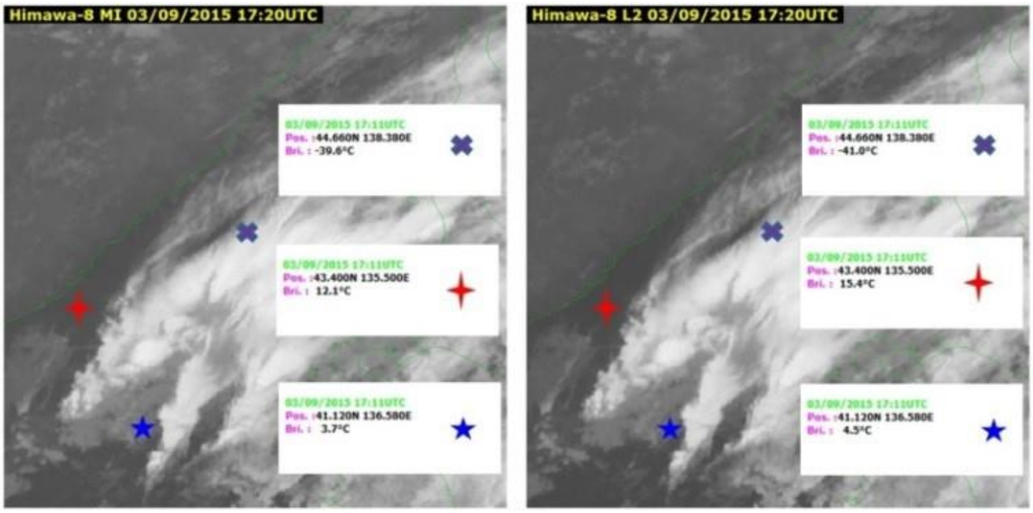

Fig. 1-2-36 Brightness temperature comparison between Bands 11 (left) and 14 (right)
Red crosses: thick high ice clouds; blue stars: low-level clouds; plus marks: clear conditions.

In Band 15, differences in absorption coefficients between water and ice crystals due to cloud phase are larger than in other window bands (Fig. 1-2-19). This makes the brightness temperature lower in thin upper clouds. Difference imagery in areas with large Band 13 – 15 values are therefore dark, making thin upper clouds appear darker (Fig. 1-2-37).

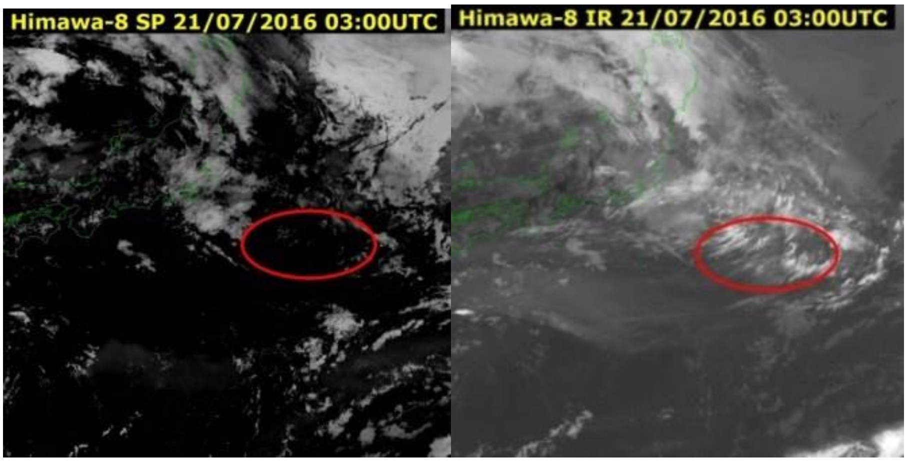

Fig. 1-2-37 Upper clouds in difference imagery between Bands 13 and 15 (left), and a Band 13 image (right). Red: thin upper clouds.

M) Ozone Analysis (Band 12)

As per Fig. 1-2-14, Band 12 is sensitive to absorption by ozone molecules, making its weighting function have a stratospheric peak above 100 hPa. Generally, ozone molecules are generated in the stratosphere in the tropics and transported to middle and high-latitude regions by Brewer-Dobson circulation, which have relatively large amounts of ozone except for the Antarctic region where the ozone hole is located. As per Fig. 1-2-38, Band 12 has a larger color gradient from low to high-latitude regions than Band 13, partially due to this ozone distribution. In Band 12 imagery, white stripes may appear in areas corresponding to dark areas of water vapor imagery, as per Fig. 1-2-39 (upper right, circled in yellow). The positive 300 hPa vorticity in the figure supports a conclusion of high ozone concentration at relatively low heights and potential tropopause folding (Zwatz-Maise, 2004). Difference imagery between bands 12 and 13 shows darker shades (lower left, Fig. 1-2-39, circled in yellow).

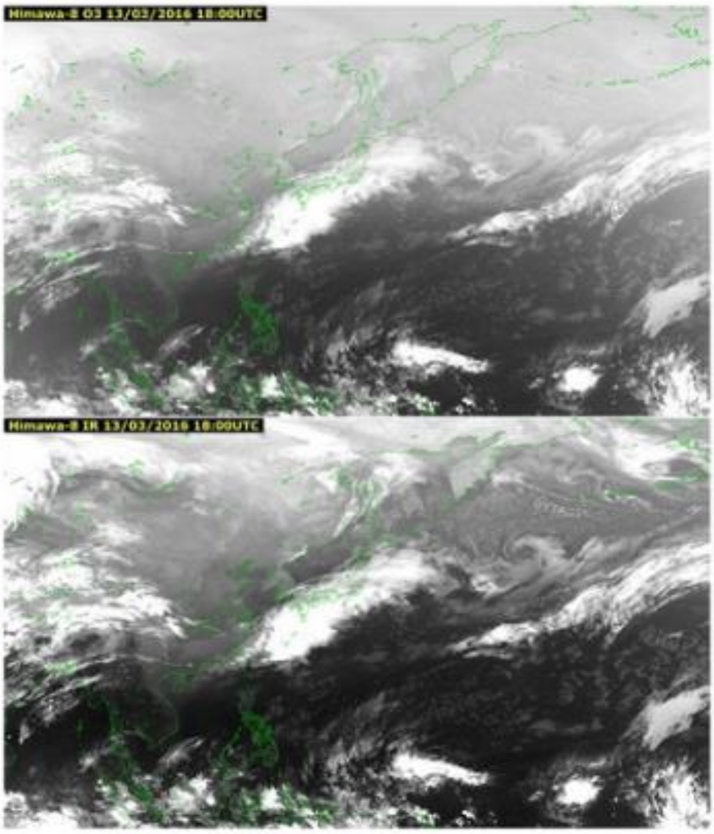

Fig. 1-2-38 Bands 12 (top) and 13 (bottom), with brightness temperature ranges of 220 to 300 K for both

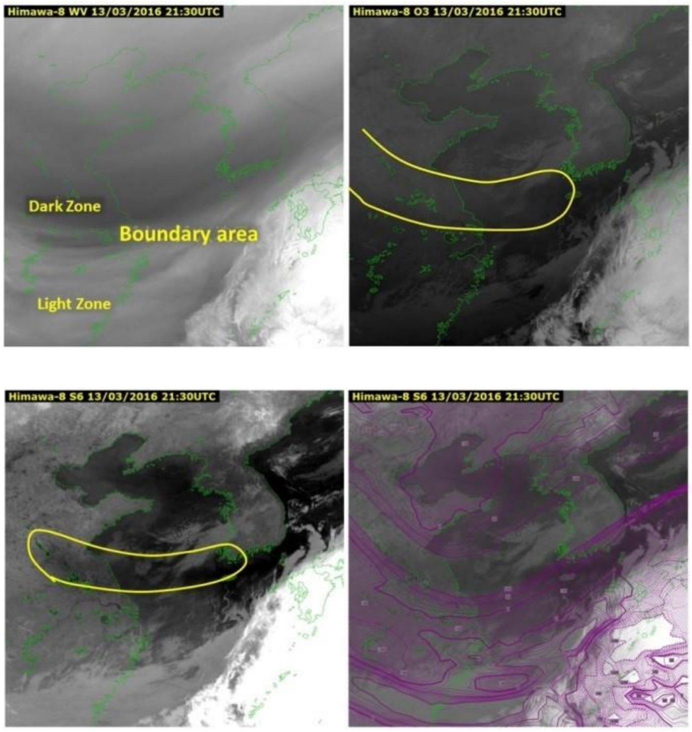

Fig. 1-2-39 White stripe in Band 12. Upper left: Band 8; upper right: Band 12; lower left: difference image between Bands 13 and 12; lower right: overlay of the same difference image and 300 hPa vorticity distribution from GSM (shading: negative vorticity).

N) Response to Silica in Volcanic Ash and Aeolian Dust (Band 15)

Since the emissivity of silica is larger in Band 15 than in Band 13, Band 15 imagery and difference imagery between the two can be used for detection of volcanic ash and Aeolian dust. This also applies to the emissivity of sand in Fig. 1-2-20. In Fig. 1-2-40, as seen from the correspondence with surface observation, the bright area in a difference image between Bands 13 and 15 corresponds to high concentrations of Aeolian dust.

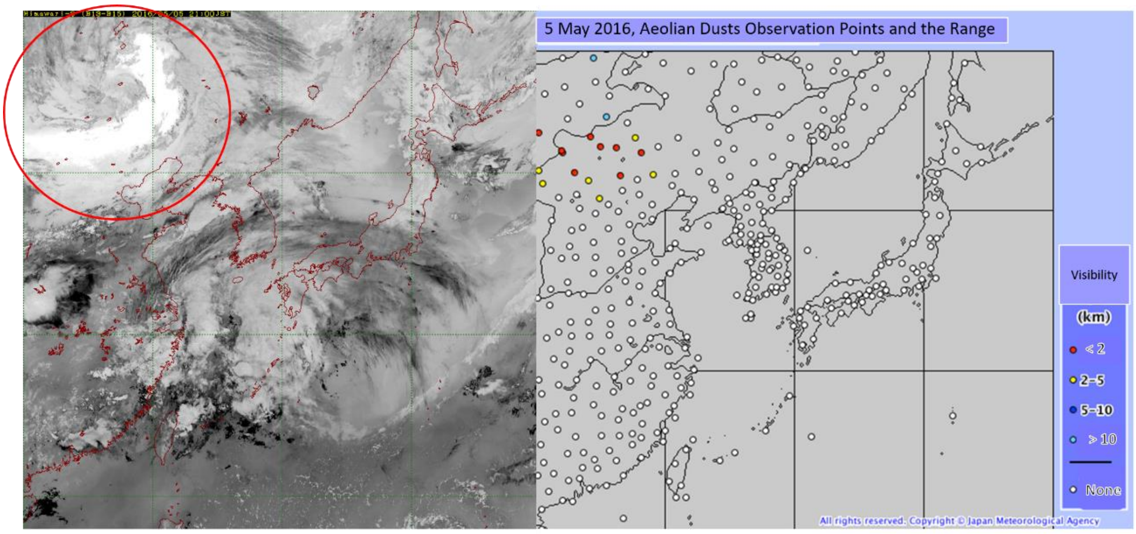

Fig. 1-2-40 Aeolian dust. The bright area within a red circle in the difference image between bands 13 and 15 (left) corresponds to high concentrations of Aeolian dust. The right panel shows surface observation of visibility at the same time (from the JMA website).

Figure 1-2-41 shows a volcanic eruption in Sakurajima in May 2016. The bright area in the difference image between Bands 13 and 15 corresponds to volcanic ash containing silica. The distinction between volcanic ash and upper clouds is much easier in the difference image than in the Band 3 image. Unlike Band 3 imagery, Band 15 imagery and related difference imagery applies to both day and night.

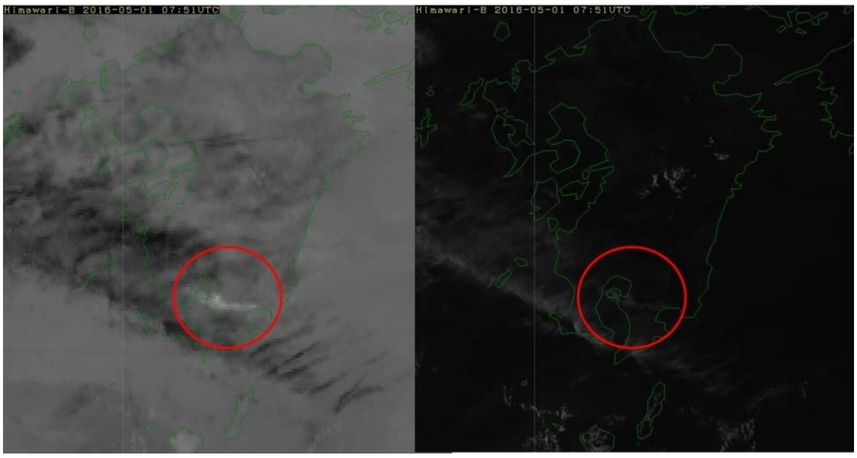

Fig. 1-2-41 Volcanic eruption in Sakurajima. Left: difference image between Bands 13 and 15; right: Band 3 image. The bright area on the left (red circle) corresponds to volcanic ash.

O) Response to Carbon Dioxide (Band 16)

As per Fig. 1-2-14, Band 16 is sensitive to absorption by carbon dioxide molecules. Accordingly, brightness temperatures in Band 16 are lower overall than in Band 13 (Fig. 1-2-42). Those in Band 16 are almost the same for thick clouds, but are much lower for lower clouds and cloudless sea surfaces (Fig. 1-2-43). This is because absorption by carbon dioxide in the lower atmosphere lowers the observed brightness temperature (Fig. 1-2-44).

It is difficult to estimate carbon dioxide distribution using only satellite imagery because temperature and water vapor distributions in the troposphere constantly change.

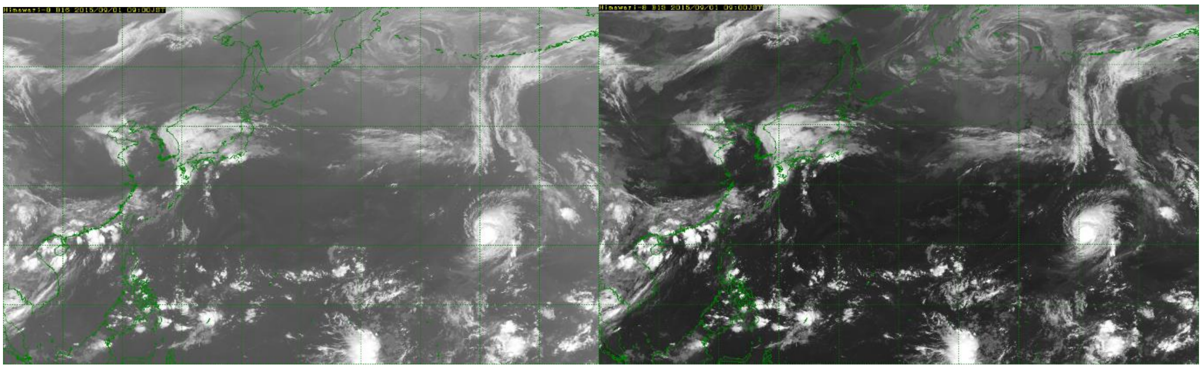

Fig. 1-2-42 Comparison of Bands 16 (top) and 13 (bottom) images. The brightness temperature range is 210 to 310 K for both.

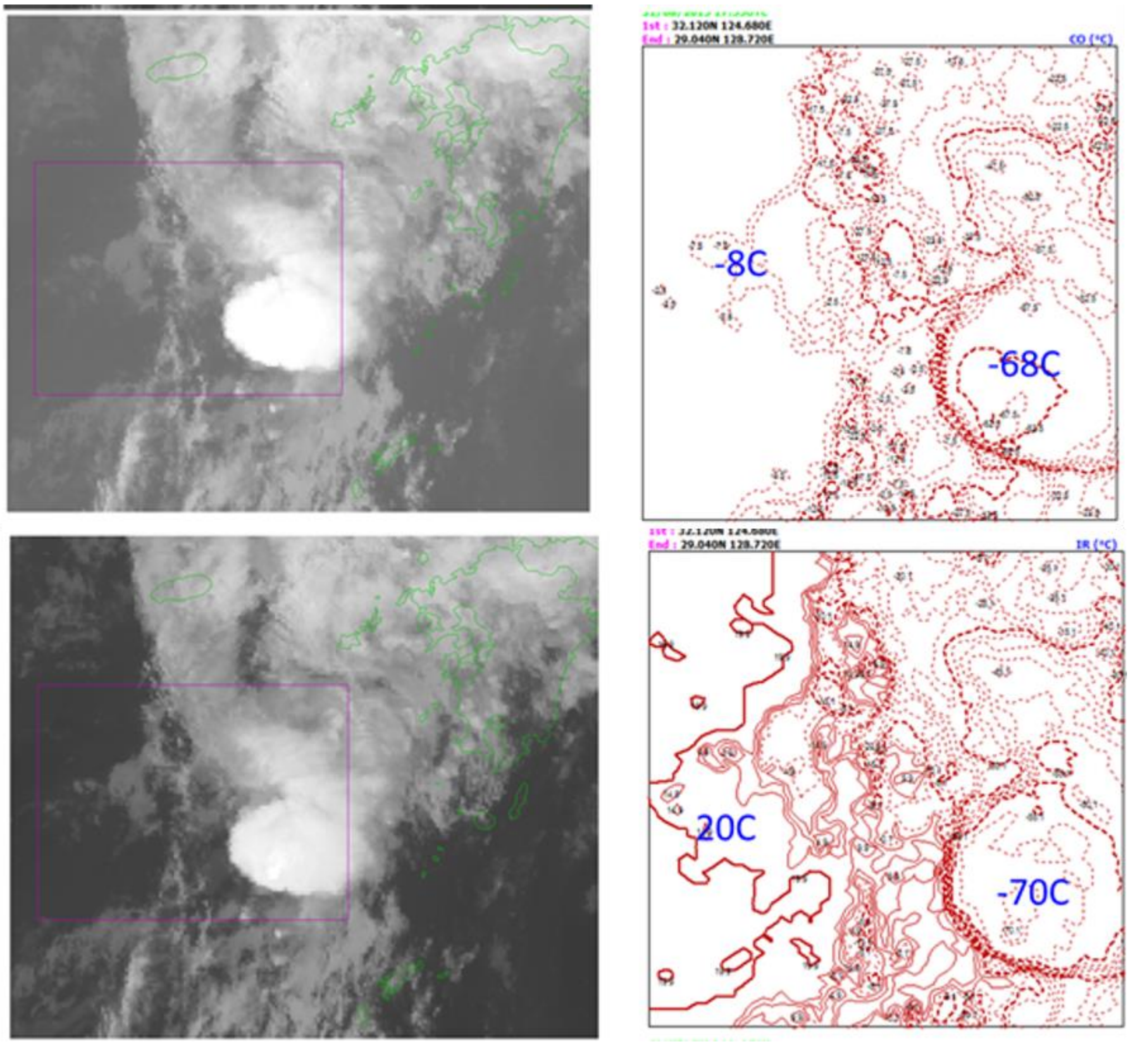

Fig. 1-2-43 Comparison of Bands 16 (top) and 13 (bottom). The right panels show brightness temperature distribution for the pink rectangle on the left.

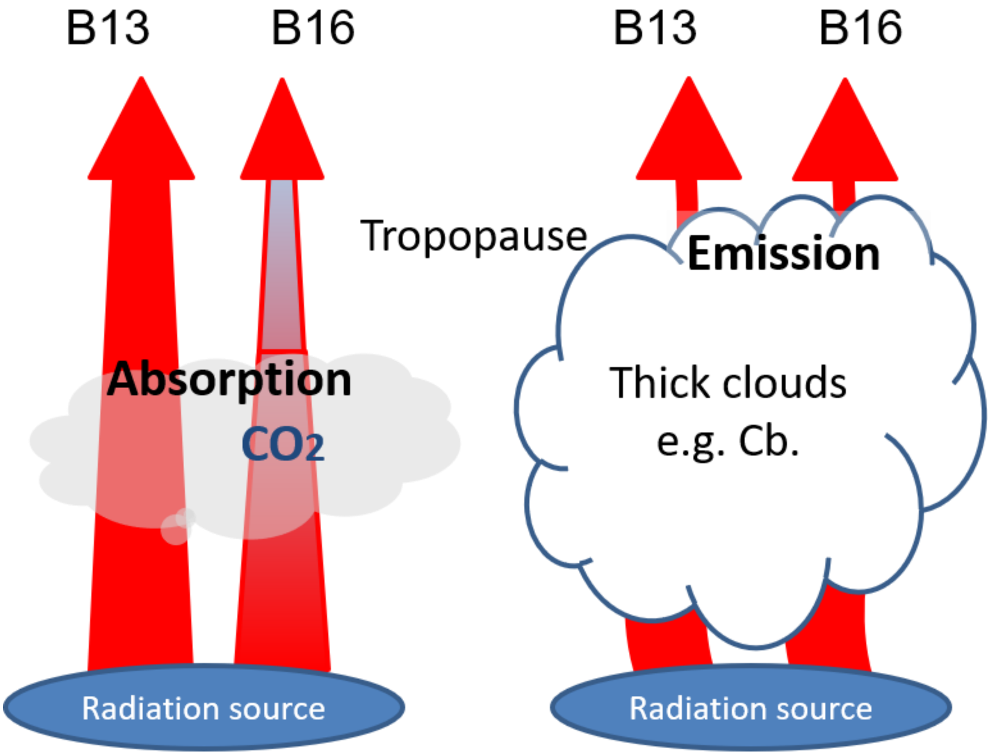

Fig. 1-2-44 Difference in radiance between Bands 13 and 16

(5) Infrared Band Characteristics

The characteristics of the bands described in this chapter are as below (values in parentheses: central wavelengths).

- Band 7 (3.9 µm)
    - One of the window bands
    - The successor to IR4 on MTSAT-2
    - Used for hotspot detection
    - Significantly affected by sunlight reflection, with observed radiance containing both reflected sunlight and Earth radiation for the daytime
    - Reflected sunlight component sensitive to cloud particle phases
- Band 8 (6.2 µm)
    - One of the water vapor bands
    - According to the weighting function, correspondence to the upper troposphere (the highest altitude among water vapor bands)
    - The successor to IR3 on MTSAT-2
- Band 9 (6.9 µm)
    - One of the water vapor bands
    - According to the weighting function, correspondence to the upper to middle troposphere (slightly below Band 8)

- Band 10 (7.3 µm)
    - One of the water vapor bands
    - According to the weighting function, correspondence to the middle troposphere (the lowest altitude among water vapor bands)
    - Sensitive to sulfur dioxide and useful for monitoring volcanic gas
- Band 11 (8.6 µm)
    - One of the window bands (more affected by atmospheric molecules than Bands 13 to 15)
    - Sensitive to cloud particle phases
    - Sensitive to sulfur dioxide and useful for monitoring volcanic gas
- Band 12 (9.6 µm)
    - Sensitive to ozone
- Band 13 (10.4 µm)
    - One of the window bands
    - The successor to IR1 on MTSAT-2.
    - Observation of radiation in the most transparent wavelength region (the closest transmittance to 1 among Bands 13 to 15; known as a clean window band)
- Band 14 (11.2 µm)
    - One of the window bands
- Band 15 (12.4 µm)
    - One of the window bands
    - The successor to IR2 on MTSAT-2
    - Observation radiation with the least transmittance among Bands 13 to 15 (known as a dirty window band)
    - Sensitive to cloud particle phases and useful for distinguishing especially thin upper clouds
    - Different characteristics from Band 13 for silica (abundant in volcanic ash and Aeolian dust)
- Band 16 (13.3 µm)
    - Sensitive to carbon dioxide

References:

- Clerbaux C., J. R. Drummond, J. Fland and J. Orphal, 2011: Remote Sensing of Tropospheric Composition from Space, https://doi.org/10.1007/978-3-642-14791-3
- Delst, P. van and Y. Han, 2008: CRTM Technical Subgroup Report, 2, available at https://itwg.ssec.wisc.edu/wordpress/wp-content/uploads/2023/05/04_13_CRTMWG_itsc16.pdf

- Ellrod, G. P., 1995 : Advance in the Detection and Analysis of Fog at Night Using GOES Multispectral Infrared Imagery, Weather and forecasting, 10, 606-619.
- GOES-R Program Office (NOAA Satellite and Information Service), 2015-2016: ABI Bands Quick Information Guides, available at http://www.goes-r.gov/education/ABI-bands-quick-info.html
- Hayashi, M., 2018: Introduction to the Computation Method for Cloud Radiative Processes and Its Application for the Advanced Himawari Imager onboard Himawari-8, Meteorological Satellite Center Technical Note, No.63, 1-38 (Japanese).
- Kumabe, R. (ed.), 2006: Meteorology from satellites: on the uses of multi-channel data, meteorological research notes, No.212, 51 – 54 (Japanese).
- Li, J., C. C. Schmidt, J. P. Nelson, T. J. Schmit, and W. P. Menzel, 2001: Estimation of total atmospheric ozone from GOES sounder radiances with high temporal resolution, Journal of Atmospheric and Oceanic Technology, 18, 157-168, available at
- https://doi.org/10.1175/1520-0426(2001)018<0157:EOTAOF>2.0.CO;2
- Murata, H., M. Takahashi and Y. Kosaka, 2015: VIS and IR bands of Himawari-8/AHI compatible with those of MTSAT-2/Imager, Meteorological Satellite Center technical note, No.60, 1-18.
- MSC, 2000: “Analysis and usages of meteorological satellite imageries”, General meteorology version, 1 - 12 (Japanese).
- MSC, 2002: “Analysis and usages of meteorological satellite imageries”, Aviation meteorology version, 27 - 28 (Japanese).
- MSC, 2005: “Analysis and usages of meteorological satellite imageries”, Analysis and Usages of 3.8μm version, 23 - 24 (Japanese).
- Nakajima, T. and M. Tanaka, 1986: Matrix formulation for the transfer of solar radiation in a plane-parallel scattering atmosphere, J. Quant. Spectrosc. Radiat. Transfer, 35, 13-21.
- Nakajima, T. and M. Tanaka, 1988: Algorithms for radiative intensity calculations in moderately thick atmospheres using a truncation approximation, J. Quant. Spectrosc. Radiat. Transfer, 40, 51-69.
- Rosenfeld, D., 2004: Applications of Meteosat Second Generation (MSG) CONVERSION FROM COUNTS TO RADIANCES AND FROM RADIANCES TO BRIGHTNESS TEMPERATURES AND REFLECTANCES, available at https://rammb.cira.colostate.edu/wmovl/vrl/pptlectures/eumetsat/PowerPoints/Channels/conversion.ppt
- Schmetz, J., Y. Govaerts, K. Marianne, H. Lutz, A. Ratier and S. Tjemkes, 2004: A short introduction to METEOSAT Second Generation (MSG), 1-9, available at http://www.eumetsat.int/website/wcm/idc/idcplg?IdcService=GET_.FILE&dDocName=ZIP_MSG_GUIDE_C&RevisionSelectionMethod=LatestReleased&Rendition=Web
- Simizu, K., K. Saito, and M. Yamamoto, 2017: “Characteristics of imageries of AHI 16

bands / Himawari-8", MSC Technical Report No.62, 39 - 71 (Japanese).

- Stamnes, K., S.-C. Tsay, W. Wiscombe, and K. Jayaweera,1988: Numerically stable algorithm for discrete-ordinate-method radiative transfer in multiple scattering and emitting layered media, Appl. Opt., 27, 2502-2509.
- WMO, 2007: RGB composite satellite imagery workshop final report (5-6 JUNE 2007 Boulder, CO, U.S.A.), available at http://www.wmo.int/pages/prog/sat/documents/RGB-1_Final-Report.pdf
- WMO, 2012: WMO/EUMETSAT workshop on RGB satellite products final report (17-19 SEPTEMBER 2012, Seeheim, Germany), available at http://www.wmo.int/pages/prog/sat/documents/RGB-WS-2012_FinalReport.pdf
- Yokota, H. and M. Sasaki, 2013: "Introduction to geostationary earth environment observation satellite "Himawari8 and 9"", MSC Technical Report, No.58, 121-138 (Japanese).
- Zwatz-Meise, V., 2004: Introduction into the Absorption Channels: Description of characteristics and content of the Ozone channel: Ch08: 9.7, 12-27, available at http://oiswww.eumetsat.org/WEBOPS/msg_interpretation/PowerPoints/Channels/O3guide.ppt

Websites:

- JMA homepage
  (Observation examples of Himawari)
  http://www.jma-net.go.jp/sat/himawari/image.html (Japanese)
  (The world distribution map of monthly average of total ozone volume)
  http://www.data.jma.go.jp/gmd/env/ozonehp/totozone_glbsat_monthave.html (Japanese)
  (Aeolian dust distribution)
  http://www.jma.go.jp/en/kosa/
- JMA/MSC
  (Himawari-8/9 Operational Information)
  http://www.data.jma.go.jp/mscweb/en/operation8/index.html
  http://www.jma-net.go.jp/msc/en/index.html
- NASA
  Spectral Response Function Database
  https://www-pm.larc.nasa.gov/cgi-bin/site/showdoc?mnemonic=SPECTRAL-RESPONSE

1.3. Imagery Comparison

In this section, the imagery characteristics described above are separated into day and night for clarification with specific examples. Table 1-3-1 lists the relevant imagery types and related transition. In difference imagery for Band 13 and Band 15 (referred to here as B13-B15) and for Band 7 and Band 13 (B07-B13), larger differences appear darker and smaller differences appear lighter.

Table 1-3-1. Imagery appearance

Types	Imagery appearance				
	White	**Light grey**	Grey	Dark grey	Black
Visible (B03)	←	High reflectance		High reflectance	→
Near-infrared (B04, 05)	←	Low reflectance		Low reflectance	→
Water vapors (B08, 09, 10)	←	Wet		Dry	→
Infrared (B13)	←	Low temperature		High temperature	→
B13-B15	←	Negative		Positive	→
B13-B07	←	Negative		Positive	→

1.3.1. Daytime Imagery

This section compares visible (Fig. 1-3-1), near-infrared (Fig. 1-3-2), water vapor (Fig. 1-3-3), infrared (Fig. 1-3-4) and infrared difference (B13-B15, Fig. 1-3-5) image from 03:00 UTC (12:00 JST) on 7 March 2016.

In visible imagery, cloud area A above the eastern sea off Amami Island is shown as a bulky cluster along with cloud area B. It has a streaky appearance and lower density than in B. The temperature is slightly higher (dark grey) in infrared imagery and related reflectance is higher (white) in near-infrared imagery for sensitivity to cloud particles in the water phase, indicating that the area is underdeveloped convective cloud (Cu).

The temperature of cloud area B is slightly lower (light grey) than in cloud area A, showing lower reflectance (grey) in near-infrared imagery. This is assumed to be an area of convective cloud containing cumulus congestus (Cg) with a higher top than the Cu of cloud area A.

Cloud area C can be judged as convective containing Cb. This is based on the overall thicker appearance in visible imagery, the lower temperature (white) than the surrounding cloud area in infrared imagery, and the display of cloud with lower reflectance (grey) in near-infrared imagery. The area is also bright in water vapor imagery and grey with little temperature difference in infrared difference imagery.

The temperature of cloud area D is low (white) in infrared imagery, with large reflectance (white) in visible imagery and low reflectance (dark grey) in near-infrared imagery, indicating a thick cloud area with a high top. Cloud area E has a lower temperature than D (white – light grey) in infrared imagery as well as being darker in visible imagery and having lower reflectance (dark grey) in infrared imagery, suggesting thin Ci. The appearance in water vapor imagery is similar to that of infrared imagery, although with obscurity at the edge of the cloud area. In infrared difference imagery, a minor temperature difference (light grey) is seen in association with cloud area D. A large temperature difference (black) is indicated for cloud area E, which appears to be thin Ci.

Region F is white in visible imagery, grey in infrared imagery and white in near-infrared imagery, altogether indicating an area with lower cloud. The smoothness of the cloud top surface with the same color tone as in visible/near-infrared imagery suggests a lower cloud area containing fog.

Region G is grey in visible/near-infrared imagery and white in infrared difference imagery. This corresponds to the region of Aeolian dust described in Section 1.2.

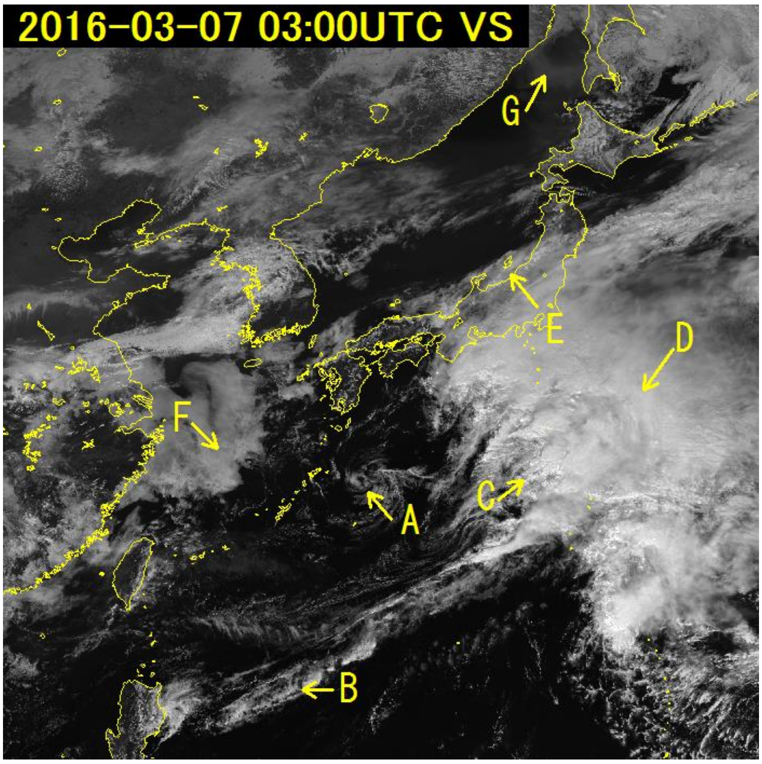

Fig. 1-3-1. B03 visible image for 03:00 UTC on 7 March 2016

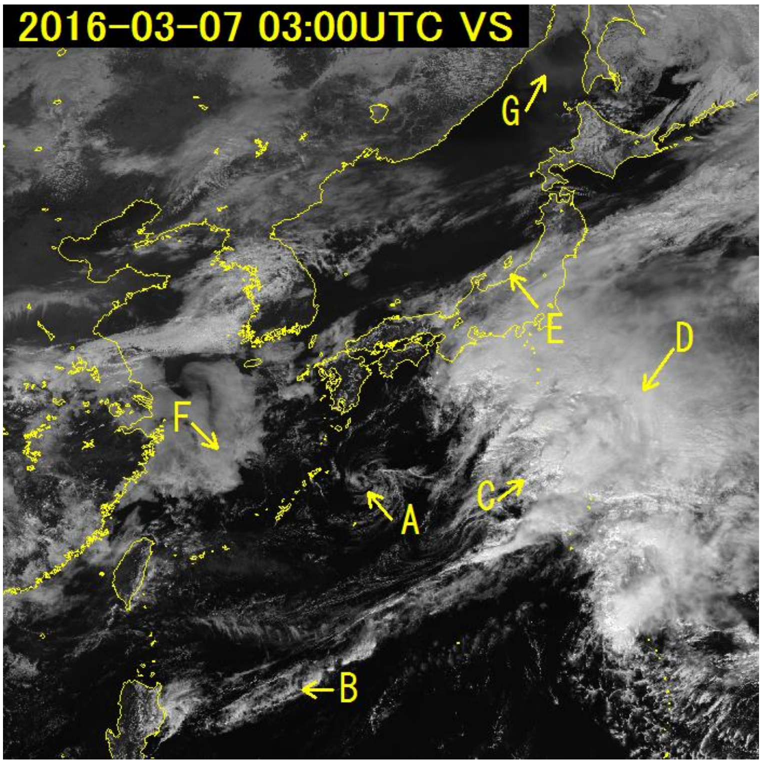

Fig. 1-3-2. B13 infrared image for 03:00 UTC on 7 March 2016

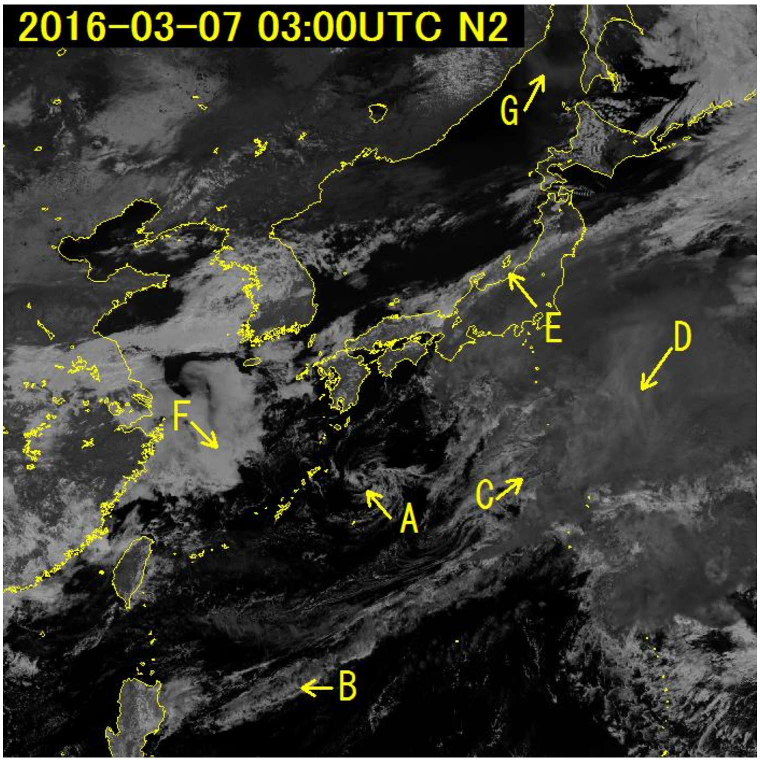

Fig. 1-3-3. B05 near-infrared image for 03:00 UTC on 7 March 2016

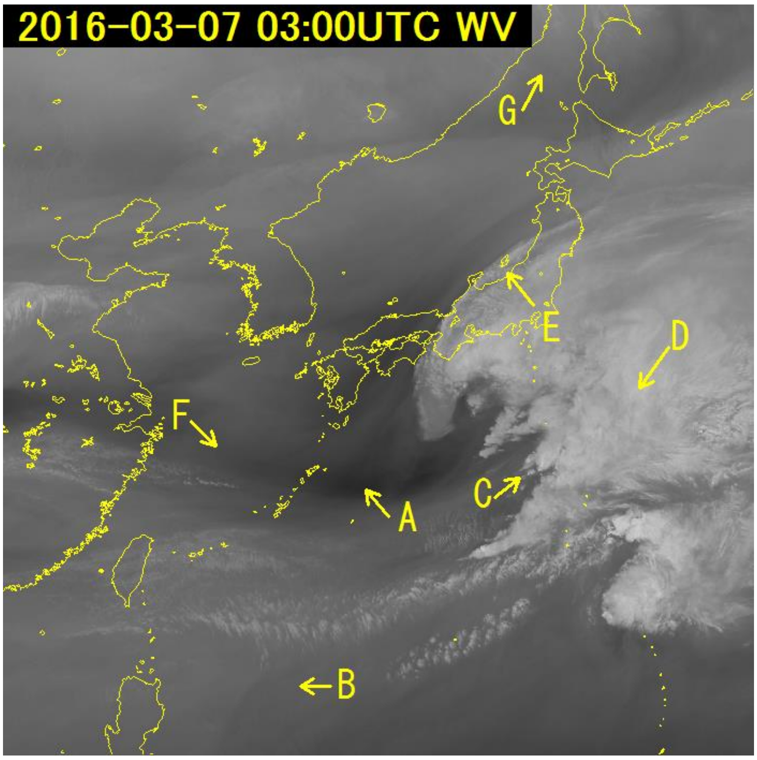

Fig. 1-3-4. B08 water vapor image for 03:00 UTC on 7 March 2016

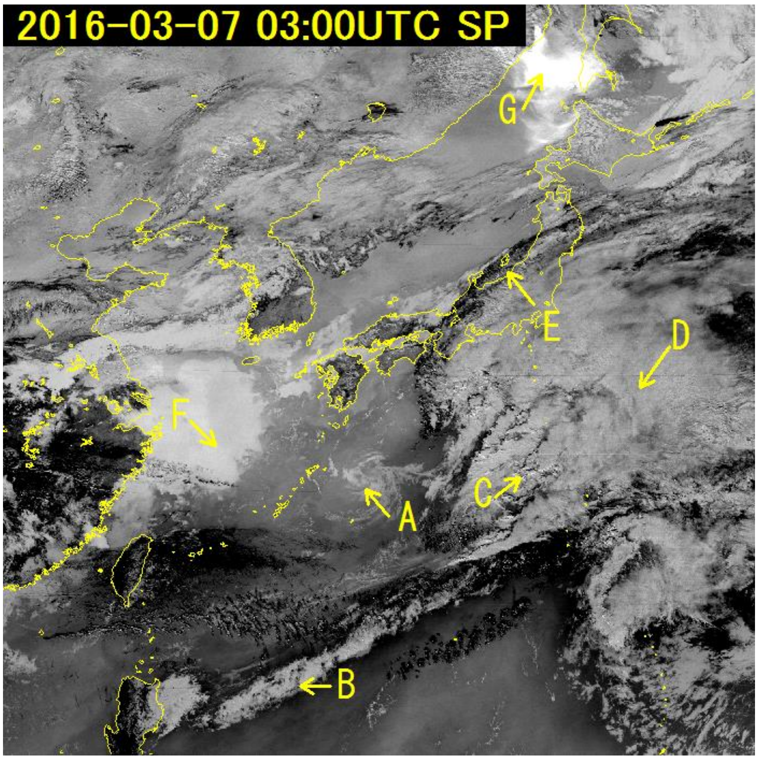

Fig. 1-3-5. B13-B15 infrared difference image for 03:00 UTC on 7 March 2016

1.3.2. Nighttime Imagery

In this section, B13 infrared (Fig. 1-3-6) imagery from 18:00 UTC on 6 March 2016 (03:00 JST on 7 March) is compared with difference image for B13-15 (Fig. 1-3-7) and B07-B13 (Fig. 1-3-8).

In Region A, a bright area is seen only in B13-B15. This corresponds to the region of Aeolian dust mentioned in the previous section. It is not seen in infrared imagery.

Region B shows a bright area in infrared imagery that displays as dark in the two difference images. As discussed above, this region corresponds to thin upper clouds. Identifying upper cloud areas is more difficult with infrared imagery; however, the B07-B03 image shows a thin upper cloud area in black since radiation from the lower layer is transmitted through it, making it easily distinguishable.

In Region C, the area is bright in infrared imagery, grey in B13-B15, and dotted in B07-B13. These correspond to an area of thick cloud with a high top, such as cumulonimbus. These areas are in a region at the front of two cyclones to the south of Japan.

Region D shows lower cloud in white/light grey in B07-B13 and grey in infrared imagery. As seen in Fig. 1-3-9, fog/mist is seen at many observation areas between northern Kyushu and the Tsushima Strait, indicating that D is a lower-cloud area containing fog.

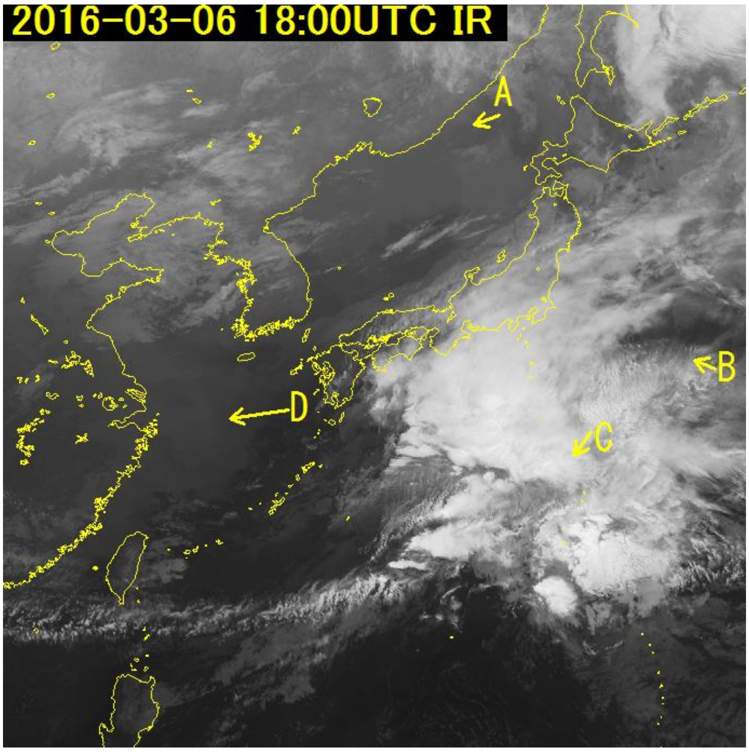

Fig. 1-3-6. B13 infrared image for 18:00 UTC on 6 March 2016

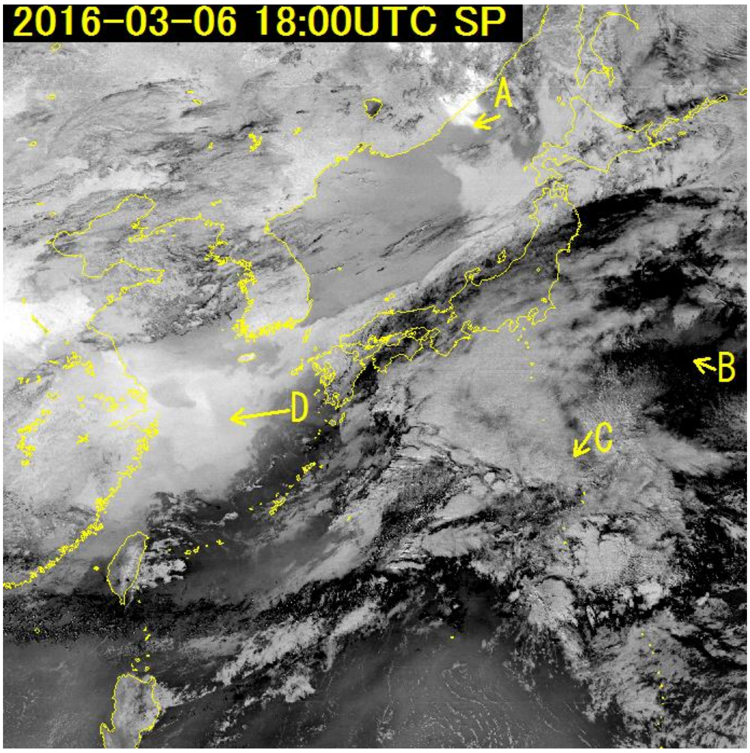

Fig. 1-3-7. B13-B15 infrared difference image for 18:00 UTC on 6 March 2016

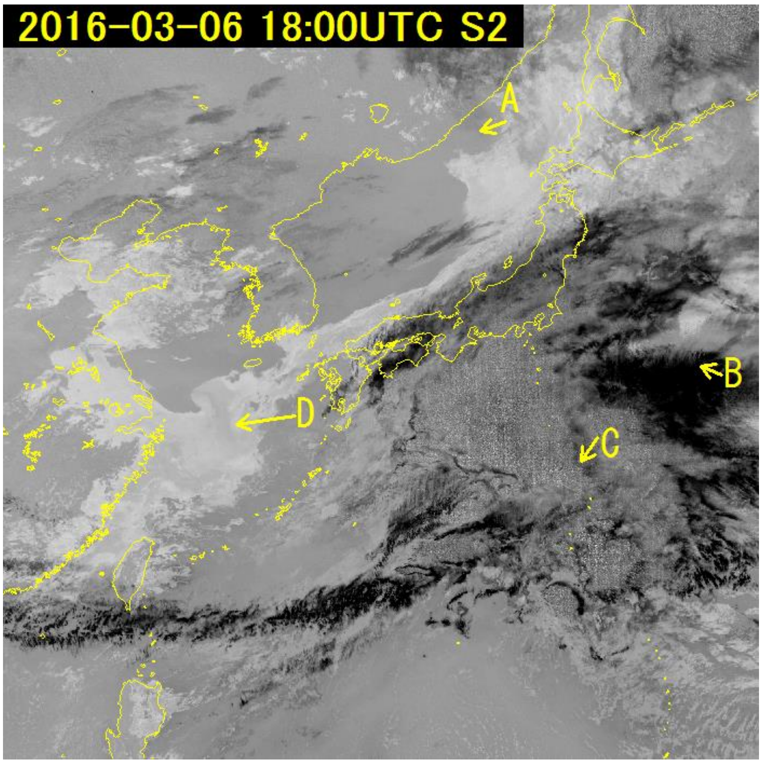

Fig. 1-3-8. B07-B13 infrared difference image for 18:00 UTC on 6 March 2016

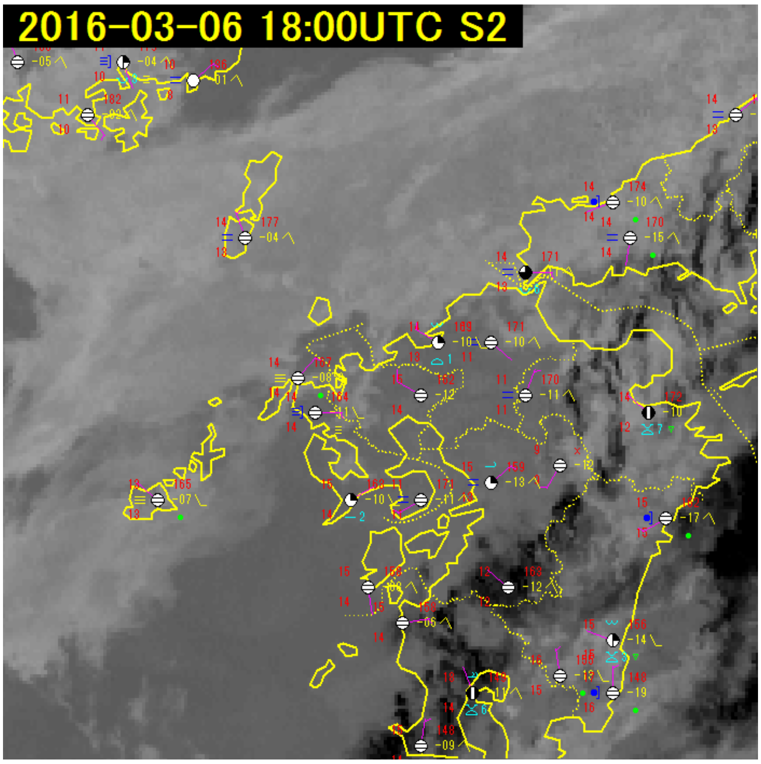

Fig. 1-3-9. B07-B13 infrared difference image for 18:00 UTC on 6 March 2016 based on surface meteorological observation

1.4. RGB Composite Imagery

1.4.1. Principles of RGB Composite Imagery

RGB (red, green, blue) composites display satellite imagery with overlays in combinations of the three primary colors (Fig. 1-4-1).

This technique makes identification of cloud areas and obscure phenomena easier than with simpler imagery based on bands or differences. However, variables such as latitude, seasonal conditions and the characteristics of satellite-mounted radiometers may require display outside the range of standard tones, making assessment based solely on color hues more difficult in certain cases. Accordingly, it is important to fully comprehend the characteristics of the bands used in compositions.

For clarity, the global standard for RGB composite imagery has been proposed by the WMO's RGB Composite Satellite Imagery Workshop.

Fig. 1-4-1. RGB light combinations

1.4.2. RGB Composite Imagery Characteristics

This section describes WMO-standard RGB composite image from 03:00 UTC on 7 March 2016 and 18:00 UTC on 6 March 2016. The relevant phenomena may not appear with the exact precision of the colors indicated above.

(1) True Color RGB

Figure 1-4-2 shows an overlay of visible imagery from Band 3 (0.64 μm), Band 2 (0.51 μm) and Band 1 (0.47 μm) bordered in red, green and blue, respectively, producing a display similar to that seen by the human eye. It is provided on the Visible (Color) Channel in Satellite Imagery (Rapid Scan) on the JMA website. These composites have the following characteristics:

- Display of cloud and snow/ice in white for ease of discrimination from land
- Facilitated viewing of smoke, Aeolian dust (yellow sand), volcanic ash and other forms of dust (Fig. 1-4-2)
- Exclusive daytime use due to application of visible imagery

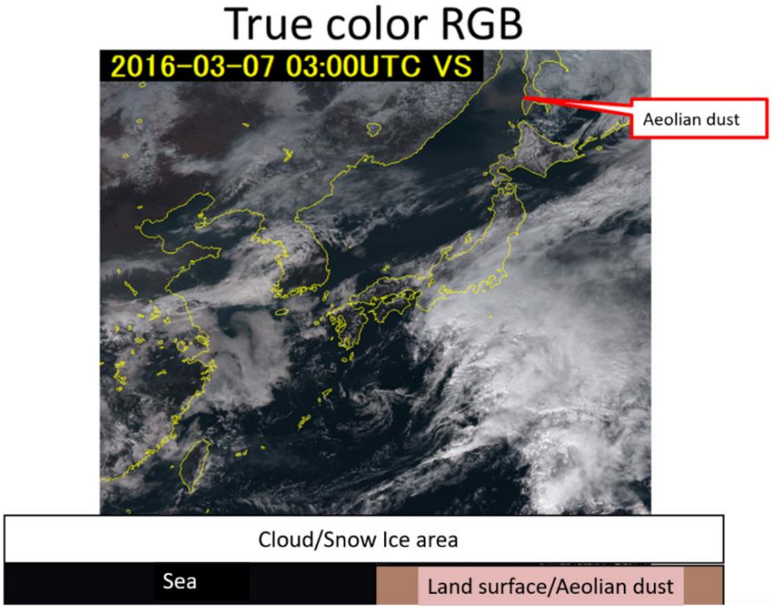

Fig. 1-4-2. True Color RGB sample

(2) Natural Color RGB

Figure 1-4-3 shows an overlay of visible image from Band 5 (1.6 μm), Band 4 (0.86 μm) and Band 3 (0.64 μm) bordered in red, green and blue, respectively, with the following characteristics:

- Band 5 (red) lower reflectance to ice crystals, resulting in regions of upper clouds and snow/ice appearing in cyan in composites of Band 4 (green) and Band 3 (blue) with higher reflectance (Fig. 1-4-4)
- High reflectance to water droplets in all three bands, causing droplet-based cloud areas (e.g., fog and low clouds) to appear in a white tone composed of the three primary colors
- Especially high Band 4 (green) reflectance against vegetation in comparison to the other two bands, causing vegetation to appear in green
- Exclusive daytime use due to application of visible and near-infrared image

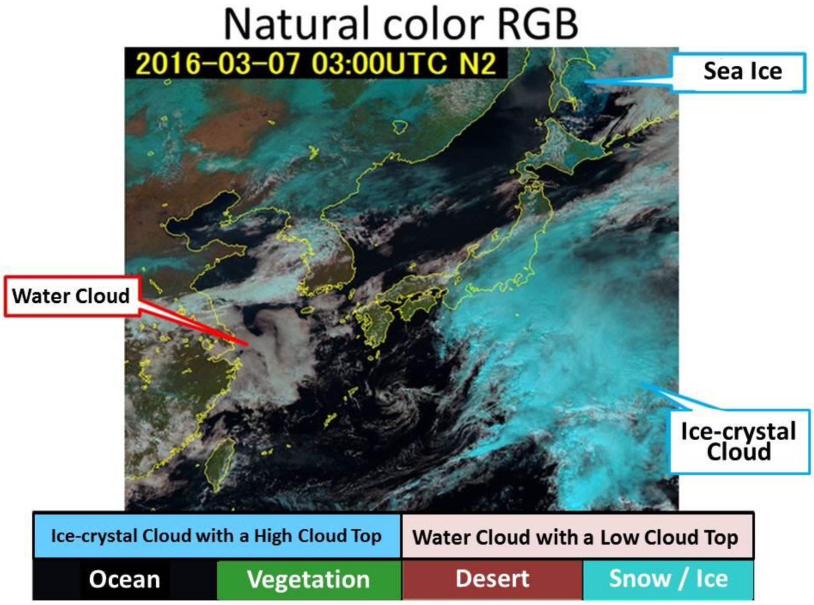

Fig. 1-4-3. Natural Color RGB sample

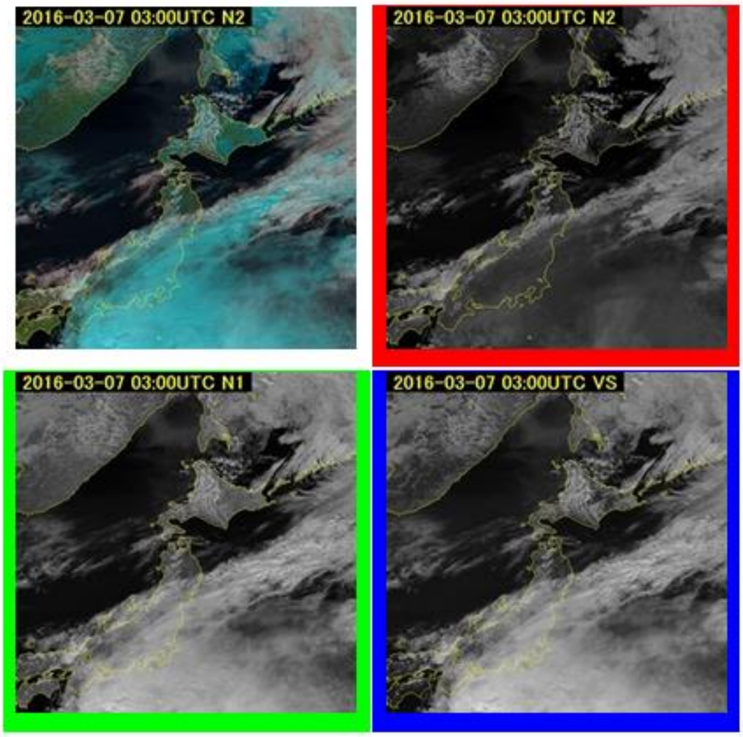

Fig. 1-4-4. Natural Color RGB composite image (top left) and source image. Top right: Band 5; bottom left: Band 4; bottom right: Band 3

(3) Dust RGB

Figure 1-4-5 shows difference image from Band 15 and Band 13 (referred to here as B15-B13), Band 13 and Band 11 (B13-B11), and contrast-inverted image (i.e., adjusted to appear in color transition with higher brightness temperature) from Band 13 overlaid with red, green and blue (B13-inverted).

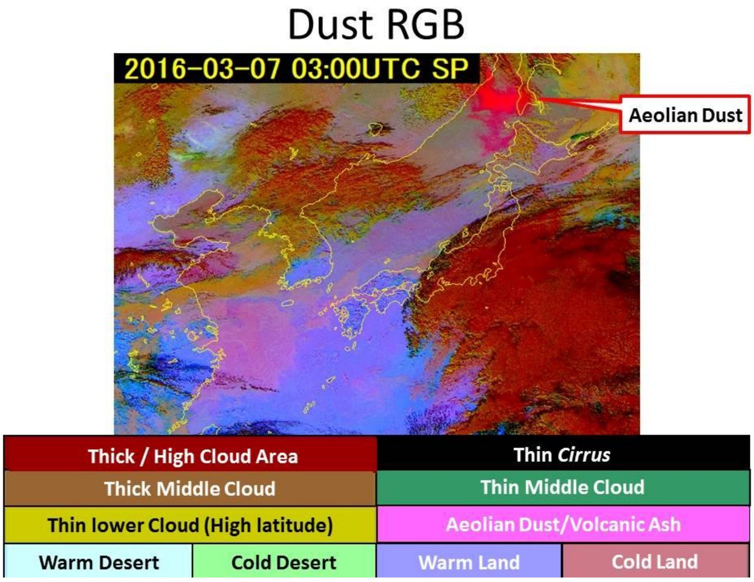

Fig. 1-4-5. Dust RGB color sample

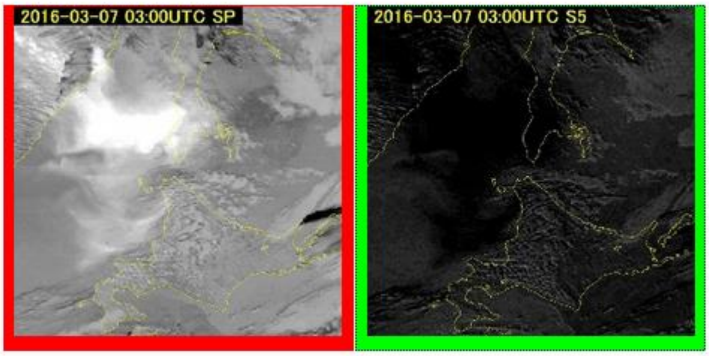

Fig. 1-4-6. Difference imagesry used in Dust RGB composites. Left: B15-B13 showing Aeolian dust and volcanic ash in clear white; right: B13-B11 with Aeolian dust and volcanic ash in black

Dust RGB imagery has the following characteristics:

- Aeolian dust brighter in B15-B13 (Fig. 1-4-6: Left) and darker in B13-B11 (Fig. 1-4-6: Right); enhanced red in the former, with Aeolian dust and volcanic ash in magenta (Fig. 1-4-5)
- Capacity for alteration of display transition and gamma values to create Ash RGB imagery for enhanced visibility of volcanic ash and 24-hour Microphysics RGB imagery to facilitate cloud discrimination
- 24-hour applicability due to the absence of visible and near-infrared band data

(4) Airmass RGB

Figure 1-4-7 shows an overlay of difference image for Band 10 (7.3 µm) and Band 8 (6.2 µm) (referred to here as B10-B08), Band 13 (10.4 µm) and Band 12 (9.6 µm) (B13-B12) and Band 8

(6.2 μm) bordered in red, green, and blue, respectively, with the following characteristics:

- Brighter upper-middle atmosphere (dry or wet throughout) in B10-B08 (Fig. 1-4-8 rigjt)
- Transition adjusted in B13-B12 to display the polar side darker and the sub-tropical high side brighter (Fig. 1-4-8 left).

Based on these characteristics, air masses and the jet stream axis can be approximated in Airmass RGB composites (Fig. 1-4-7). 24-hour application is also possible due to the absence of data from visible and near-infrared bands.

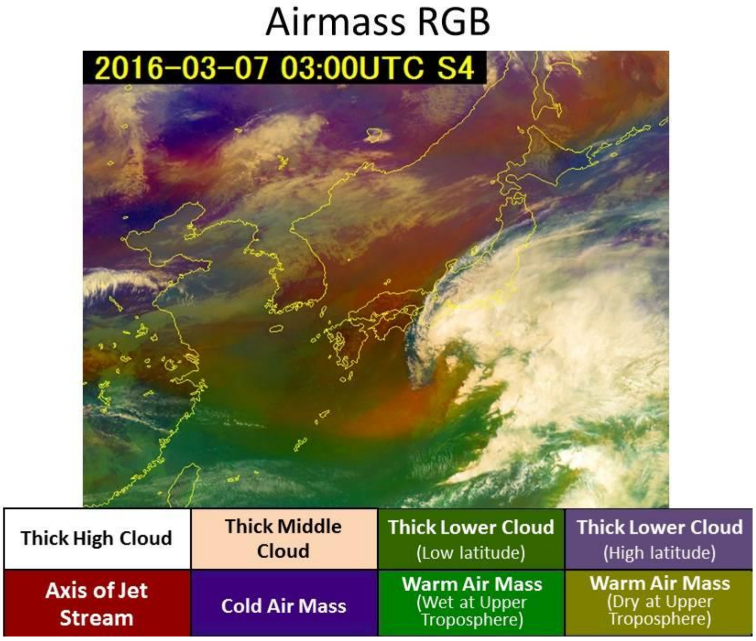

Thick High Cloud	Thick Middle Cloud	Thick Lower Cloud (Low latitude)	Thick Lower Cloud (High latitude)
Axis of Jet Stream	Cold Air Mass	Warm Air Mass (Wet at Upper Troposphere)	Warm Air Mass (Dry at Upper Troposphere)

Fig. 1-4-7. Airmass RGB color sample

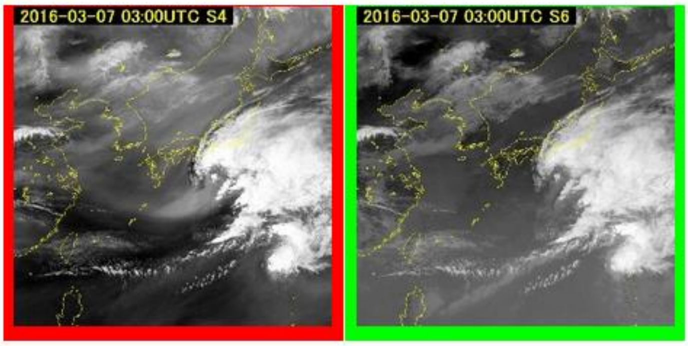

Fig. 1-4-8. Difference images used for Airmass RGB compositing. Left: B08-B10; right: B13-B12

(5) Night Microphysics RGB

B15-B13, B13-B07 and B13-inverted are bordered in red, green, and blue, respectively in Fig. 1-4-9. Night Microphysics RGB image has the following characteristics:

- Brighter fog/low cloud areas in all three types (in white with traces of green) (Fig. 1-4-

10)

- Poor resolution in Band 7 for lower-temperature regions; increased noise in B13-B07, causing yellow dots to appear in thick high-top cloud areas such as cumulonimbus (Fig. 1-4-10)
- Exclusivity to nighttime usage to avoid Band 7 sunlight influence

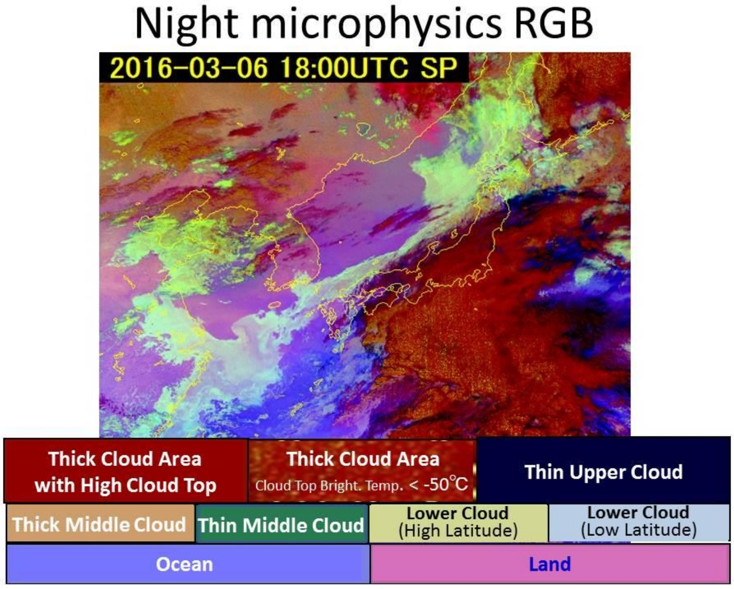

Fig. 1-4-9. Night Microphysics RGB sample

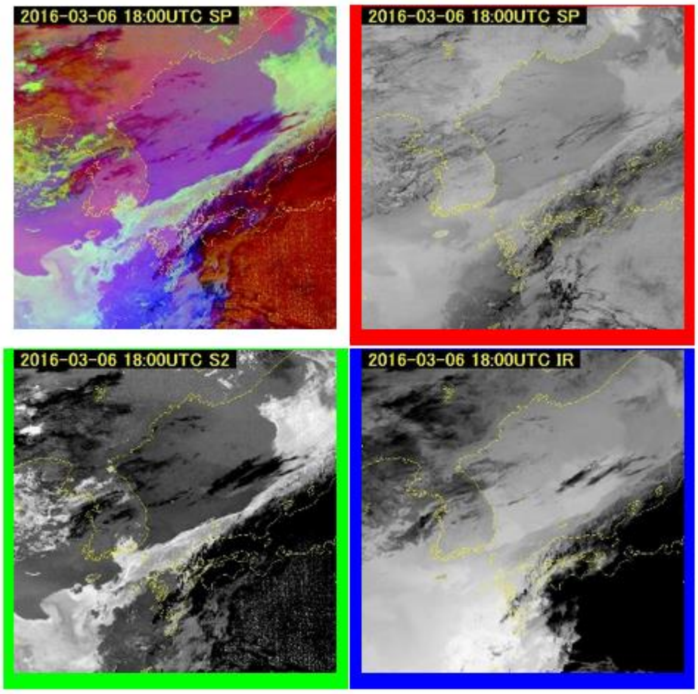

Fig. 1-4-10. Night Microphysics composite imagery (top left) and source images. Top right: B15-B13; bottom left: B13-B07; bottom right: B13-inverted

(6) Day Convection Storm RGB

Figure 1-4-11 shows difference image for Band 1 and Band 8 (referred to here as B10-B08), Band 7 and Band 13 (B07-B13) and Band 5 and Band 3 (B05-B03) bordered in red, green and blue, respectively. Day Convection Storm RGB composite imagery has the following characteristics:

- Cloud particles brought up to the cloud top by strong updrafts faster, even before particle development, in cloud areas with extreme phenomena such as gusting winds and tornadoes, resulting in the formation of small ice crystals at the cloud top in areas with active convection. Cloud areas are notably brighter in B07-B13 and B10-B08 and darker in B05-B03 (displayed in yellow in composite image) (Fig. 1-4-12).
- Exclusive to daytime applicability due to the use of visible and near-infrared imagesy

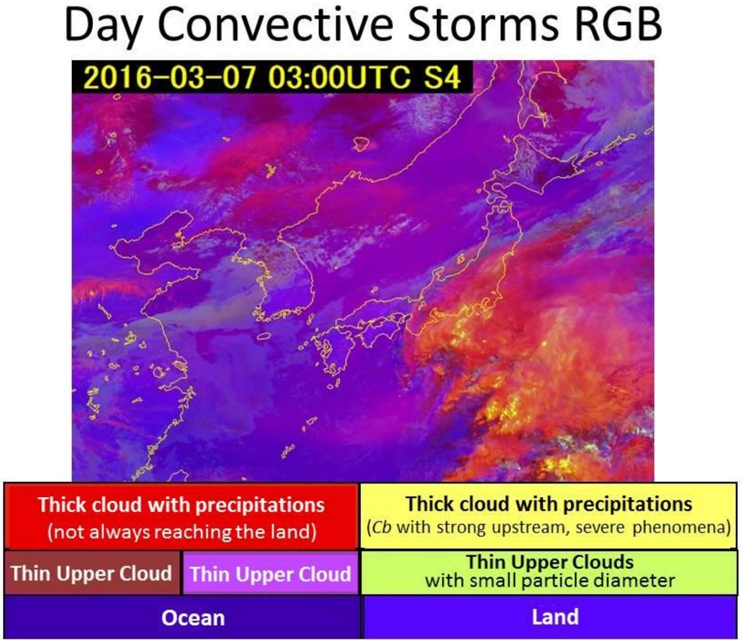

Fig. 1-4-11. Day Convective Storm RGB sample

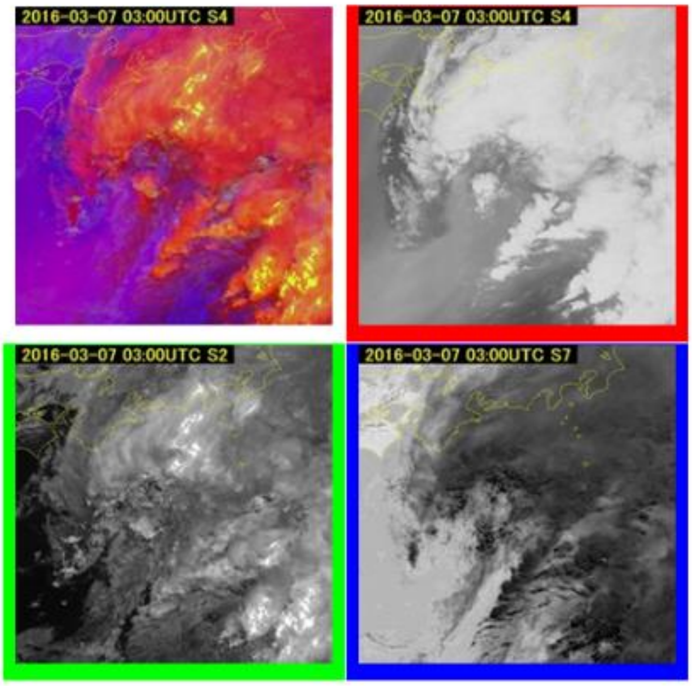

Fig. 1-4-12. Composite image for Day Convective Storm RGB (top left) and source images. Upper right: B10-B08; lower left: B07-B13; lower right: B05-B03

2. RGB Composite Imagery Comparison

(1) Infrared Imagery

In Fig. 1-4-13, a cloud area in front of a cyclone toward the south of Japan appears bright (a), mainly having Cb and Ci with high cloud tops. In contrast, cloud areas (b), (d) and (a) between the Korean Peninsula and the continent are dark. These are assumed to have lower cloud tops than (a).

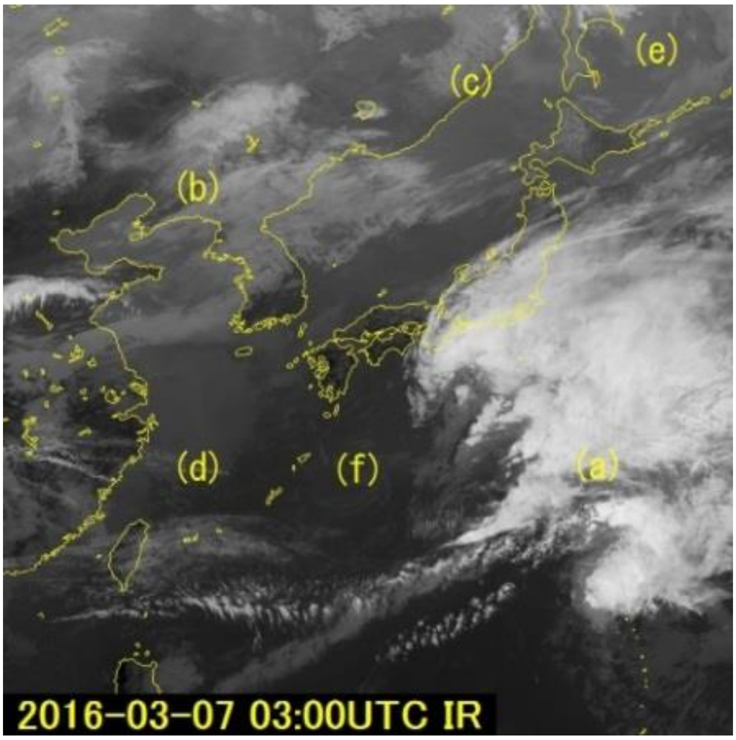

Fig. 1-4-13. Infrared image for 03:00 UTC on 7 March 2016

(2) True Color RGC Composite Imagery

In Fig. 1-4-14, the cloud area (a) appears bright, consisting mainly of thick clouds. Aeolian dust (c) is seen in brown between Hokkaido and Siberia. The cloud area (d) appears smooth on its surface; the obscurity in (a) indicates the presence of fog or low cloud. In (2), sea ice and cloud areas are visible, but are difficult to distinguish from this image alone.

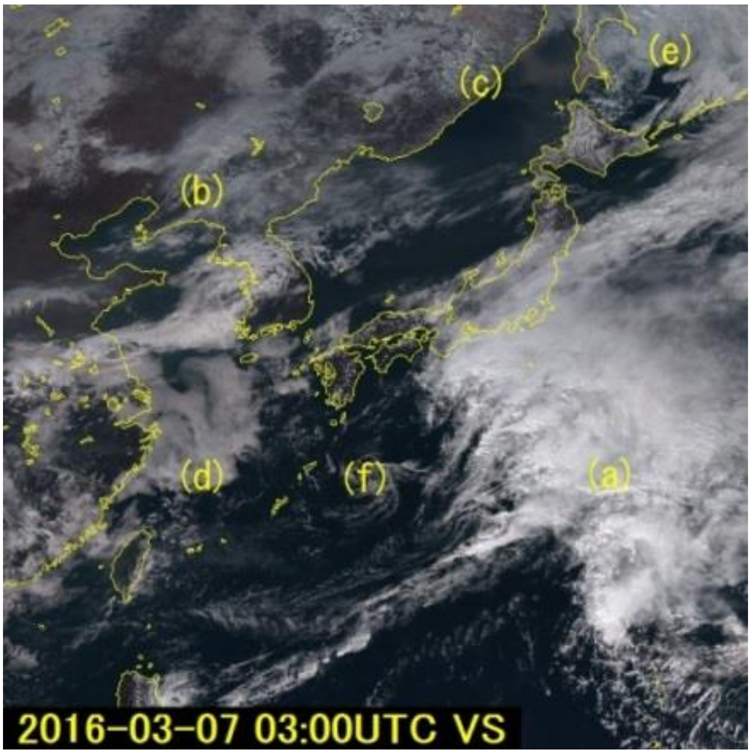

Fig. 1-4-14. True Color RGB composite image for 03:00 UTC on 7 March 2016

(3) Natural Color RGB Composite Imagery

In Fig. 1-4-15, the cloud areas (d) in white and (a) in cyan are easily distinguishable. Aeolian dust (c) is shown thinner than in True Color; ground surface ice/seawater is in cyan and low cloud is in white, also facilitating identification. However, in (b), upper cloud and ice/sea ice areas are both in cyan. Accordingly, infrared imagery comparison and checking of multiple images are crucial in related discrimination.

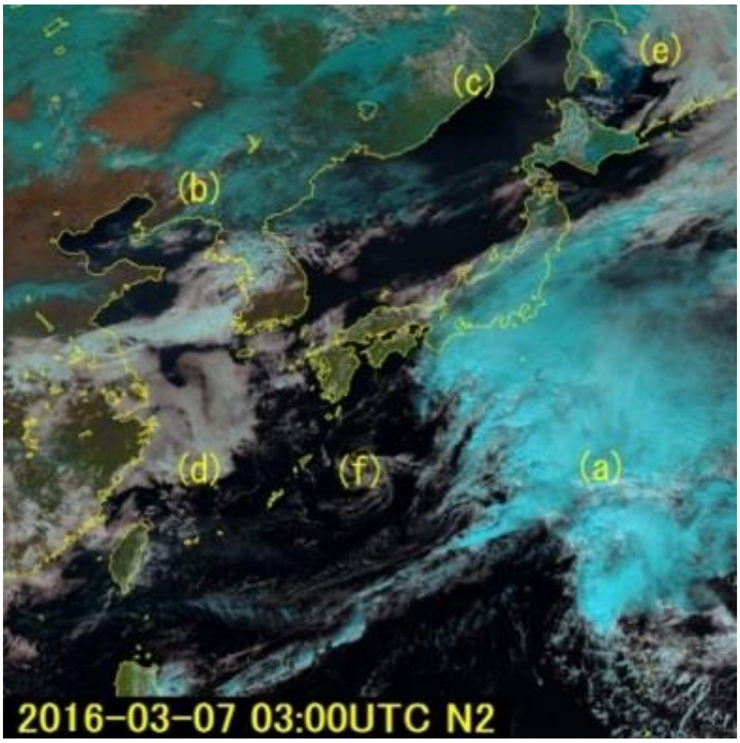

Fig. 1-4-15. Natural Color RGB composite image for 03:00 UTC on 7 March 2016

(4) Dust RGB Composite Imagery

In Fig. 1-4-16, Aeolian dust (c) is displayed in magenta, enabling easier identification than in B and C.

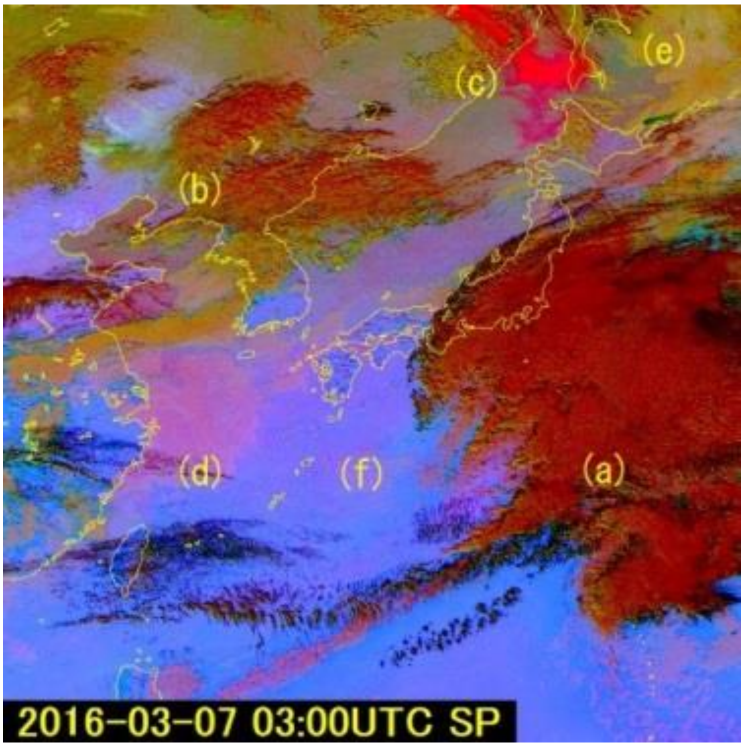

Fig. 1-4-16. Dust RGB composite image for 03:00 UTC on 7 March 2016

(5) Airmass RGB Composite Imagery

In Fig. 1-4-17, high cloud top areas such as (a) are shown in white. Orange indicates the presence of dry air or the jet stream axis. Here, the orange in (d) and (f) corresponds to the jet stream axis shown on the upper-level weather chart H throughout (b), (c) and (e), and an area of depression corresponding to the trough shown as H on the weather chart (Fig. 1-4-20).

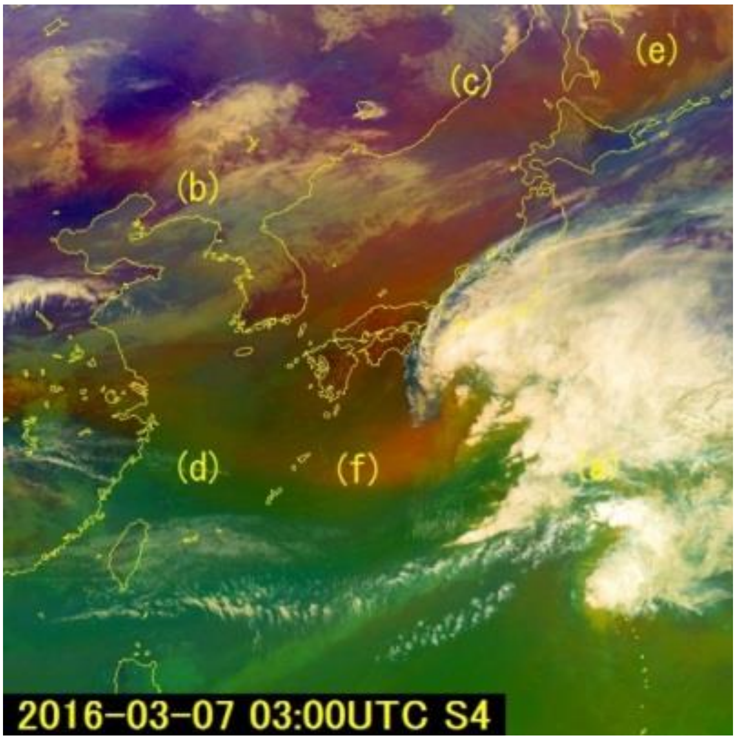

Fig. 1-4-17. Airmass RGB composite image for 03:00 UTC on 7 March 2016

(6) Day Convective Storm RGB Composite Imagery

In Fig. 1-4-18, particularly active convection in the cloud area (a) is shown in yellow. The B08-B10 difference image used here shows an area of depression corresponding to the trough of (d) and (f) in magenta.

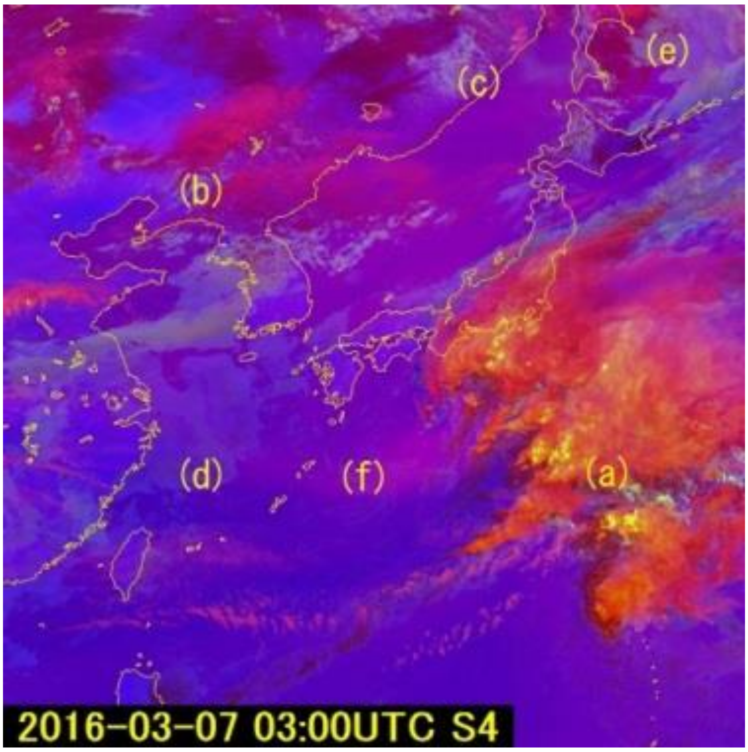

Fig. 1-4-18. Day Convective Storm RGB composite image

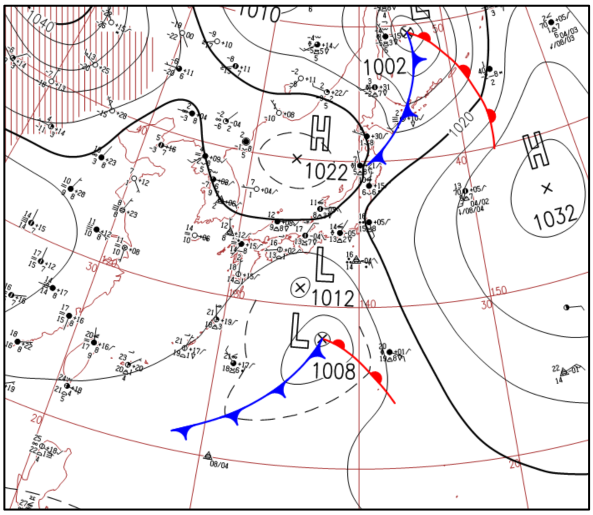

Fig. 1-4-19. Weather chart prompt report for 00:00 UTC on 7 March 2016

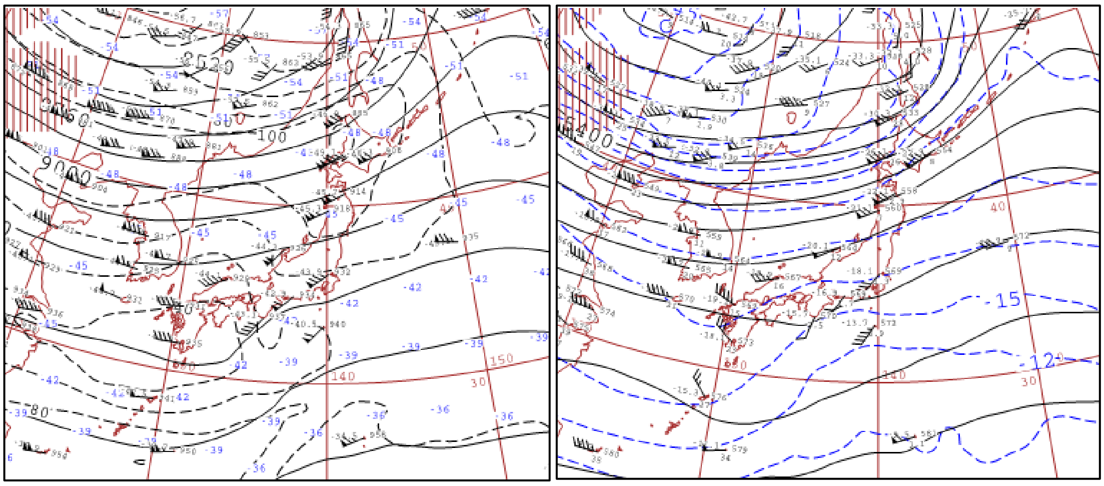

Fig. 1-4-20. Upper-level weather chart for 00:00 UTC on 7 March 2016. Left: 300 hPa; right: 500 hPa

Nighttime RGB composite images are compared below. For reference, a weather chart prompt report for the same time period is shown (Fig. 1-4-19 and 1-4-20).

(7) B13 Infrared Imagery (Nighttime)

The cloud area (a) appears brighter in front of a cyclone to the south of Japan, indicating the presence of Cb and Ci with higher cloud top as its main body (Fig. 1-4-21). The cloud area (b) over the Korean Peninsula and the continent is darker, indicating a lower cloud top than in (a).

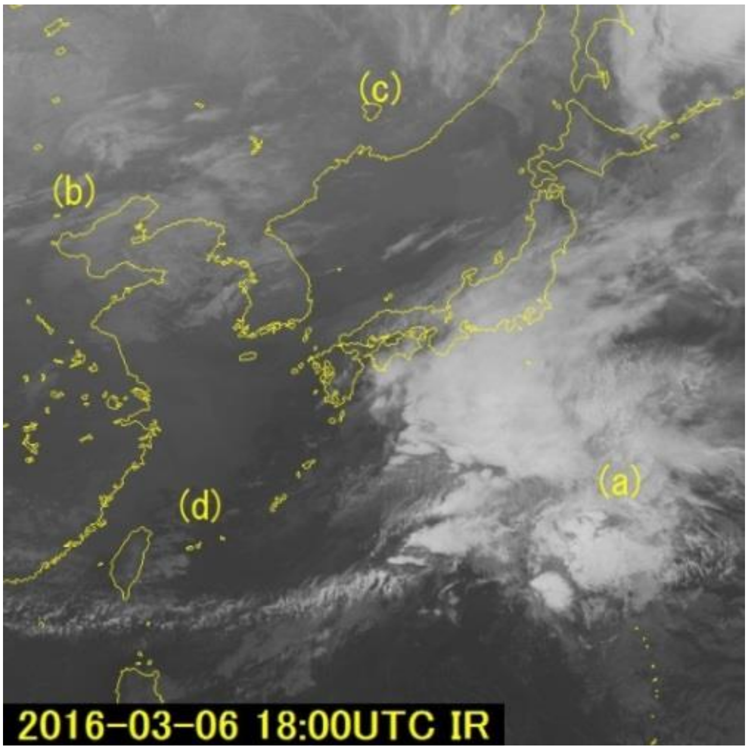

Fig. 1-4-21. B13 Infrared image for 18:00 UTC on 6 March 2016

(8) Dust RGB Composite Imagery (Nighttime)

The region (c) corresponding to Aeolian dust over Russia and China is clearly highlighted in magenta. The cloud area (a) appears in dark orange (Fig. 1-4-22). The cloud area (b) is difficult to identify due to its display in the same color.

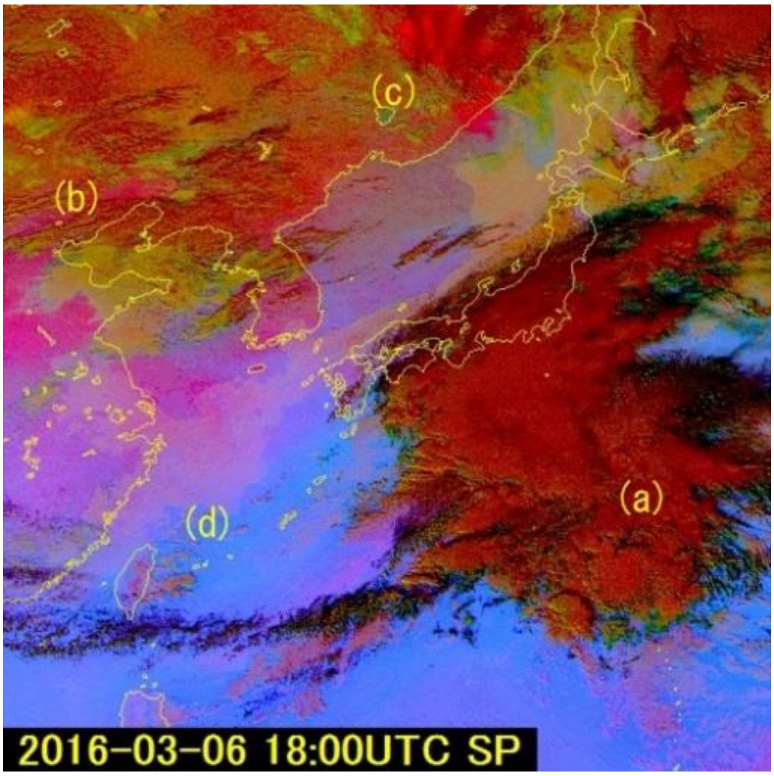

Fig. 1-4-22. Dust RGB composite image for 18:00 UTC on 6 March 2016

(9) Night Microphysics RGB Composite Imagery

The fog and low-cloud area (d) is shown in white with traces of green (Fig. 1-4-23). The cloud area (a) is shown in red with yellow dots, which are particularly prominent in the area reaching the tropopause. The cloud area (b) is clearer than in Dust RGB. Figure 1-4-24 shows a surface weather chart for 12:00 UTC on 6 March 2016.

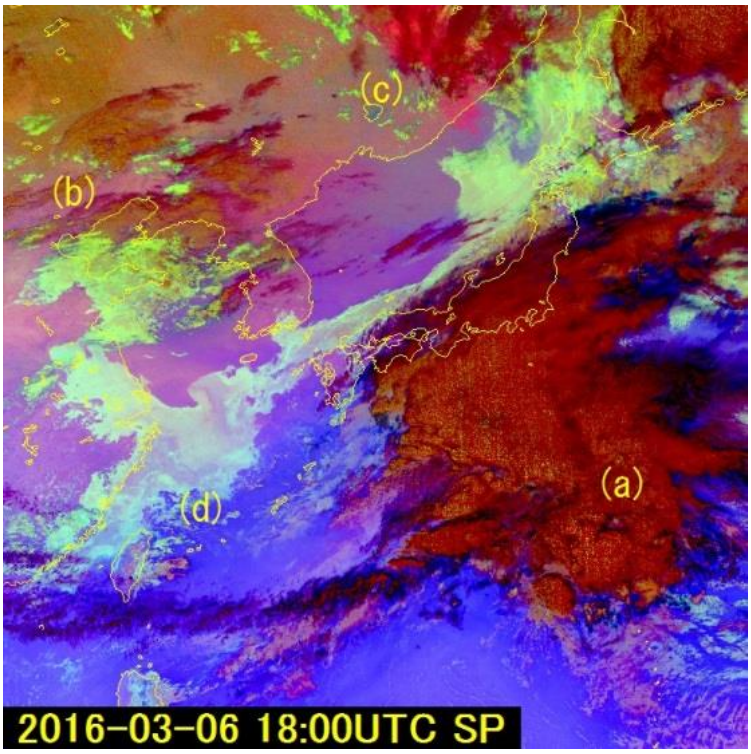

Fig. 1-4-23. Night Microphysics RGB composite image for 18:00 UTC on 6 March 2016

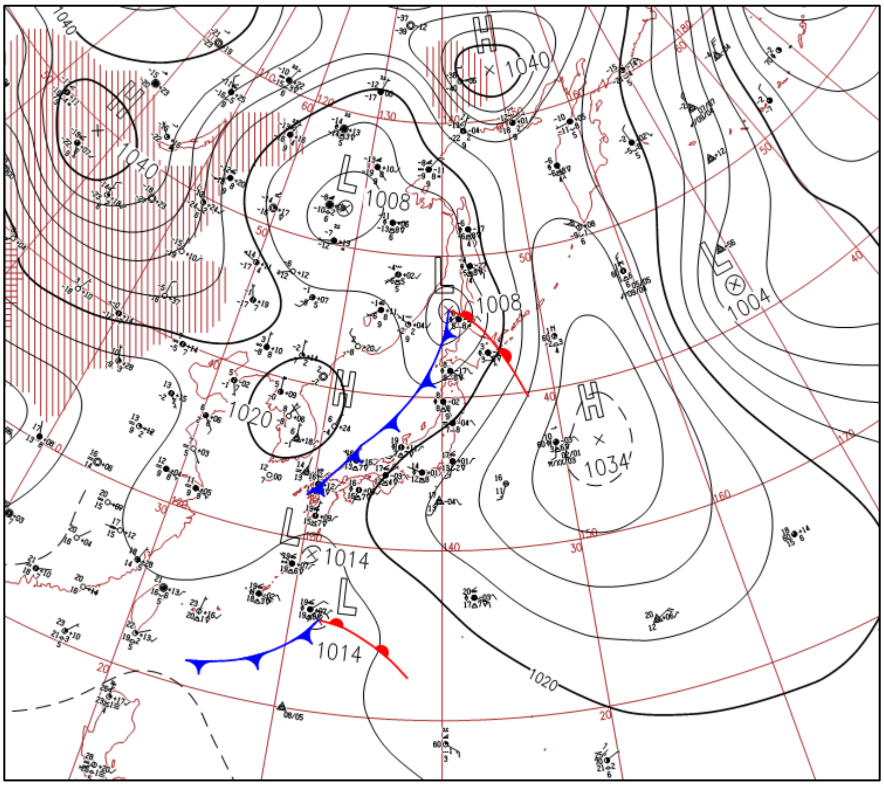

Fig. 1-4-24. Weather chart prompt report for 12:00 UTC on 6 March 2016

2. Cloud Type Identification via Meteorological Satellite Observation

2.1. Via Satellite Imagery

Clouds identified from satellite observation are referred to here as “cloud types,” and those determined from surface observation are “cloud forms.”

In contrast to ground-surface cloud observation with the human eye, satellites observe cloud tops from space. Visibility at the resolution of meteorological satellite sensors (approx. 0.5 – 1 km in visible/near-infrared and 2 km in infrared for Himawari-8/9) is coarser than seen with the human eye from the ground, and does not allow cloud type identification with as much detail as surface observation. Accordingly, satellite-based cloud identification is essentially different. For convenience, the terminology for cloud types classified via satellite imagery is based on that of clouds similar in origin and structure in surface observation.

2.2. Cloud Type Classification

In satellite-based identification, clouds may be classified as high-level (Ci), mid-level (Cm), stratus/fog (St), cumulonimbus (Cb), cumulus congestus (Cg), cumulus (Cu) or stratocumulus (Sc) (Table 2-2-1). As above, this differs from surface observation-based classification.

Clouds can be divided into stratiform (Ci, Cm, St) and convective (Cb, Cg, Cu) types, with Sc combining the characteristics of both.

The extent of stratiform clouds is much more horizontal than vertical, with coherent forms, smooth surfaces and uniform top heights. Convective clouds are thicker and smaller, with readily recognizable discrete cellular forms and uneven surfaces.

Clouds are also categorized as high-, mid- or low-level. It should be noted that satellite-based identification is based on top height, unlike surface observation, which relies on base height. Generally, top heights above 400 hPa are high-level, 400 to 600 hPa are mid-level, and below 600 hPa are low-level. As detailed in the previous chapter, top heights are estimated using brightness temperature in infrared imagery and vertical temperature profiling based on objective analysis and numerical weather prediction. Cg and Cb are generally not included in such classification because they develop vertically and belong to multiple altitude classes.

Table 2-2-1. Satellite imagery-based cloud type classification

Cloud type	Classification	
High-level clouds Ci	Stratiform clouds	High-level clouds
Middle-level clouds Cm		Middle-level clouds
Stratus/fog St		Low-level clouds
Stratocumulus Sc	----	
Cumulus Cu	Convective clouds	
Cumulus congestus Cg		----
Cumulonimbus Cb		

2.3. Principles of Subjective Identification

Conventional subjective cloud type identification with the human eye is based on visible and infrared imagery supported by meteorological expertise. Although the development of meteorological satellites has facilitated computerized objective identification with imagery highlighting near-infrared, water vapor and infrared differences, precise determination of weather conditions remains challenging. This section describes the principles of subjective cloud type identification.

2.3.1. Visible and Infrared Imagery

In visible imagery, clouds with high water content and thick clouds show high solar reflectance. Convective clouds appear brighter than stratiform clouds because they are thicker and contain more droplets, and higher development equates to higher reflectance. Cb is generally brighter than Cg, which in turn is brighter than Cu. Low-level clouds tend to be brighter than high-level clouds (e.g., St is brighter than Ci).

As lower-temperature areas appear brighter in infrared imagery, clouds with higher tops are more pronounced. Ci is generally the brightest stratiform cloud, followed by Cm and St. However, radiation from below thin clouds is added to radiation from the clouds themselves, which can lead to underestimation of cloud top heights. For instance, Ci is often a thin cloud type that can be mistaken as Cm in infrared imagery. Meanwhile, very thick Ci has a cloud top temperature similar to that of Cb, making them harder to distinguish. For St with lower top heights, the temperature difference between the top and the ground is smaller than for other cloud types, making identification harder from infrared imagery. The development stage in convective clouds can be categorized by top height, with Cb being the highest in convective clouds followed by Cg and Cu.

Figure 2-3-1 shows qualitative relationships in cloud type identification based on visible and infrared imagery.

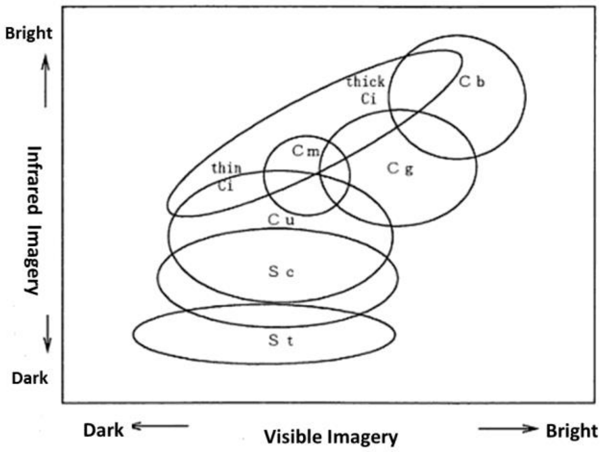

Fig. 2-3-1 Cloud type identification

2.3.2. Identification via Form

Stratiform clouds tend to have uniform top heights and expansive areas. The edge of St in contact with mountains often follows topography contours. Ci shows characteristic shapes, such as streaks, feather-like blowing from Cb (e.g., anvil cirrus) and fiber-like structures perpendicular to the subtropical jet axis (e.g., transverse lines).

Convective clouds are usually relatively small, increasing in thickness with development, combining and appearing larger in satellite imagery. Cloud size generally follows the order of Cb, Cg and Cu from largest to smallest. Convective clouds often form characteristic patterns (carrot-shaped/cellular) and lines.

The edges of convective and low-level clouds are clear in satellite imagery, while high-level clouds are influenced by strong winds and tend to exhibit vague feathery forms.

2.3.3. Identification via Texture

The relatively high spatial resolution of visible imagery reveals fine cloud-surface textures. The surface of stratiform clouds is smooth and uniform, while that of convective clouds is rough and uneven. Cloud surface conditions can be determined from the unevenness of shadows appearing when illuminated by the sun from a steep angle.

2.3.4. Identification via Movement

The relatively strong winds generally observed in the upper atmosphere cause Ci clouds to move faster than low-level types such as St, Sc and Cu. Tall clouds such as Cb and Cg move more slowly than Ci due to the influence of faster winds at cloud tops and slower winds at cloud bottoms.

2.3.5. Identification via Temporal Evolution

Convective clouds have a relatively short lifespan, with rapidly changing shapes and top heights. As such changes are more subtle in stratiform clouds, Cb and Ci can be distinguished using these characteristics.

2.4. Examples

2.4.1. Identification from Visible and Infrared Imagery

Figures 2-4-1 and 2-4-2 show examples of cloud type identification. **A** to **G** below correspond to the symbols in the figures. **H** and **I** are outlined in Section 2.4.3.

- A bright cloud area **A** appears between northern Hokkaido and the Sea of Okhotsk in the infrared image along the wind direction in the upper layer, with an underlying lower cloud area through it in the visible image. Hence, A is identified as thin Ci.
- The cloud area **B** over the sea southeast of Okinawa is Cm. This has a uniform surface and appears light grey in the infrared image because of its higher temperature as compared to **A**. It appears white in the visible image and stretches along the wind direction in the middle layer.
- The cloud area **C** at around 150 degrees east longitude to the east of Japan is St. This appears darker than surrounding cloud in the infrared image and is approximately the same temperature as the sea surface, making it difficult to identify. It appears light grey with a smooth surface in the visible image.
- The cloud area **D** over the East China Sea off the southwestern coast of Kyushu is Sc. It appears dark grey in the infrared image and light grey with a distinct border in the visible image.
- The partially streaky cloud area **E** between the Yellow Sea and the East China Sea is Cu. In the infrared image, it appears brighter than the Sc in area **D**. In the visible image, it appears white with clusters featuring distinct edges.
- The cloud area **F** (arrow marking) over the sea near the Ogasawara Islands is Cb. Its rim to the west is clear in the infrared image but obscure to the east under the influence of upper-level winds. It has a clustered appearance in the visible image with a relatively white form.
- The belt-shaped latitudinal cloud area **G** over the Yellow Sea is associated with a cold-air mass, as per **E**. However, it contains Cb and Cg, and is more developed than the Cu of **E** and brighter in both the infrared and visible images.

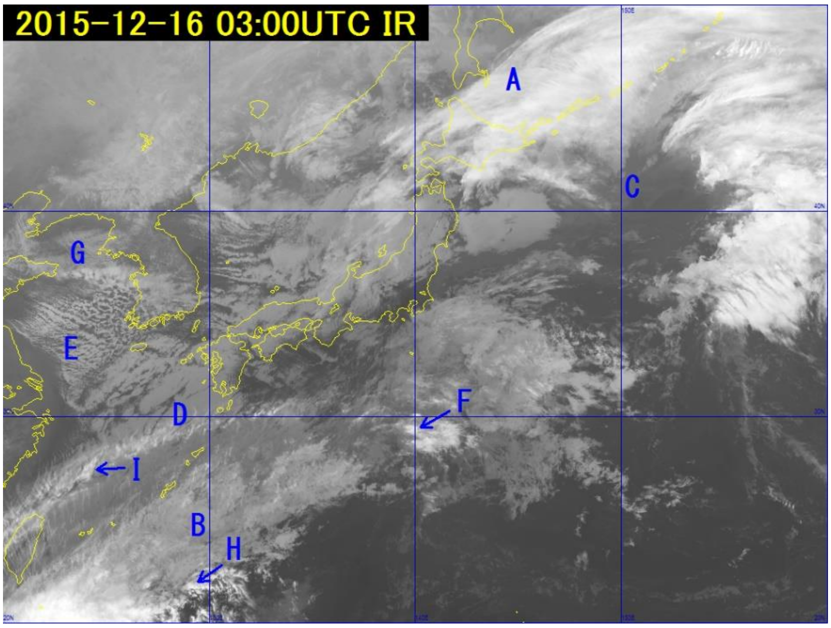

Fig. 2-4-1 B13 infrared image for 03:00 UTC on 16 December 2015

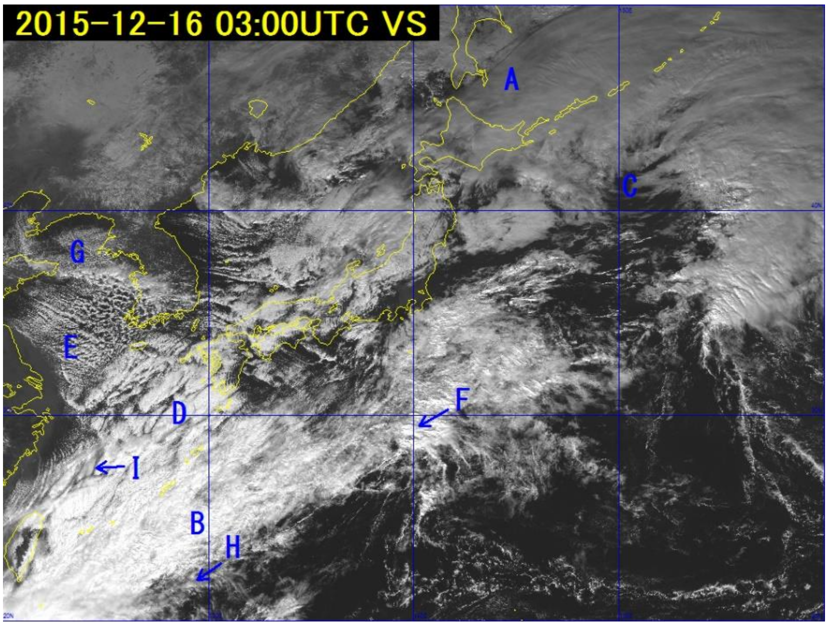

Fig. 2-4-2 B03 visible image for 03:00 UTC on 16 December 2015

2.4.2. Cb and Cg Examples

Cb and Cg examples are shown in Figs. 2-4-3 and 2-4-4.

- The cloud area **K** (arrow marking) to the south of Japan is Cb. In the visible image, it appears clustered in white. To the west, the cloud line **J** (arrow marking) with Cg is seen. In the infrared image, low-temperature areas corresponding to the Cg clouds show a line form with particular intervals. In the visible image, this formation appears as spaced white clusters with convective cloud lines.
- The cloud areas **L** and **M** incorporate both Cb and Ci. The unclear Cb boundaries can be estimated by comparing the brightness and texture of Cb itself with the surrounding areas

in infrared and visible imagery.

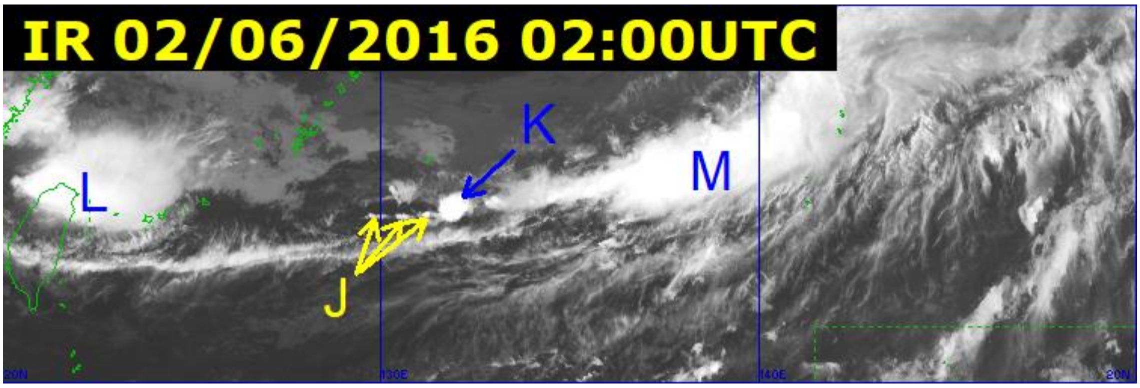

Fig. 2-4-3 B13 infrared image for 02:00 UTC on 2 June 2016

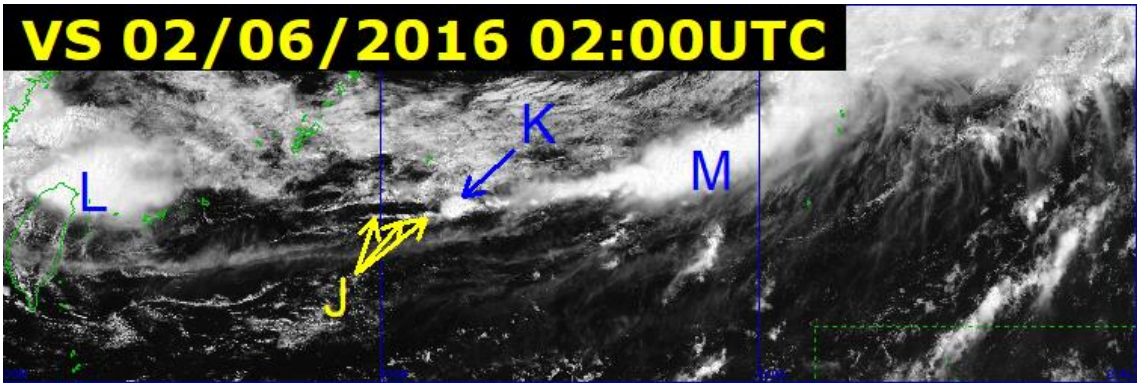

Fig.2-4-4 B03 visible image for 02:00 UTC on 2 June 2016

2.4.3. Ci and Cb Examples

The distinction between Ci and Cb is based on the shapes of each cloud described above in consideration of differences in movement speed and synoptics.

- In Figs. 2-4-1 and 2-4-2, the cloud area **F** (arrow marking) over the sea east of Japan is Cb (as previously described), which moves more slowly than surrounding cloud areas because it is affected by wind in the upper, middle and lower layers, but its shape changes faster than that of Ci. The cloud area **I** (similar to **F**; arrow marking) over the East China Sea is Ci, as determined by its rapid movement. The cloud area **H** (arrow marking) south of Okinawa in the infrared image is also Ci. Both Ci instances may be easily mistaken as Cb based on their shapes and top temperatures. Ci can be identified by its slow evolution in both infrared and visible imagery.

2.5. Differences Between Cloud Types Identified via Meteorological Satellites and Cloud Forms in Surface Observation

2.5.1. Introduction

This section describes cloud types identified via meteorological satellites and cloud forms identified via surface observation in comparison. Surface observation produces 10 cloud form categories depending on base heights and textures (World Meteorological Organization, 2017). In contrast, as meteorological satellite observation is conducted from above the Earth, cloud types are determined from 1. top temperatures and textures in infrared imagery, and 2. sunlight reflectance and cloud textures in visible imagery. However, it is difficult to distinguish cirrostratus, cirrus, altostratus and nimbostratus in satellite imagery due to limited spatial resolution.

In satellite imagery, upper- and mid-level clouds are each classified as single types. Cloud masses overall are classified as stratiform, convective, or both, resulting in seven classifications in total. Stratiform clouds are categorized as upper (Ci), mid (Cm) or stratus/fog (St) in order from the highest top, while convective clouds are categorized as cumulonimbus (Cb), cumulus congestus (Cg) or cumulus (Cu) in order from the tallest. Cg appears only in satellite cloud classification with development to an intermediate extent between Cb and Cu. Stratocumulus (Sc) has intermediate characteristics between stratiform and convective. Table 2-5-1 compares related characteristics.

Table 2-5-1 Cloud types identified via meteorological satellites and cloud forms in surface observation

Identification via meteorological satellites

Type	Abbreviation
Upper-level clouds	Ci
Mid-level clouds	Cm
Stratocumulus	Sc
Stratus/Fog	St
Cumulus	Cu
Cumulus congestus	Cg
Cumulonimbus	Cb

Identification via surface observation

Level	Type	Abbreviation
High	Cirrus	Ci
	Cirrocumulus	Cc
	Cirrostratus	Cs
Mid	Altocumulus	Ac
	Altostratus	As
	Nimbostratus	Ns
Low	Stratocumulus	Sc
	Stratus	St
	Cumulus	Cu
	Cumulonimbus	Cb

Below are comparisons between cloud photographs taken on the ground and satellite images (infrared and visible) at corresponding times. Unless otherwise stated, the cloud type abbreviations here refer to satellite-based cloud classification.

2.5.2. Case Studies

2.5.2.1. Case 1: Ci Only

In both the infrared image (Fig. 2-5-1) and the visible image (Fig. 2-5-2), hardly any cloud is seen over the Kanto Plain except for a latitudinal band extending from the vicinity of Mt. Fuji to the area south of the Meteorological Satellite Center (MSC) in Kiyose, Tokyo. This cloud area appears relatively bright in the infrared image but grey in the visible image, and land can be seen through it. Hence, it can be identified as Ci. In a photograph taken from the ground (Fig. 2-5-3), the sky above the MSC is clear and the upper-level cloud stretches from west to south. In this example, it can be identified as an upper-level cloud area both from the ground and from the satellite.

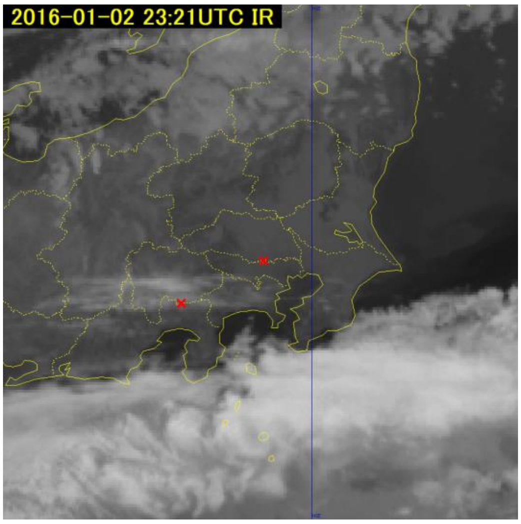

Fig. 2-5-1 B13 infrared image for 23:21 UTC on 2 January 2016; red crosses: Mt. Fuji (left) and MSC (right)

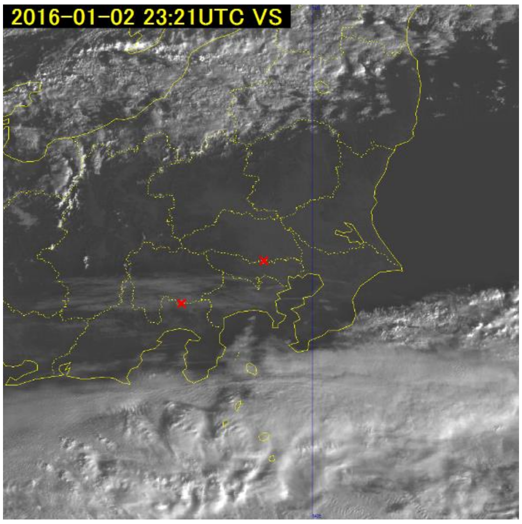

Fig. 2-5-2 B03 visible image for 23:21 UTC on 2 January 2016; red crosses: Mt. Fuji (left) and MSC (right)

Fig. 2-5-3 View of upper-level clouds looking southwest from the MSC, 23:21 UTC, 2 January

2.5.2.2. Case 2: Ci Cloud Area Only

In the infrared image (Fig. 2-5-4), a straight cloud line extends from the area west of the MSC toward the prefectures of Chiba and Ibaraki. In the visible image (Fig. 2-5-5), the cloud area around the MSC appears white, but the further east it goes, the thinner and more transparent it becomes. The area around the MSC exhibits relatively thick upper-level cloud, and the area eastward shows thin upper-level cloud with an almost static western end that appears to be the origin. A photograph taken at the MSC (Fig. 2-5-6) shows the edge of the area, which can be identified as upper-level cloud both from the ground and from the satellite.

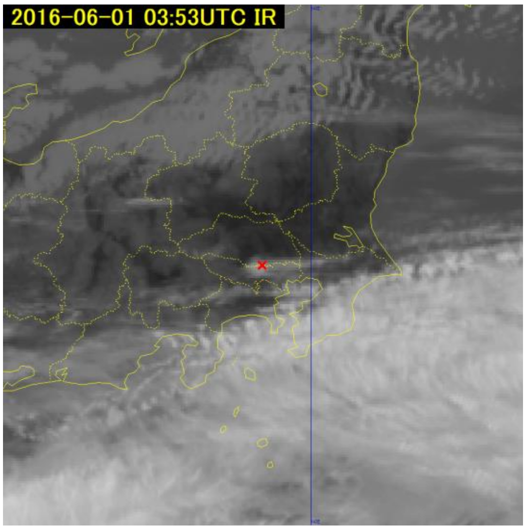

Fig. 2-5-4 B13 infrared image for 12:53 JST on 1 June 2016; red cross: MSC

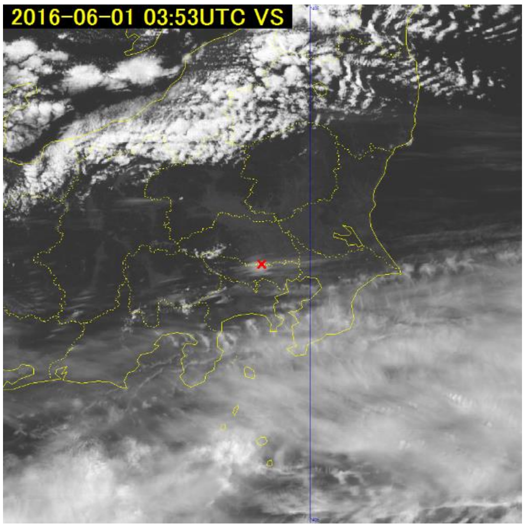

Fig. 2-5-5 B03 visible image for 12:53 JST on 1 June 2016; red cross: MSC

Fig. 2-5-6 View west from MSC for 12:53 JST on 1 June 2016. Upper-level clouds were observed from the ground.

2.5.2.3. Case 3: Ci Cloud Area Only

In the infrared image (Fig. 2-5-7), a white belt-form cloud area is observed from the west of Jogashima (Miura, Kanagawa). In the visible image (Fig. 2-5-8), this appears grey, and the ground can be seen through it. Accordingly, it can be judged as upper-level cloud. The thin cloud area spreading northward (Fig. 2-5-9) corresponds to the thin upper-level cloud area or its edge, as also seen in satellite imagery. The undeveloped Cu in the center of the photograph is not recognized in satellite imagery because its is too small for the satellite's spatial resolution.

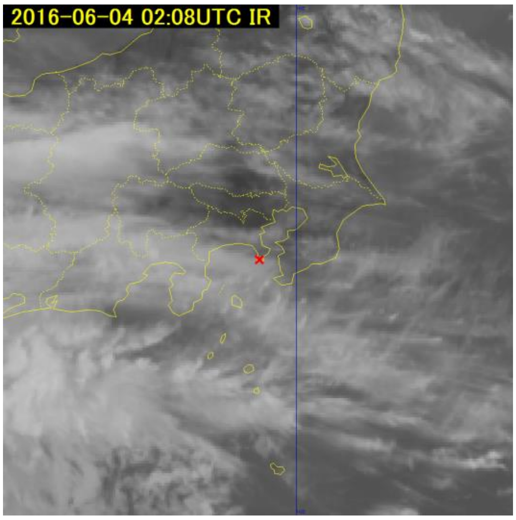

Fig. 2-5-7 B13 infrared image for 02:08 UTC on 4 June 2016; red cross: Jogashima

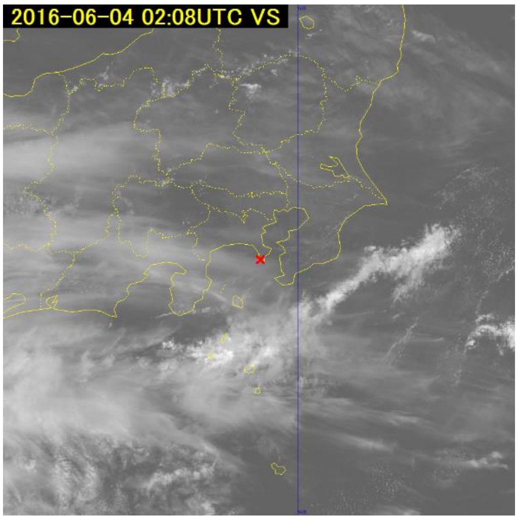

Fig. 2-5-8 B03 visible image for 02:08 UTC on 4 June 2016; red cross: Jogashima

Fig. 2-5-9 View north from Jogashima for 02:07 UTC on 4 June 2016. Upper- and lower-level clouds were observed from the ground.

2.5.2.4. Ci and Cm Overlap

In the infrared image (Fig. 2-5-10), a large thick cloud mass approached from the sea south of Honshu. The clouds in the sky above the MSC were broken and thin. As land can be seen around the MSC in the visible image (Fig. 2-5-11), this can be judged as a thin upper-level cloud area. Although it is difficult to distinguish these clouds from single-shot images, video shows different speeds of movement, indicating an overlay of upper- and mid-level clouds. These can be distinguished here both via surface observation and satellite imagery, but the thin mid-level clouds appear dominant in photography (Fig. 2-5-12). Since infrared radiation is transmitted from lower-level clouds, their observation brightness temperature in infrared imagery is higher than the actual value. Accordingly, it is difficult to estimate cloud top height from brightness temperature alone.

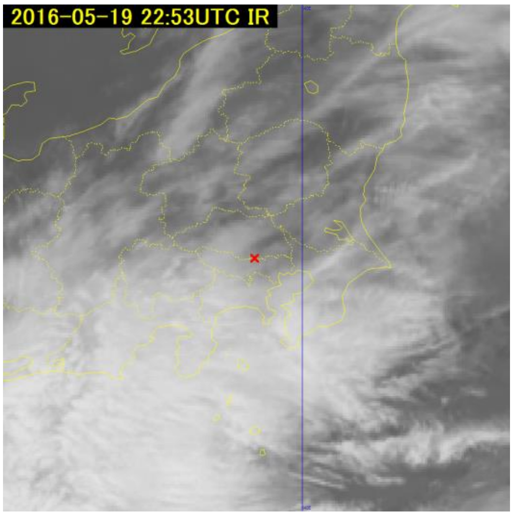

Fig. 2-5-10 B13 infrared image for 22:53 UTC on 19 May 2016; red cross: MSC

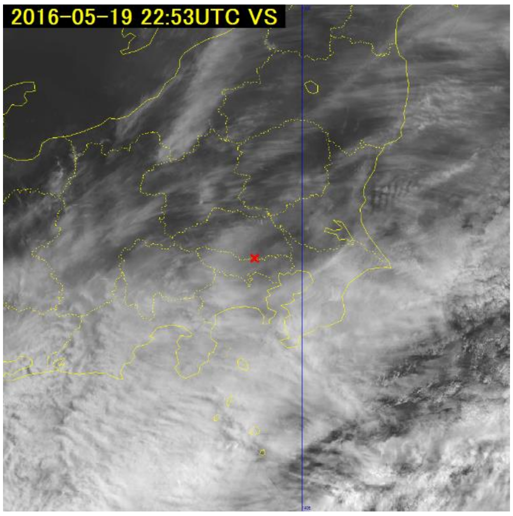

Fig. 2-5-11 B03 visible image for 22:53 UTC on 19 May 2016; red cross: MSC

Fig.2-5-12 View east-northeast from the park next to the MSC for 22:52 UTC on 19 May 2016. Upper- and mid-level clouds were observed from the ground.

2.5.2.5. Ci and Sc/Cu Overlap

In the infrared image (Fig. 2-5-13), a thin upper-level cloud area was observed from west-northwest to east-southeast. Lower-level cloud over the Kanto region is seen in grey, but this is difficult to distinguish from land in places where the temperature difference from the ground is small. In the visible image (Fig. 2-5-14), the cloud area and land surface are clearly distinguishable, and lower-level clouds are seen over the Kanto Plain. In this example, the presence of mid- and upper-level clouds cannot be judged via surface observation because lower-level clouds covered the entire sky (Fig. 2-5-15). However, both upper- and lower-level clouds are recognizable in satellite imagery. These are difficult to identify from such imagery when thick upper-level clouds are present.

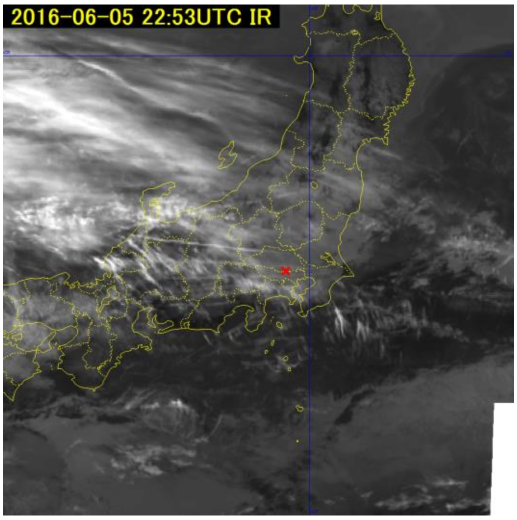

Fig. 2-5-13 B13 infrared image for 22:53 UTC on 5 June 2016; red cross: MSC

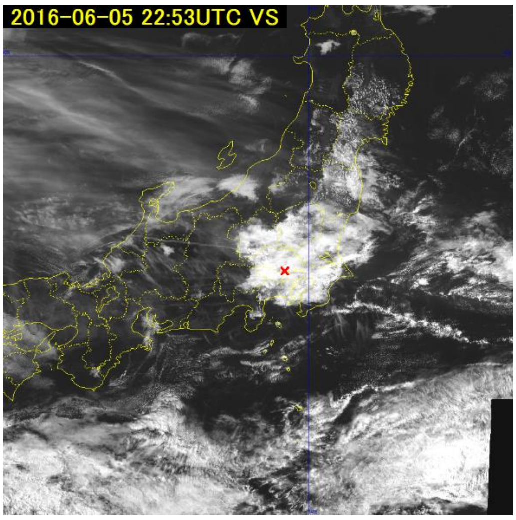

Fig. 2-5-14 B03 visible image for 22:53 UTC on 5 June 2016; red cross: MSC

Fig. 2-5-15 View southwest at the park next to MSC for 22:52 UTC on 5 June 2016. Lower-level clouds were observed from the ground.

2.5.2.6. Sc Only

In the infrared image (Fig. 2-5-16), grey clouds are observed around Tokyo. These appear slightly darker than clouds over the sea in the visible image (Fig. 2-5-17), but are still bright and show a wavy pattern. Accordingly, they can be identified as Sc. In this example, these can be identified as lower-level cloud from both surface observation and satellite imagery. However, the wavy pattern at the cloud top at intervals of 3 to 5 km in satellite imagery is not seen in surface observation, and the tiny gaps of several hundred meters between clouds seen in surface observation (Fig. 2-5-18) are not seen in satellite observation.

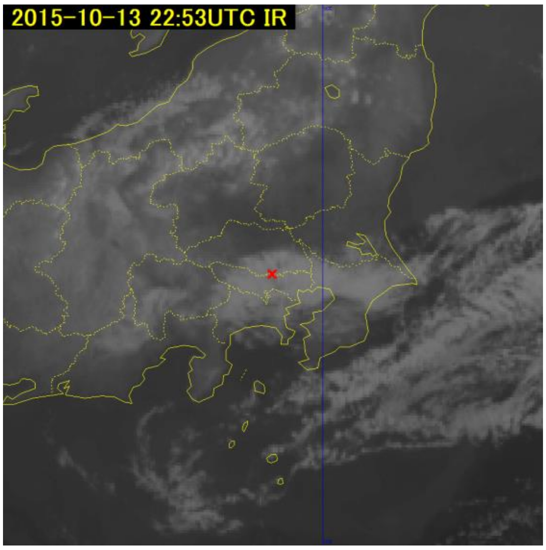

Fig. 2-5-16 B13 infrared image for 22:53 UTC on 13 October 2015; red cross: MSC

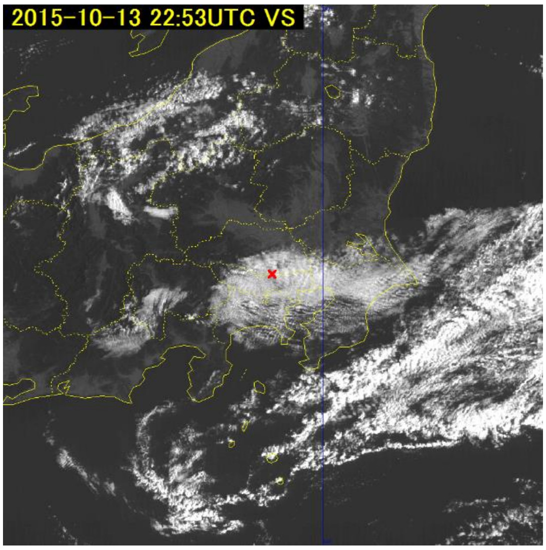

Fig. 2-5-17 B03 visible image for 22:53 UTC on 13 October 2015; red cross: MSC

Fig. 2-5-18 View southwest at the park next to MSC for 22:53 UTC on 13 October 2015. Lower-level clouds were observed from the ground.

2.5.2.7. Cb, Cg and Cu Co-presence

In the infrared image (Fig. 2-5-19), a remarkably bright cloud area is seen around the border of Tokyo and Saitama, along with a white area from the northern part of Ibaraki Prefecture to the northeast. In this example, the sun was shining from a westerly direction in the late afternoon. This cloud can be identified as an active convective type incorporating Cb because its western side appears bright in visible imagery (Fig. 2-5-20), which indicates vertical development. In a photograph taken near Kotesashi Station in Tokorozawa, Saitama Prefecture (Fig.2-5-21), anvil-shaped cirrus is seen around the top of the Cb, indicating significant cloud development. The minimum brightness temperature of the cloud area was –51.9°C, corresponding to an altitude of 196 hPa (41,577 ft, or approximately 12,700 m) when converted using JMA numerical weather prediction model (GSM: Global Spectral Model) data. The estimated distance from the shooting location to the cloud with the lowest brightness temperature was around 30 km.

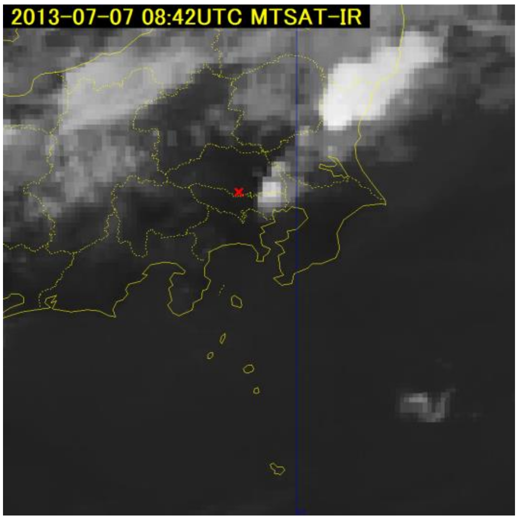

Fig. 2-5-19 Infrared image for 08:42 UTC on 7 July 2013; red cross: Kotesashi Station

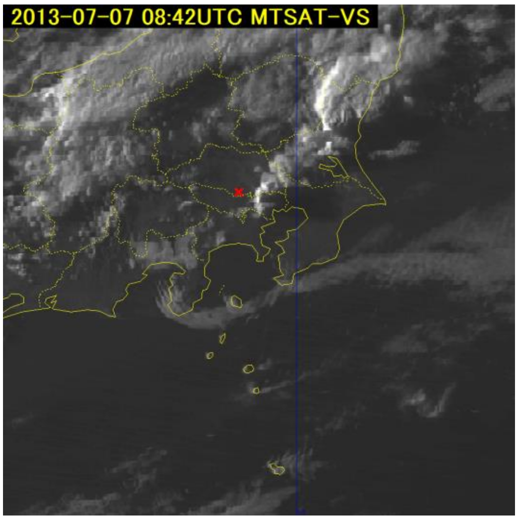

Fig. 2-5-20 Visible image for 08:42 UTC, 7 July 2013; red cross: Kotesashi Station

Fig. 2-5-21 Near Kotesashi Station, 08:42 UTC on 7 July 2013. Lower-level clouds were observed from the ground.

2.5.2.8. Cu and Cg Co-presence

In the infrared image (Fig. 2-5-22), a white cloud area is seen at the border of Saitama and Chiba. Vertically developed convective clouds are seen in visible imagery (Fig. 2-5-23) as in the previous case. No anvil-shaped cirrus is seen in a photograph taken near Kotesashi Station (Fig. 2-5-24), but a developed cloud area and cumulus congestus (or cumulonimbus calvus) are observed. The minimum brightness temperature of this cloud area was –37.0°C, corresponding to an altitude of 340 hPa (27,574 ft, or approximately 8,400 m) when converted using GSM data. The distance was estimated to be around 40 km from the shooting location to the cloud with the lowest brightness temperature.

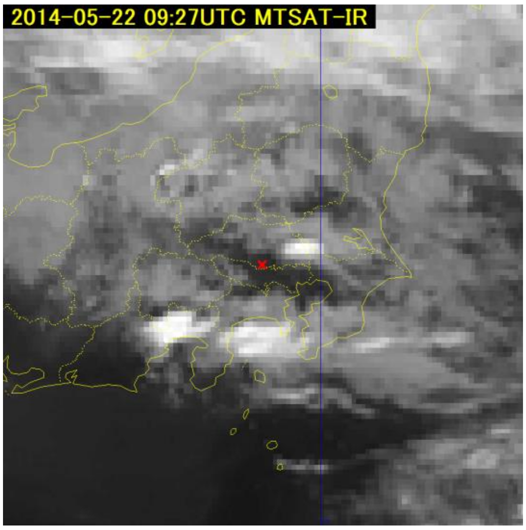

Fig. 2-5-22 Infrared image for 09:27 UTC on 22 May 2014; red cross: Kotesashi Station

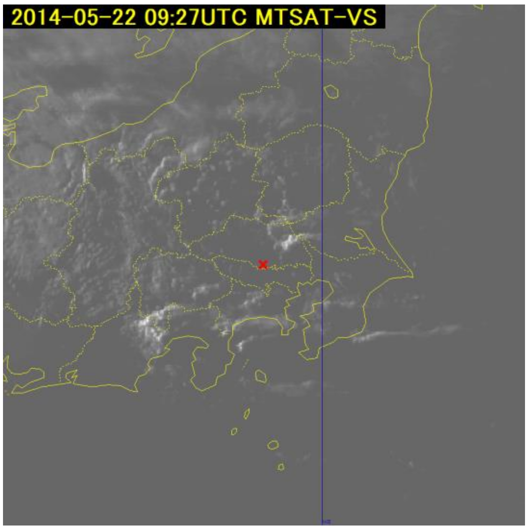

Fig. 2-5-23 Visible image for 09:27 UTC on 22 May 2014; red cross: Kotesashi Station

Fig. 2-5-24 View from the area near Kotesashi station for 09:28 UTC on 22 May 2014. Lower-level clouds were observed from the ground.

References:

- World Meteorological Organization (2017) International Cloud Atlas: Manual on the Observation of Clouds and Other Meteors (WMO-No. 407). https://cloudatlas.wmo.int/en/home.html

3. Cloud Patterns

Cloud patterns are represented in visual imagery in relation to proximity to atmospheric flow, as well as the distribution and vertical stability of temperature and water vapor. Analysis of individual patterns is crucial in understanding 3-D atmospheric structures.

3.1. Ci Streaks

Long thin Ci streaks from jet streams and other sources are observed in the upper atmosphere with anticyclonic curvature corresponding to upper-trough conditions. Cloud areas also develop further when lower clouds are enhanced. Ci streaks (indicated with arrows) are seen over the Bohai Sea in Fig. 3-1-1 and along the jet in Fig. 3-1-2.

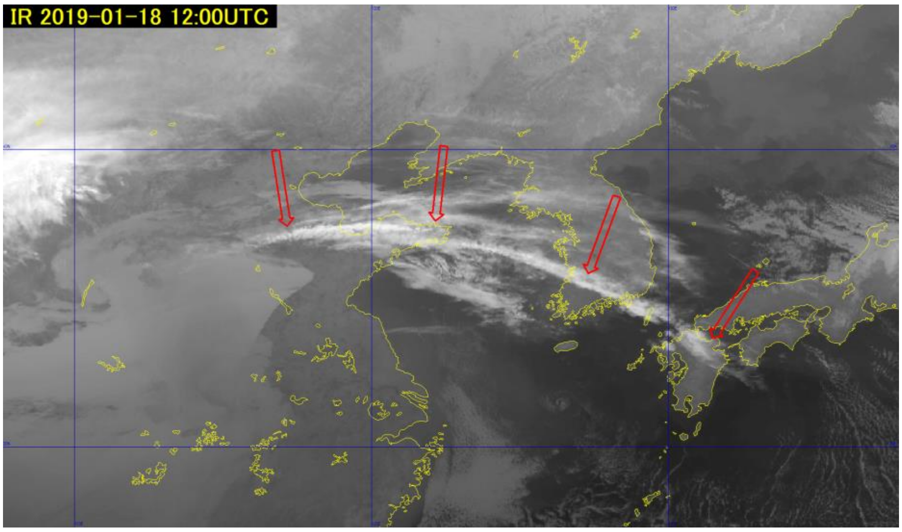

Fig. 3-1-1. B13 Infrared image of Ci streaks for 00:00 UTC on 13 October 2016

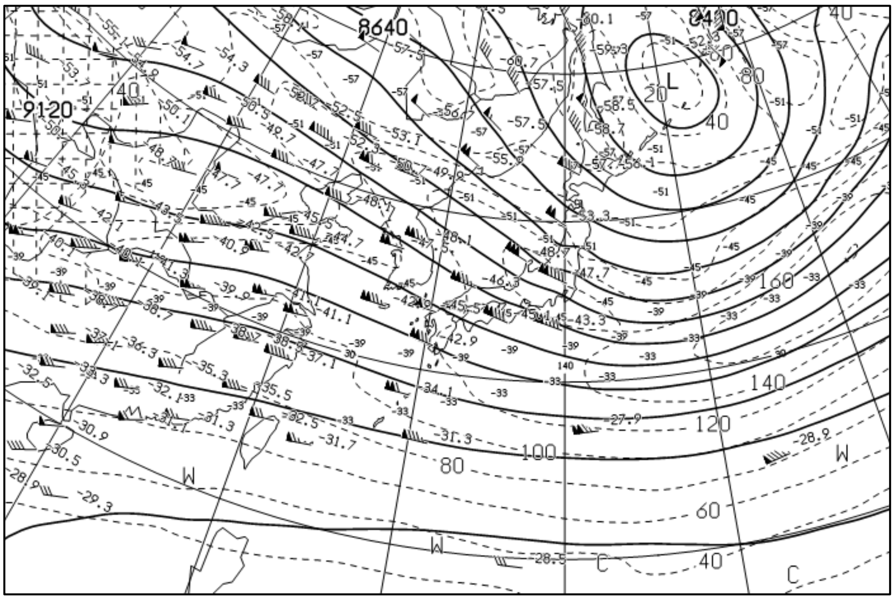

Fig. 3-1-2. Image for 00:00 UTC on 13 October 2016, 200 hPa isohypse

3.2. Transverse Lines

Ci cloud streaks known as transverse lines form in small wavelets approximately at right angles to the direction of the prevalent air current. These are usually observed along jet streams with wind speeds exceeding 80 kt. As per Ono and Miura (1982), they are known as Kelvin-Helmholtz waves, and are excited by tropopause conditions.

Turbulence is known to occur at high frequencies in the vicinity of transverse lines, which may emerge from developing typhoons in association with currents along upper divergence.

In Fig. 3-2-1, a transverse line is seen offshore of the Sanin and Hokuriku areas (arrows). This corresponds roughly to the jet axis at 200 hPa (Fig. 3-2-2). In Fig. 3-2-3, a transverse line is visible (arrows) along Typhoon Haima (T1622) above the sea east of the Philippines.

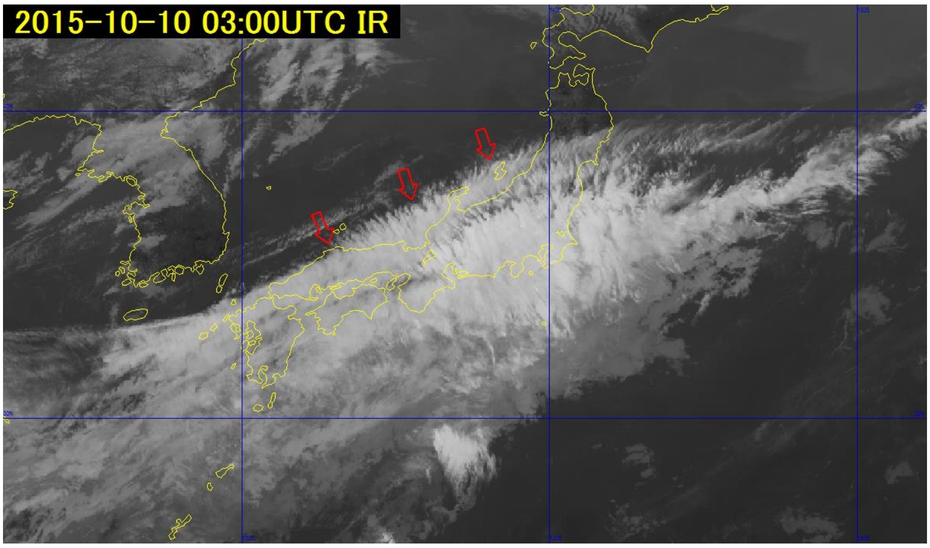

Fig. 3-2-1. B13 infrared image for 03:00 UTC on 10 October 2015

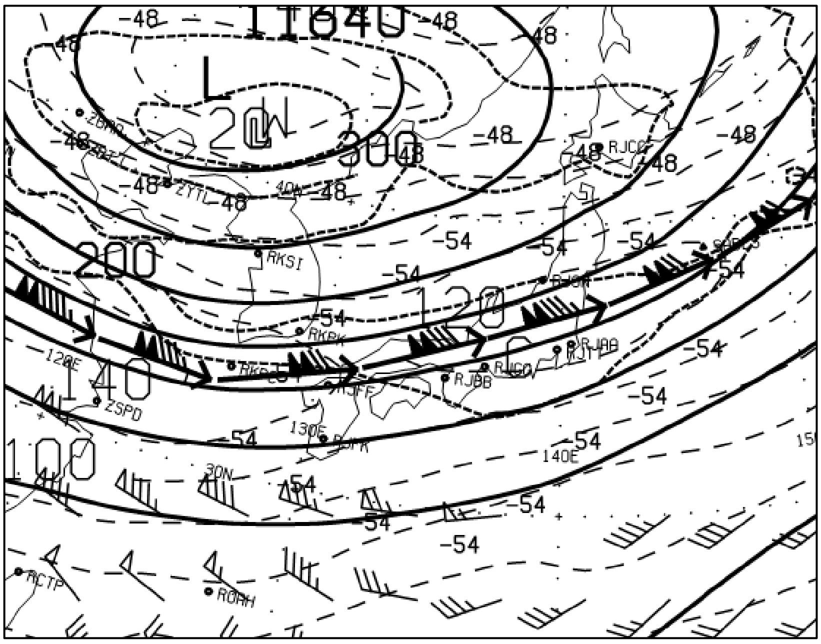

Fig. 3-2-2. 200 hPa contour lines for 00:00 UTC on 10 October 2015

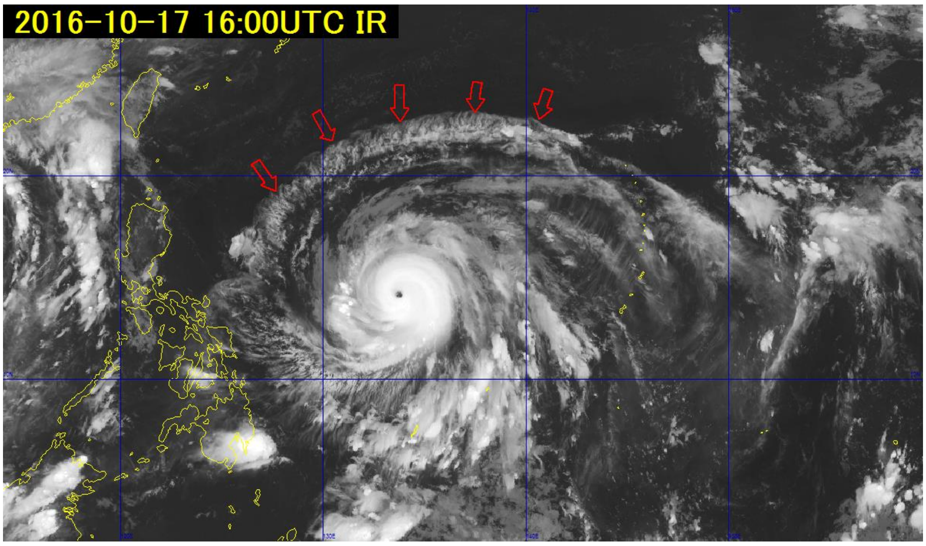

Fig. 3-2-3. B13 infrared image for 16:00 UTC on 17 October 2106

3.3. Orographic Ci Clouds

The stagnant orographic high clouds observed on the leeward side of mountain ranges appear white in infrared imagery, with a rim on the windward side parallel to the range and elongated to the leeward side. They are easily identifiable in footage, as the rim on the windward side hardly moves. They are observed in association with roughly stable stratification between mountain ranges and the upper tropopause with roughly steady wind speeds (Kobana, 1981), causing a transfer of mountain-associated waves to the upper layer in the updraft region via wave motion with significant upper-layer humidity. The waves remain stationary as long as the synoptic field remains unchanged, manifesting as stagnant upper clouds.

Figure 3-3-1 shows B13 infrared image from Himawari-8, with orographic Ci occurring leeward east of the Ou mountains (arrow indication), and Fig. 3-3-2 shows B03 visible image for the same time period. The pictures show transparent cirrus cloud in the upper layer.

Figure 3-3-3 shows numerical prediction grid point values from JMA's mesoscale numerical weather prediction model (MSM) around Sendai at 00:00 UTC on the same day. Upper cloud with humidity is seen at around 250 – 300 hPa, with strong vertical western wind distribution in the upper troposphere creating stable stratification.

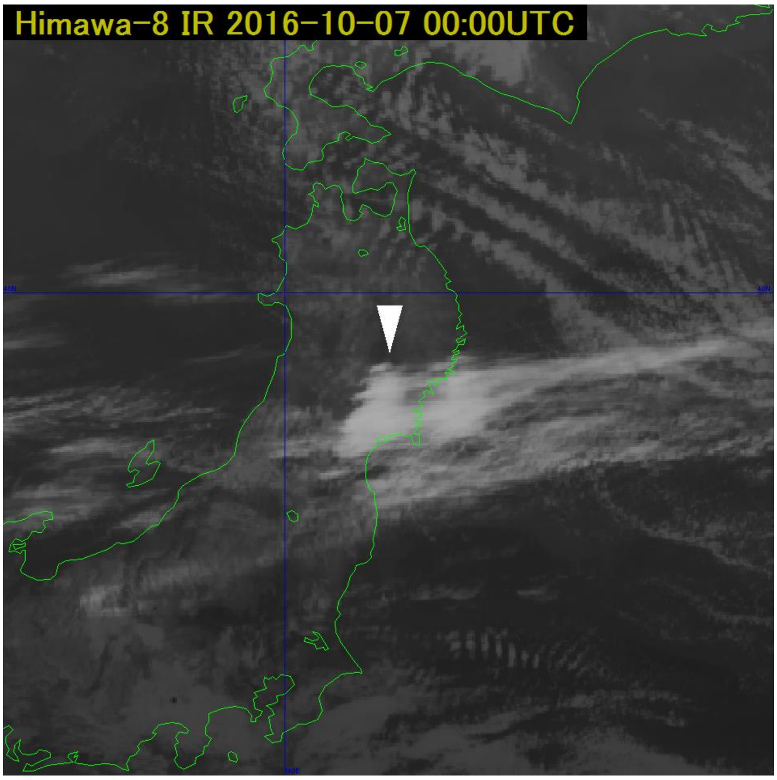

Fig. 3-3-1. B13 infrared image for 00:00 UTC on 7 October 2016

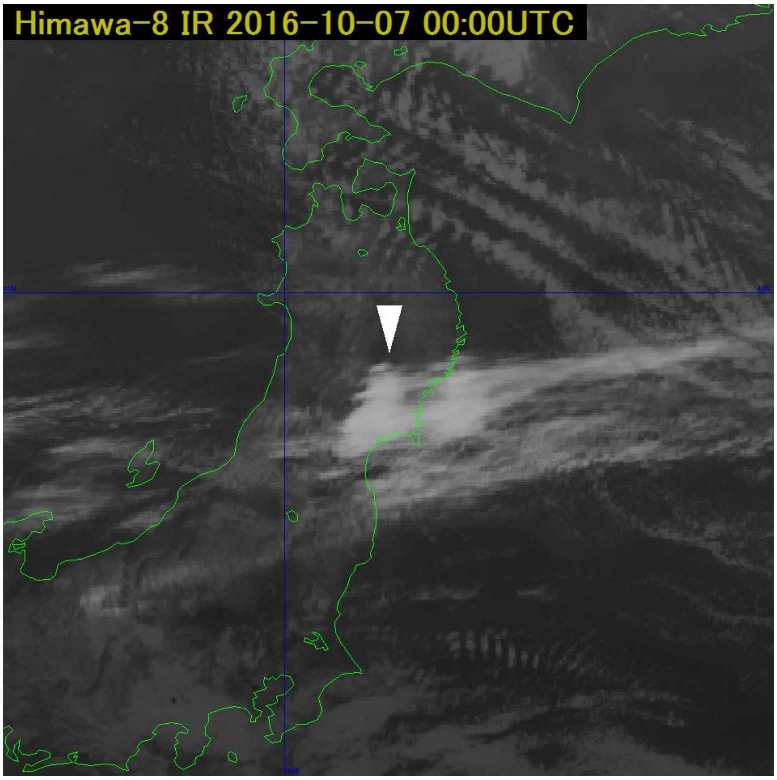

Fig. 3-3-2. B03 visible image for 00:00 UTC on 7 October 2016

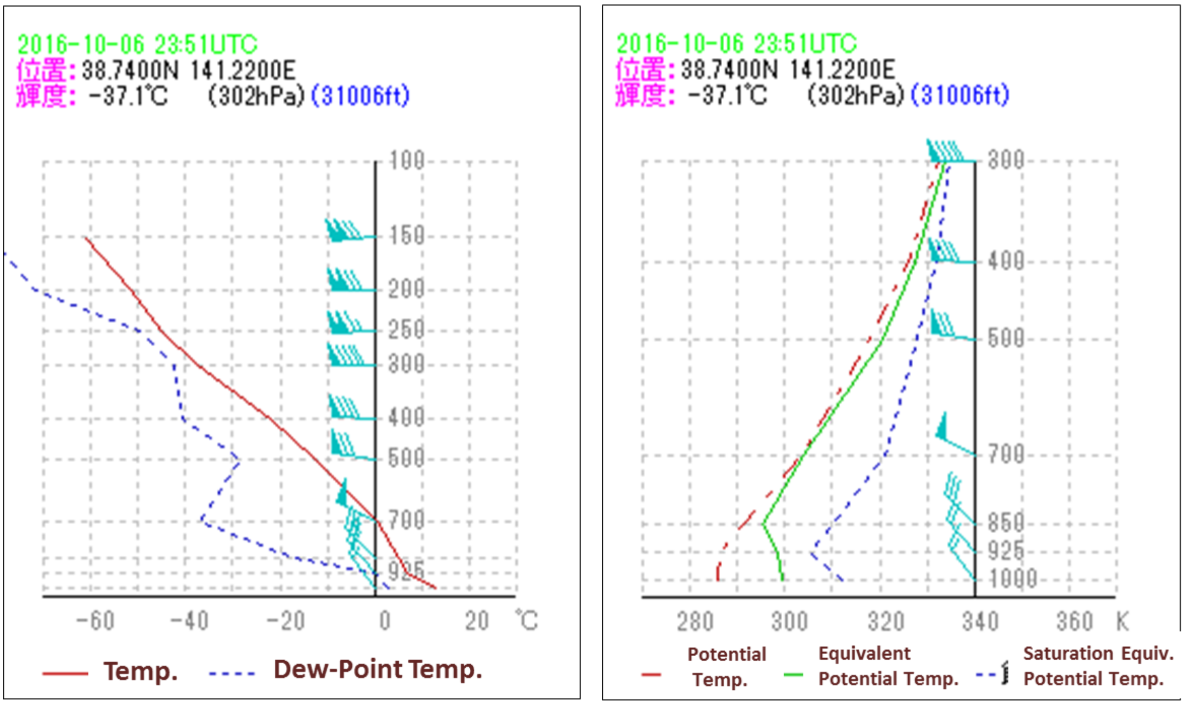

Fig. 3-3-3. Emagram (left) amd potential temperature emagram (right)
for 00:00 UTC on 7 October 2016

In Day Convective Storm RGB image, it should be noted that orographic Ci appears in the same color as active cumulonimbus areas accompanying strong updrafts (Fig. 3-3-4) with stable stratification and strong winds over mountainous areas. Ice-crystal sizes in cirrus cloud are similar to those of the cloud top of active cumulonimbus accompanying strong updrafts.

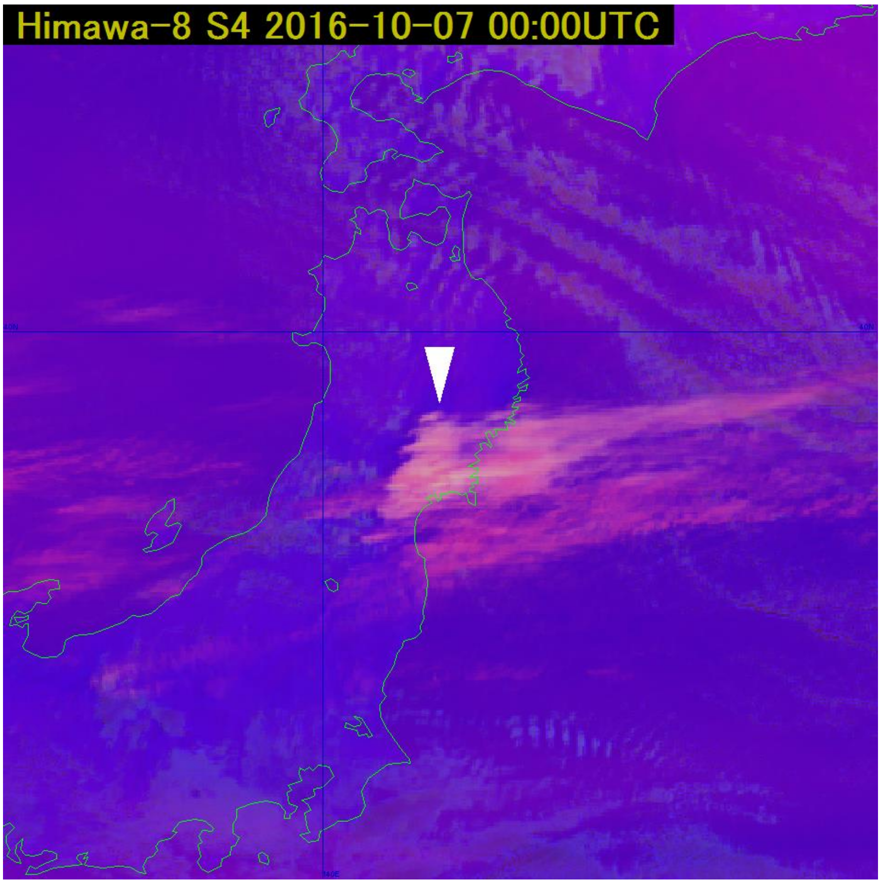

Fig. 3-3-4.　Day Convective Storm RGB image for 00:00 UTC on 7 October 2016

3.4. Anvil Ci

Cumulonimbus (Cb) clouds in phases between the most active and the dissipation phases often take on an anvil-like structure due to horizontal Ci flow suppressed by the tropopause at the cloud top.

Anvil-type Ci extends in a feather-like manner mostly on the leeward side from cumulonimbus with a fuzzy edge (Fig. 3-4-1). The cloud top height of anvil Ci is roughly equivalent to the center of cumulonimbus, but the formation is not accompanied by strong rain. Hence, it is important to distinguish this cloud type from Cb centers.

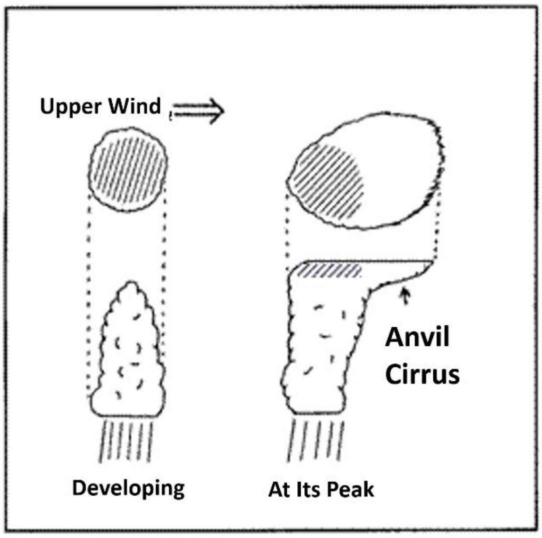

Fig. 3-4-1. Anvil Ci

Figures 3-4-2 and 3-4-3 show visible and infrared image of cumulonimbus over the Boso Peninsula in Japan’s Chiba Prefecture with anvil Ci extending from the center for 05:00 UTC on 4 August 2016. The cumulonimbus center appears as an uneven part at the cloud surface in the visible image.

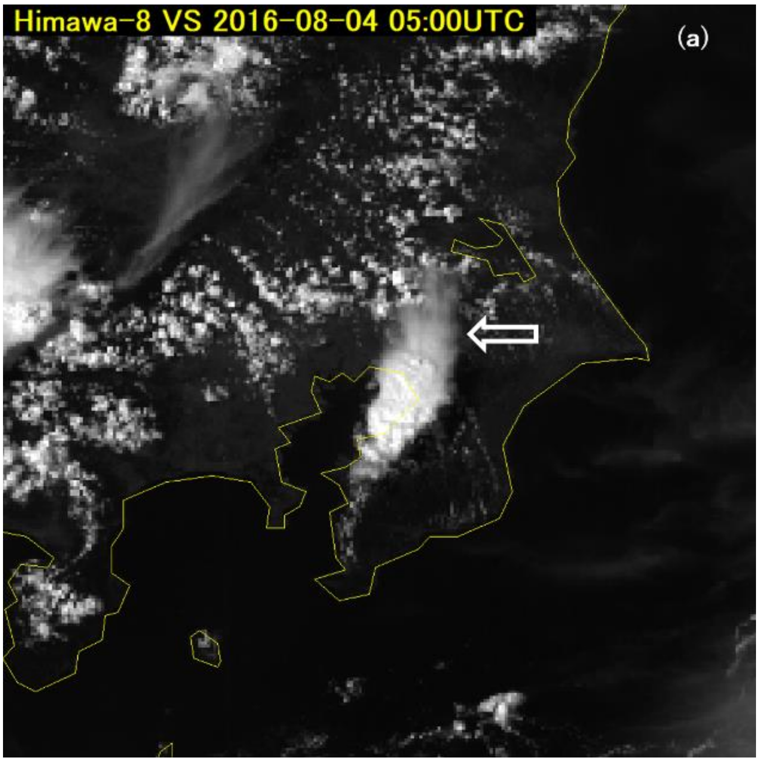

Fig. 3-4-2. B03 visible image for 05:00 UTC on 4 August 2016

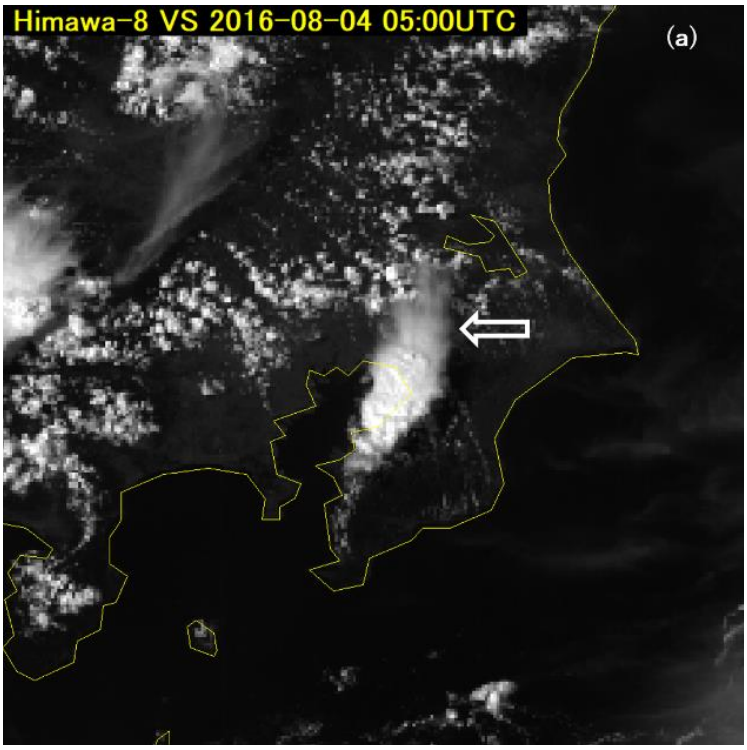

Fig. 3-4-3. B13 infrared image for 05:00 UTC on 4 August 2016

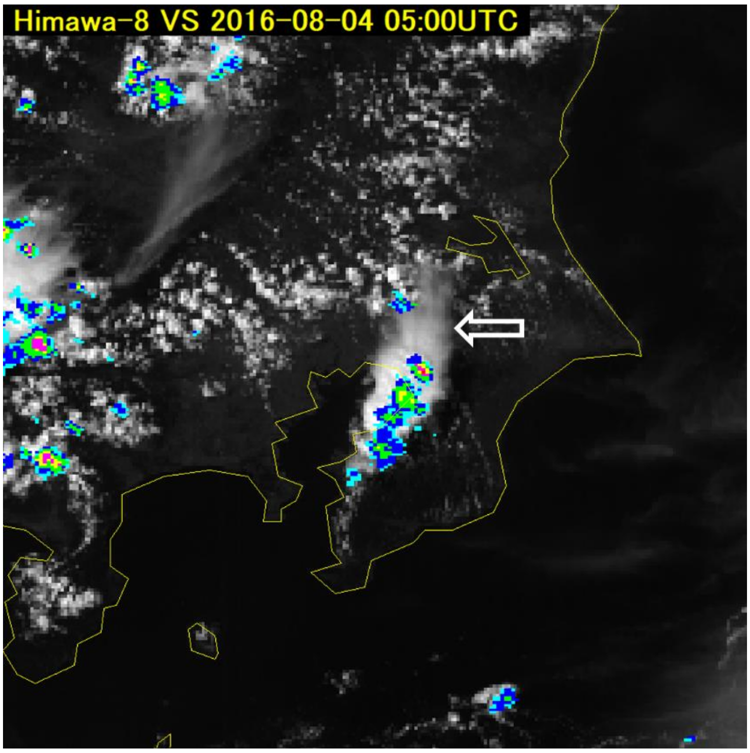

Fig. 3-4-4. B03 radar composite image for 05:00 UTC on 4 August 2016

Figure 3-4-4 shows an overlay of visible image and radar echo from the same time period. The cumulonimbus center is accompanied by precipitation observed as radar echoes. However, the anvil Ci extending northeastward from the center of the cumulonimbus was not visualized by radar because it was an upper-cloud type. Figure 3-4-5 shows shoreline cloud in Kanagawa Prefecture with anvil Ci on the left.

Fig. 3-4-5. Anvil Ci as per the cumulonimbus shown in Fig. 3-4-4

3.5. Bulge

Bulge is a phenomenon involving convex expansion with anticyclonic curvature of frontal cloud bands toward a cold polar side. It represents a developing cloud area with a warm wet wind current rising in correspondence with cyclonic development or a frontal wave brought by an approaching trough. The curvature increases as the cloud area develops, and expansion toward the cold side may also be seen in non-developing cloud areas. Temporary formations with no continuation are not classified as bulges. In Fig. 3-5-1, bulges are seen between Pyongyang and Lake Khanka (arrows).

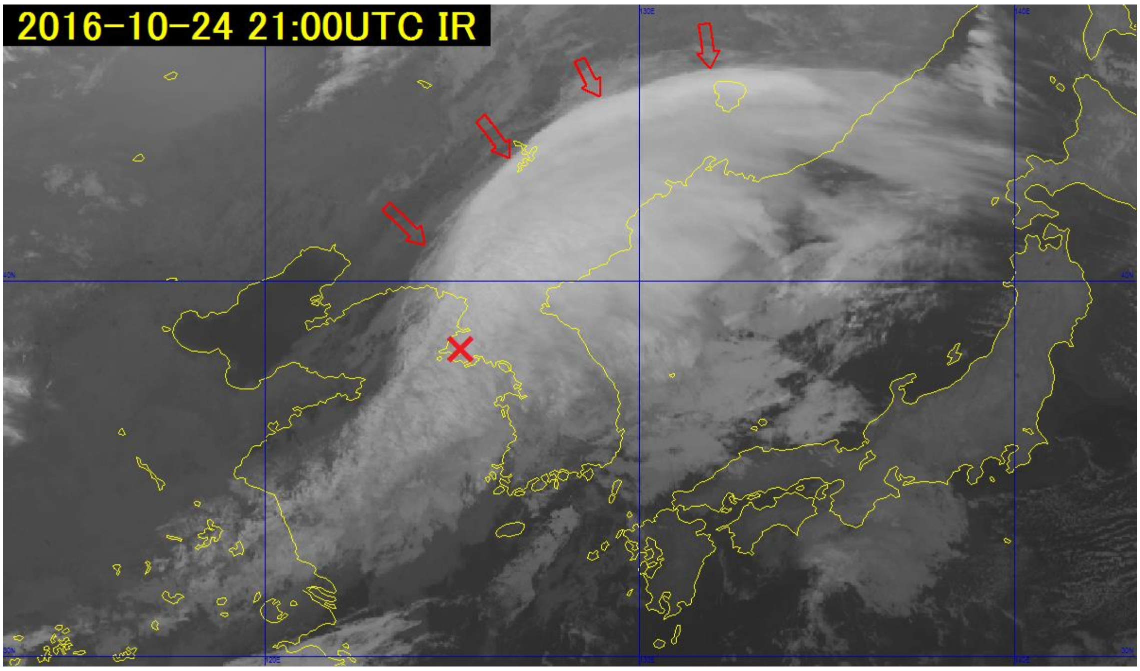

Fig. 3-5-1. B13 infrared image for 21:00 UTC on 24 October 2016

3.6. Hook Patterns

Anticyclonic curvature in developing cloud areas may increase at the northern edge and present cyclonic curvature at the southwestern edge in a formation known as a hook, representing the presence of cold air entering from the rear of the cloud area. There is also a rough correlation between hooks and ground-level low-pressure centers (Section 5.2.1). Internationally, comma-shaped forms observed by radar or otherwise are more broadly called hook patterns. Figure 3-5-1 shows a cloud area with a hook pattern by the Korean Peninsula (red cross).

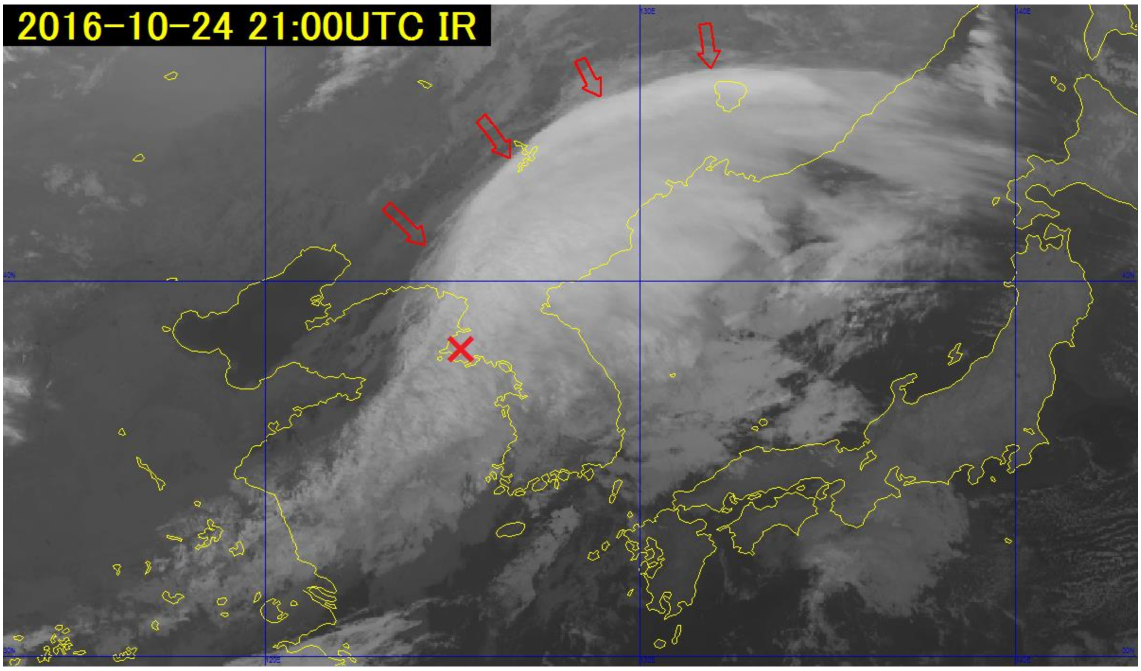

Fig. 3-5-1. B13 infrared image for 21:00 UTC on 24 October 2016

3.7. Lee Wave Clouds

Lee wave clouds align in a regular pattern leeward of mountain ranges and island forms. Figure 3-7-1 shows such cumulus and stratocumulus clouds aligning parallel to the Ou mountains. With long thin forms such as mountain ranges, these clouds have a strike parallel at the leeward side.

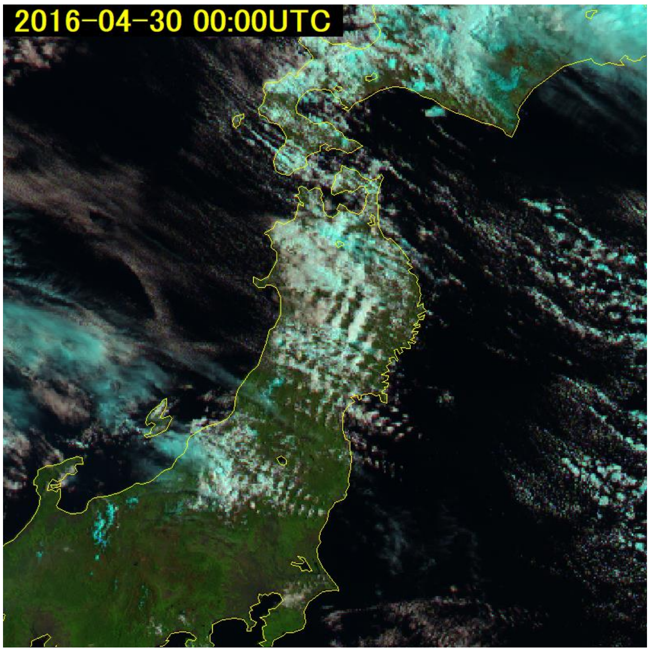

Fig. 3-7-1. Natural color RGB image for 00:00 UTC on 30 April 2016

3.7.1. Environmental Conditions for Lee Wave Clouds

The following conditions support lee wave cloud formation:

1. The wind direction is roughly steady through a thick layer up to the upper layer orthogonal to the strike of an obstacle.
2. Absolutely steady conditions exist throughout a very thick space up to the upper layer.
3. Sufficient water vapor for cloud formation is present.
4. Wind speed around the mountain top is above 10 m/s.
5. Stratospheric development with a decreasing Scorer number is observed.

Figure 3-7-2 shows a potential temperature emagram for Akita at the time of lee wave cloud emergence with the following characteristics:

1. The wind direction is roughly steady throughout the thick layer up to the upper layer west-northwest to northwest, approximately at a right angle to the strike of the Ou mountains.

2. Neutrality is observed up to around 700 hPa from the equivalent potential temperature, with convective stability above this region along with static stability.
3. Humidity exceeds 80% between 925 and 700 hPa, providing sufficient water vapor for lower clouds to form.
4. The Ou mountain altitude is 1,500 – 2,000 m, with a wind speed of 14 m/s at 850 hPa and 17 m/s at 800 hPa.
5. Wind speed increases from the lower to the upper layers, with the Scorer number decreasing toward the upper layer.

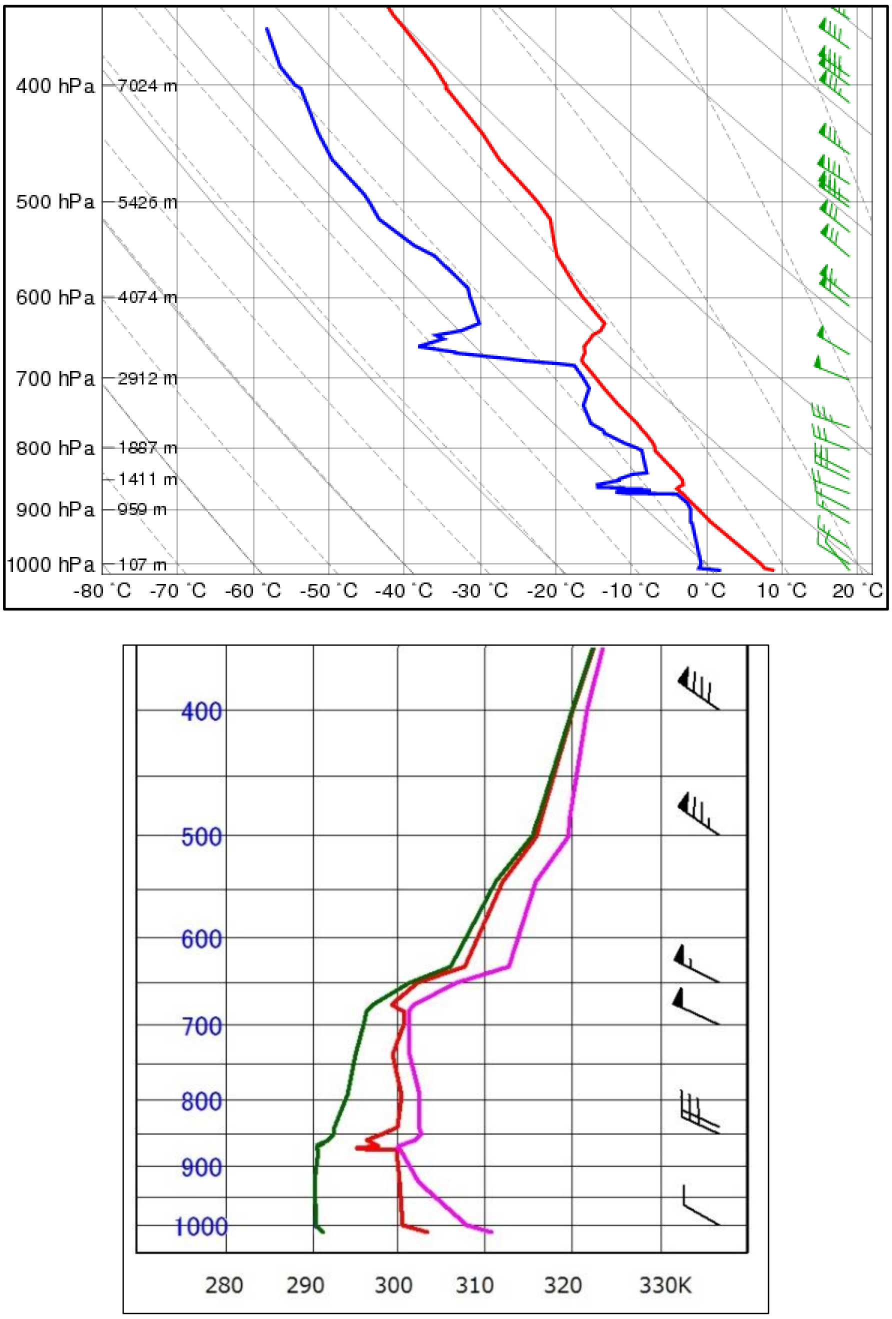

Fig. 3-7-2. Emagram (uper) and potential temperature emagram (bottom) for Akita at 00:00 UTC on 30 April 2016

Green: potential temperature; red: equivalent potential temperature; pink: saturation potential temperature

The lee wave theory proposes that intervals of such clouds are directly proportional to wind speed (Section 3.7.2). The potential for related turbulence along mountain lee waves must also be examined, with consideration of elements other than wind speed such as inversion layer altitude, vertical stability and mountaintop formations. Lee wave clouds observed in satellite imagery may not be directly associated with turbulence, but can be seen as an indicator of potential for the phenomenon. In addition, as such waves tend to move to the upper-stream side of mountains, lee wave clouds may also appear slightly toward the windward side rather than only on the leeward side (Fig. 3-7-3).

3.7.2. Relationship Between Intervals of Lee Wave Clouds and Wind Speed

Figure 3-7-4 shows infrared image and brightness temperatures for lee wave clouds with a top at around –10°C. Aerological observation in Akita revealed temperatures of –6.8°C at 800 hPa and –14.7°C at 700 hPa, suggesting a lee wave cloud altitude of around 2,500 m. Lee wave cloud intervals are proportional to wind speed, which allows wind speed estimation.

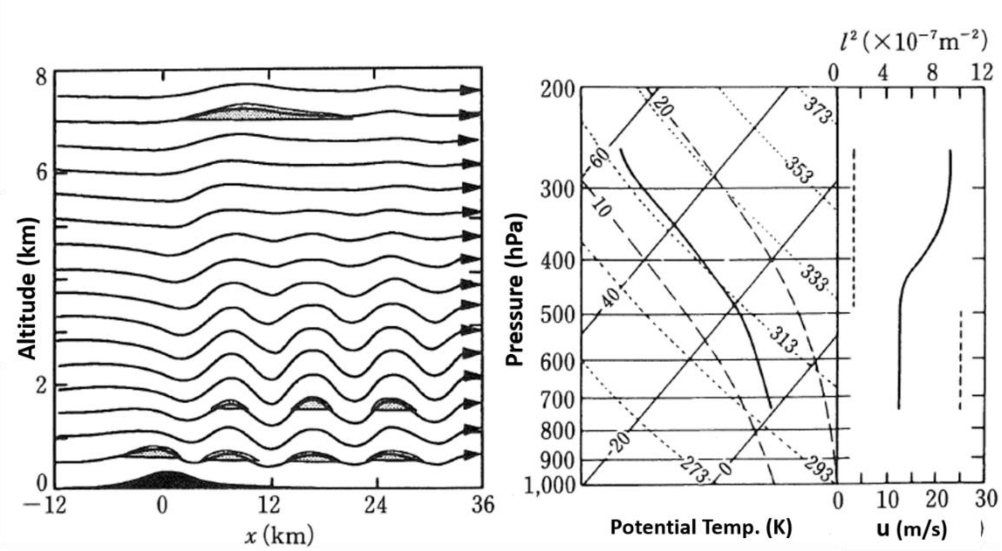

Fig. 3-7-3. Schematic diagram of lee wave clouds (Ogura, 1997)

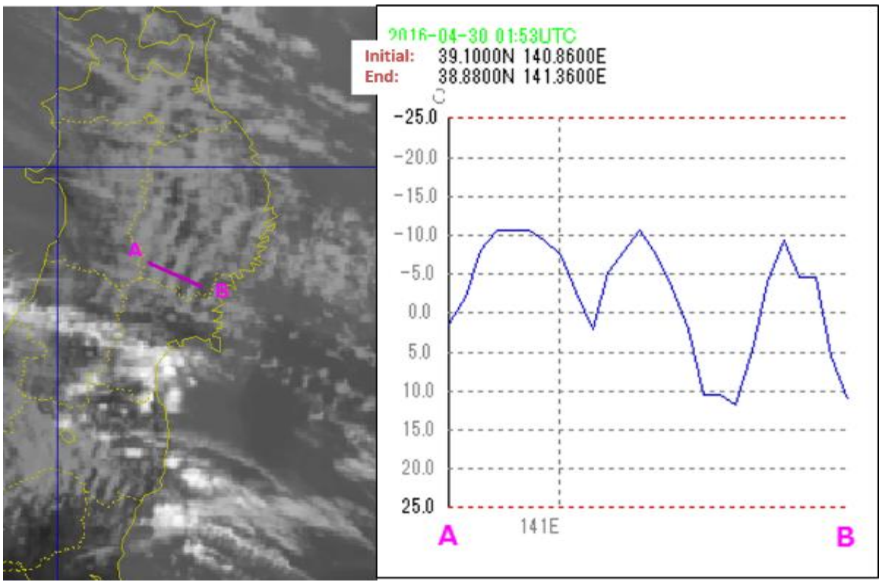

Fig. 3-7-4. B13 infrared image and brightness temperatures (line section indicated by the yellow arrow) for 02:00 UTC on 30 April 2016

Supplementary Information

With wind speed as U (in m/s) and the wavelength of leeward wind as λ (in km), the relationship can be written as follows (Corby G.A., 1957):

$$U = 1.7\lambda + 4.8$$

Measuring λ in satellite imagery, $5 \text{ km} < \lambda < 10 \text{ km}$.

By substituting the values into the equation,

$$13.3 \text{ m/s} < U < 21.8 \text{ m/s (where } \lambda = 8 \text{ and } U = 18.4)$$

Aerological observation in Akita shows 14 m/s at 850 hPa, 17 m/s at 800 hPa, and 26 m/s at 700 hPa. The height of lee wave clouds estimated from brightness temperatures is around 2,500 m, which is roughly in agreement with the equation value.

* Scorer number

This dimensionless quality is represented by the equation below.

h: mountain height: s: static stability;

g: gravitational acceleration;

u: wind speed; z: altitude

$$h^2\left(\frac{sg}{u^2}-\frac{1}{u}\frac{\partial^2 u}{\partial z^2}\right)$$

3.8. Open Cells

In satellite imagery, cloud patterns forming a donut shape or a U-shape in otherwise cloudless areas are called open cells. Those consisting of convective clouds descend to previously cloudless areas (Fig. 3-8-1) with vertical circulation ascending within the wall cloud surroundings. Donut patterns are sustained with smaller vertical wind shear and lower wind speeds. Faster winds and larger vertical wind shear may cause the ring to collapse with no open cell pattern formation.

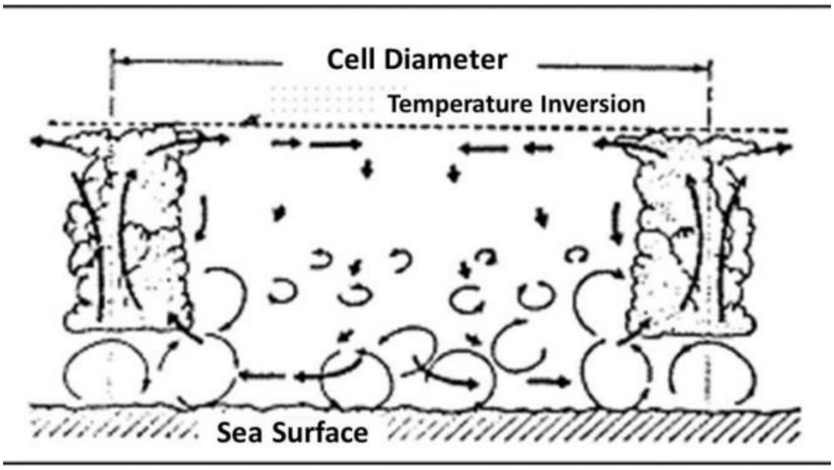

Fig. 3-8-1. Open cell formation (Asai, 1983)

Bader *et al.* (1995) described how the shape of open cells depends on lower-layer wind speed (Fig. 3-8-2). Such cells appear in polygon or donut form with winds below 20 kt in the lower layer, whereas the ring around cloudless areas begins collapsing at higher wind speeds to form a U-shape. As wind speed rises, formation irregularity increases with further spreading along the current.

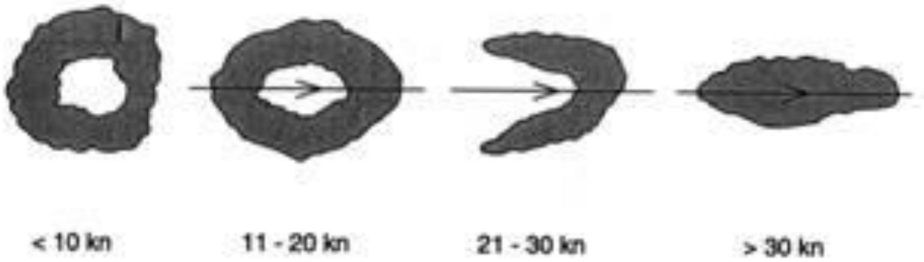

Fig. 3-8-2. Open-cell development with specific wind speeds (in knots)
Arrows indicate wind direction (Bader *et al.* 1995)

As open cells are associated with large temperature differences between cold air and warm seas surfaces, they can be used to estimate the strength of cold air running from the rear of developed cyclones. Such patterns tend to emerge in lower layers when strong cyclonic currents are present. Cold advection is generally stronger with larger temperature differences between air and the sea surface.

Figure 3-8-3 shows True-Color Reproduction image for visible bands from 00:00 UTC on 12 February 2016, with various cloud patterns emerging in a cold area over sea areas east of Japan. The pattern marked O is an open cell in cyclonic circulation. Figure 3-11-2 (Section 3.11) shows the corresponding surface weather chart.

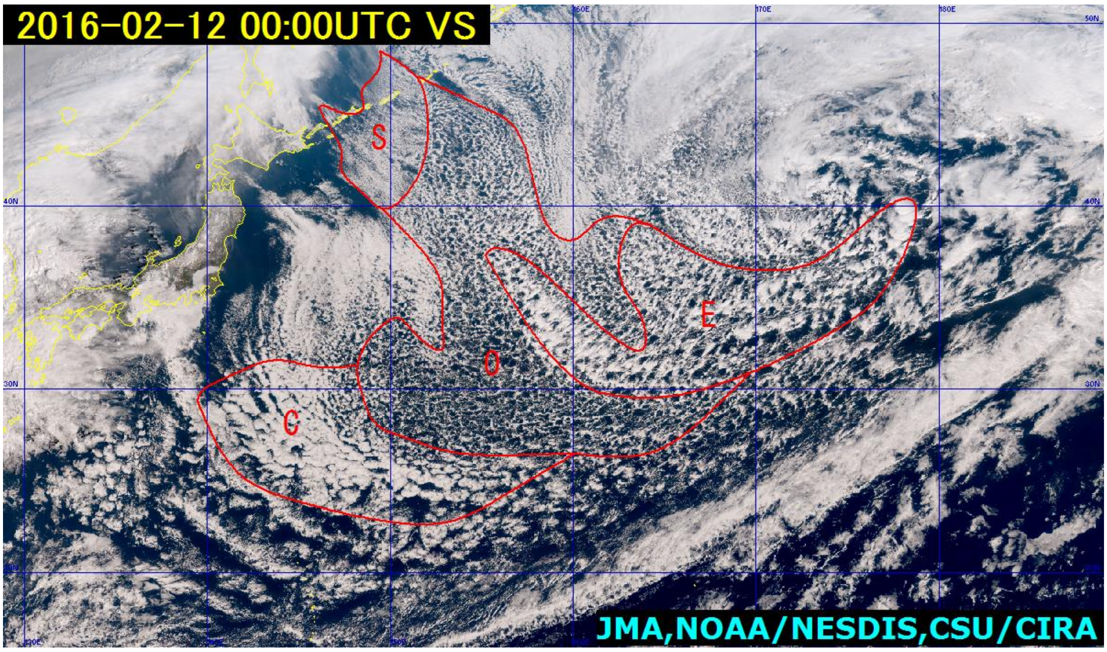

Fig. 3-8-3. True Color Reproduction image for 00:00 UTC on 12 February 2016

3.9. Closed Cells

In satellite imagery, polygonal and dense clouds forming a cell surrounded by a clear area are called closed cells. These are stratocumulus clouds with relatively small vertical wind shear and wind speeds often under 20 Kt. With a cloud top restrained by an inversion layer, they tend to emerge in areas of anticyclonic currents in the lower layer corresponding to the southeastern quadrant. As shown in Fig. 3-9-1, the central cloud is formed by an updraft with vertical circulation descending in the surrounding clear area.

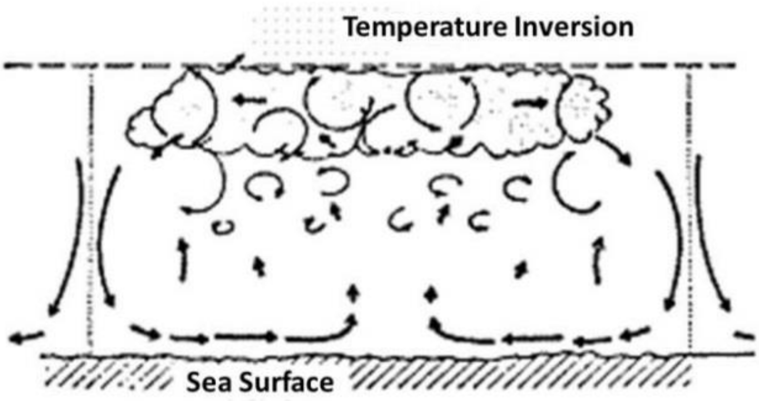

Fig. 3-9-1. Closed cell model (Asai, 1983)

Closed cells emerge with smaller temperature differences between air and the sea surface than open cells, and may form with less cold air entering or by weakened cold areas that turn open cells into closed cells. The open/closed status is generally based on the strength of the cold. The border between a region with an open cell and one with a closed cell may indicate jet stream positioning in the lower layer, as shown in Fig. 3-9-2 (Bader *et al.*, 1995).

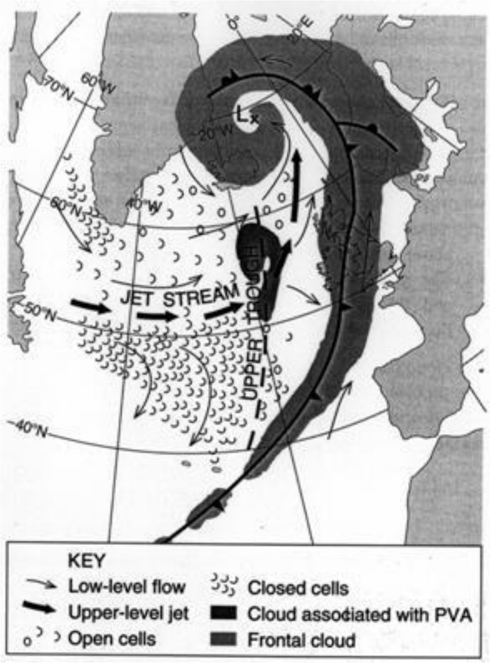

Fig. 3-9-2. A general cell-form cloud pattern in a cold area and a synoptic field (Bader *et al.*, 1995)

Cloud pattern C in Fig. 3-8-3 (Section 3.8) is a closed cell in circulation at the southeastern quadrant of an anticyclone, presumably corresponding to an area with weakened cold.

3.10.　Cloud Streets

In satellite imagery, parallel patterns of Cu and Cg clouds are called cloud streets, with near-parallel tracks to lower-layer winds and a roughly uniform cloud top height. Vertical shear in the wind direction is relatively small inside the cloud layer but larger than that of open/closed cells, creating a roll formation (with lines or bands) parallel to the shear of lower wind. As seen in Fig. 3-10-1, there is helical motion of the air parcel in the roll-shaped convection and formation of convective cloud in the upper part of the updraft region.

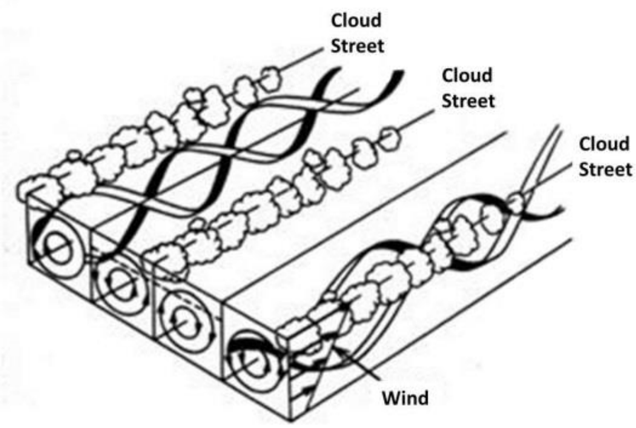

Fig. 3-10-1. Roll-shaped convection (Asai 1996)

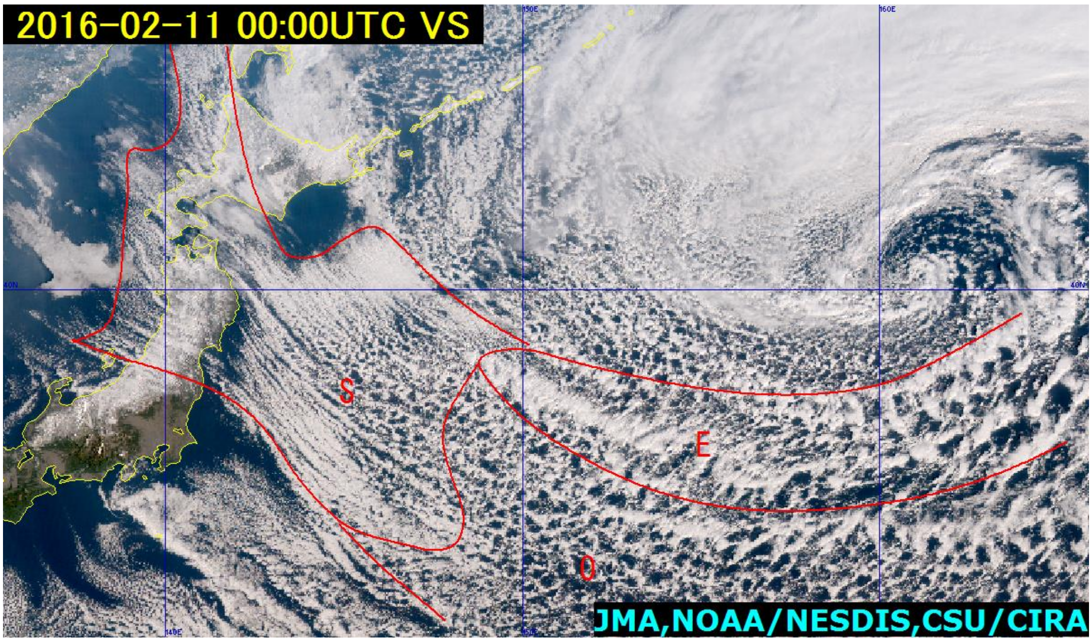

Fig. 3-10-2. True Color Reproduction image for 00:00 UTC on 11 February 2016

3.11. Enhanced Cu

Satellite imagery of open cell regions consisting of Cu in cold areas behind cyclones shows Cb and Cg clouds in areas referred to as enhanced Cu. These arise due to intense cold air migrating southward from behind a developed cyclone, activating Cu into Cb or Cg. The presence and intensity of cold air can be estimated from the characteristics of the enhanced Cu.

Figure 3-11-1 shows a day snow-fog RGB composite image of day snow-fog on the same day as Fig. 3-8-3 (Section 3.8), indicating the cloud pattern E as enhanced Cu. Orange indicates thick cloud areas with precipitation, which are more active with a higher cloud top than other parts of the open cell, and more organized with anvil cloud. Figure 3-11-3 shows a 500 hPa upper-level weather chart for 00:00 UTC on 12 February 2016. A trough accompanying cold air below –36°C is seen moving eastward, causing Cu to develop into Cb or Cg due to convective instability.

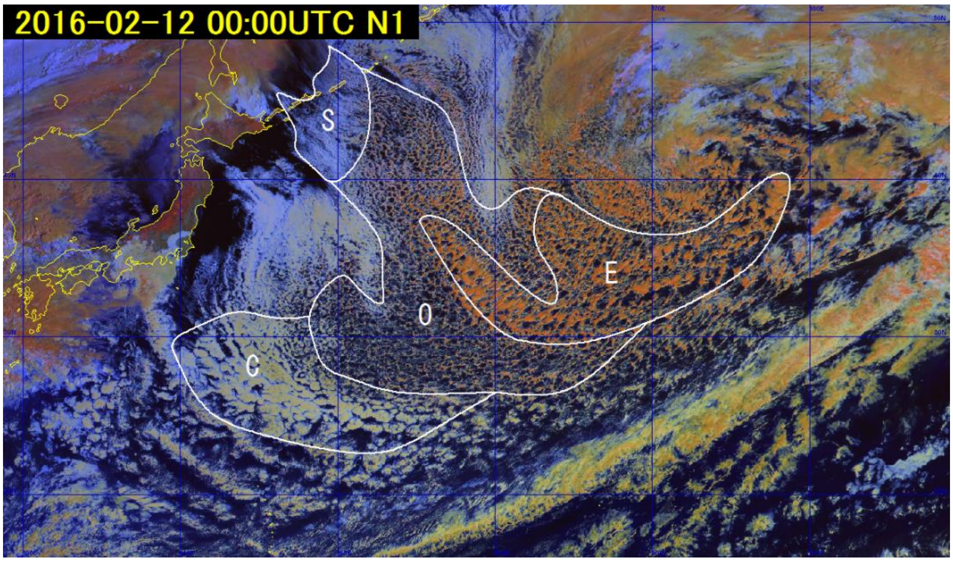

Fig. 3-11-1. Day snow-fog RGB composite image for 00:00 UTC on 12 February 2016

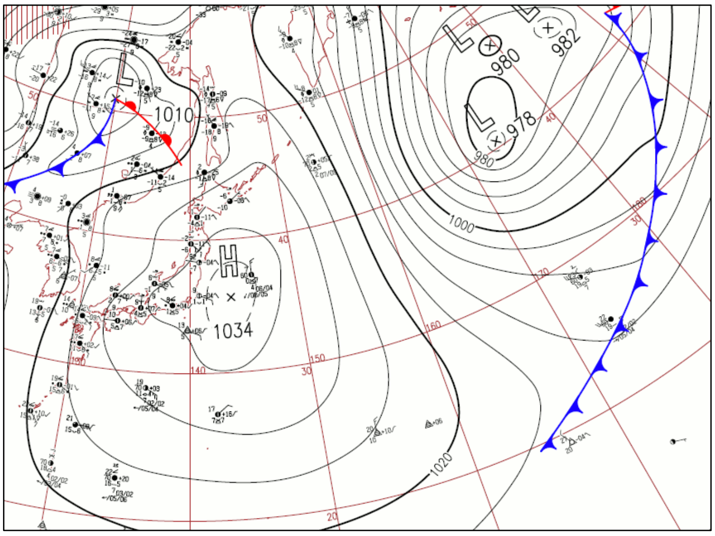

Fig. 3-11-2. Surface weather chart for 00:00 UTC on 12 February 2016

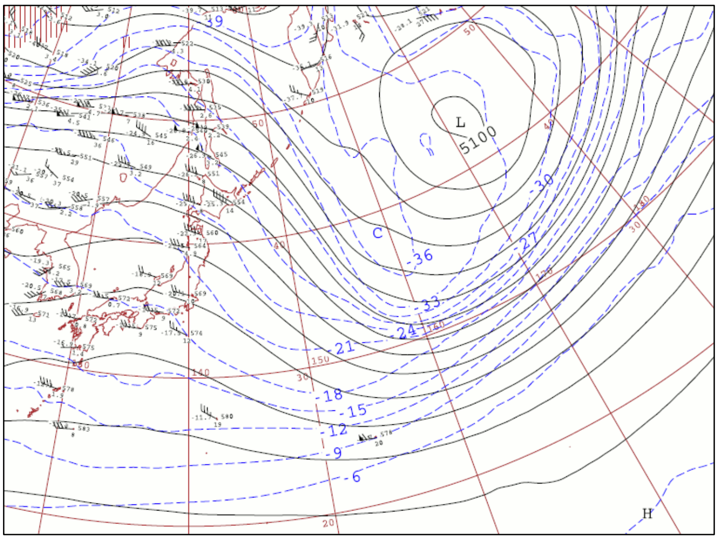

Fig. 3-11-3. 500 hPa upper-level weather chart for 00:00 UTC on 12 February 2016

3.12. Cb Cloud Clusters

Cb is often observed as individual clouds, but may also aggregate to form large parcels called cloud clusters or Cb clusters. Clusters are composed of convective clouds of various sizes at different stages during development, reaching up to several hundred kilometers on a horizontal scale. Meso-convective systems such as squall lines and multi-cells are recognizable in radar imagery, and cloud clusters (convective systems on a larger scale) are recognizable in satellite imagery, often appearing in the tropics or over continental areas in summer.

In the field of satellite observation, Maddox (1980) defined α-scale mesoscale convective complexes (MCCs) as systems producing extreme phenomena such as tornadoes, hail and thunderstorms over north America. MCCs are defined as cloud areas with a top temperature below –32°C and a size exceeding 0.1 million km^2 (diameter: approx.: 350 km), with a near-circular formation (i.e., a major/minor axis ratio above 0.7) persisting for six hours or more. These tend to develop over continental areas between late evening and nighttime in unstable atmospheric conditions with weak forced convection on a synoptic scale. Figures 3-12-1 and 3-12-2 show MCC conditions observed by Himawari-8, with a near-circular cluster over 300 km in diameter (cloud area C) above China.

For the area around Japan, Iwasaki and Takeda (1993) investigated regional appearance characteristics of mesoscale cloud clusters during Asia's rainy season. Such clusters were defined as cloud areas with a brightness temperature below –50°C forming a circular or oval shape with a diameter over 100 km, a rim (particularly on the western side) exhibiting a large gradient of brightness temperature, and emergence in mid-latitudes. Clusters over Japan were found to generally have an average life span of less than 14 hours and an average maximum diameter of 170 km. Those with a larger maximum diameter tended to have a longer life span. Larger clusters with a maximum diameter over 200 km often emerged over continental areas, whereas smaller ones were more likely to emerge over sea areas. Around Japan, the majority of large cloud clusters emerged and developed over the East China Sea, with some bringing heavy rainfall to the Kyushu region.

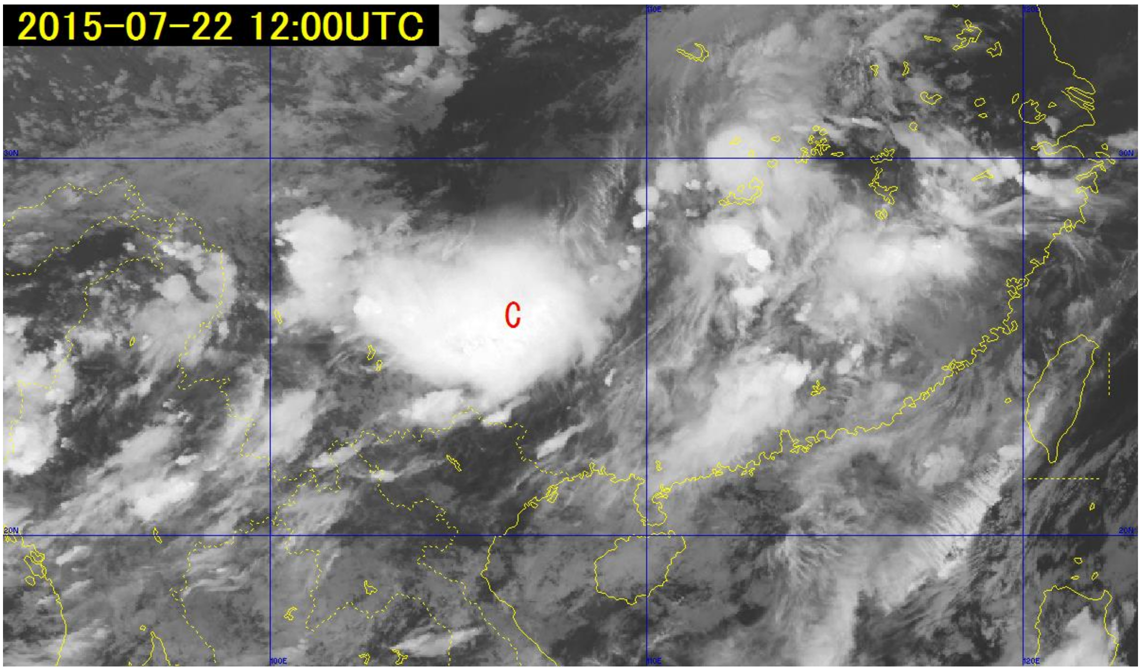

Fig. 3-12-1. B13 infrared image for 12:00 UTC on 22 July 2015

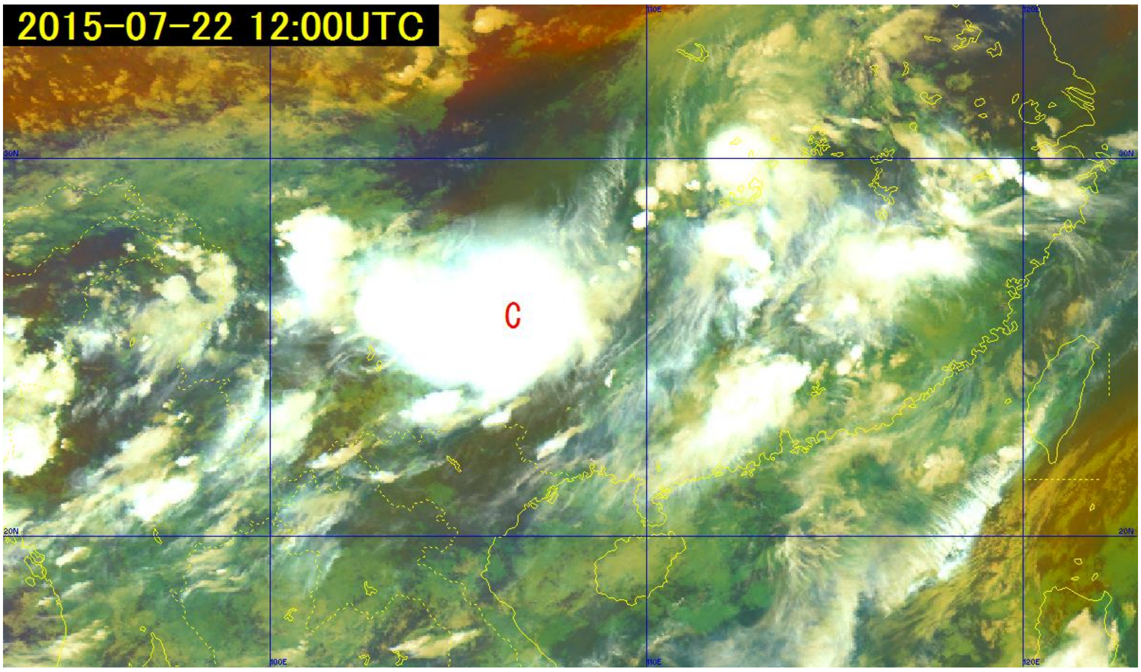

Fig. 3-12-2. Airmass RGB composite image for 12:00 UTC on 22 July 2015

Figures 3-12-3 and 3-12-4 show mesoscale cloud cluster conditions with a near-circular form over the western coast of Kyushu. Although on a smaller scale, the cluster is approximately equivalent to MCC conditions. It subsequently progressed eastward and weakened after passing over central Kyushu, causing heavy rainfall (hourly totals: 124.5 over Mt. Unzen in Nagasaki Prefecture, 150.0 mm in Kosa in Kumamoto Prefecture, 126.5 mm in Yamato in Kumamoto Prefecture). Figure 3-12-5 shows a surface weather chart for the period.

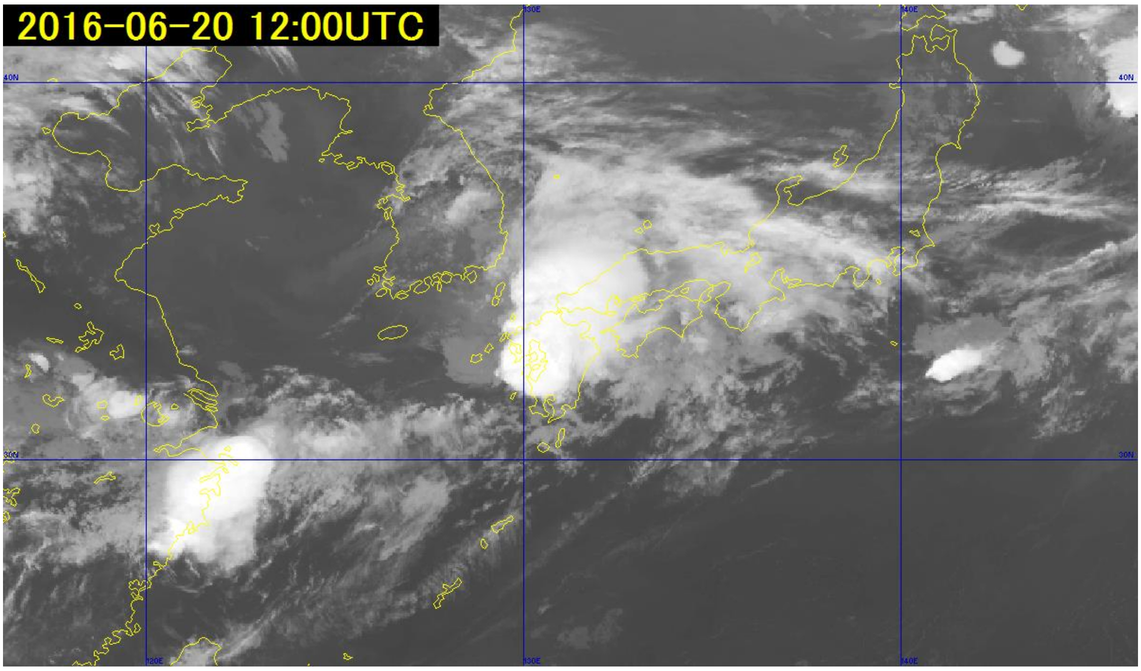

Fig. 3-12-3. B13 infrared image for 12:00 UTC on 20 June 2016

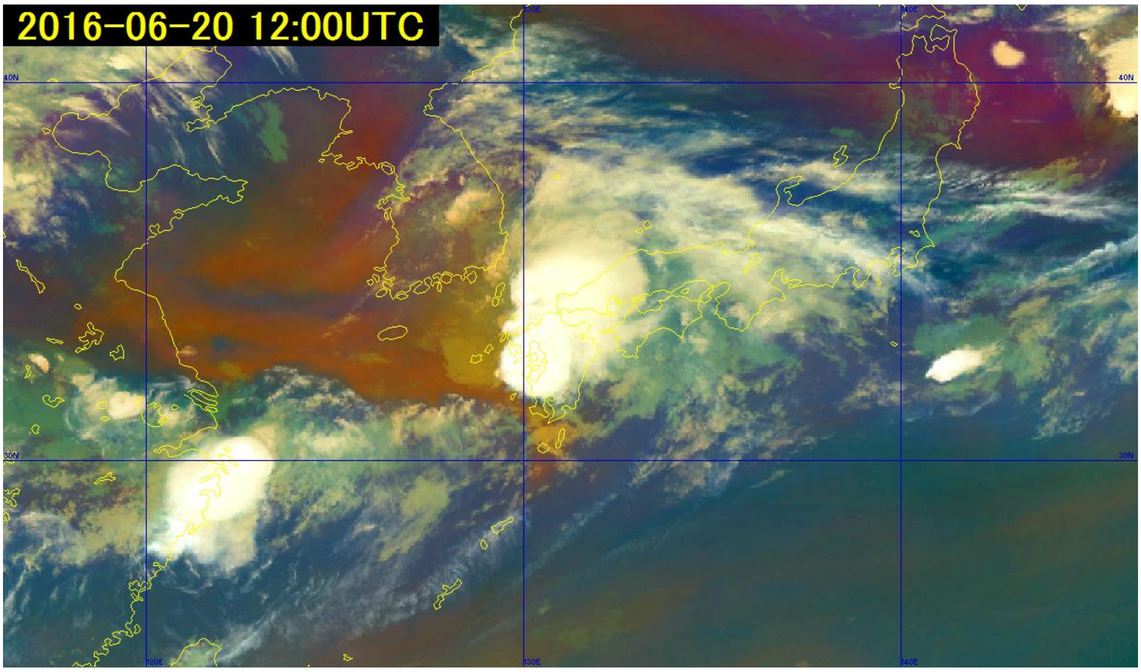

Fig. 3-12-4. Airmass RGB composite image for 12:00 TC on 20 June 2016

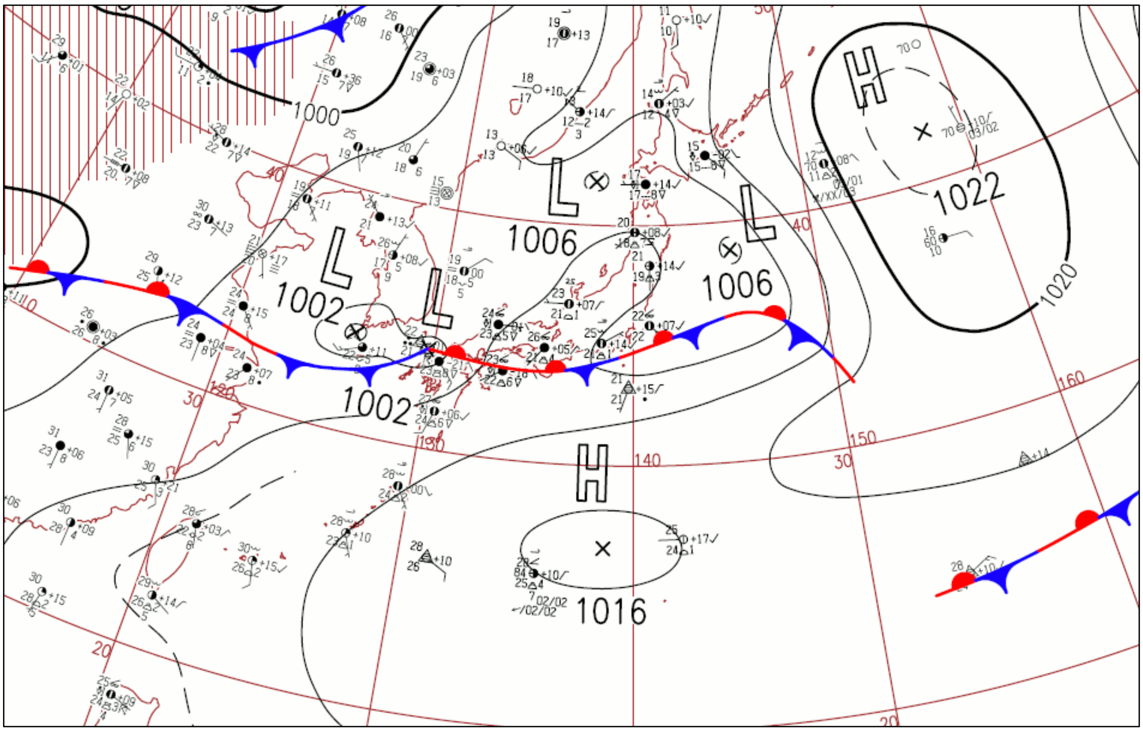

Fig. 3-12-5. Surface weather chart (prompt report) for 12:00 UTC on 20 June 2016

3.13. Central Dense Overcast (CDO) areas

CDOs are circular cloud areas with a smooth cloud top formed by an assemblage of Cb around the eye and center of typhoons. These form when a typhoon is developing, and act as an indicator of typhoon intensity in satellite observation. Figures 3-13-1, 3-13-2 and 3-13-3 show image for typhoon Nepartak (T1601) in 2016, with red arrows surrounding the CDO cloud area.

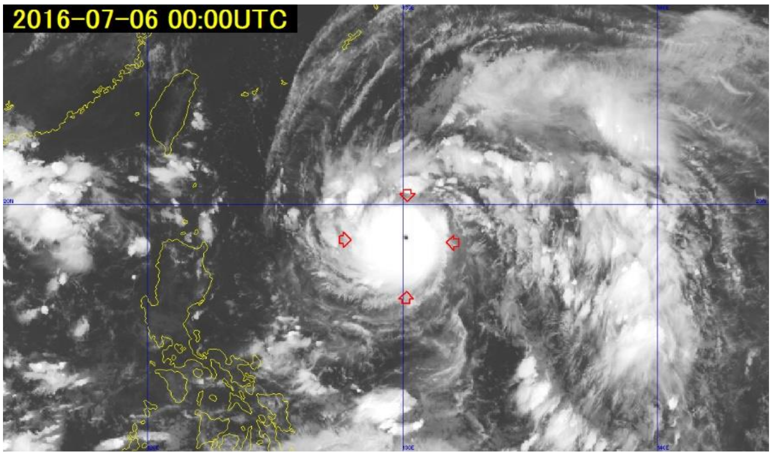

Fig. 3-13-1. B13 infrared image for 00:00 UTC on 6 July 2016

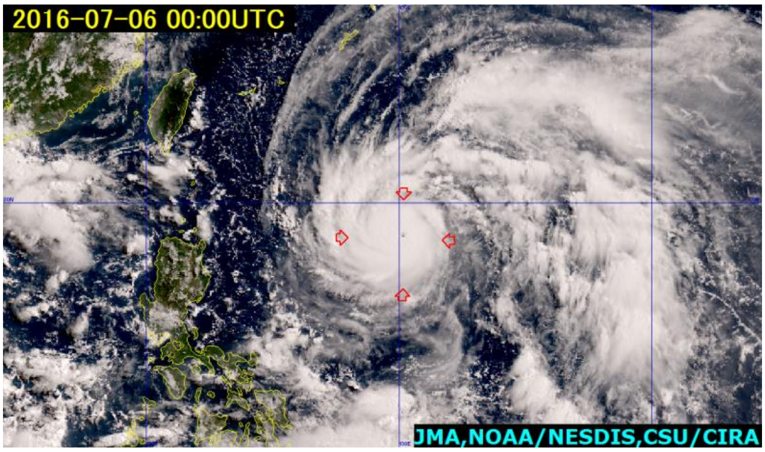

Fig. 3-13-2. True Color Reproduction image for 00:00 UTC on 6 July 2016

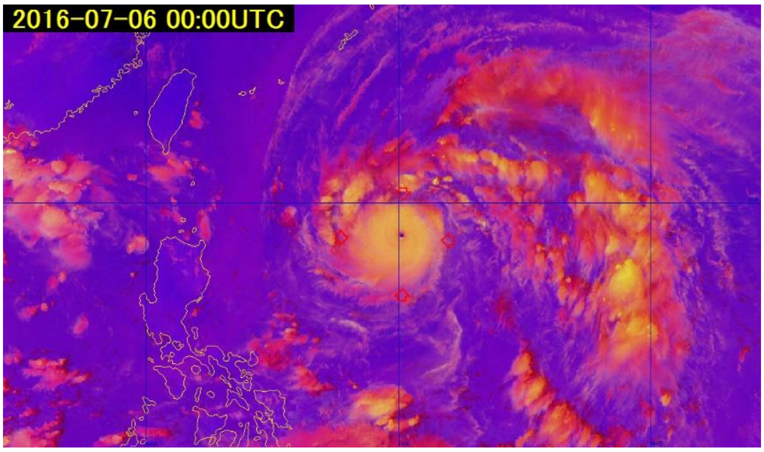

Fig. 3-13-3. Day convective storm RGB composite image for 00:00 UTC on 6 July 2016

3.14. Carrot-Shaped Clouds

These clouds are shaped like a carrot or the tip of a calligraphy brush, with gradual thinning toward the middle and upper layers windward. They consist of Cb cloud streets spreading from the windward to the leeward side and anvil Ci brought by upper winds. They are often associated with heavy rain, gusting winds, storm conditions and hail, particularly at the tip. Monitoring of their emergence and migration routes is essential.

MSC (1991) reported that convective masses containing individual Cb forms comprising carrot-shaped clouds tend to migrate downstream of middle and upper winds, occasionally stagnating, and sometimes occurring along convective cloud streets stretching windward. They usually have a life span of 10 hours and are associated with the following conditions:

1. Location predominantly over sea areas in connection with a ground-level low pressure center near fronts in warm areas
2. Prominence of warm moisture advection into the lower troposphere with dry air convection above
3. A relatively strong wind band, clear vertical shear and upper divergence in the upper troposphere

Figure 3-14-1 shows a carrot-shaped cloud southeast of Ishigaki Island in the region encircled in red, along with anvil Ci extending northeastward. In B03 visible image (Fig. 3-14-2), a Cb line stretches from the tip of the southern part toward the north-northeast. In the radar observation image shown in the upper-right panel of Fig. 3-14-1, echoes are observed with a precipitation intensity of 32 – 64 mm/h corresponding to the Cb street.

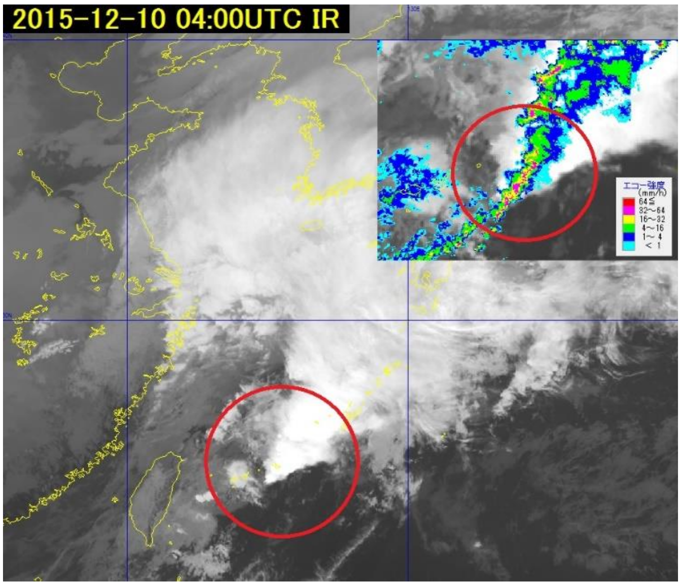

Fig. 3-14-1. B13 infrared image and radar precipitation intensity for 04:00 UTC on 10 December 2015

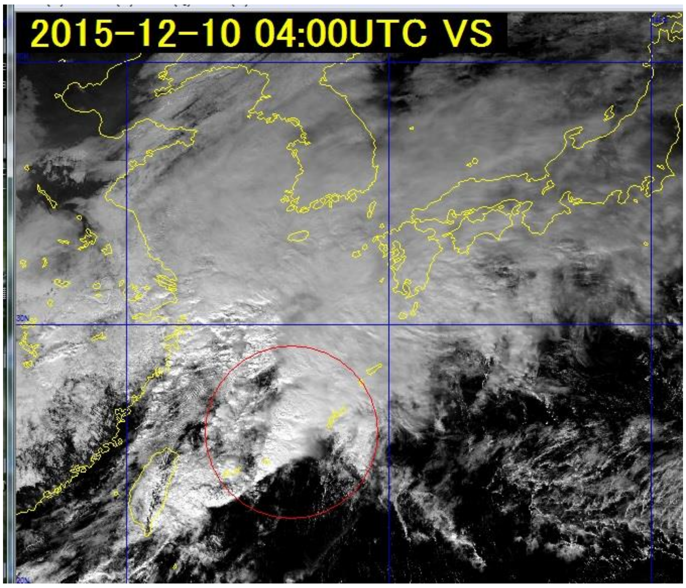

Fig. 3-13-2. B03 visible image for 04:00 UTC on 10 December 2015

Figure 3-14-3 shows an overlay of a B08 water vapor image and a wind diagram at 200 hPa altitude. It illustrates an accelerating zone (i.e. a divergent area) with faster wind speeds from the windward to the leeward areas of a carrot-shaped cloud. A strong wind band exceeding 100 kt is also seen to the north of the isotach. In the water vapor image, the carrot-shaped cloud emerges at the border of a relatively humid area and a dry area, indicating dry-air entry via the wind field.

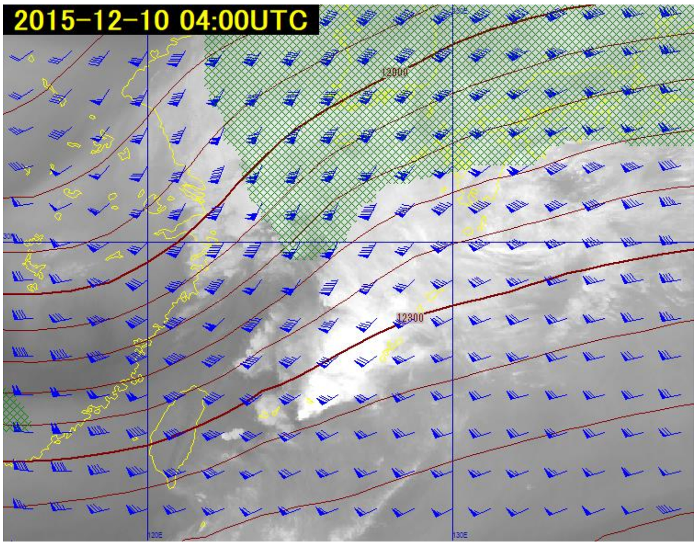

Fig. 3-14-3. B08 water vapor image for 04:00 UTC on 10 December 2015
200 hPa geopotential height (brown), winds, isotach (black)

Figure 3-14-4 shows wind and equivalent potential temperature at 850 hPa. In the area of the carrot-shaped cloud, a high equivalent potential temperature zone over 330 K enters from the south into the warm area near the cold front. As in the cross-sectional view of Fig. 3-14-4, shear with high wind speeds toward the upper atmosphere is seen, corresponding to conditions increasing the likelihood of occurrence as described previously.

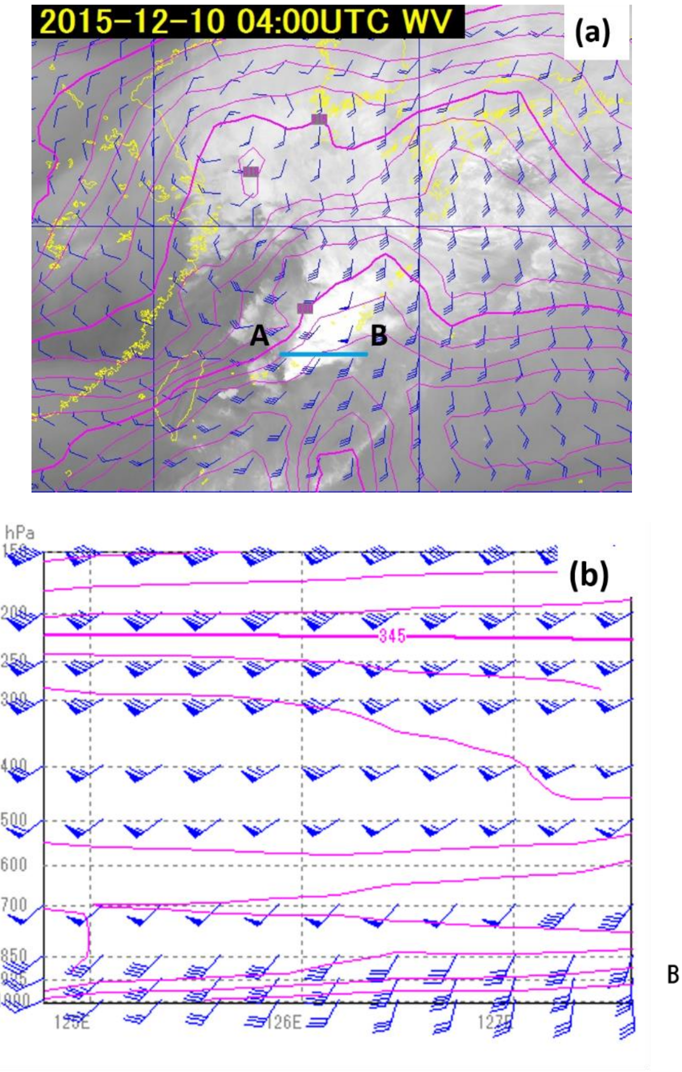

Fig. 3-14-4. B13 infrared image for 04:00 UTC on 10 December 2015 (a), with equivalent potential temperature at 850 hPa and winds (b). The lower panel shows a cross-sectional view along the blue line of the upper figure.

3.15.　Cloud Bands

Cloud bands are areas in belt form with upper, middle and lower layers, or middle and lower layers accompanied by a front line (i.e., a frontal cloud band) or belt-form areas of convective clouds.

Figures 3-15-1 and 3-15-2 show a frontal cloud band (**A-A**) comprising middle and lower layers with 200 – 300 km widths between Japan's Kanto district and the northern area of the Sakishima islands for latitudinal lengths of around 2,000 km. Another band (**B-B**) comprising mostly convective clouds is also observed between the Kanto district and the southern area of mainland Okinawa.

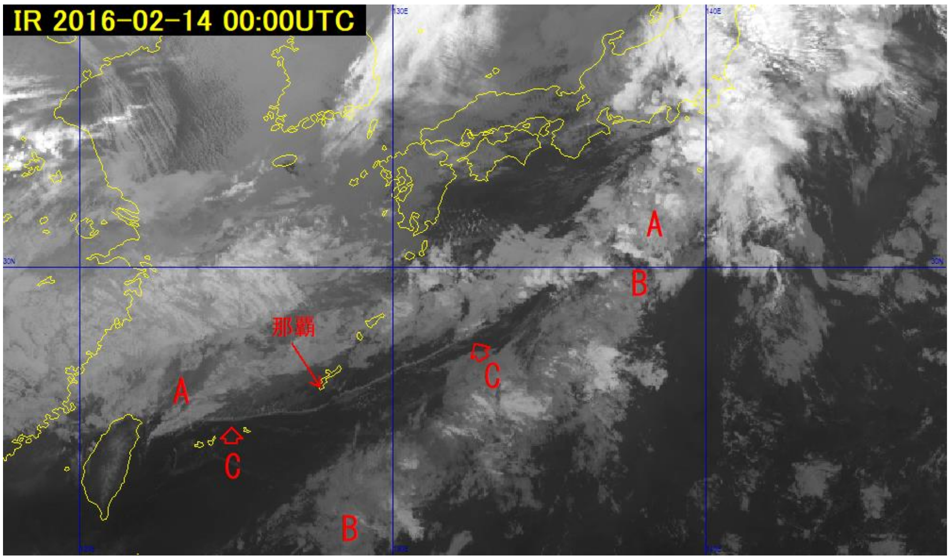

Fig. 3-15-1. B13 infrared image for 00:00 UTC on 14 February 2016

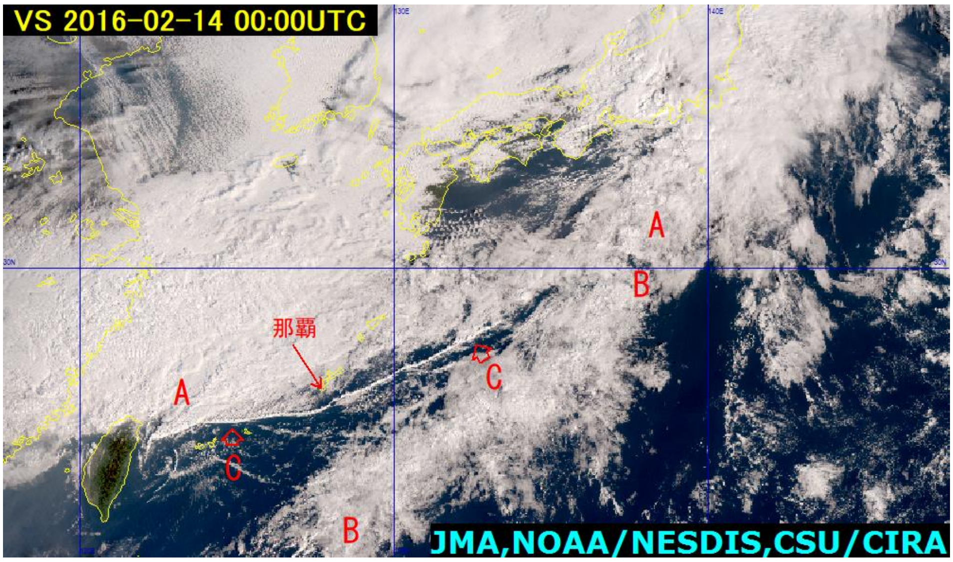

Fig. 3-15-2. True Color Reproduction image for 00:00 UTC on 14 February 2016

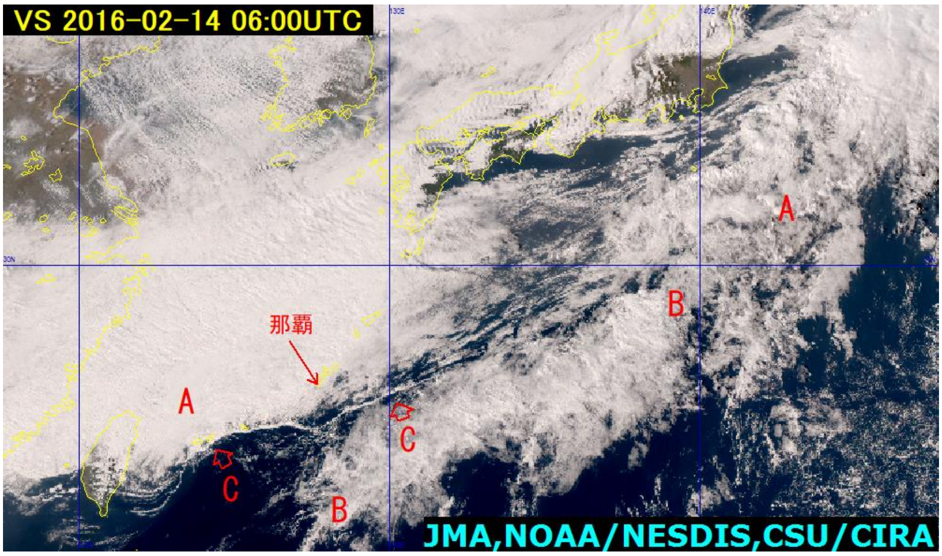

Fig. 3-15-3. True Color Reproduction image for 06:00 UTC on 14 February 2016

3.16. Cloud Lines

Cloud lines are strings of aligned convective clouds, with those containing Cb and Cg called Cb-Cg lines and those consisting solely of Cu called Cu lines.

In Figs. 3-15-1 and 3-15-2, the cloud line **A-A** stretches between the southern edge of Taiwan and the area offshore of Shikoku, while **C** and **D** stretch from west-southwest to east-northeast. **C** is a Cu line between the Sakishima Islands and the area offshore of Shikoku with convective clouds, and **D** around Taiwan contains Cg (i.e., a Cg-Cu line).

3.17. Rope Clouds

Rope clouds are long thin Cu formations with a usual width of around 10 – 30 km and in some cases lengths of 2,000 – 3,000 km. They are seen mainly over sea areas along the warm side of frontal cloud bands, often corresponding to cold fronts, as winds and temperatures vary beyond the cloud line. They often occur when frontal activity is weakened and the cloud line contains no developed convective clouds such as Cb or Cg.

The surface weather chart in Fig. 3-17-1 shows a cold front stretching over to the sea south of Okinawa from a cyclone with a center above the northern Sea of Japan, generating waves on the front seen around Awaji Island. This cold front corresponds to the cloud line **B**, presenting an example of an active convective cloud line corresponding to a cold front generating rope cloud that passed over mainland Okinawa at around 21:00 UTC on 13 February. In time-series AMeDAS for Naha (Fig. 3-17-2), rapid changes in wind direction and temperature decreases were observed with the passing of the rope cloud. The cloud line **C** was attenuated whilst descending south along with weakening of the cloud band **A-A** (Fig. 3-15-3).

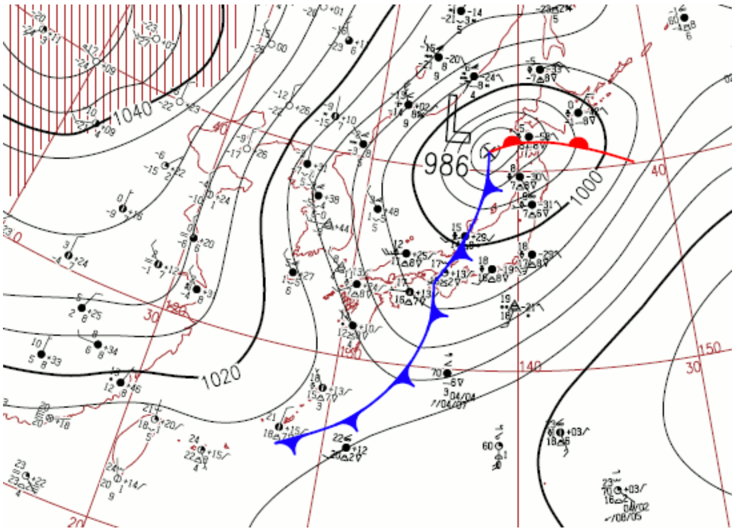

Fig. 3-17-1. Surface weather chart for 00:00 UTC on 14 February 2016

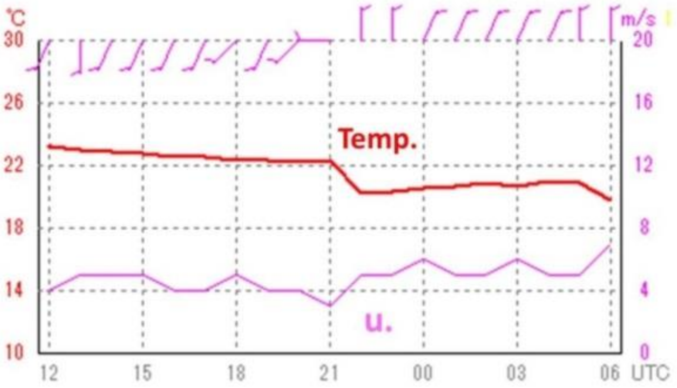

Fig. 3-17-2. Time-series AMeDAS data for Naha between 12:00 UTC on 13 February and

06:00 UTC on 14 February 2016, with temperatures in red and wind speeds in pink

3.18. Karman Vortices

As per the surface weather chart shown in Fig. 3-18-1, when winter pressure patterns collapse, anticyclonic conditions over continental areas move toward Japan. As northwestern winds weaken, vortices forming in relation to lower clouds leeward of the Jeju or Yakushima islands may subsequently align, rotating downstream anti-clockwise on the right and clockwise on the left (Fig. 3-18-2) in a phenomenon known as a Karman vortex.

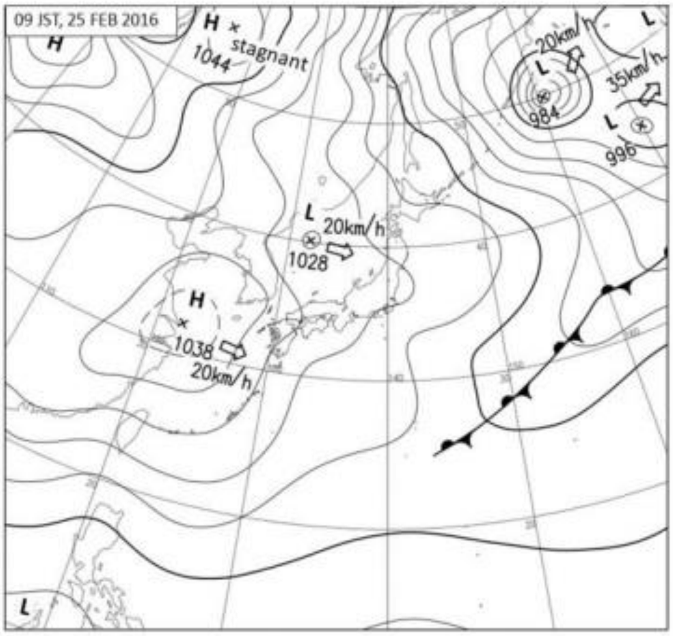

Fig. 3-18-1. Surface weather chart for 09:00 JST on 25 February 2016

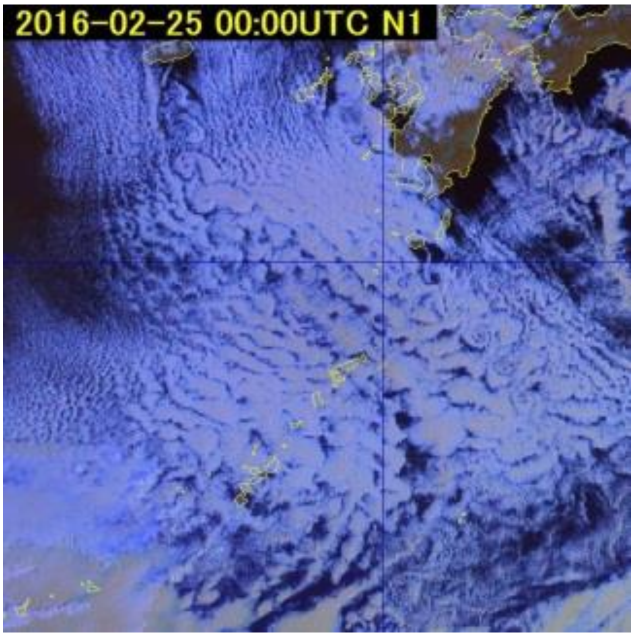

Fig. 3-18-2. Day Snow-Fog RGB composite image for 00:00 UTC on 25 February 2016

Karman vortices in satellite imagery are seen mainly as Sc leeward of island areas, aligning periodically. Satellite imagery analysis by Hubert and Krueger (1962) and Thompson, Grower and Bowker (1977) proposed three conditions for Karman vortex occurrence:

1. Open sea covered by St or Sc under a strong temperature inversion layer
2. Persistent strong wind with a steady direction in the lower layer
3. Island topography with a mountain top exceeding hundreds of meters over the temperature inversion layer

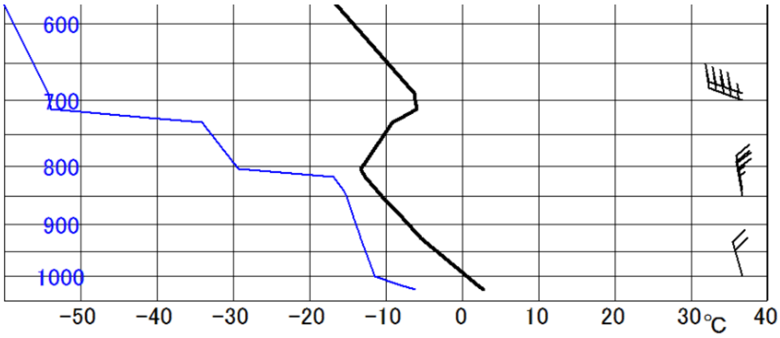

Fig. 3-18-3. Vertical profile of upper air over Jeju Island for 00:00 UTC on 25 February 2016

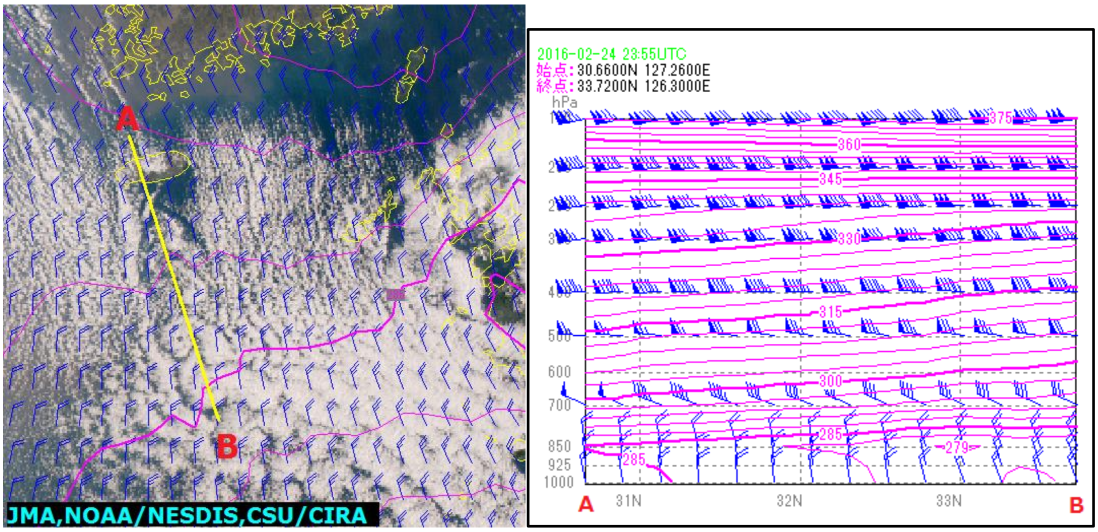

Fig. 3-18-4. True Color Reproduction image (left) and LFM (right) for 00:00 UTC on 25 February 2016; vertical section around Jeju Island for the same time period based on the initial value (a 925 hPa surface vertically sectioned at the yellow line); equivalent potential temperature (red lines) and wind (kt)

In the aerological vertical profile above Jeju Island (Fig. 3-18-3), a strong inversion layer is seen around 800 – 700 hPa with relatively high humidity around 800 hPa, providing a base for Sc cloud formation. Figure 3-18-4 shows a cross-section based on LFM in the vicinity of Karman vortices, indicating neutrality with no significant change in equivalent potential temperature under 800 hPa, and a dry stable layer above.

There is a significant uniform northern wind under 800 hPa without shears either in direction or wind speed. The environment satisfies the occurrence conditions as per Fig. 3-18-5.

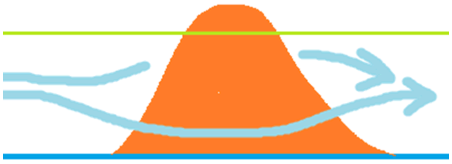

Fig. 3-18-5. Karman vortex emergence
The mountain top surpasses the inversion layer (green line),
with wind detouring around the mass.

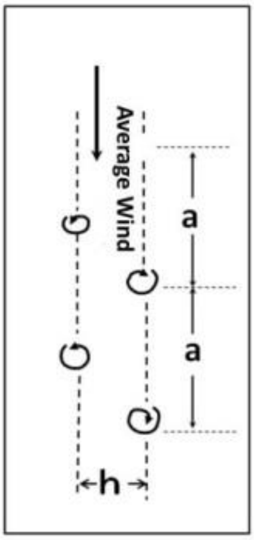

Fig. 3-18-6. Space **h** between vortex lines and space **a** between vortices in the line

Such conditions occur when air from the cold season gradually warms up, with Karman vortices running along lower-wind currents. They are frequently seen leeward of Jeju Island (1,950 m altitude), Yakushima Island (1,935 m) to the south, Rishiri Island (1,721 m), Urup Island (1,426 m) in the Kuril Islands, and Paramushir (1,816 m) to the north.

In satellite imagery (Fig. 3-18-2), a low cloud area with cold air is seen between the Yellow Sea and the East China Sea with prominent stratification around the Sakishima Islands. Two vortex lines (marked by arrows) appear, anticlockwise on the right and clockwise on the left, southward of Jeju Island. The ratio of the space **h** between the vortex lines and the space **a** between vortices in the line is expressed from a study by Chopra and Hubert (1965) as follows (Fig. 3-18-6):

$$0.28 < h/a < 0.52$$

Here, the vortices on the left and right are aligned with 3 – 4 turns each comprising Sc, with an **h/a** value of approximately 0.5.

The Reynolds number (Re) relating to Karman vortex generation is:

$$Re = U \cdot d/v$$

Here, U is natural fluid velocity, d is the obstacle diameter, v is the molecular kinematic viscosity coefficient, and $v = \mu/\rho$ is the static viscosity coefficient of fluid divided by fluid density. Instead of applying the molecular kinematic viscosity coefficient, an eddy viscosity value of 107 cm^2/s is used, with the diameter of Jeju Island as 30 × 1,000 m (the average diameter of the island's Hallasan volcano), wind speed as 10 m/s from aerological data, and Re as 300. Hence, Karman vortices on the leeward side of the mountain are in the range of $50 < Re < 300$ (from Science of Fluids, T. Kimura, 1979).

3.19. Belt-Form Convective Clouds

Numerous cloud streaks often appear along prominent winter winds over the Sea of Japan. These are typically seen in development from cloud streets reaching the Sanin district of Hokuriku in Japan from the edge of the Korean Peninsula. These are called belt-form convective clouds, and are closely related to heavy snowfall near the Sea of Japan. In the satellite imagery of Fig. 3-19-1, which corresponds to wind distribution around 925 hPa, a convergence zone of horizontal wind with strong horizontal shear is seen along the southwestern lining of the cloud band in the region enclosed with a broken line. This is known as the Japan Sea Polar air-mass Convergence Zone (JPCZ), considered to form under the influence of the range around South Korea's Mt. Paektu and the geographical distribution of land and sea (from Meteorology of Heavy Rain and Snow, Yoshizaki and Kato, 2007). Belt-form convective cloud is seen in response to the JPCZ.

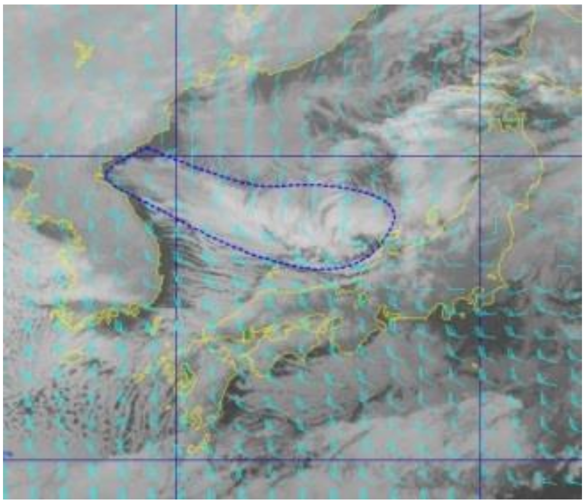

Fig. 3-19-1. B13 infrared image and MSM 925 hPa wind for 18:00 UTC on 23 January 2016

When belt-form convective cloud emerges, a synoptic scale trough tends to occur at the upper layer above Japan. A lower vortex (corresponding to a mesoscale cyclone, which in some cases develops into a synoptic-scale cyclone) may form within such cloud, causing heavy snowfall.

The process of belt-form convective cloud development and dissipation between 20 and 24 January 2016 is described below. Southern oscillation covering the entire formation was accompanied by a passing meso-α-scale trough (500 hPa), with a low vortex forming above the cloud in correspondence to a temperature trough (cold core: 700 hPa) behind the trough (MSC, 1992).

(1) Early Stage of Emergence

On a 500 hPa weather chart for 00:00 UTC on 20 January, the center of a cold low is seen over the sea east of Hokkaido, bringing a deep trough to the area around Japan and strong air influx below –30°C to the Sea of Japan (recorded as –36.7°C in Wajima). A strong wind axis also passed from the area north of the Korean Peninsula and approached the Kii Peninsula (Fig. 3-19-2).

In satellite imagery, cloud streets are seen widely along with the cold air over the Sea of Japan, the Pacific and the East China Sea. No belt-form convective cloud is observed over the Sea of Japan, but cloud streets with a high top including Cg are seen moving toward Japan's Chugoku region. Also, at 925 hPa MSM, north-northwest flow fields are prominent around Japan, whilst a shear line (shown by the broken line in Fig. 3-19-3) formed over the east of the Korean Peninsula, corresponding to a high peak of equal potential temperature.

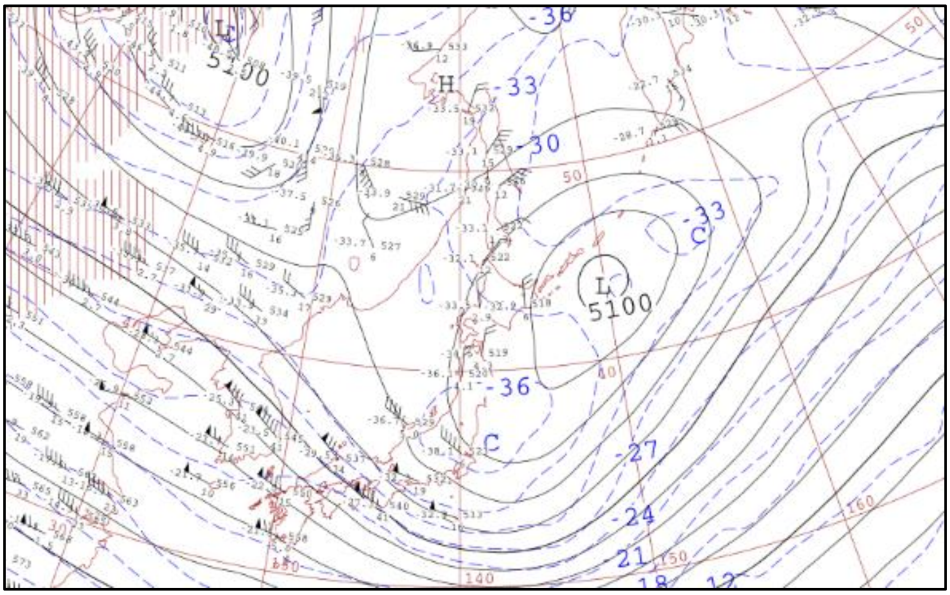

Fig. 3-19-2. 500 hPa weather chart for 00:00 UTC on 20 January 2016

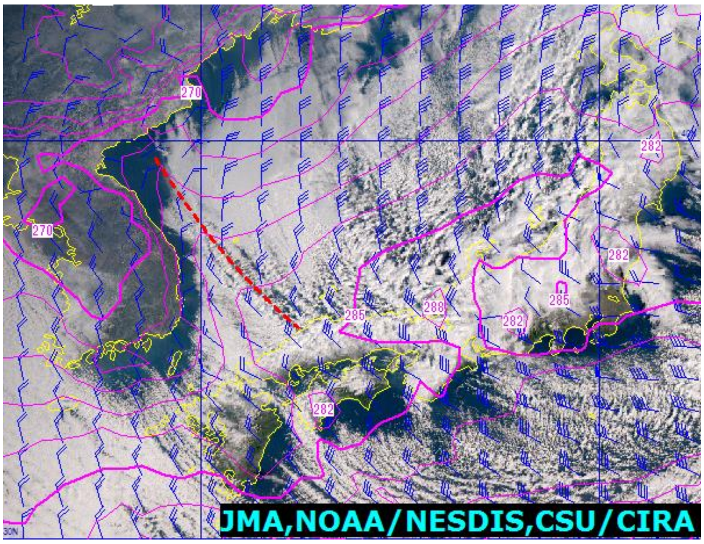

Fig. 3-19-3. True Color Reproduction image for 00:00 UTC on 20 January 2016 with equivalent potential temperatures and winds, MSM 925 hPa

(2) Development to Maturity

In satellite image for 21 January, a belt-form cloud band area is seen around lower shear over the Sea of Japan, with convective cloud containing Cg starting to develop to its west (Fig. 3-19-4).

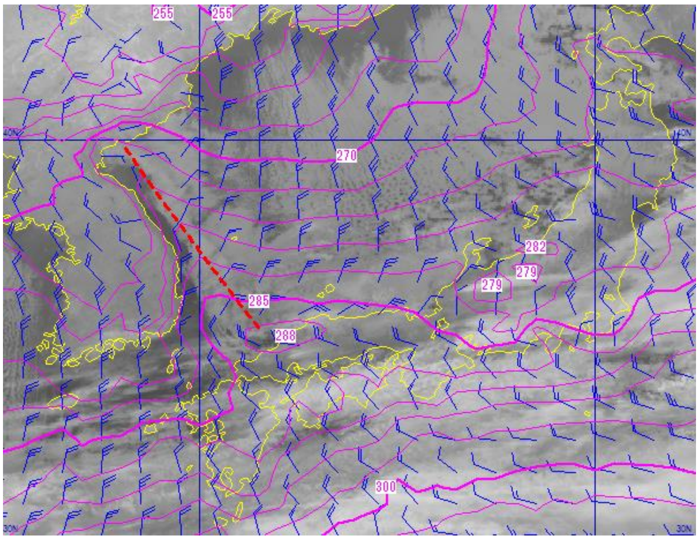

Fig. 3-19-4. B13 infrared image for 18:00 UTC on 21 January 2016 and equivalent potential temperature and wind, MSM 925 hPa

On the 500 hPa weather chart for 00:00 UTC on 23 January, a low with intense cold air under –45°C descended southward to around 41°N from Manchuria, bringing extremely cold air to the upper atmosphere toward western Japan. Short wave troughs around this cold low are observed over the western Sea of Japan and around the Yellow Sea (Fig. 3-19-5).

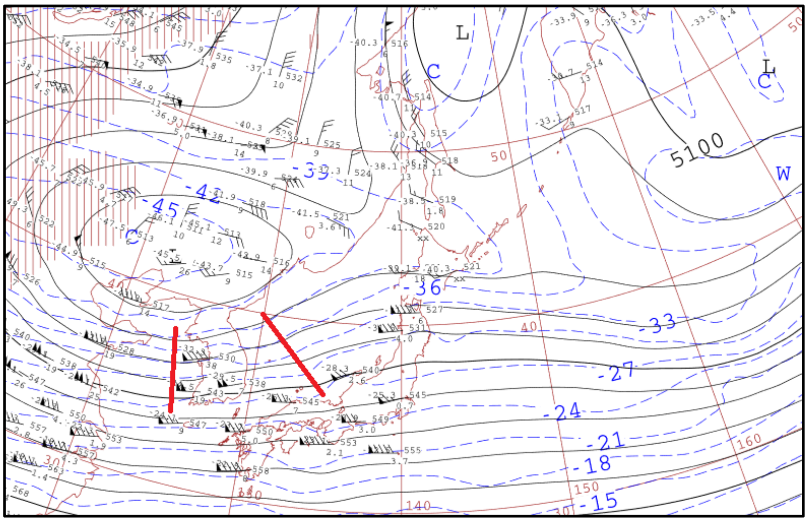

Fig. 3-19-5. 500 hPa weather chart for 00:00 UTC on 23 January 2016

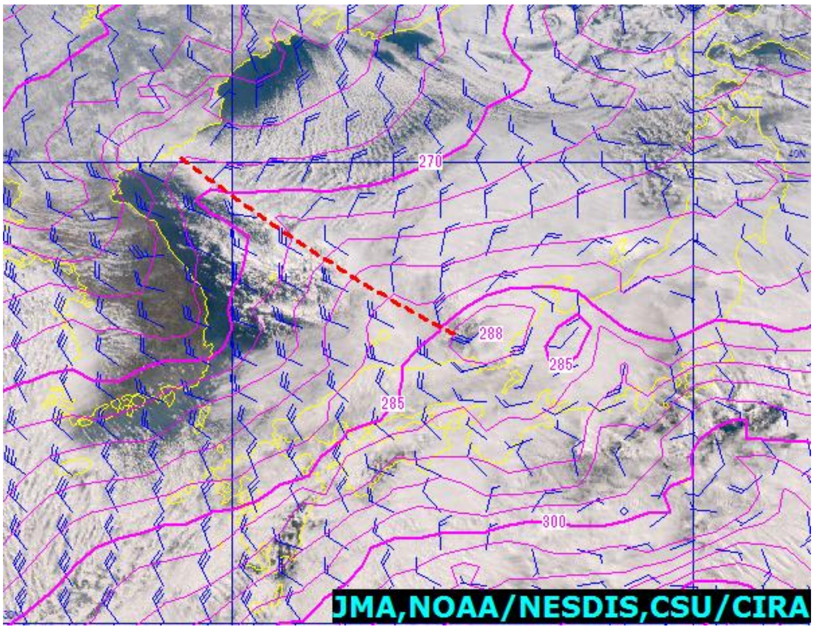

Fig. 3-19-6. True- Color Reproduction image with equivalent potential temperatures and wind, MSM 925 hPa for 06:00 UTC on 23 January 2016

The eastern edge of the belt-form convective clouds ascended northward alongside the current of a 500 hPa baroclinic zone toward the Hokuriku region. In the region indicated with a broken line in Fig. 3-19-6, north-northeast wind and northwest wind converge, with the highest cloud top at the south of the belt-form convective cloud, containing Cb and Cg, mixed with T-mode convective cloud. At the southern edge, a cloud vortex on a β-scale emerged, with a small cyclone observed around Wakasa Bay on the surface weather chart (Fig. 3-19-7). These belt-form convective clouds around minor cyclonic conditions are observed migrating toward Japan's Hokuriku district.

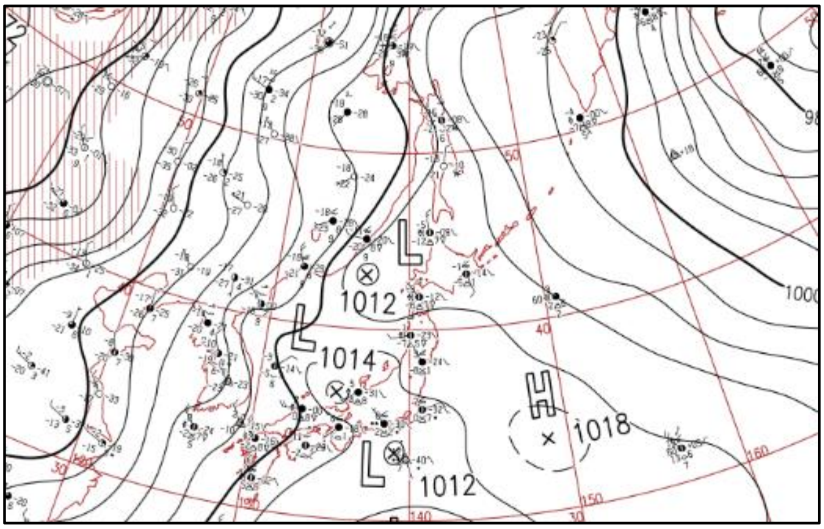

Fig. 3-19-7. Surface weather chart for 06:00 UTC on 23 January 2016

(3) Dissipation Stage

On the 500 hPa weather chart for 00:00 UTC on 24 January, a low above northeastern

China is seen descending southward to the Sea of Japan with air at –42°C at its center. The trough is latitudinal over western Japan with a strong wind axis descending south toward the Pacific coast, bringing a flow field between western and west-southwestern Japan (Fig. 3-19-8).

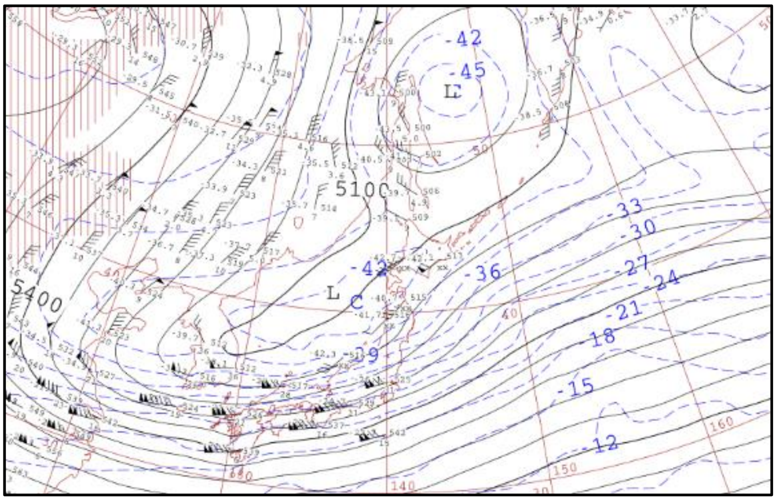

Fig. 3-19-8. 500 hPa weather chart for 00:00 UTC on 24 January 2016

In the corresponding satellite imagery (Fig. 3-19-9), belt-form convective cloud is seen descending southward along lower-layer shear at 925 hPa with a latitudinal strike. A lower eddy made landfall on the Hokuriku district and then disappeared. At 12:00 UTC on the same day, the belt-form convective cloud descended further south to the Sea of Japan coast with Cg and Cb (Fig. 3-19-10). In the Cb region, snowfall of over 10 cm was observed within the space of an hour. After making landfall, the formation dissipated with gradually descending cloud top heights and did not cross Japan's backbone mountain range. Cloud streets were prominent at the north of the formation, resulting in a strong winter-type pressure pattern.

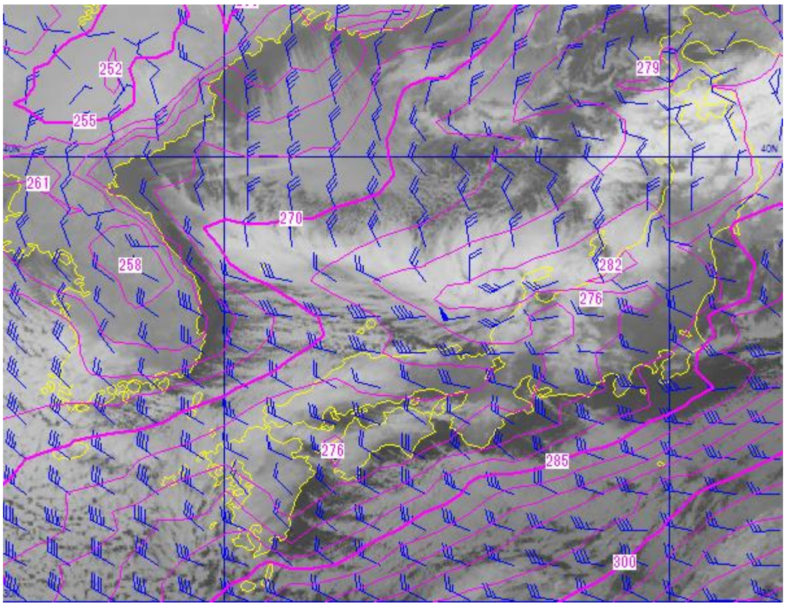

Fig. 3-19-9. B13 infrared image for 00:00 UTC on 24 January 2016 and equivalent potential temperatures and winds, MSM 925 hPa

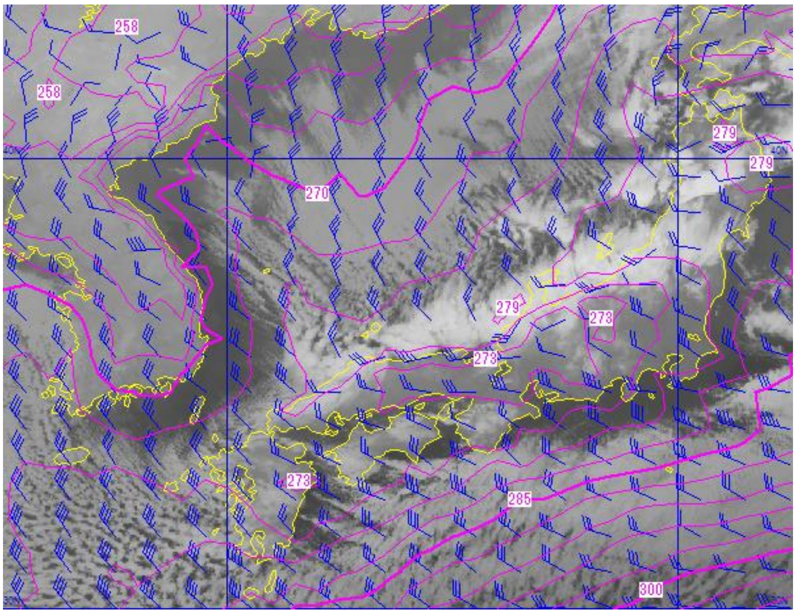

Fig. 3-19-10. B13 infrared image for 12:00 UTC on 24 January 2016 and equivalent potential temperatures and winds, MSM 925 hPa

Below is a summary of the changes and movements of the belt-form convective cloud provided in this example.

- Belt-form convective cloud emerged at the lower shear part over the western Sea of Japan with gradually rising top height, forming a band extending southeastward.
- The cloud position showed a parallel tendence to a large scale stream, changing direction along with localized streams depending on progressive short-wave phases with temporal

and spatial developments.

- The cloud form was at its least stable under short wave trough conditions with maximum air mass change and then developed significantly, in some cases displaying meso-β-scale lower-eddy conditions above nearby trough areas.
- The cloud exhibited latitudinal strike conditions along the movement of cold low and trough areas, and dissipated after making landfall between the Sanin and Hokuriku districts. In both areas, snowfall intensified after landfall.

In other cases of dissipation, belt-form convective cloud is weakened and disappears with decreased air-mass modification over sea areas when tropospheric conditions are stable due to the passage of troughs that raise density over the Sea of Japan.

3.20. Ship Trails

Over sea areas with lower clouds, stratocumulus cloud streets with widths of 10 – 30 km and lengths of up to 1,000 km may form. These are called ship trails for their close association with shipping operations, and are a man-made phenomenon. Ship trails often form around July with a high frequency of sea fog, resulting in multiple cloud streaks lasting for several days (Takasaki, 1984). The main cause of ship trails is flue gas generated by ships operating along particular passages, forming small cloud particle nuclei that generate denser cloud than natural stratocumulus over the sea. They exhibit higher brightness than surrounding clouds in visible and near-infrared image, but are harder to identify in infrared image (Band 13) because of their lower cloud top. Ship trails can also be identified in particular time zones with sunlight via Band 7 data or differences between Band 7 and Band 13 image.

The visible imagery (Band 3) in Fig. 30-20-1 shows ship trails. Several cloud streaks with lengths of around 100 km are seen eastward from around 200 km over the sea to the east of the Kamchatka Peninsula. In the center of the figure around Attu Island (circled), ship trail deformation is seen due to the geographical effects of the terrain. In Natural Color RGB composite image, ship trails can be identified through upper-layer clouds in semi-transparent cyan in the areas around the red ovals in Fig. 3-20-2.

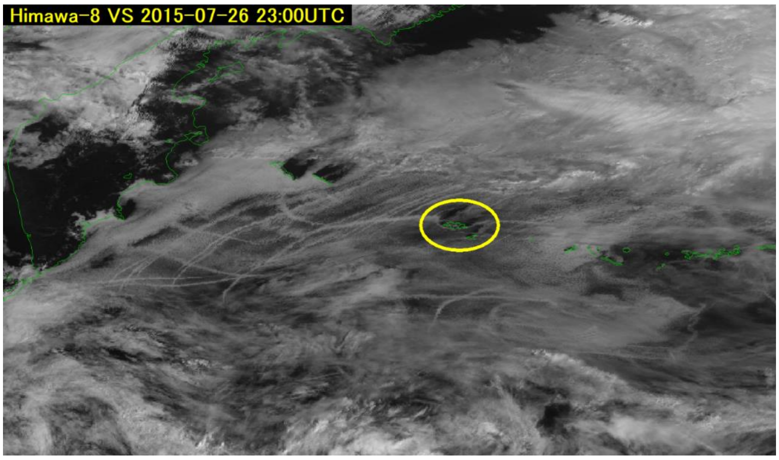

Fig. 3-20-1. B03 visible image of ship trails for 23:00 UTC on 26 July 2015

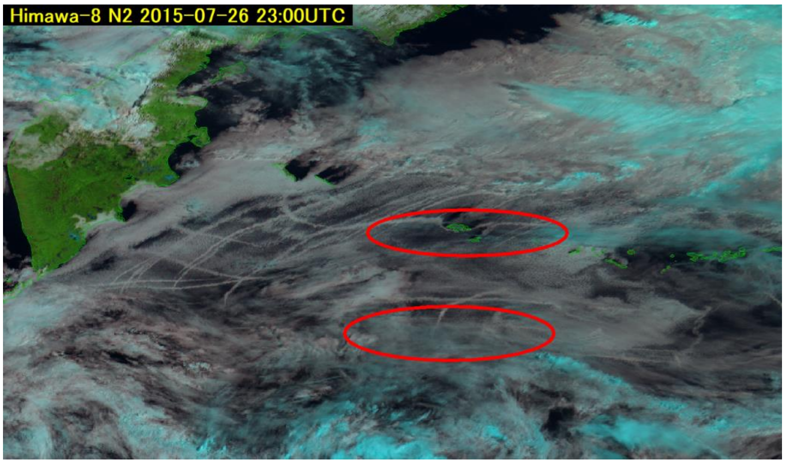

Fig. 3-20-2. Natural- Color RGB composite image of ship trails for 23:00 UTC on 26 July 2015

Reference:

- Maddox, R. A., 1980: Mesoscale Convective Complexes, Bull. Amer. Met. Soc., 61, 1374 - 1387.
- Iwasaki, H and Takeda T.,1993: Characteristic features on meso-scale cloud clusters around Japan in the Baiu-season from 1985 to 1988, Tenki, 40, 3, 161 – 170 (in Japanese)
- Shimizu K. and Tsuboki K., 2004: Observational study on the process of transverse-type snowfall band formation; Hydrospheric Atmospheric Research Center (HyARC), Nagoya University; Snow and Ice Research Center, National Research Institute for Earth Science and Disaster Resilience (in Japanese)
- Yagi S., 1985: Large scale snow clouds with roll axes roughly perpendicular to the direction of winter monsoon burst: observational studies of convective cloud roll axes and some theoretical consideration, Tenki, 32,4, 175-187 (in Japanese).
- Takasaki H., 1984: Peculiar cloud streets in the north pacific region, Tenki, 31, 5, 315-318 (in Japanese)

4. Water Vapor Patterns

4.1. Introduction

In water vapor imagery, airflow in upper and middle tropospheric layers can be visualized using water vapor as a tracer, even in the absence of clouds. The positions of troughs, ridges, vortices and jet streams in these layers can be estimated from bright and dark patterns in such imagery, as well as trough deepening from temporal changes in bright and dark patterns. However, the imagery provides little information about the lower troposphere due to strong absorption by water vapor.

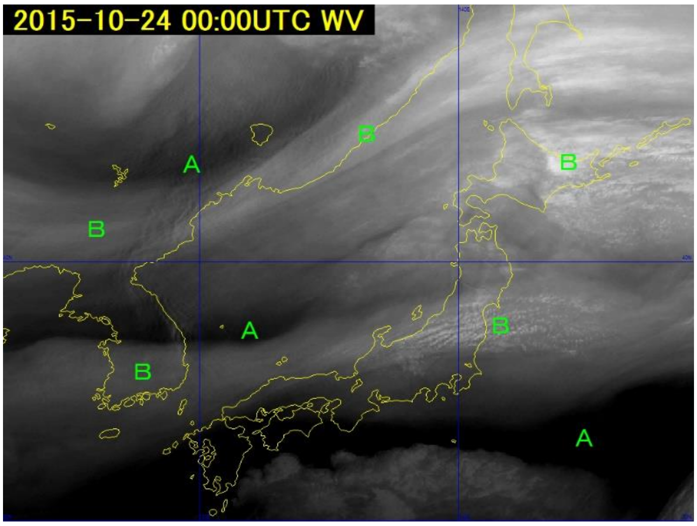

Fig. 4-1-1 Water vapor image for 00:00 UTC on 24 October 2015

4.1.1. Dark Regions

Relatively dark areas in water vapor imagery are called dark regions, which have high brightness temperature indicating dry upper and middle troposphere layers. Each water vapor band has a different sensitive altitude. Areas with **A** in Fig. 4-1-1 are dark regions.

4.1.2. Bright Regions

Relatively bright areas in water vapor imagery are called bright regions, which have low brightness temperature indicating humid upper and middle troposphere layers or cloud areas with tops in the upper and middle troposphere. Areas with **B** in Fig. 4-1-1 are bright regions. Dark and bright regions are determined qualitatively rather than quantitatively.

4.1.3. Darkening

Darkening is a phenomenon in which the darkness of areas increases over time. Darkening regions correspond to active subsidence fields, indicating trough deepening and anticyclone strengthening. Comparison of areas with **C** in Figs. 4-1-2 and 4-1-3 shows darkening.

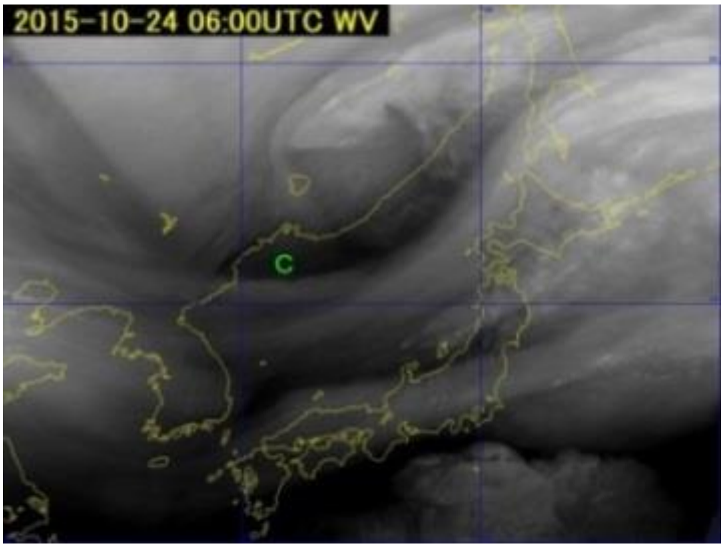

Fig. 4-1-2 Water vapor image for 06:00 UTC on 24 October 2015

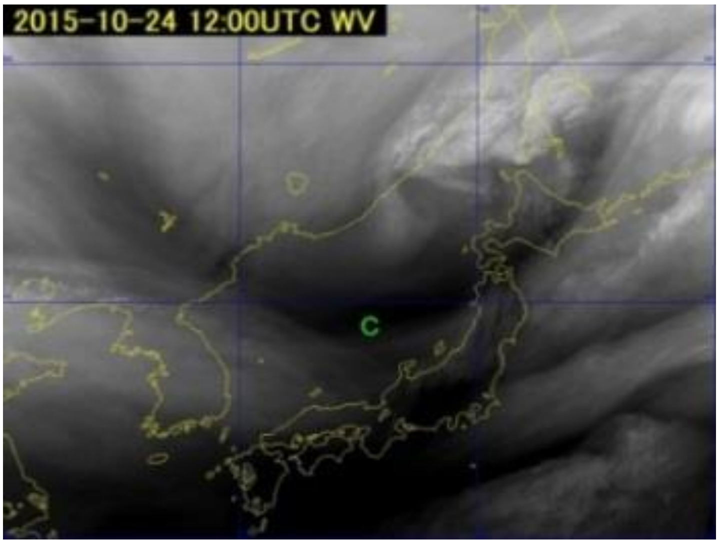

Fig. 4-1-3 Water vapor image for 12:00 UTC on 24 October 2015

4.1.4. Dry Intrusion

The descent of extremely dry air into lower layers near a cyclone is called dry intrusion. In water vapor imagery, descending dry air masses appear as clear dark or darkening regions, highlighting the development of dry intrusion. Browning (1999) emphasizes that such intrusion affects the structure of extratropical cyclone fronts, clouds and precipitation because the dry air mass descends from near the tropopause with low potential temperature, and is associated with convective instability and the occurrence of convection. The descending mass is separated at the rear of a cold front into flow toward the cyclone center and anticyclonic flow. This may produce a dark region with a hammerhead pattern in water vapor imagery (Fig. 4-1-4).

Figure 4-1-5 shows a dry intrusion, with a belt-form dark region heading from the northwest to a cyclone near Mongolia. The intrusion separates at the rear of the cyclone, with one part heading toward the cyclone center and the other west-southwestward around 40°N, with a hammerhead pattern.

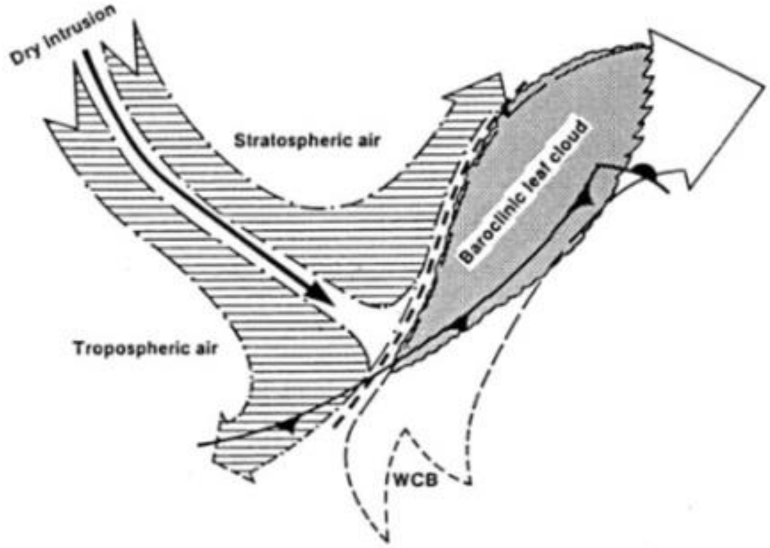

Fig. 4-1-4 Dry intrusion with a hammerhead pattern (Young *et al.,* 1987)

4.1.5. Dry Slots

Dry air masses flowing from a cold air mass side toward a developing cyclone center are called dry slots. In water vapor imagery, these appear as dark regions resembling narrow grooves around the cyclone center. In visible and infrared imagery, they appear as cloudless or lower-cloud areas. Dry slots are formed by dry intrusions.

In the dry slot shown in Figs. 4-1-5 and 4-1-6, there is a thin dark region around the cyclone center (arrow) at the cyclone center near Mongolia, forming a partial hammerhead pattern. In visible imagery, this is a mostly clear-sky area.

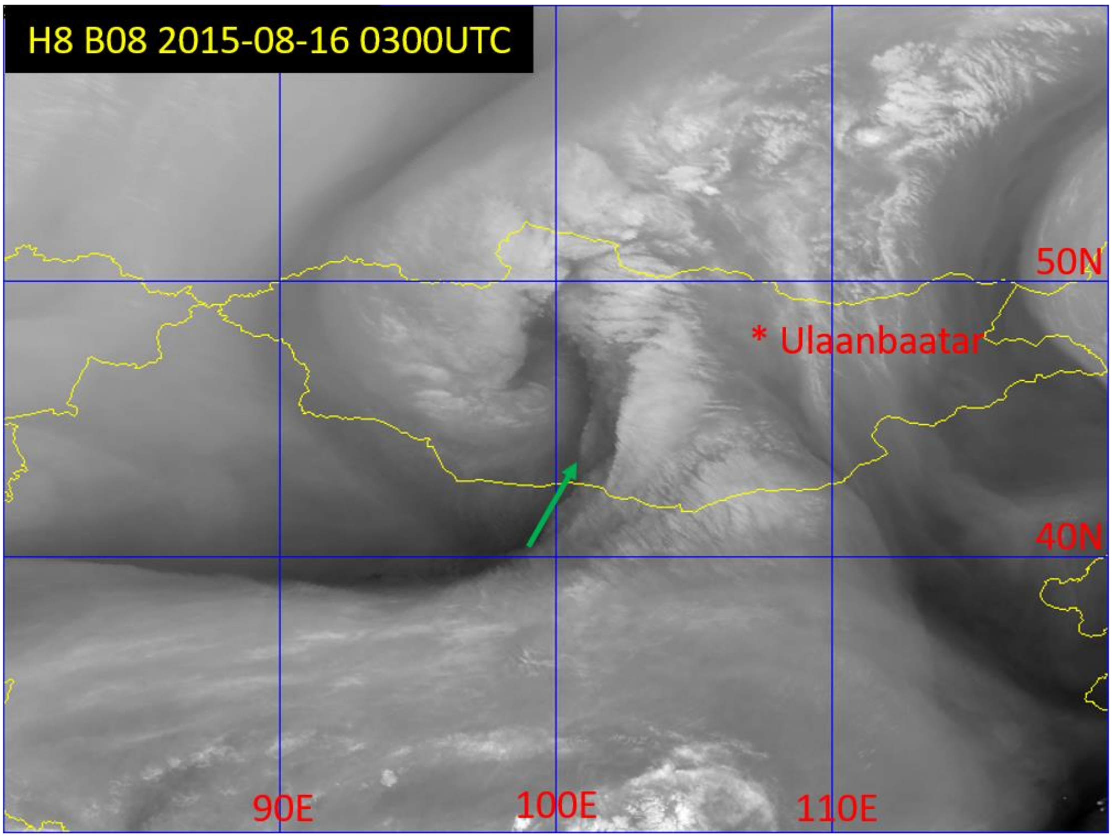

Fig. 4-1-5 Water vapor image of a dry intrusion for 03:00 UTC on 16 August 2015. Green arrow: dry slot.

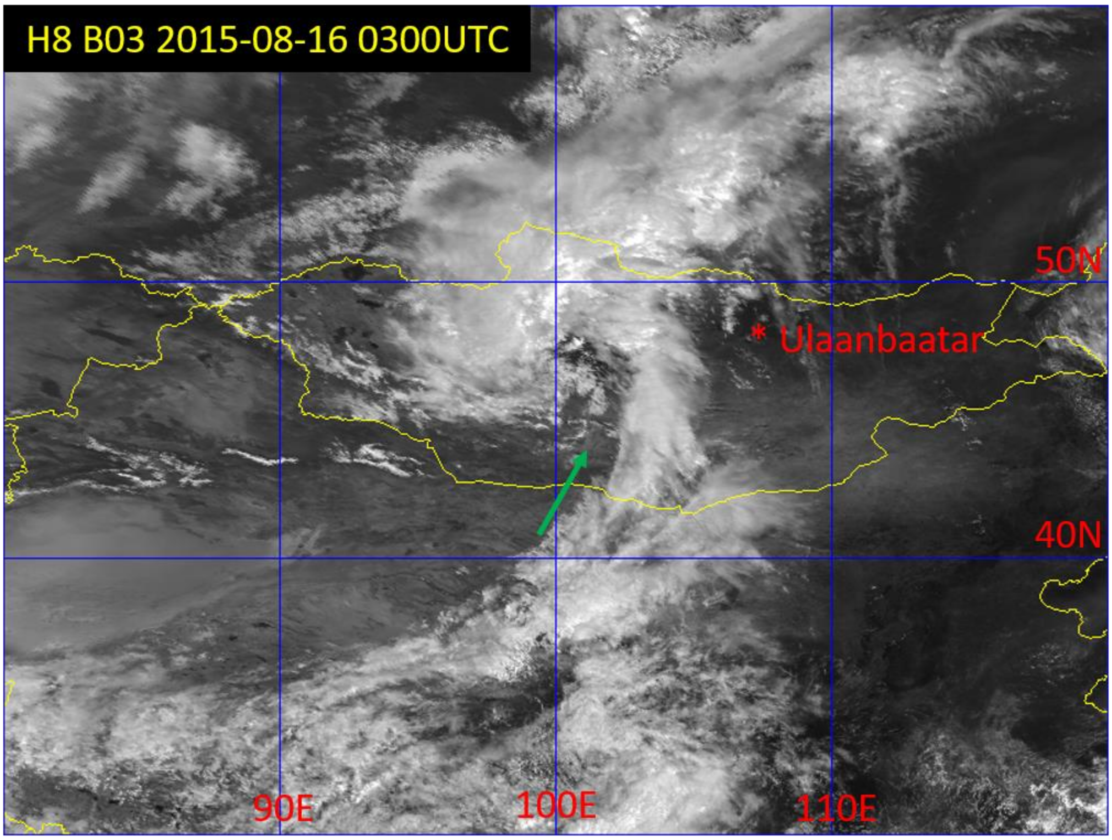

Fig. 4-1-6 Visible image of a dry intrusion for 03:00 UTC on 16 August 2015. Green arrow: dry slot.

4.1.6. Upper Troughs

Using water vapor imagery, upper troughs can be seen at the maximum cyclonic curvature of a boundary between bright and dark regions (i.e., a dark region with a convex shape to the south; Fig. 4-1-7). Troughs in the upper and middle layers can be determined from the boundary shape, and trough deepening can be estimated from the degree of darkening. From Fig. 4-1-8, a trough over Northeast China can be seen from the boundary curvature and from GSM 500 hPa contour lines.

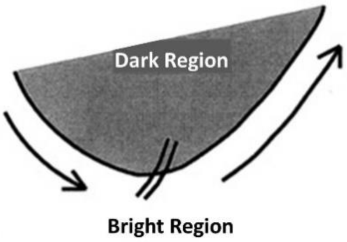

Fig. 4-1-7 Upper trough

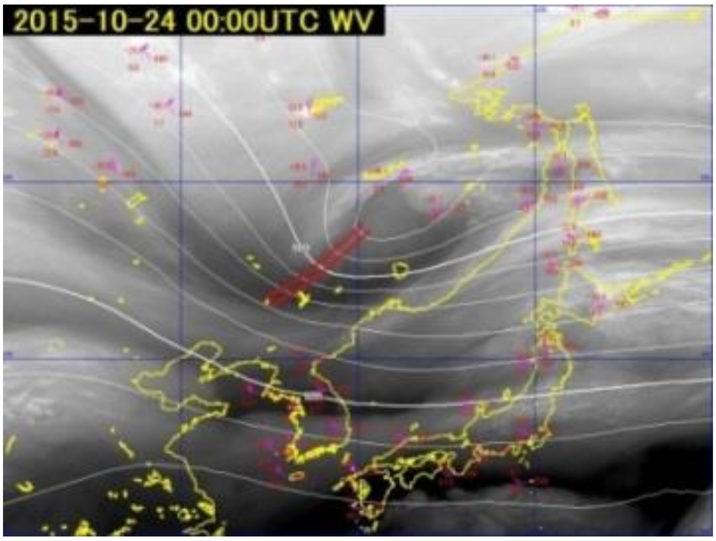

Fig. 4-1-8 Water vapor image for 00:00 UTC on 24 October 2015.
White lines: contours every 60 m (geopotential height) at 500 hPa from GSM data; red double line: upper trough.

4.1.7. Upper Vortices

Vortices can be identified from temporal changes in water vapor imagery showing spirals of bright and dark regions and their rotation. Those identifiable in such imagery are called upper vortices, which are useful for detecting cyclones and troughs in upper and middle troposphere layers. Figure 4-1-9 shows an upper vortex (arrow) identifiable from the spiral of bright and dark regions.

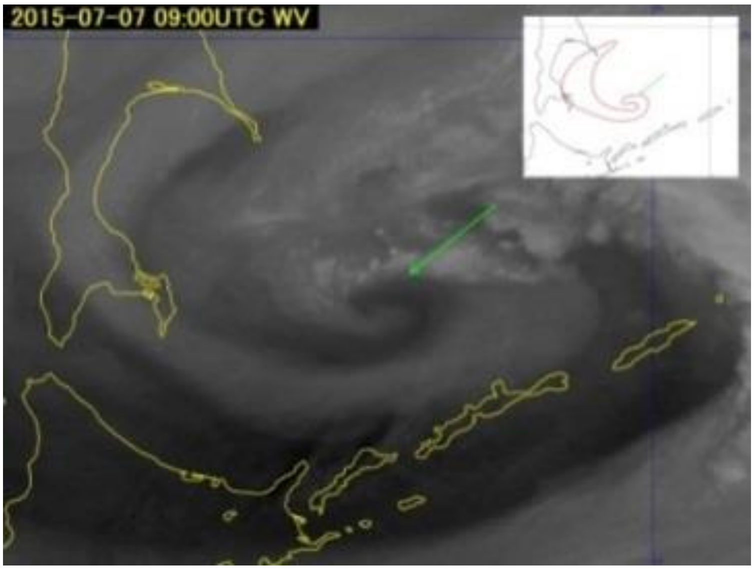

Fig. 4-1-9 Water vapor image for 09:00 UTC on 7 July 2015, showing an upper vortex (green arrow).

Reference

- Young *et al.,* 1987: Interpretation of Satellite Imagery of A Rapidly Deepening Cyclone, Quarterly Journal of the Royal Meteorological Society 113 (478), 1089-1115,

4.2. Boundaries

Borders between bright and dark regions in water vapor imagery are called boundaries. These represent divisions between air masses with different moisture levels in the upper and middle layers, therefore appearing clearly when the spatial gradient of moisture is significant. Boundaries are formed by vertical flow and horizontal deformation of the atmosphere, each exhibiting a characteristic pattern.

Weldon and Holmes (1991) classify boundaries into seven types (Table 4-2-1) and describe their characteristics (including those related to jet streams, those exhibiting blocking, and those exhibiting surges) based on causes and structures. The type of boundary can change both temporally and spatially, such as when transitioning from a base surge boundary to an inside boundary and when the upstream part of the boundary is a dry surge type but the downstream part is a baroclinic leaf type. This section outlines the boundary types classified by Weldon and Holmes (1991).

Table 4-2-1 Classification of boundaries (Weldon and Holmes, 1991)

Boundary related to jet stream	Parallel jet stream boundary
	Baroclinic leaf boundary
Boundary exhibiting a blocking	Head boundary
	Inside boundary
Boundary exhibiting a surge	Dry surge boundary
	Base surge boundary
Others	Return moisture boundary

4.2.1. Boundaries Related to Jet Streams

One of the most effective uses of water vapor imagery involves observation of changes in jet streams. Air masses to the poles of the jet stream are generally cold and dry, while those to the equator are warm and humid. A boundary appears when the cloud area corresponding to the front brightens.

Figure 4-2-1 illustrates subtropical and polar frontal zones (Ramond *et al.,* 1981). Subsidence strengthens on the pole side above the frontal zone near the jet, and a dry region hangs down from the tropopause. The dark region to the north of the jet corresponds to this region and forms a boundary with clear contrast. Subtropical frontal zones are generally wide and steep, tending to form wider and clearer boundaries than polar frontal zones.

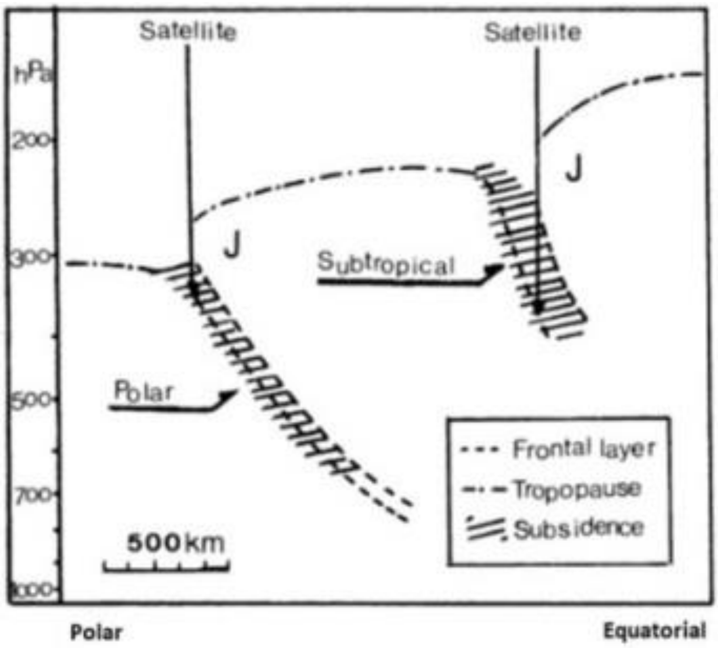

Fig. 4-2-1 Schematic drawing of subtropical and polar frontal zones (Ramond *et al.,* 1981)

4.2.1.1. Parallel Jet Stream Boundaries

Parallel jet stream boundaries form at the border between cloud areas (bright) accompanying jet streams and dark regions on the polar side (Fig. 4-2-2). These often exhibit sharp contrast and quasi-linear shapes. Dark regions often appear as bands on the polar side of the jet stream. The positions of the jet axis and the boundary often coincide, but in the westerly wind zone, the western edge of the jet axis is often in the deformation field. Accordingly, the shape and contrast of the boundary may be less clear than those of the eastern edge, or may not coincide with the jet axis.

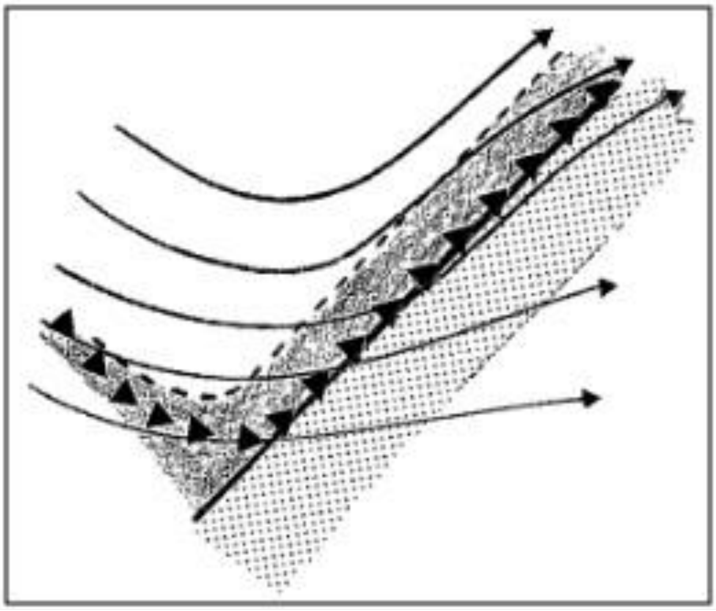

Fig. 4-2-2 Schematic illustration of a parallel jet stream boundary. Shading: dark region;

white: bright region; dotted area: cloud; thick line: boundary; thin arrows: streamlines; black triangles: axis of maximum wind speed.

Figure 4-2-3 shows a parallel jet stream boundary. There is clear boundary from the coast of San’in to the coast of Akita, which coincides with the jet stream core at around 80 kt. The boundary extends from the San’in region through northern Kyushu to East China, but since northern Kyushu is located at the inlet to the jet core, correspondence between the boundary and the jet axis is unclear.

In Fig. 4-2-3, the area that can be identified as a parallel jet stream boundary in front of a clear trough is less than 1,000 km. Conversely, in Fig. 4-2-4, a clear parallel jet stream boundary extends at least 4,000 km from the area near the Yellow Sea to around 180° longitude.

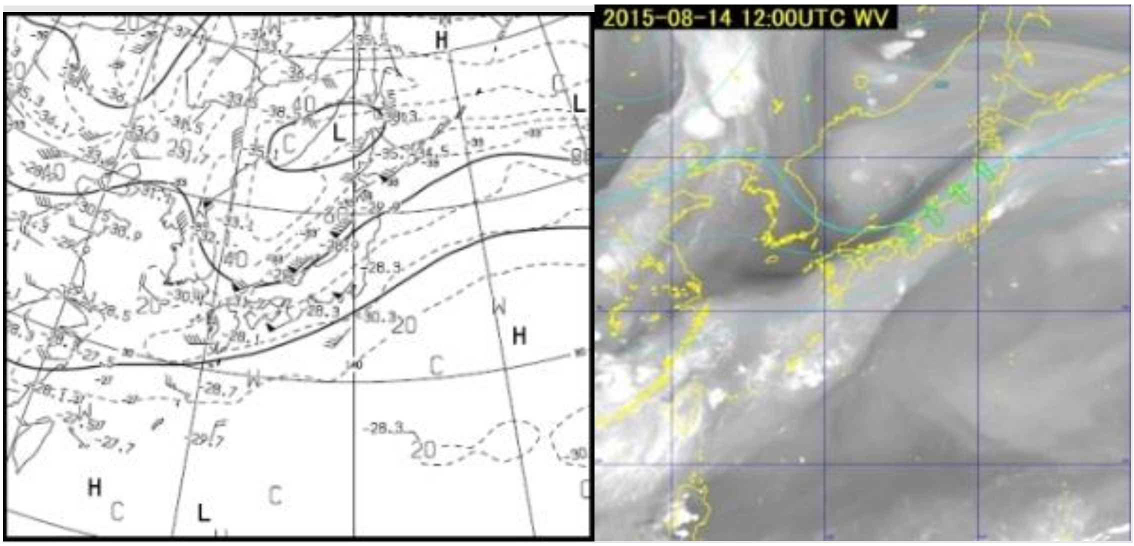

Fig. 4-2-3 Parallel jet stream boundary for 12:00 UTC on 14 August 2015. Left: 300 hPa weather chart; right: water vapor image; green arrows: boundary.

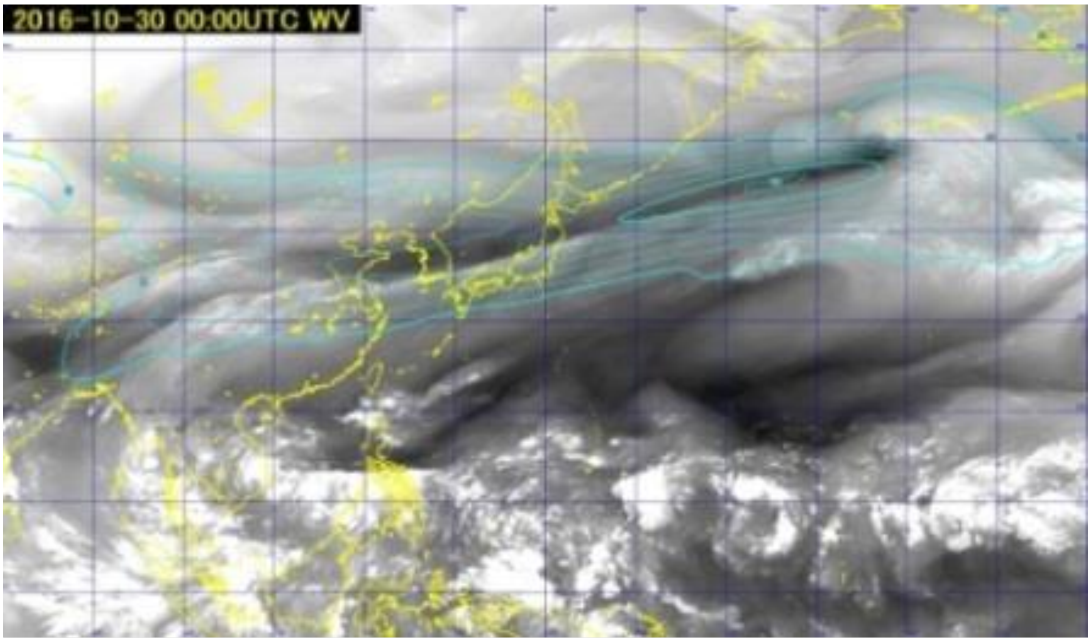

Fig. 4-2-4 Water vapor image for 00:00 UTC on 30 October 2016, showing a parallel jet stream boundary. Cyan lines: isotachs (60 kt or more, every 20 kt) at 300 hPa from GSM.

4.2.1.2. Baroclinic Leaf Boundaries

Baroclinic leaf boundaries are also related to jet streams, and are accompanied by leaf-shaped cloud areas (cloud leaves) that appear at the early stage of cyclogenesis in the westerly wind belt. Due to the warm conveyor belt (WCB; Section 5.1), which is a warm and humid current in the early stage of cyclogenesis, the cloud area forms a leaf pattern in front of the trough, as shown in Fig. 4-2-5, and the boundary exhibits an S-shape. Generally, the side of the S-shape where the bright region bulges toward the poles is parallel to the jet axis, while the other side (where the dark region bulges toward the tropics) is closer to the deformation field and may not be parallel to the jet axis.

Figure 4-2-6 presents a baroclinic leaf boundary. To the west of the Bohai Sea, there is a leaf-shaped cloud area corresponding to a developing cyclone. Its northern edge has an anticyclonic curvature and is aligned with the jet axis. Baroclinic leaf boundaries are often formed where jets converge.

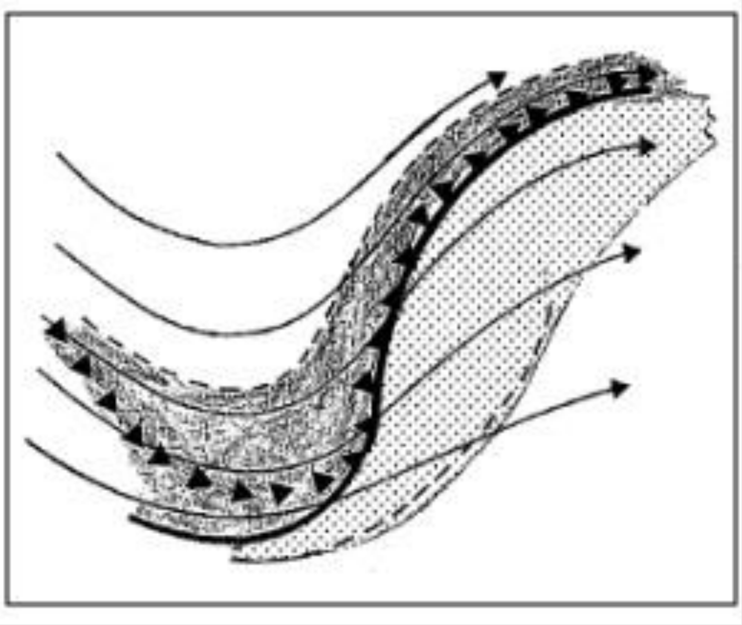

Fig. 4-2-5 Schematic illustration of a baroclinic leaf boundary. Shading: dark region; white: bright region; dotted area: cloud; thick line: boundary; thin arrows: streamlines; black triangles: axis of maximum wind speed.

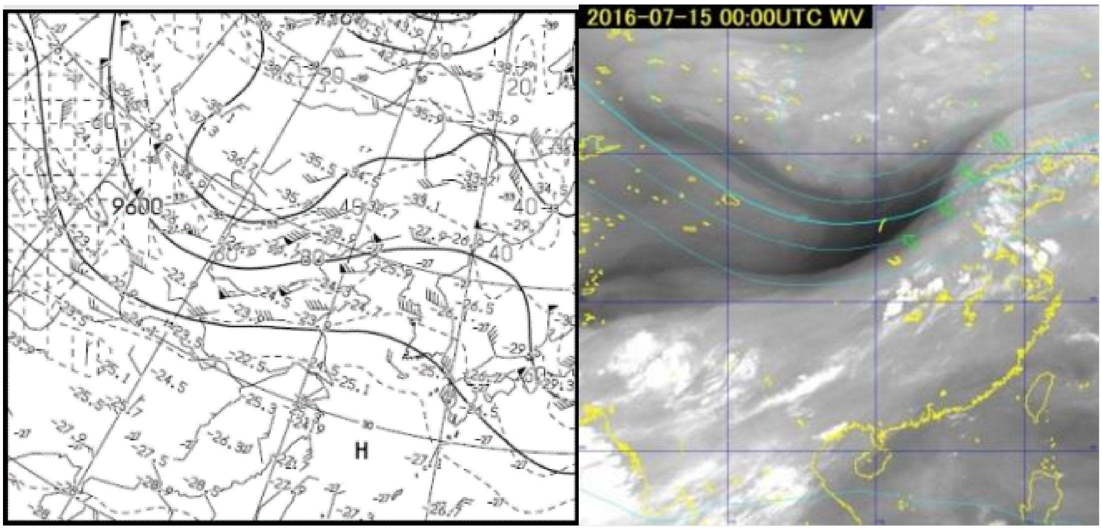

Fig. 4-2-6 Baroclinic leaf boundary for 00:00 UTC on 15 July 2016. Left: 300 hPa weather chart; right: water vapor image; green arrows: boundary.

4.2.2. Boundaries Exhibiting Blocking

This type of boundary is formed by the development of circulation with a wind field in the opposite direction to the surrounding wind in an area with relatively weak upper-level wind. As a circulation field that blocks the surrounding wind is formed in such cases, the phenomenon is referred to as a boundary exhibiting blocking. Based on the origin of the circulation field, these can be divided into head boundaries related to cyclone formation, and inside boundaries related to anticyclone formation.

4.2.2.1. Head Boundaries

Head boundaries are borders between convex bright regions and surrounding dark regions. This type moves and changes slowly, and is formed by synoptic-scale streams associated with cyclogenesis. As per Fig. 4-2-7, cyclones cause moist air masses to rise from the lower layer and form a head-shaped bright region divided into a stream along the cyclone and an anticyclonic flow north of the cyclone. The stream in the bright region is blocked by surrounding dry westerly winds and becomes a downward stream at the border. In the field of the upper stream, a boundary is formed along the elongation axis of the deformation field.

Figure 4-2-8 shows a head boundary. A clear boundary is seen over the sea south of the Kamchatka Peninsula at the border between easterly wind associated with cyclonic circulation east of the Kuril Islands and northwesterly wind from the Sea of Okhotsk at 300 hPa. The presence and scale of upper cyclones, which are difficult to judge from weather charts alone, can be estimated from boundaries.

Fig. 4-2-7 Schematic illustration of a head boundary. Shading: dark region; white: bright region; thick line: boundary; thin arrows: streamlines; black triangles: axis of maximum wind speed.

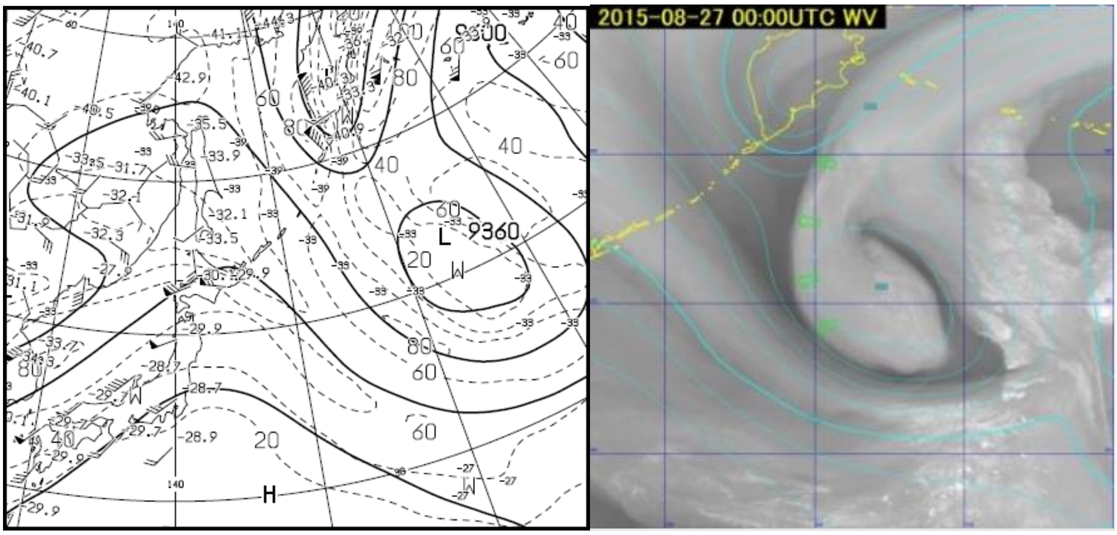

Fig. 4-2-8 Head boundary for 00:00 UTC on 27 August 2015. Left: 300 hPa weather chart; right: water vapor image; green arrows: boundary, cyan lines: 300 hPa contour line from GSM.

4.2.2.2. Inside Boundaries

As subsidence due to anticyclones in the upper layer causes dry areas to form and spread, a border is formed between the dry area and any relatively wet current alongside an upper trough. Such borders formed by anticyclonic circulation are called inside boundaries. As per Fig. 4-2-9, these form between convex dark regions toward the upstream side and surrounding bright areas. This type moves and changes slowly, and can be used to monitor the degree of development and movement of blocking anticyclones.

Figure 4-2-10 shows an inside boundary. A vortex corresponding to an upper cyclone can be seen near Primorye, while a ridge in the opposite phase can be seen to the north. This is difficult to understand from the 300 hPa weather chart (Fig. 4-2-10) alone, but the contours on the water vapor image suggest an upper anticyclone extending westward from northern Sakhalin at the north of the upper cyclone. An inside boundary is formed between this anticyclonic stream and the moist westerly wind (bright region) in front of the trough upstream.

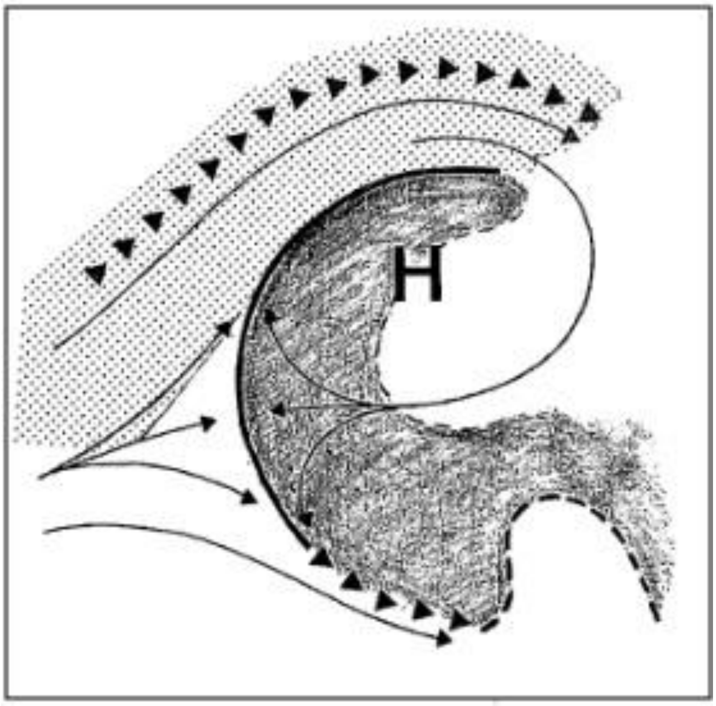

Fig. 4-2-9 Schematic illustration of an inside boundary. Shading: dark region; white: bright region; dotted area: cloud; thick line: boundary; thin arrows: streamlines; black triangles: axis of maximum wind speed.

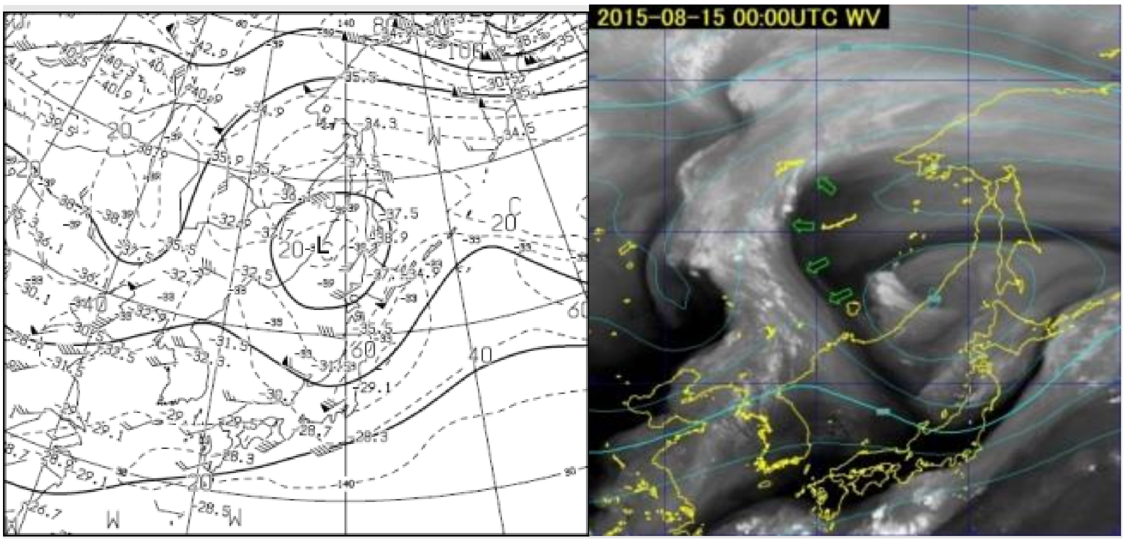

Fig. 4-2-10 Inside boundary for 00:00 UTC on 15 August 2015. Left: 300 hPa weather chart; right: water vapor image; green arrows: boundary, cyan lines: 300 hPa contour line from GSM.

4.2.3. Boundaries Exhibiting a Surge

In water vapor imagery, dark regions rushing in from upstream are called surges. Boundaries formed by such regions and bright regions at the front in the direction of movement are called surge boundaries, which can be divided into dry surge boundaries (where the dark region extends in a convex manner eastward) and base surge boundaries (where the dark region extends in a convex manner toward the equator). Surge boundaries provide important information in analysis of water vapor imagery because they promote convective activity and contribute to the generation of turbulence due to the presence of dry air masses in the upper layer.

4.2.3.1. Dry Surge Boundaries

Cold air mass advection in the upper and middle layers, deceleration downstream of the jet core, and subsidence at the rear of developed cyclones are factors in downward stream development. Dark regions associated with downward streams form a clear boundary between the cloud area associated with the cyclone in front, known as a dry surge boundary. As per Fig. 4-2-11, the dark region moves in a convex manner downstream and the boundary moves rapidly.

When there is a warm and humid air mass in the lower layer near the dry surge boundary, an associated dry air mass in the upper layer flows in and promotes instability, necessitating caution for convective cloud development. Disturbances such as clear air turbulence (CAT) are likely to emerge between this boundary and the dark region on the upstream side (Ikeda and Okumura, 1999).

Figure 4-2-12 shows a dry surge boundary. The tip of the dark region moving eastward from near Primorye has reached the sea east of Hokkaido, forming a boundary at the rear of the trough extending over the Sea of Okhotsk to the area east of Japan. This is a dry air mass accompanied by a cold air mass moving quickly eastward with increasing darkness, indicating a strong downward stream in the deceleration area behind the trough.

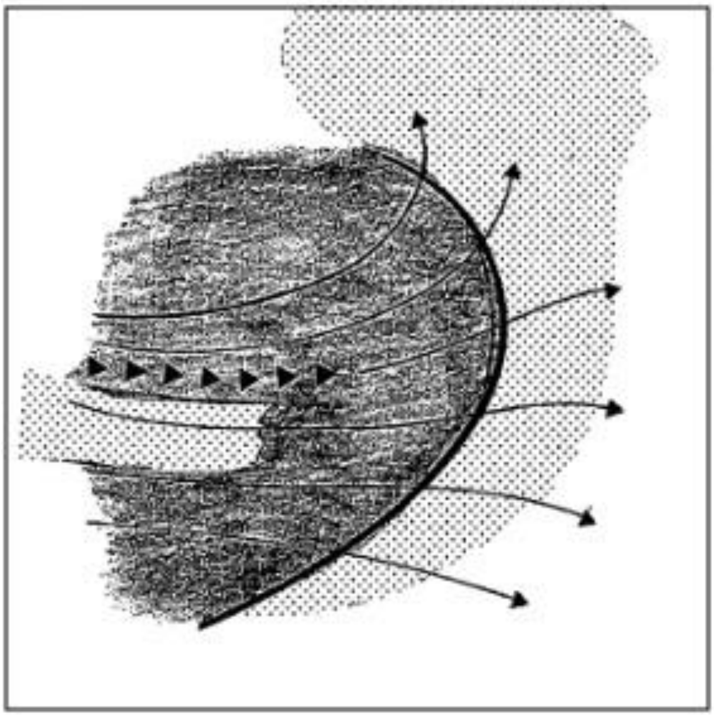

Fig. 4-2-11 Schematic illustration of a dry surge boundary. Shading: dark region; white: bright region; dotted: cloud; thick line: boundary; arrows: streamlines; black triangles: axis of maximum wind speed.

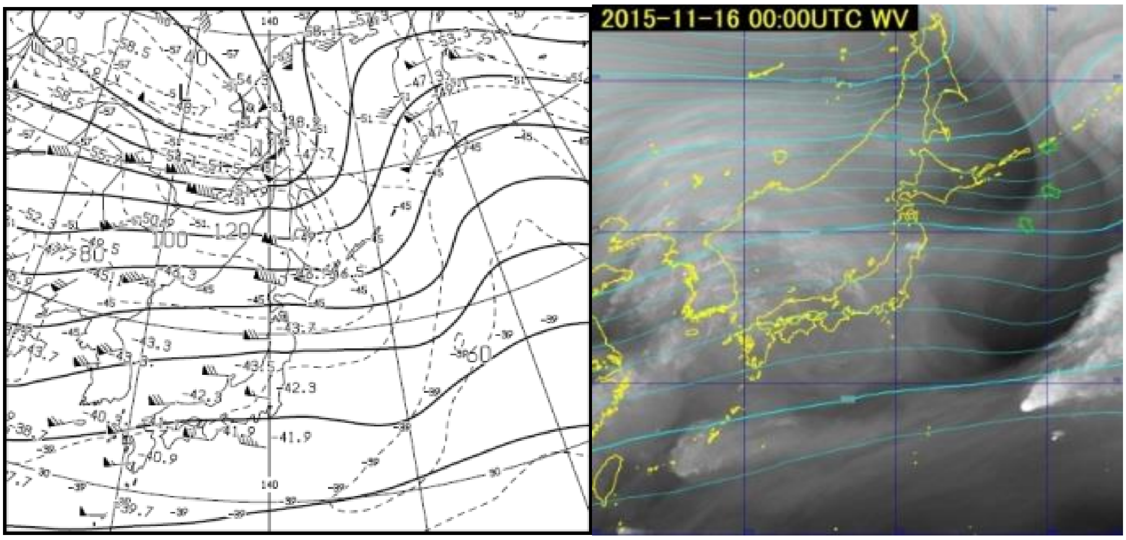

Fig. 4-2-12 Dry surge boundary for 00:00 UTC on 16 November 2015. Left: 300 hPa weather chart; right: water vapor image; green arrows: boundary, cyan lines: 300 hPa contour line from GSM.

4.2.3.2. Base Surge Boundaries

Due to upper-ridge strengthening, northerly winds fortify to the east of the ridge and the dry air mass moves southward, forming a base surge boundary between itself and the humid air mass on the tropical side. Boundaries usually appear as narrow strips, but in Fig. 4-2-13 a dark region representing a base surge boundary expands southward. Similar to the situation with dry surge boundaries, forms of turbulence such as CAT tend to occur between such boundaries and dark regions upstream (Ikeda and Okumura, 1999). Base surge boundaries may move southward to the Intertropical Convergence Zone (ITCZ) and activate convection. Especially in the tropics, monitoring of such boundaries is important in the generation and development of convective systems.

Figure 4-2-14 shows a base surge boundary formed between a dry air mass (dark region) moving southward from a ridge developing near Japan and a moist air mass to the south (bright region).

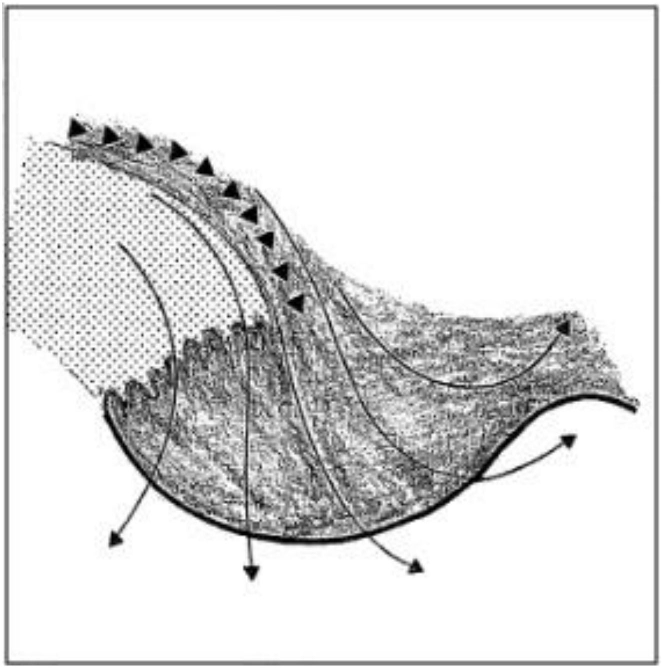

Fig. 4-2-13 Schematic illustration of a base surge boundary. Shading: dark region; white: bright region; dotted area: cloud; thick line: boundary; thin arrows: streamlines; black triangles: axis of maximum wind speed.

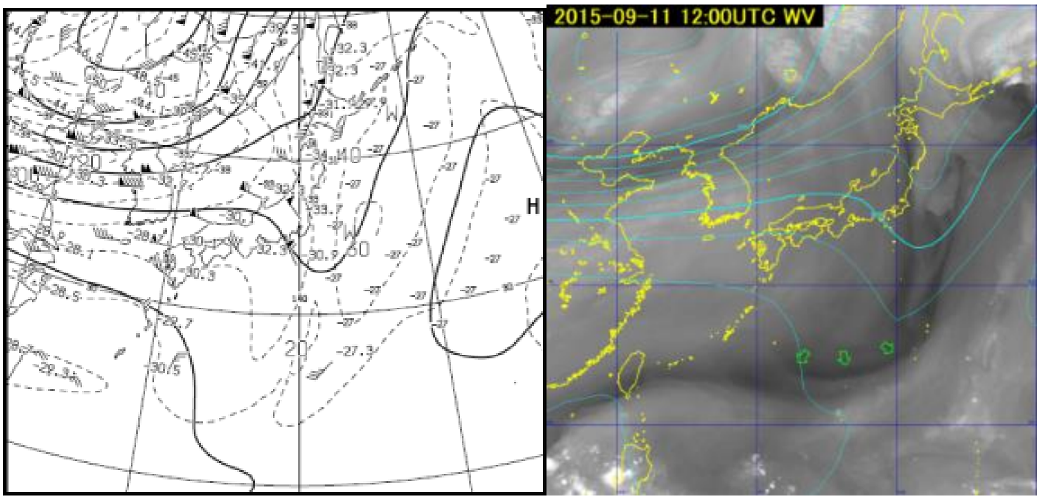

Fig. 4-2-14 Base surge boundary for 12:00 UTC on 11 September 2015. Left: 300 hPa weather chart; right: water vapor image; green arrows: boundary, cyan lines: 300 hPa contour line from GSM.

4.2.4. Others

4.2.4.1. Return Moisture Boundaries

In Fig. 4-2-15, a return moisture boundary is seen on the eastern side of an upper ridge between a moist air mass (bright region) moving southward and a dry area (dark region). This formed due to a upper-level moist air mass flowing toward the equator with no influence from synoptic-scale vertical motion. The name “return moisture boundary” reflects how moisture moving northward in front of the trough crosses over the ridge and returns toward the equator. Such boundaries have a bright/dark pattern opposite to that of base surge boundaries in water vapor images, but are not related to downward streams and do not correspond to significant weather disturbances such as fronts and cyclones.

Figure 4-2-16 shows a return moisture boundary formed between a bright region in a convex form toward the equator, extending from the area east of Japan to the area far east of Japan, and a dark region on the polar side of the jet stream extending from Primorye to the area far east of Japan.

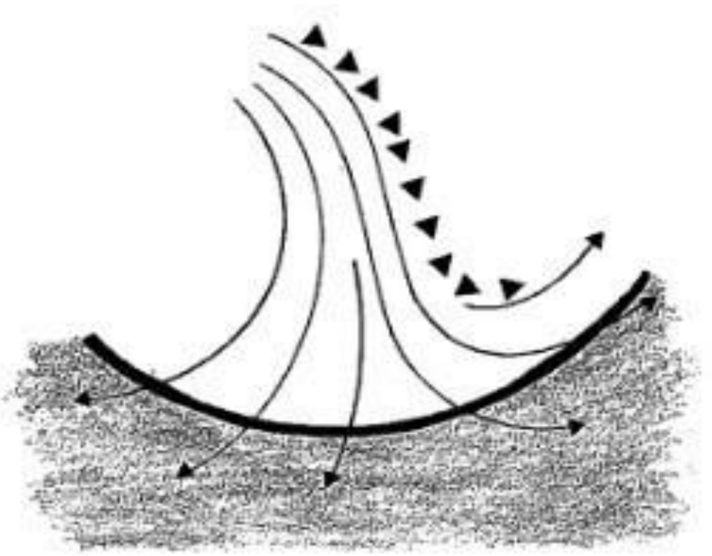

Fig. 4-2-15 Schematic illustration of a return moisture boundary. Shading: dark region; white: bright region; thick line: boundary; thin arrows: streamlines; black triangles: axis of maximum wind speed.

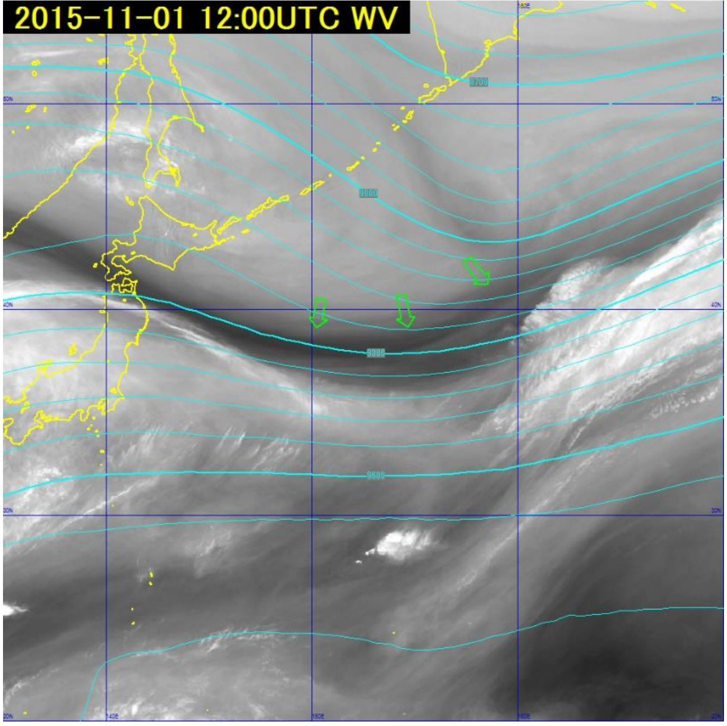

Fig. 4-2-16 Water vapor image for 12:00 UTC on 1 November 2015, showing a return moisture boundary (green arrows).

Reference

- Ramond *et al.,* 1981: The Dynamics of Polar Jet Streams as Depicted by the METEOSAT WV Channel Radiance Field, Monthly Weather Review, 109, 2164-2176.
- Weldon and Holmes, 1991: Water Vapor Imagery, NOAA Technical Report NESDIS 57.

4.3. Analysis Using Water Vapor Imagery

4.3.1. Cold Lows

Upper vortices are visualized in patterns in water vapor imagery, allowing analysis and tracking even in the absence of clouds. These often correspond to cold lows.

Figures 4-3-1 and 4-3-2 show water vapor images for an upper vortex moving eastward from the sea near the Kuril Islands. 500 hPa weather charts (Figs. 4-3-3 and 4-3-4) show that the center of the upper vortex and the cold low largely coincide.

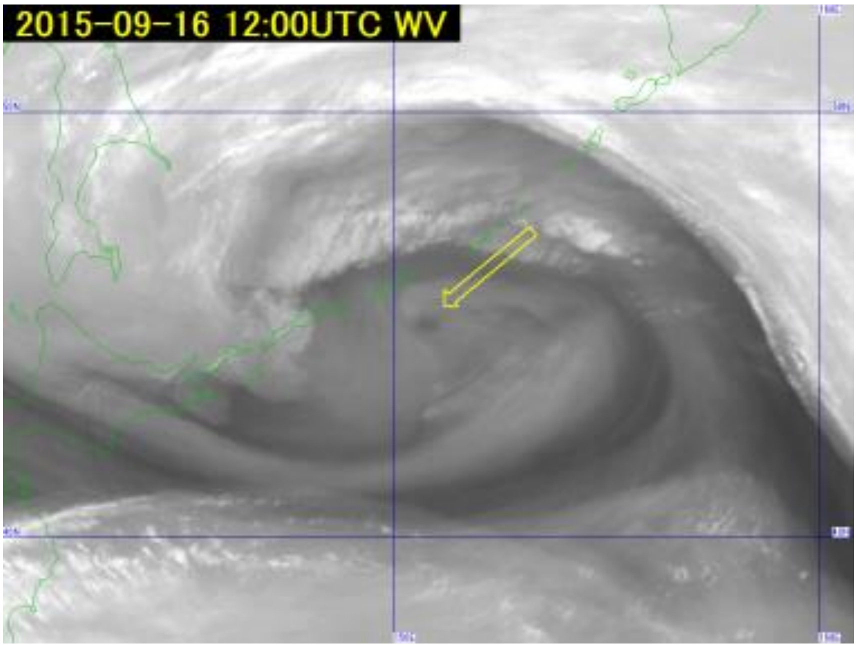

Fig. 4-3-1 Water vapor image of a cold low for 12:00 UTC on 16 September 2015

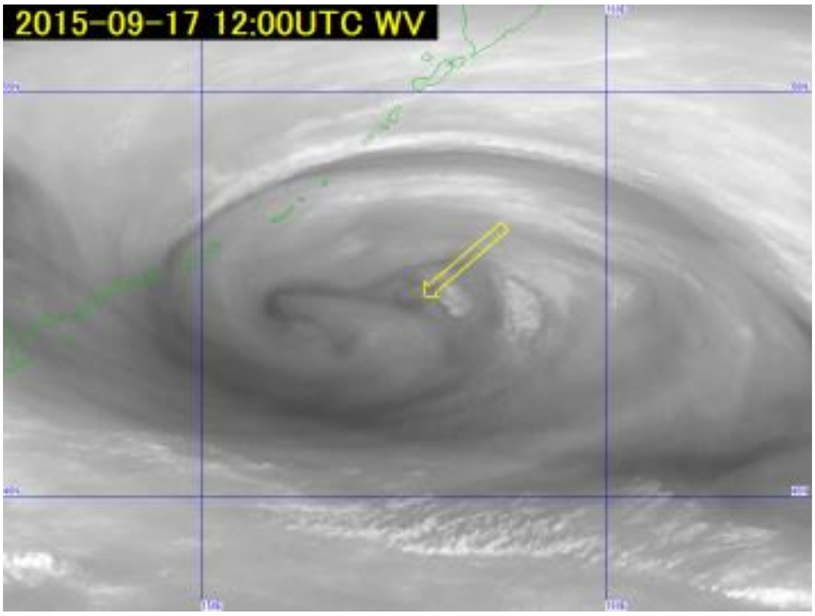

Fig. 4-3-2 Water vapor image of a cold low for 12:00 UTC on 17 September 2015

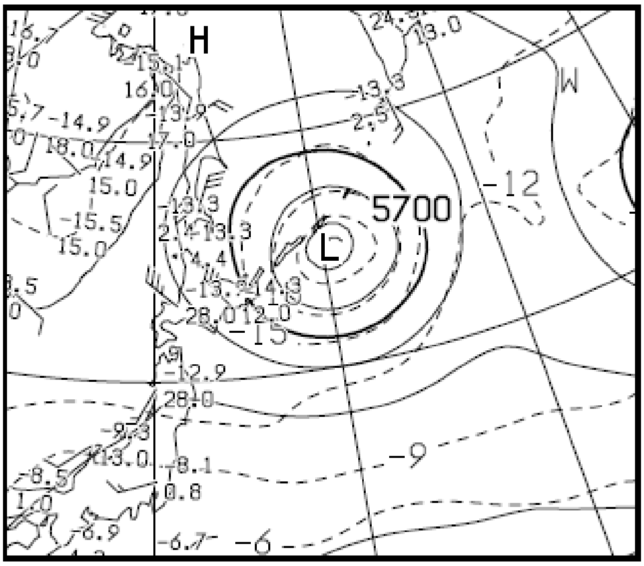

Fig. 4-3-3 500 hPa weather chart for 12:00 UTC on 16 September 2015

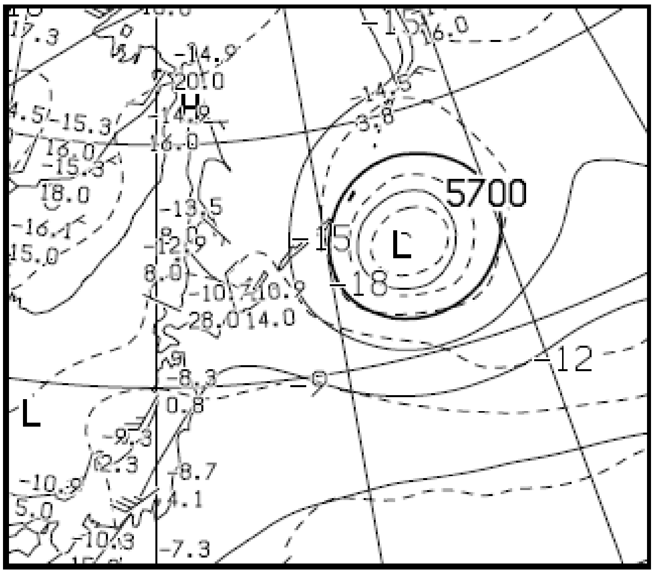

Fig. 4-3-4 500 hPa weather chart for 12:00 UTC on 17 September 2015

4.3.2. Upper Cold Lows (UCLs)

Shimamura (1981) refers to cold low-type cyclonic circulation analyzed in tropical and subtropical regions as an upper cold low (UCL), with the following notations:

1. Early UCL stages often feature a humid area to the east of the center and a dry area near/westward of the center in correspondence with the cloud area.
2. Convective clouds are active around the UCL, and the surrounding area may develop typhoon conditions.

Naito (1993) and Takamine (1995) state that UCLs are often observed along tropical upper tropospheric troughs (TUTTs), which are formed by streams descending southward from the upper layer near Japan and streams moving northward while sinking from the upper layer of ITCZ. Thus, it is important to track UCLs in monitoring of tropical disturbances.

Figure 4-3-5 shows a water vapor image for a clearly identifiable upper vortex corresponding to a UCL moving westward from Wake Island (green arrow). The 250 hPa weather chart (Fig. 4-3-6) shows the vortex and cyclone centers almost at the same location. The minimum cold value **C** (abbreviation for cold; the local minimum point of temperature) is just to the north of **L** on the weather map, indicating that the temperature around the upper vortex is lower than in the surrounding area. Although not prominent here, convective cloud areas containing Cb tend to emerge and develop around vortices due to the presence of upper cold air. Cold lows in the westerly wind belt generally move southward or eastward, whereas UCLs separated from the westerly wind belt sometimes approach Japan while moving northward or westward over southern and eastern sea areas.

Meanwhile, a clear vortex is seen over the sea near Chichijima (red arrow) in association with a typhoon, rather than being a UCL. The major difference from a UCL is that the upper layer near the center is accompanied by warm air **W** rather than cold air **C**, as seen on the 250 hPa weather chart.

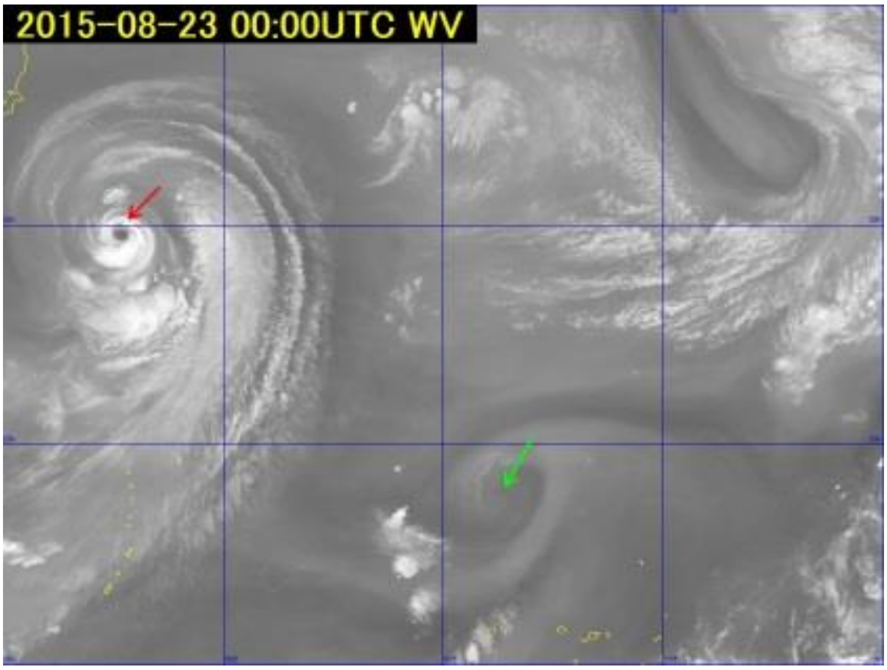

Fig. 4-3-5 Water vapor image of UCL for 00:00 UTC on 23 August 2015

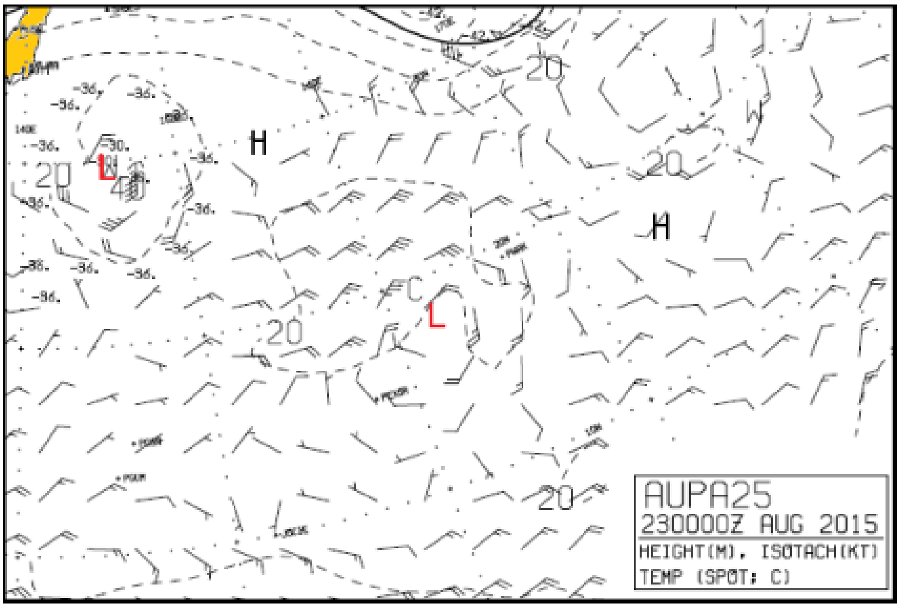

Fig. 4-3-6 250 hPa weather chart for 00:00 UTC on 23 August 2015

4.3.3. Promotion of Convective Activity

An inflow of dry air mass (i.e., a low equivalent-temperature air mass) into the upper layer corresponds to deterioration of stability when the lower layer condition exhibits no change. When a dark region enters an area where convective clouds are present, stability deteriorates and convective activity is promoted. This is likely to occur at the front of the dark region in the direction of movement, and convection may turn active near the boundary. The dark region forming the surge boundary is often accompanied by cold air that increases instability, meaning that convective clouds are likely to develop.

Figures 4-3-7 and 4-3-8 show a dry surge boundary. The tip of the dark region moving eastward south of Japan forms a boundary behind a cloud area in a cyclone moving eastward south of Japan while occluding. This is a dry air mass with cold air, and a strong downward stream is seen behind the cyclone. Convective activity is limited at 12 UTC, but cumulonimbus (green arrows, Fig. 4.3.8) develops near the boundary at 18 UTC. These clouds were cumulus congestus and cumulus (green arrows on Fig. 4.3.7) six hours previously, and the dark region inflow appears to have promoted convective activity.

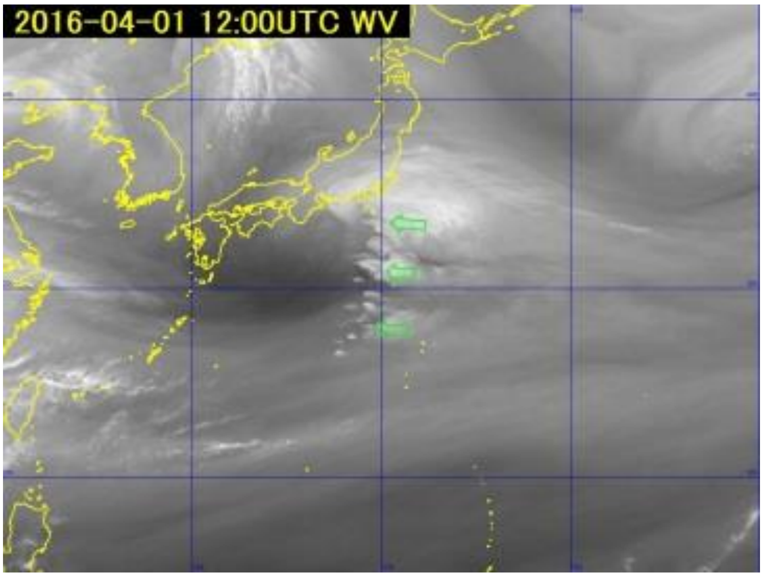

Fig. 4-3-7 Water vapor image for 12:00 UTC on 1 April 2016

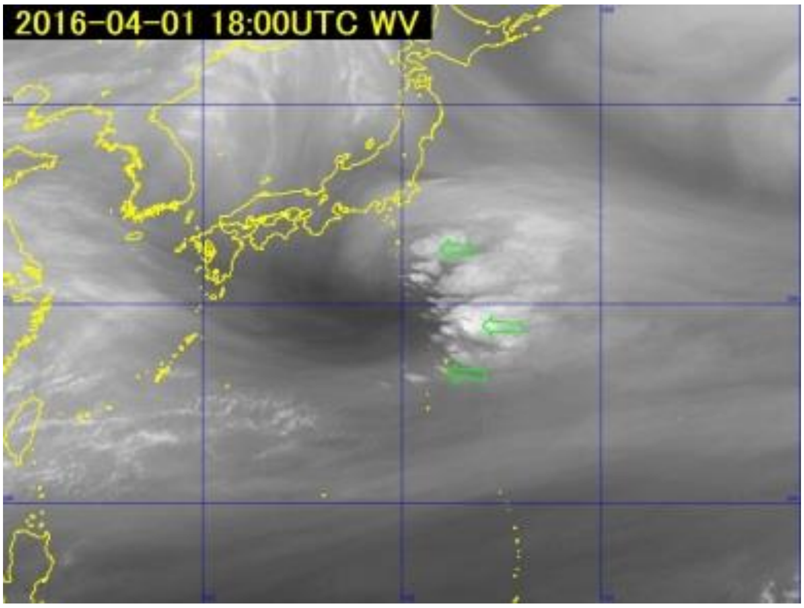

Fig. 4-3-8 Water vapor image for 18:00 UTC on 1 April 2016

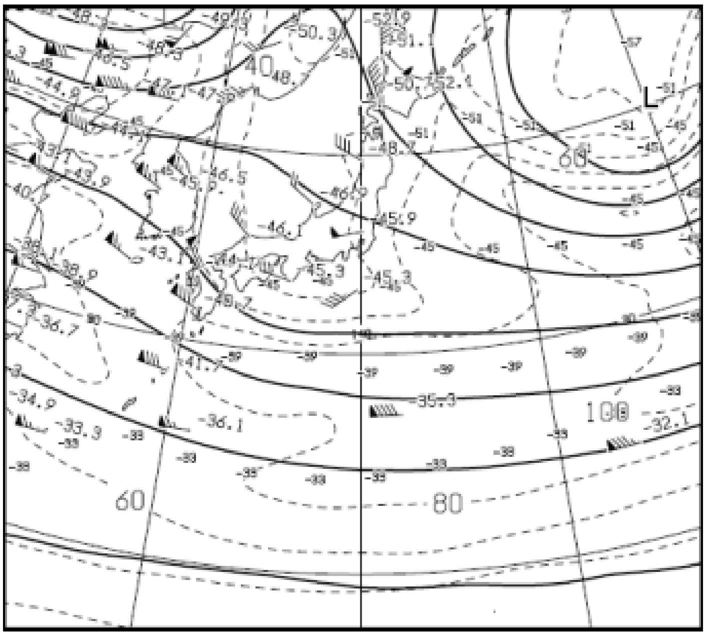

Fig. 4-3-9 300 hPa weather chart for 12:00 UTC 1 April 2016

5. Synoptic-scale Phenomena

5.1. Front Analysis

5.1.1. Concept of Fronts

Fronts are defined as boundaries between air masses, with clouds emerging when vertical circulation is active at divisions between areas with different densities. Belt-form cloud bands are observed in the vicinity of fronts on a synoptic scale, providing a starting point for front analysis in satellite imagery. Cases in which no clouds form with vertical circulation are occasionally seen over dry continental areas, with only a band consisting of upper cloud carried by strong winds in the upper troposphere. It should therefore be noted that fronts cannot be identified from cloud bands alone.

To highlight the structure of disturbances, Browning (1990) proposed the concepts of warm conveyor belts (WCBs) and cold conveyor belts (CCBs) in reference to major atmospheric currents on a coordinate system relative to the disturbance. The WCB and CCB concepts were also adopted by Carlson (1980) to clarify cyclonic and frontal structures (Fig. 5-1-1).

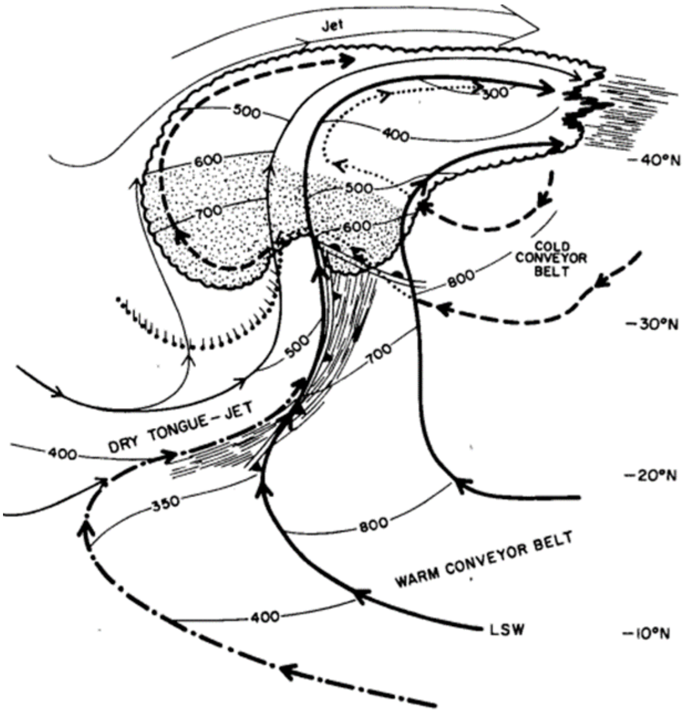

Fig. 5-1-1. Conveyor belt model (Carlson (1980), with open-arrow addition). Solid lines: WCB; dashed lines: CCB; numbers: current altitudes; dash-dots: low cloud edge

WCB currents carry warm wet air upward, contributing significantly to cloud formation. This creates southeastern winds in the lower layer at the edge of anticyclones, ascending northward in warm cyclone areas and gradually changing direction clockwise. These currents are associated with warm advection ahead of troughs. Cloud emerges when WCBs reach condensation level, with a cloud top height directly proportional to the distance of northern shift. WCBs meeting an upper-jet axis change direction eastward as northward ascension is suppressed.

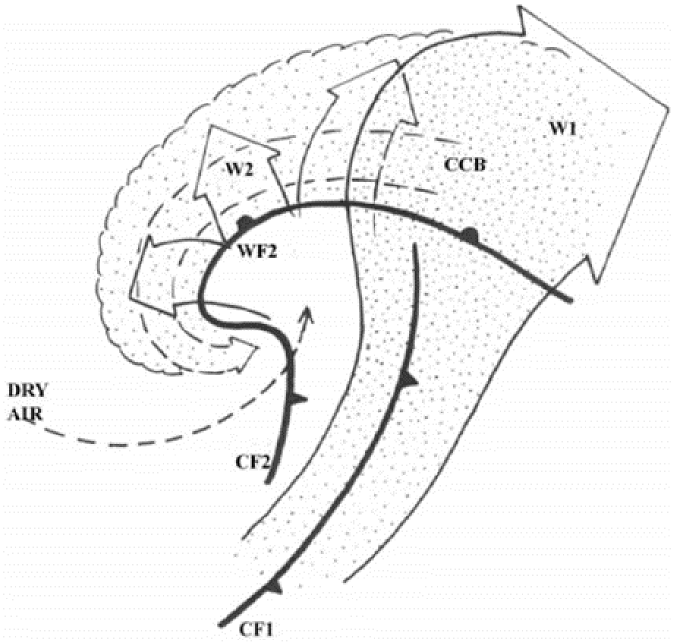

Fig. 5-1-2. Secondary WCB model (Browning, 2004)
W1: WCB; W2: secondary WCB

CCBs are currents located toward the cyclonic center, moving in parallel to the frontal side of a warm front. In satellite imagery, they are recognized as lower cloud and progress westward, moving under WCBs. This makes them unrecognizable by satellites, but they cross WCBs at a large angle at the western edge of the WCB cloud band, thereby manifesting as middle- and low-cloud areas extending westward. Along with such extension, part of the cloud mass rises, creating anticyclonic currents with subsequent eastward movement at jet-stream altitude. Other parts move with no height change toward the cyclonic center along with cyclonic currents, maintaining middle- and low-cloud status (bold open arrows in Fig. 5-1-2). Among CCB types, Bader *et al.* defined secondary WCBs (referred to here as W2s) as currents that assume anticyclonic curvature as they ascend (Fig. 5-1-2).

W2s are thought to develop under WCB conditions from updraft ahead of short-wave troughs. In the definition of Bader *et al.*, the term CCB refers specifically to currents at lower altitudes moving toward the cyclonic center.

Figure 5-1-3 shows a conveyor belt formation in infrared imagery, with the cloud area **W-W** associated with a WCB. The **W-W** cloud top is higher in the north, and a stratified cloud area is seen. This area appears to consist of thicker clouds than in visible imagery. The eastern terminal of the cloud area **E** consists of thin Ci, indicating that the upper clouds in the WCB formation turned eastward with jet-stream axis encounter. The **C1-C2-C3** cloud band is associated with a CCB. As the clouds around **C1** move above the CCB, many upper clouds are seen. The CCB is below the WCB, making it unrecognizable in satellite imagery. This is seen as a protrusion to the west of the WCB cloud band around **C2**. The **C2-C3** cloud top rises with westward progression, and the mass then joins the WCB upon turning eastward as it encounters the jet axis. A current diverted from the CCB is also seen entering the cyclonic circulation (from **C2** to **d**), maintaining a low cloud top.

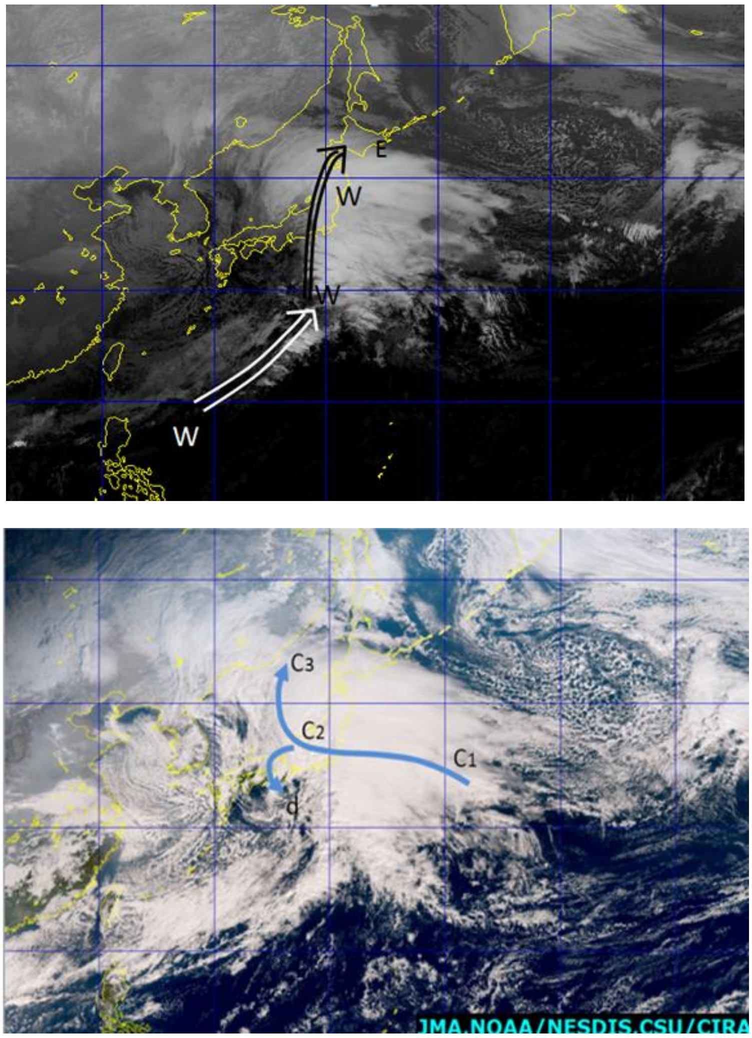

Fig. 5-1-3. Conveyor belt at 00:00 UTC on 18 January 2016
Top: B13 infrared image (arrow: WCB)
Bottom: True Color Reproduction image (arrow: CCB)

5.1.2. Warm Fronts

Warm fronts form at the boundaries of warm-air masses migrating along and creeping over cold-air masses, such as WCBs gliding over CCBs. These are observed as boundaries of WCB currents ascending northward from warm areas and beginning to slide over cold CCBs flowing toward a cyclonic center. This corresponds to the southern rim of stratiform cloud formations among currents along WCBs. In addition to stratiform clouds, convective clouds are also present near the front, as reported by Neiman (1993) with an elevator-escalator model illustrating mesoscale convective clouds around a CCB-WCB cross-point (Fig. 5-1-4).

In this model construction, warm fronts can be identified from satellite imagery in correspondence to the southern edge of cloud areas containing convective clouds. However, it is often difficult to determine the southern edge of cloud areas associated with warm fronts due to cloud development in warm areas and coverage by upper and middle clouds. Accordingly, identifying warm fronts in satellite imagery can be challenging. CCB formation is often minimal in the early cyclonic phase or in comma-style cyclones (see below), making lower clouds along warms front unclear.

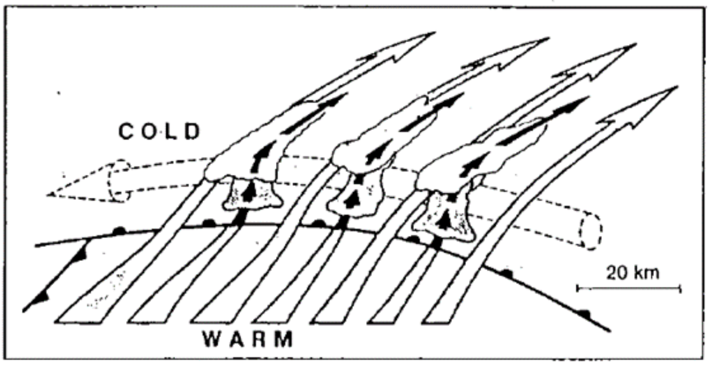

Fig. 5-1-4. Elevator-escalator model (Neiman, 1993)
Dashed lines: CCB; open arrows: WCB (escalator); black dots: clouds; black arrows: ascending currents associated with mesoscale convection (elevator)

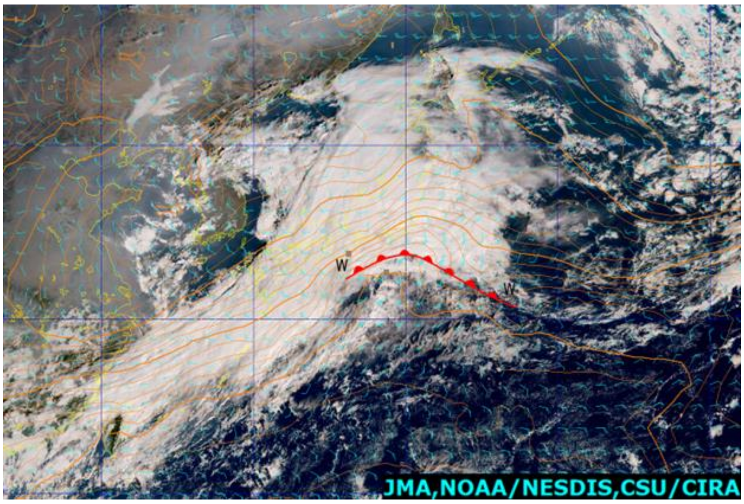

Fig. 5-1-5. Warm-front analysis for 00:00 UTC on 2 November 2015
True Color Reproduction image and objective analysis for 850 hPa (temperature, wind)

Figure 5-1-5 presents a simple case of warm front determination, with a cloud area along a cyclone between the Tokai and Kanto regions. The southern rim of the cloud area **W-W** is distinct, with convective cloud lines and a northern part consisting of upper and middle clouds. In satellite imagery, a warm front is observed along the southern rim, corresponding to a 12°C isotherm at 850 hPa based on objective analysis.

Warm fronts can be identified when lower cloud along a warm front is obscure, as when cold air regions are identified from cloud patterns within cold air fields ahead of a cyclone, or with estimation of wind direction from low-cloud movement. The dashed line in Fig. 5-1-6 indicates the estimated southern limit of a lower cold-air region behind the developed cyclone. The low cloud area **W-W** is seen westward of this line. A warm front associated with a cyclone passing near Japan is identified from the cloud area around **W-W** progressing eastward overall and from individual clouds migrating northwestward, enabling identification of a southeastward wind field ahead of the warm front.

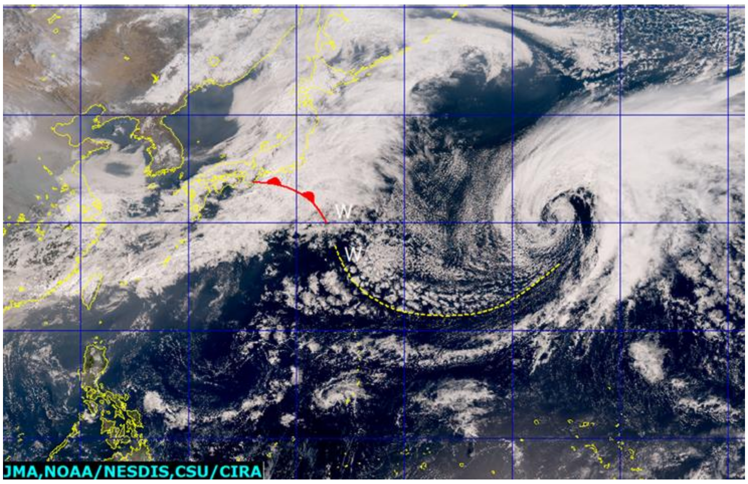

Fig. 5-1-6. Challenging warm-front analysis
True-Color Reproduction image for 00:00 UTC on 19 March 2016

5.1.3. Cold Fronts

Cold fronts may be Ana-type (associated with extreme weather changes near fronts) or Kata-type (associated with milder weather changes). Ana fronts are the textbook type, often featuring in cold-front analysis, but the Kata type is also common. The characteristics of each type in satellite imagery are described below, along with notable key features in cold-front analysis.

5.1.3.1. Ana Cold Fronts

Ana-type cold fronts are categorized as rearward-ascending types in the WCB model described by Browning (1990; Fig. 5-1-7). They are associated with inflows of intense cold air with a WCB inclined rearward, with an intense updraft arising in association with the cold front and warm air ascending relatively gently toward its rear. The band comprising the front features convective line cloud convection in a narrow part of the front edge alongside warm air, and the rear edge of the band consists of stratiform clouds. In satellite imagery, cloud bands corresponding to the Ana type have an aligned convective structure on the warm-air side, and the position of the cold front corresponds to convective cloud lines at the front of the band. Over sea areas during cold periods, cell-form convective clouds develop in association with cold-air inflow at the rear of the front, allowing identification of Ana-type forms from this cloud presence and related activity.

In Fig. 5-1-8, a cloud band is seen extending southwestward from a cyclone south of the Kamchatka Peninsula. At its southeastern edge (i.e., the warm-air side), active convective clouds align along **C**-**C**, allowing identification of the band as the Ana type. The position of the cold front can be estimated to be along **C**-**C**.

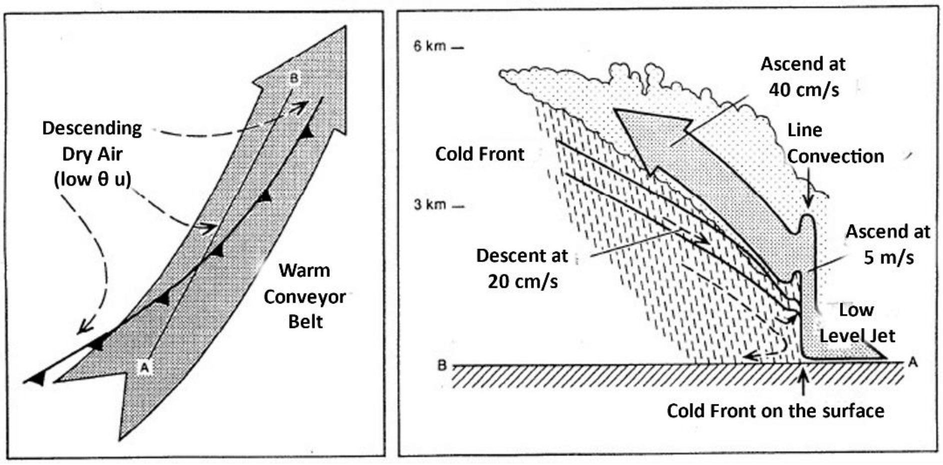

Fig. 5-1-7. Flows in a typical Ana cold front (from Kitabatake *et al.*, 1995)

Open arrow: rearward ascending WCB at the cold front under descending cold air (dashed lines)

Left: plane view; right: section along **A**-**B** in the diagram on the right

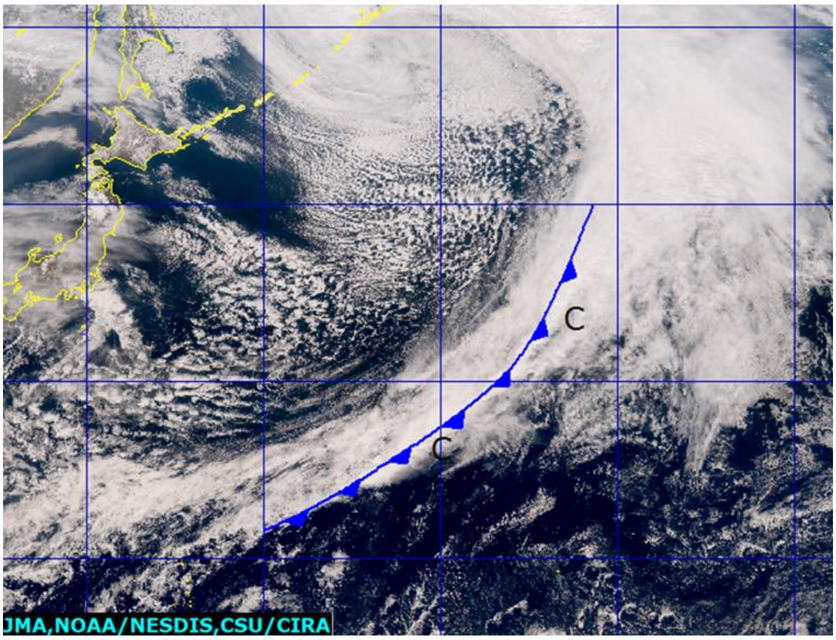

Fig. 5-1-8. An Ana cold front at 00:00 UTC on 16 March 2016

True Color Reproduction image indicating cold-front position (see the main text for alphabetical designations)

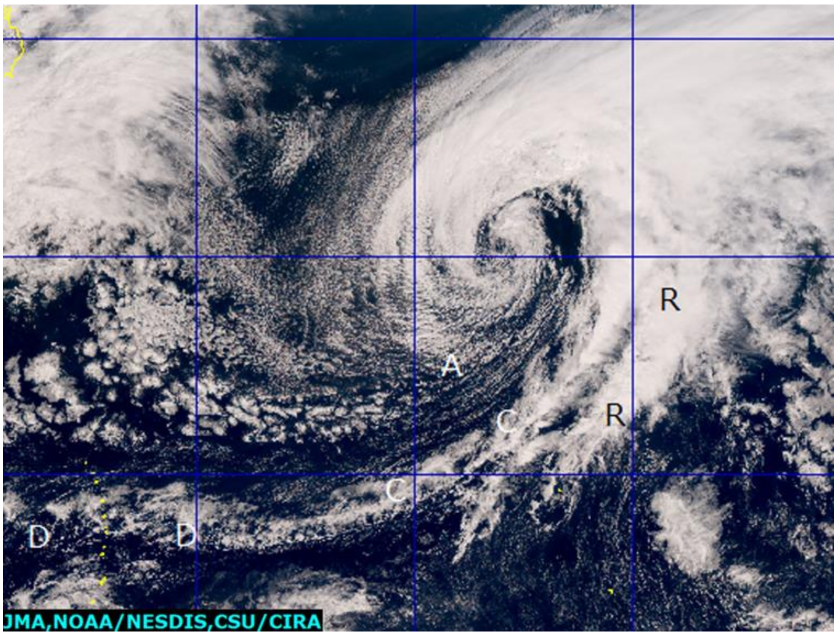

Fig. 5-1-9. An Ana cold front at 00:00 UTC on 19 March 2016
True Color Reproduction image indicating cold-front position (see the main text for alphabetical designations)

In Fig. 5-1-9, a rope cloud formation marked by **C-C** is seen at the front edge of the cloud band. Rope clouds are often observed at the advancing front edge of cloud bands extending from cyclones at maturity or during dissipation. A cold front can be determined at the position of the rope cloud in this case. Although the cloud area **D-D** is also present west of **C-C**, this is not considered to correspond to the cold front as it is distant from the cloud band and discontinuous. A cell-form convective cloud formation marked **A** is seen over the sea at the rear of the front in association with strong cold advection. The active convective cloud band **R-R** is also seen with a 100 – 200 km width in front of the rope cloud, representing a rain band within the warm area. As such bands are often seen in warm areas, care should be taken to avoid misidentification as cold fronts.

5.1.3.2. Kata Cold Fronts

Kata-type cold fronts are categorized as forward-ascending types in the WCB model described by Browning (1990; Fig. 5-1-10). Upper cold fronts (UCFs) may emerge when dry air with a low equivalent potential temperature descends from the upper atmosphere and overtakes the surface cold front, thereby initiating convective instability between the WCB beneath and warm wet air within warm areas, increasing the likelihood of rain band development that may bring extreme phenomena such as intense rainfall and gusting winds. Shallow moist zones (SMZs) consisting of low convective clouds with light rain may be present between rain bands and surface cold fronts. Such Kata formations are known as split fronts.

Changes in Kata cold-front weather accompanying surface cold-front passage are limited in comparison to those of rain-band passage. Rain bands and UCFs are clearly recognizable in satellite imagery, while identification of surface cold fronts comprising lower clouds with coarser organization is more challenging.

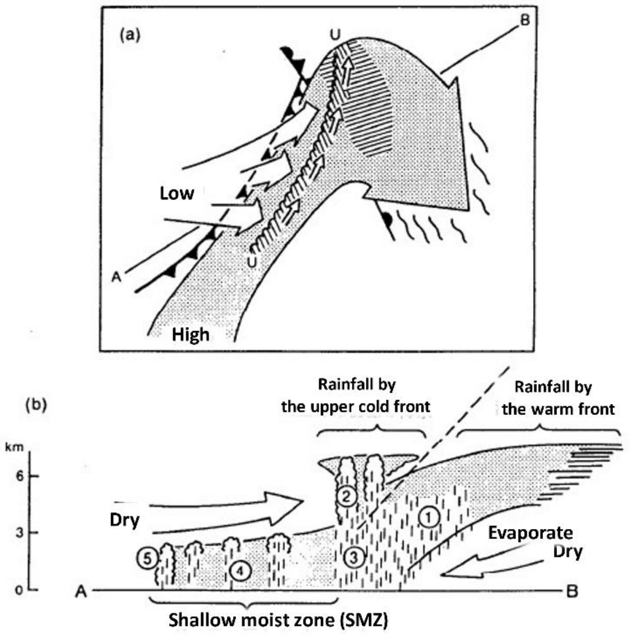

Fig. 5-1-10. Kata cold front (split front) (Kitabatake *et al.*, 1995)
(a): plane view, with open dotted arrows representing forward-type WCB forms and open arrows representing dry air; (b): section view of (a) along **A-B** 1.: rainfall from warm front; 2.: upper cell generating convective precipitation with UCF (indicated by **U-U** in (a)); 3.: rainfall from UCF; 4.: shallow moist zone (SMZ) between UCF and surface cold front; 5.: shallow precipitation from cold front

In Fig. 5-1-11, a cloud band is seen extending southwestward from a cyclone east of Hokkaido. The tall convective cloud **A-A** corresponds to a surface cold front, which in turn corresponds to the western edge of a low cloud area (**B**, with a cloud top height under 700 hPa) to the west of **A-A**, as seen by the entry position of warm air and a concentration zone with an equivalent potential temperature at 850 hPa. In the vertical section view, the upper layer above 700 hPa is dry over the surface cold front, suppressing the top of the cloud area **B-B** with dry air. This dry air is a characteristic of Kata cold fronts, overtaking the surface cold front with intense southwestern winds in the middle and upper layers. A split-front structure is indicated by the correspondences of **A-A** to UCF conditions and **B-B** to SMZ conditions.

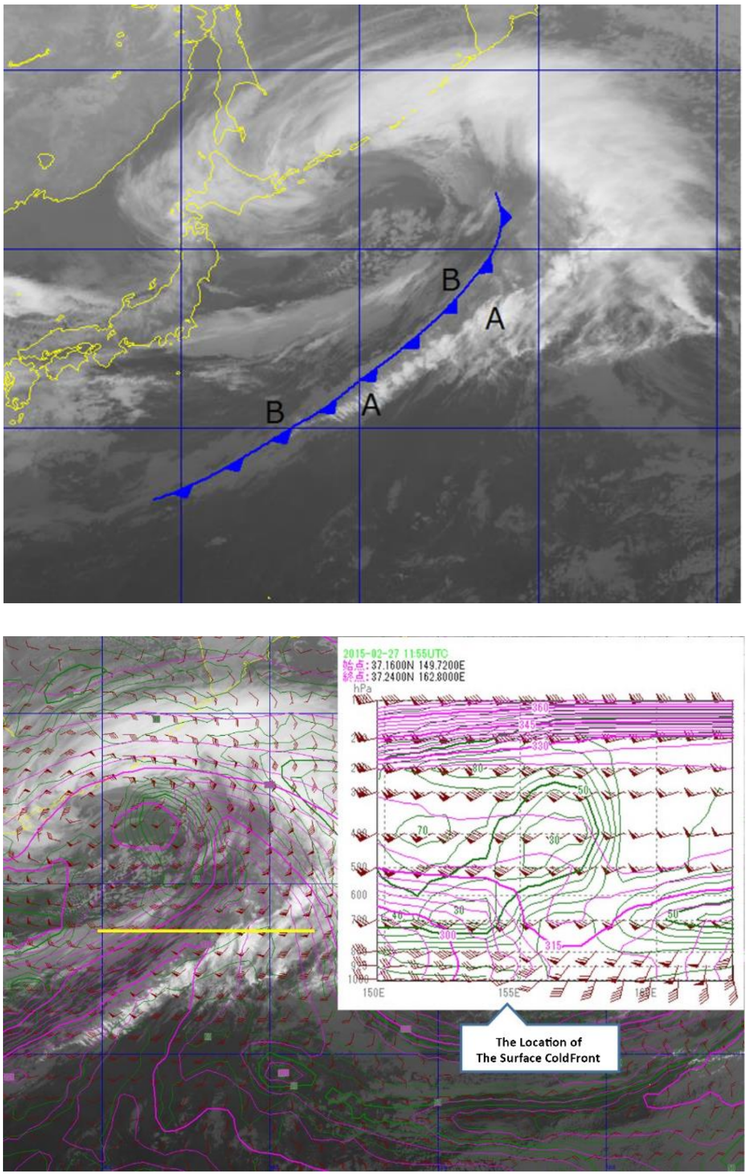

Fig. 5-1-11. A Kata cold front at 12:00 UTC on 27 February 2015
Top: B13 infrared image with a surface cold front; bottom: B13 infrared image with 850-hPa equivalent potential temperature, humidity and a vertical section view for the yellow latitudinal line. Pink: equivalent potential temperature; green: humidity; brown: wind

5.1.3.3. Points to Note Regarding Analysis

The points below regarding cold-front analysis should be noted (Fig. 5-1-12).

1. Even single cold fronts may exhibit a Kata-type structure near the cyclonic center due to dry-air descent from the upper atmosphere or an Ana-type structure away from the cyclonic center. Cyclones tend to be associated with such characteristics after the development stage. Hence, cold fronts associated with developing cyclones are generally located at the western edge of a cloud band (open arrows in the figure) and the southern edge of a cloud band (black arrows in the figure) at a distance.

2. In Ana-type structures, the front is identified as the position of a rope cloud formation. However, care should be taken in analysis of multiple rope cloud formations and fronts without cloud bands, which appear similar to convective cloud lines in warm areas and elsewhere.
3. Prominent convective clouds in warm areas may merge with cold fronts along marginal currents of anticyclones in a linear structure (e.g., cloud **A** in the figure), and may cause cold-front misidentification. In such cases, convective cloud lines in warm areas can be categorized by whether they pursue an anticyclonic path or have an anticyclonic curvature.

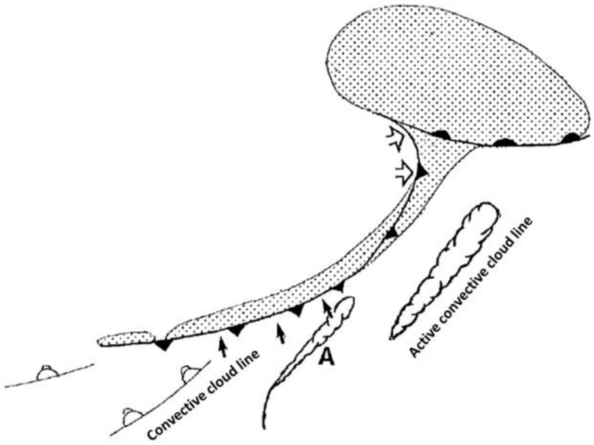

Fig. 5-1-12. Points of focus in cold-front determination
Dotted area: cloud; bold line: convective cloud; cloud areas: active convective cloud line (see the main text for a description of **A**)

5.1.4. Occluded Fronts

As shown in Fig. 5-1-13, occlusions can be either cold (man (人) type) or warm (lambda (λ type). Discrimination is based on the temperature field and cloud patterns.

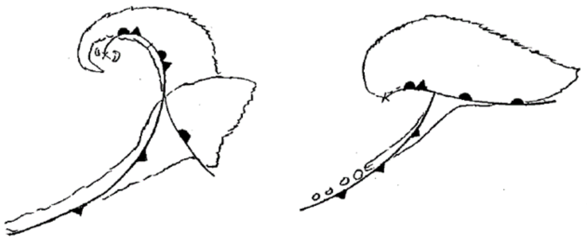

Fig. 5-1-13. Left: cold-occluded model (man (人) type); right: warm-occluded model (lambda (λ type)

5.1.4.1. Decision-making on Occlusion Points

Saito (1979) identified the characteristics of occlusions (disappearances of warm areas in a cyclonic zone from the ground surface) as follows:

- A significant fall in air pressure

- A rapid decrease in phase differences between an 500-hPa trough and a cyclone on the ground
- A single pressure valley or a single shear current at 850 hPa or on the ground
- A wedge-shaped upper warm air mass immediately above or slightly ahead of a surface trough with no simultaneous increase in the surrounding temperature gradient
- An upper strong wind zone to the south outside the cyclonic center on the ground

Among these characteristics, the position of a strong wind zone can be determined in satellite imagery, and its axis can be estimated from Ci streaks in infrared imagery and boundaries in water vapor imagery. Fronts can also be identified from indicators such as frontal cloud bands largely parallel to the strong wind axis and cloud bands corresponding to CCB extending to the polar side across the frontal cloud band.

The general procedure for determination of occlusion points is outlined below, with reference to Fig. 5-1-14.

1. Strong-wind axis determination

   A strong wind axis is seen along a boundary corresponding to a jet stream at **J-J** in the water vapor image.
2. Cold-front determination

   In both visible and infrared imagery, a clear cloud band with a width of 200 – 400 km corresponding to a cold front is seen along **B-B**.
3. Warm-front determination

   In visible imagery, **W1-O-W2** is a cloud band equivalent to a CCB, corresponding to a warm front to the east of the cold frontal cloud band **W1-O**. This crosses the cold band, extending to the polar side **O-W2**. The imagery shows a clear CCB formation.
4. Occlusion point/occluded front determination

   An occlusion point is observed around the cross point **O** of the southern edge **W1-W2** at the warm side of a CCB and the boundary **J-J** corresponding to a jet stream. The cloud area **A** with a high top advances eastward from the occlusion point. This pattern tends to develop after the occlusion progresses toward dissipation. The cloud band **O-W2** associated with the CCB extends westward from the polar side of the cold frontal cloud band **B-B.** Below this, the southern edge of the low cloud corresponds to the occluded front.

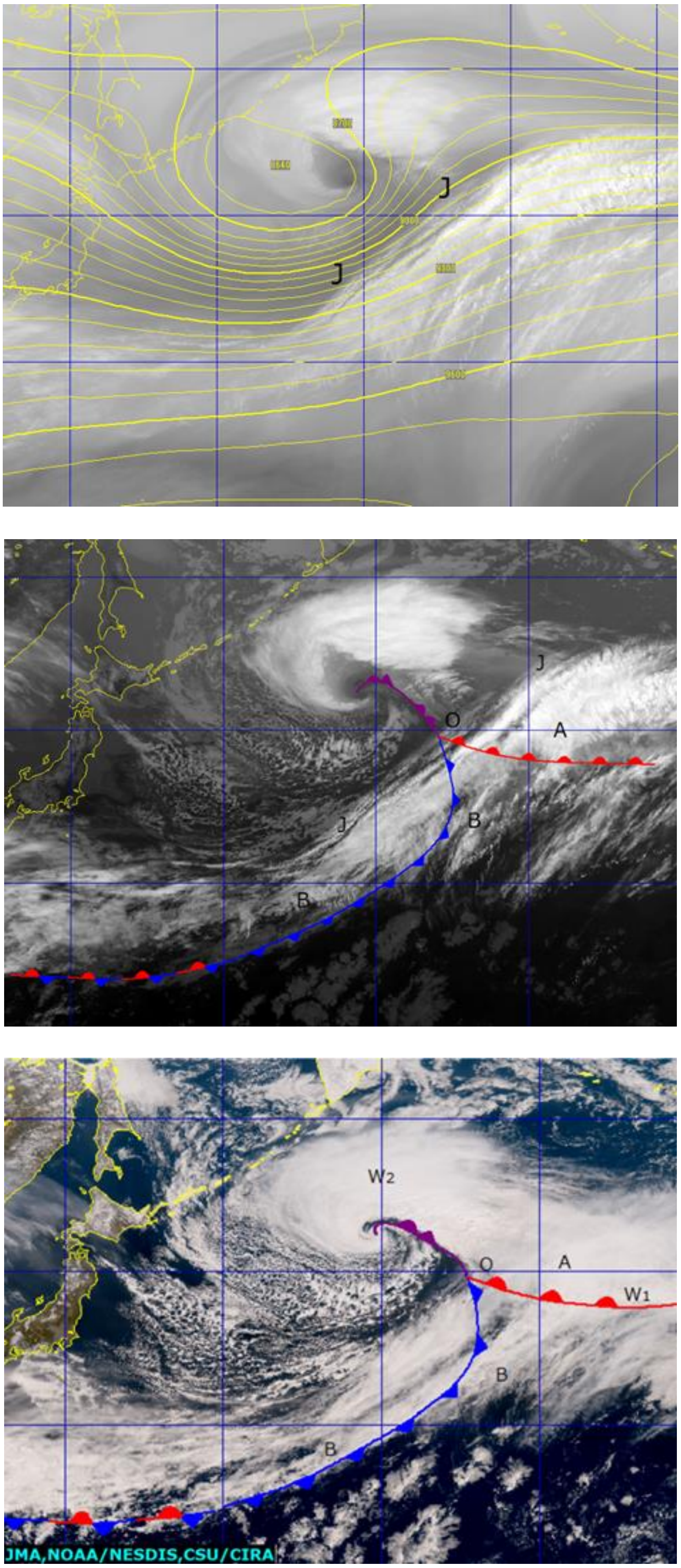

Fig. 5-1-14. Occlusion front at 00:00 UTC on 12 April 2016

Top: B10 water vapor image with 300-hPa isohypse; middle: B13 infrared image; bottom: True Color Reproduction image (see the main text for alphabetical designations)

5.1.4.2. Cold Occlusions

Cold occlusions often accompany developing cyclones ahead of a trough with intense cold air descending southward from the polar side. Characteristics of cold occlusions in satellite imagery include formation of comma-form clouds with latitudinal extension, weak warm fronts despite obvious cloud bands corresponding to cold fronts, cell-form or streaky convective clouds to the rear of a cyclone associated with intense cold air, and clear dry slots. However, the structure of warm fronts remains largely unclear; with obscure CCB conditions, occlusion point identification is challenging.

The cyclone around Sakhalin in Fig. 5-1-15 can be identified as a cold occlusion due to characteristics such as comma-shaped clouds, the streaky cloud area **B** at the rear of the cyclone in association with cold air, and a dry slot intertwining with the center. A jet axis is present along the boundary **J-J** in the water vapor image. Although warm fronts are hard to determine with minimal low-cloud scatter, such a front can be identified here from cell-form cloud area movement (around **W-W**) corresponding to the current around the anticyclone edge.

In this example, the cell-form cloud associated with the warm area heads northward, and northwestward around W-W. The cold front corresponds to the cloud band **C-C**. An occlusion point **O** is seen around the intersection of the cold frontal cloud band **C-C** and the warm frontal low cloud line **W-W**, and around the intersection of **J-J** for the upper strong-wind axis and **W-W**. Upper dry air forming a dry slot (seen as a dark area in the water vapor image) passes north of the occlusion point and is engulfed into the cyclonic center. Here, the dry slot overtakes the occlusion point, moving farther northward.

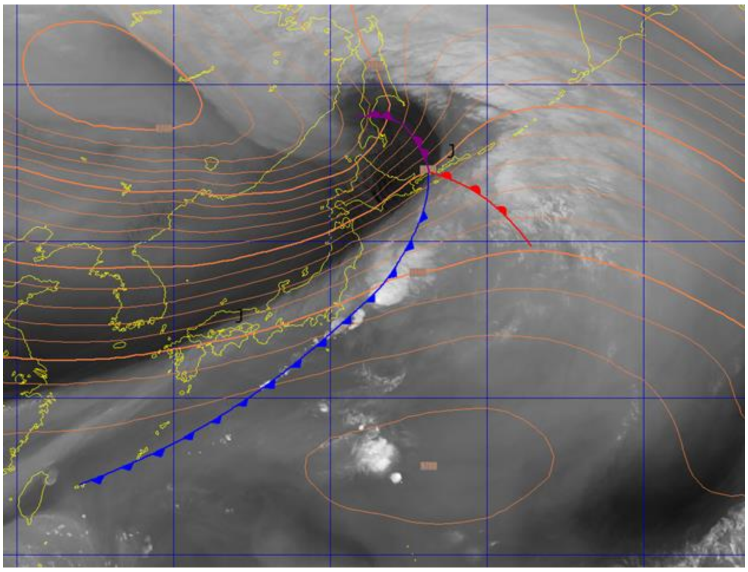

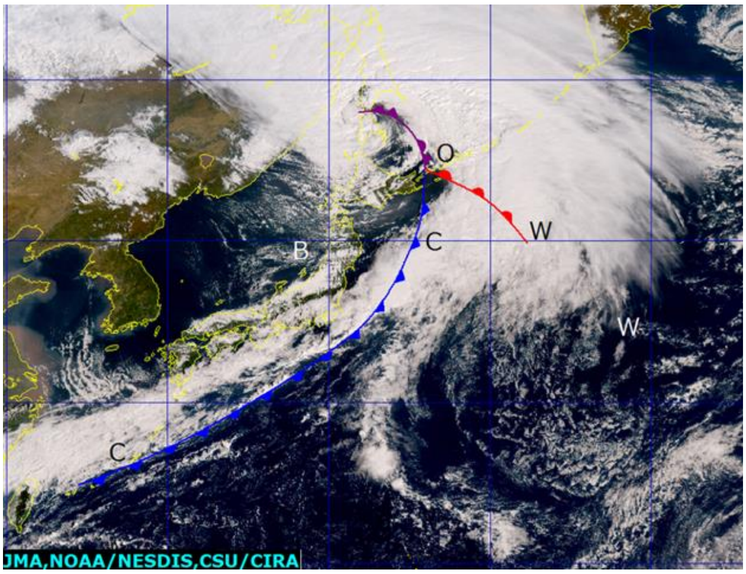

Fig. 5-1-15. A cold occlusion at 00:00 UTC on 2 October 2015
Top: B10 water vapor image, 300-hPa isohypse; bottom: True Color Reproduction image (see the main text for alphabetical designations)

5.1.4.3. Warm Occlusions

Warm occlusions correspond to inflow of weak cold air from the rear of cyclones. In satellite imagery, visible characteristics include λ-shaped or T-shaped cloud formations with a longitudinal strike, more distinct cloud bands corresponding to warm fronts than with cold occlusion, frequent obscuring of dry slots, and cell-form clouds accompanying cold air appearing obscure with limited extension at the rear of cyclones. Cold fronts can be either active or inactive. These characteristics contrast with those of cold occlusions, indicating the absence of intense cold-air inflow.

The cyclone to the east of Japan in Fig. 5-1-16 appears as a warm occlusion based on a λ form cloud pattern and unseen cell-form clouds with a clear area at the rear of the cyclone. In the water vapor image, a jet axis is seen along the boundary **J-J.** An occlusion point is observed at the intersection of the jet axis and a cloud band extending from northwest to southeast. The occlusion front extends to the occlusion point along the southern edge of a cloud band running from the cyclonic center **L**. A cloud area corresponding to a warm front is seen at **W-W**, with a stationary front to the east of the extension corresponding to the air mass boundary. The convective cloud line **C-C** corresponding to a cold front is clearly visible, albeit with weak activity.

The boundary corresponding to the jet here was relatively distinct, but the boundaries in the warm occlusion tended to be obscure. Occlusion points are also determined from the intersection of the cold and warm fronts.

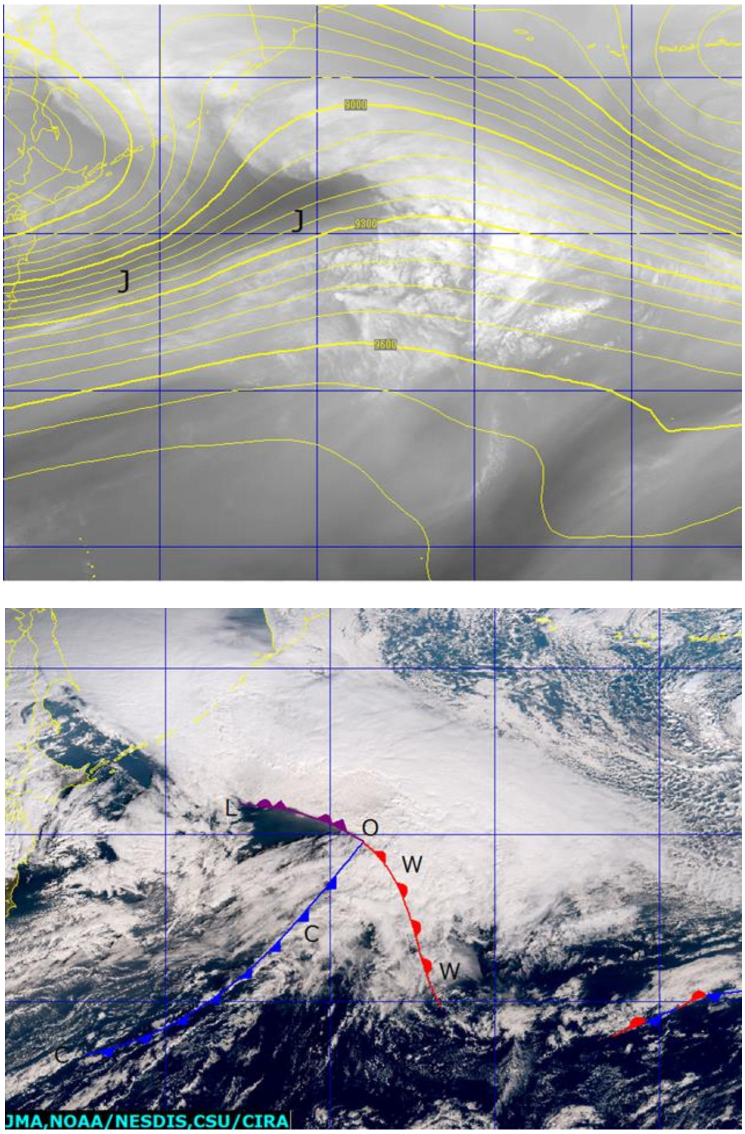

Fig. 5-1-16. An warm occlusion at 00:00 UTC on 4 December 2015
Top: B10 water vapor image, 300-hPa isohypse; bottom: True Color Reproduction image (see the main text for alphabetical designations)

5.1.5. Stationary Fronts

Movement perpendicular to the extension axis is limited in stationary fronts, and such forms are recognized as cloud bands stretching several thousand kilometers in satellite imagery. Mesoscale cyclones and frontal kinks in such fronts appear as active convective cloud band forms or cloud areas extending to the polar side with anticyclonic curvature on the northern edge.

Stationary fronts during cold periods frequently form long wide cloud bands, often with limited convective activity. Conversely, those during warm periods tend to be accompanied by active convective clouds along an inflow of warm wet air from the south, typically associated with the Baiu rain front and the autumn rain front.

5.1.5.1. Stationary Fronts during Cold Periods

During cold periods, stationary fronts often exhibit cloud bands connecting to a cold front extending from a developed cyclone. Such forms run parallel to the upper jet axis, presenting as long cloud bands with widths of 500 – 1,000 km and lengths of several thousand kilometers. These mainly consist of upper and middle clouds, with limited activity except at the southern edge. Stationary fronts on the ground are seen at the southern edge of cloud bands at 5 – 10° south latitude from the upper jet axis corresponding to the northern edge of the cloud band.

Figure 5-1-17 shows a stationary front during a cold period. Far east of Japan, a cold front accompanying a cyclone connected with a stationary front extends farther to the south of Okinawa. In B10 water vapor images, the dark area **B-B** corresponding to the upper jet stream is parallel to a cloud band at its northern edge. This band, with a 500 – 800 km width, consists mainly of upper and middle clouds and has no active convective clouds. Rain (0 – 1 mm per hour) was observed from stratiform clouds in the band over Okinawa. A stationary front is observed at the southern edge of the band. In surface observation, no notable change was seen for wind and temperature across the cloud band. The surface front was positioned at 7° south latitude from the jet axis. The gradient of the frontal surface was under 1/100, which was slightly steeper than a typical warm frontal surface (analysis by section at 35 degrees indicates a frontal surface gradient of 4.5 x 500 km).

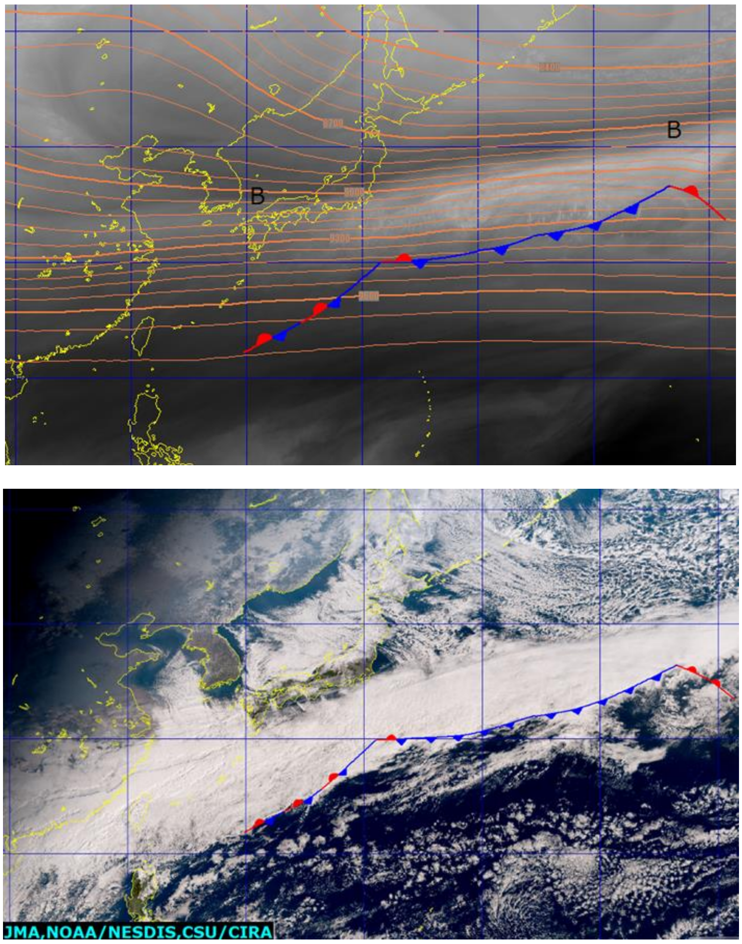

Fig. 5-1-17. A stationary front during a cold period at 00:00 UTC on 2 February 2016 Top: B10 water vapor image with 300-hPa isohypse; bottom: True Color Reproduction image (see the main text for alphabetical designations)

5.1.5.2. Stationary Fronts during Warm Periods

The Baiu rain front is a typical stationary formation that emerges around Japan during warm periods. It characteristically shows water vapor content with a larger gradient than that of temperature. It is narrower than stationary fronts observed during cold periods, appearing as a band mostly of convective clouds.

Figure 5-1-18 shows a Baiu front with a 100-km-wide cloud band, mostly consisting of middle and lower layers with active convection, extending from China to the area east of Japan. The Baiu front may be located at a position where convective clouds are aligned. It does not have a large temperature gradient and does not correspond closely to the upper strong wind axis. In the water vapor imagery, a dark region corresponding to a Pacific high is seen over southern Japan and around the Korean Peninsula across a bright region in a long thin belt form corresponding to the Baiu front. The dark region **N** to the north is a dry area formed by subsidence associated with anticyclonic conditions in the mid-latitudes. The dark region **S** to the south corresponds to the Pacific high.

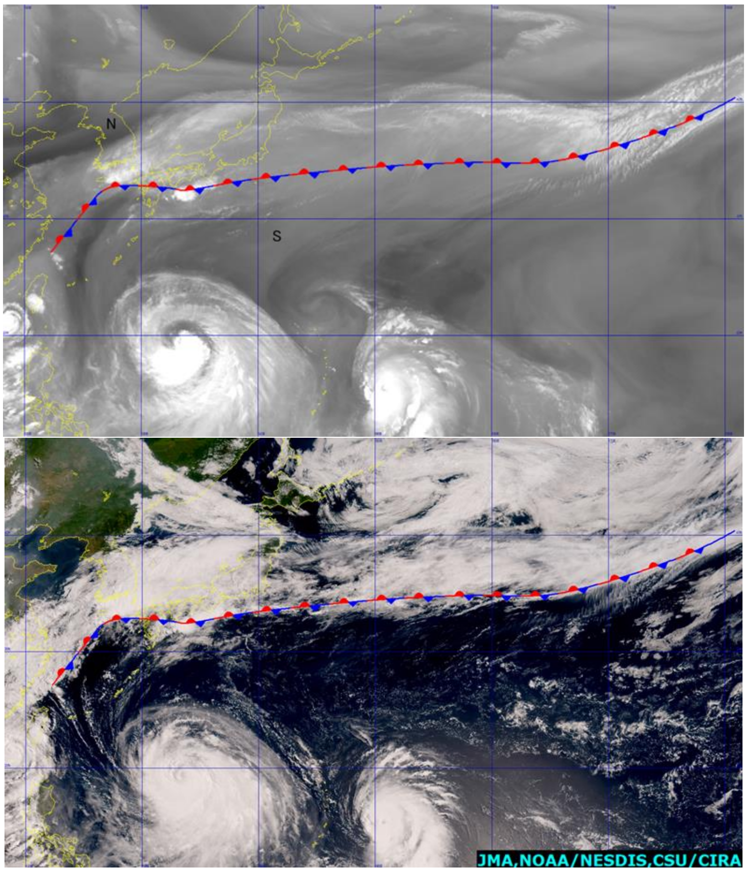

JMA,NOAA/NESDIS,CSU/CIRA

Fig. 5-1-18. Baiu front at 00:00 UTC on 8 July 2015
Top: B10 water vapor image, 300-hPa isohypse; bottom: True Color Reproduction image (see the main text for alphabetical designations)

5.2. Classification of Cyclonic Development Patterns

The Bergen School Cyclone Model proposed by J. Bjerknes and Solberg in the 1920s remains the most common representation of cyclone system lifespans. Based mostly on surface observation data and resulting insights, it comprehensively expresses the concepts of cyclogenesis from frontal waves in the mid-latitudes onward. As is evident from satellite observation of cyclogenesis, the model supports ready recognition of cloud patterns. The cloud model of these types is regarded here as standard.

Observation of cyclone lifespans in satellite imagery also reveals patterns other than the standard type (Fig. 5-2-1). Accordingly, developmental patterns not covered by the Bjerknes model are separately characterized for satellite imagery. Specifically, these are comma-type and instant occlusion-type phenomena occurring poleward from the mid-latitude baroclinic zone. Comma-type cyclones develop until comma-shaped cloud areas come into contact with a mid-latitude frontal zone after descending southward from the polar side of a baroclinic area. In instant occlusions, a rapid shift toward an occlusion pattern is seen as frontal cloud bands merge with such comma-shaped areas. Shapiro and Keyser (1990) presented a developmental model for T-bone-shaped cloud patterns as a type of cyclone developing in baroclinic zones. Here, the structure around the cyclonic center is governed by the detachment mechanisms of fronts and warm nuclear isolation, representing cloud areas different from those of the Bjerknes model.

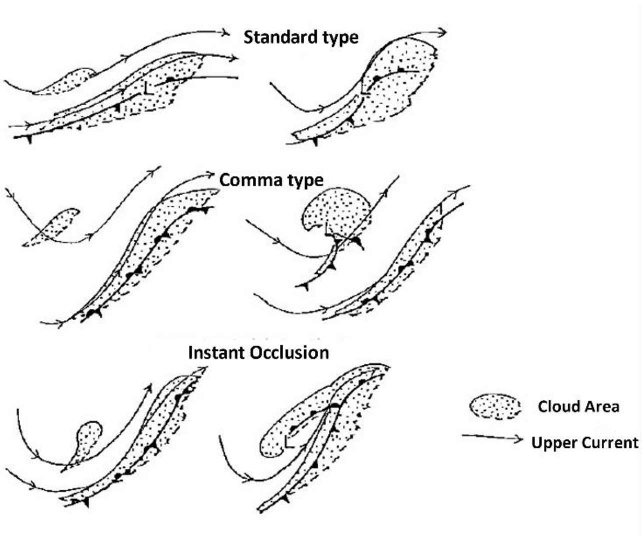

Fig. 5-2-1. Standard, comma and instant occlusion models

This chapter outlines the characteristics of each cloud pattern in the context of synoptic-scale cyclonic development. Various forms of cyclogenesis recognizable in satellite imagery outside the scope of the Bjerknes model are also presented, as these models were developed in relation to Western areas and cyclonic behavior around Japan may differ due to greater sub-tropical influence in the relevant lower latitudes.

The terms “development stage” and “mature stage” here are judged from satellite imagery, and may not match the cyclogenesis stages seen in weather charts. The mature stage in satellite imagery is considered to be reached slightly earlier than the lowest cyclonic pressure period. In frontal drawing too, analysis is focused on satellite imagery, and may not necessarily match that derived from weather charts.

5.2.1. Standard-type Development

As reported by Yamada and Suzuki (1994), the standard type represents approximately a third of cyclones rapidly developing over the sea east of Japan in winter, typically taking three days after emergence to reach maturity. In satellite imagery, the characteristics seen in the formative and development stages are cloud area formation and northward ascent associated with warm advection at the front of the cyclone, with cloud areas dissipating and descending southward in association with dry cold inflow at the rear of the cyclone. These characteristics represent the development of baroclinic instability via frontal waves, as readily highlighted by the Bjerknes model.

Okabayashi (1982) proposed a cyclogenesis cloud model based on the Bjerknes model (Fig. 5-2-2) as represented in the standard-type example shown below. Temporal changes in cyclonic central pressure here are illustrated in Fig. 5-2-3. The formative and development stages correspond to the development stage in the example.

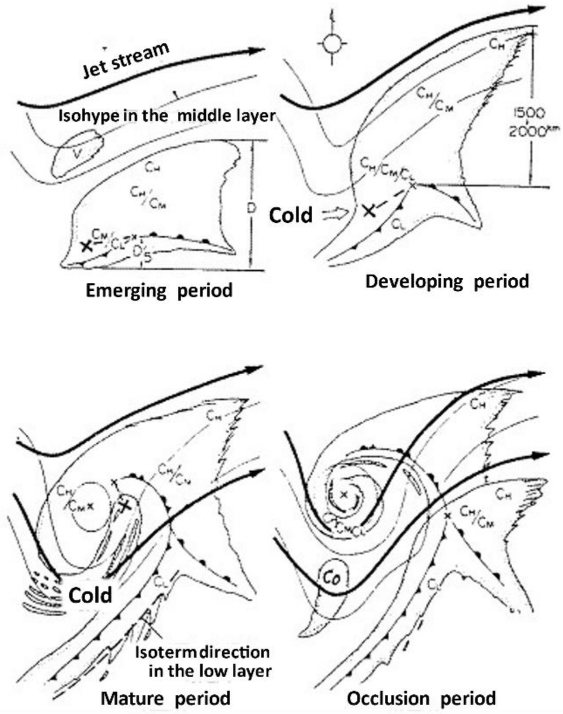

Fig. 5-2-2. Cyclone model (Okabayashi, 1982)

X represents the cyclonic center, **x-x** is the area encompassing the center, and **CH**, **CM** and **CL** represent upper, middle and lower clouds, respectively.

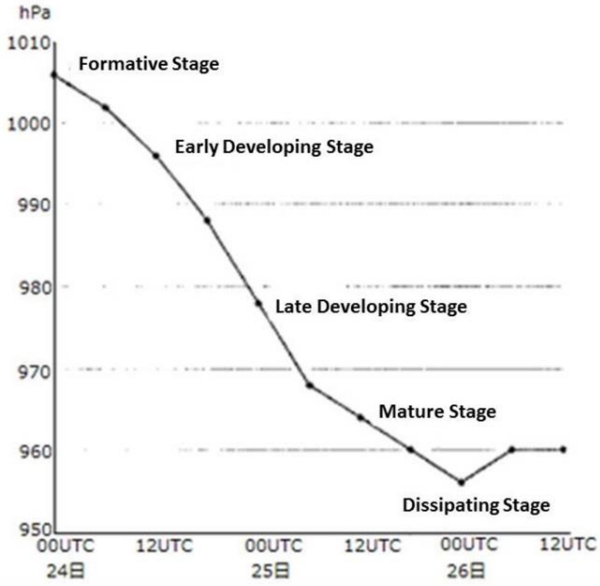

Fig. 5-2-3. Temporal changes in cyclonic central pressure

1. Formative Stage (Fig. 5-2-4)

In the early stages of baroclinic-zone disturbances, a cloud pattern with an S-shaped edge (known as a cloud leaf or baroclinic leaf form) appears, as sometimes observed between the East China Sea and the Sea of Japan. This morphology is associated with warm conveyor belt (WCB) wet currents, indicating a strengthening of warm advection.

Cyclone centers in the formative stage are hard to identify from cloud patterns, tending to be positioned near the center or around the southern edge of the cloud area. In this example, the cyclone and the front are considered to be in this stage. In the Okabayashi model, the northern edge of the cloud area and the jet stream appear separate but generally in proximity. The jet stream also corresponds to the northern edge of the cloud leaf, based on the analysis position of the boundary and the northern edge of the cloud leaf as clearly seen in the water vapor image.

In the Okabayashi-model formative stage, the area V comprising mostly upper cloud appears to head northwestward toward a cyclonic cloud area. Although not seen here, it should be noted that the cloud area often corresponds to an upper trough, potentially reaching the cyclonic cloud area and exacerbating development.

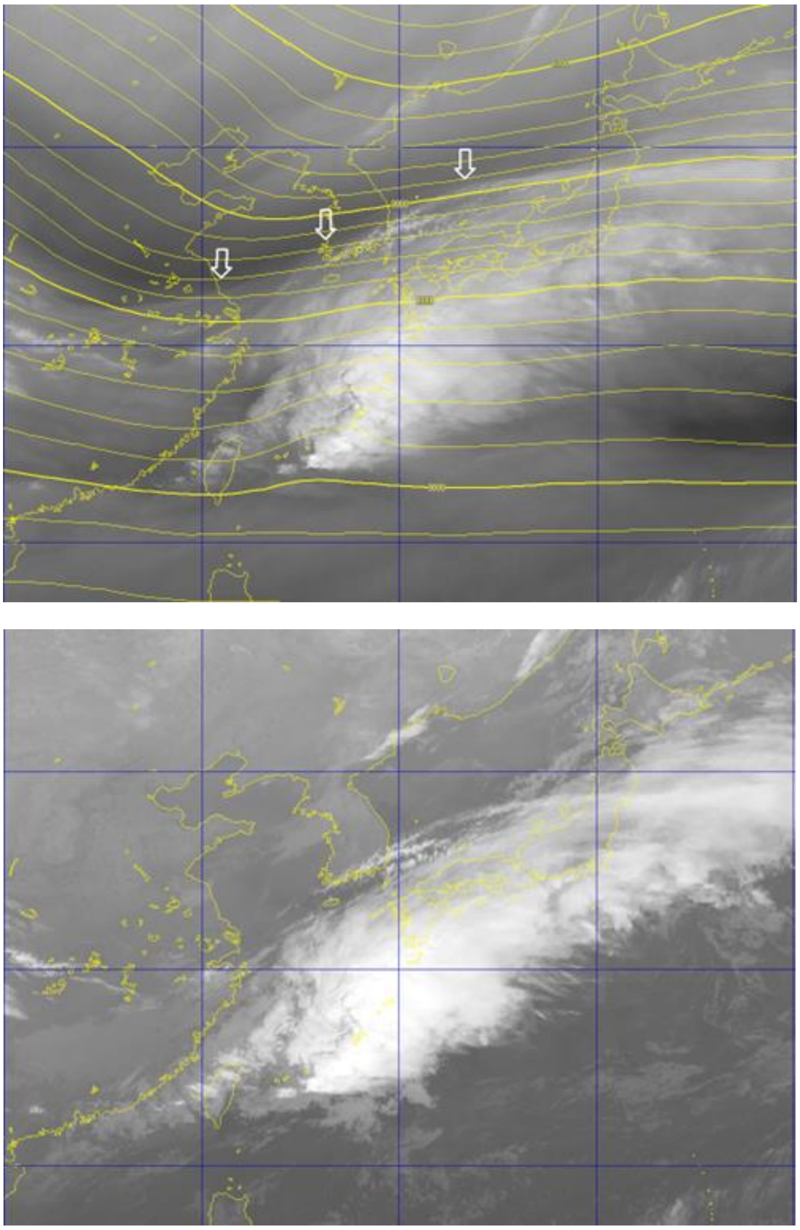

Fig. 5-2-4. Standard type, formative stage, at 18:00 UTC on 13 March 2016

Top: B10 water vapor image with 300-hPa isohypse and arrows marking the boundary; bottom: B13 infrared image

2. Early Development Stage (Fig. 5-2-5)

Bulge patterns in the early development stage with increased anticyclonic curvature at the northern edge of a cloud area expanding northward from a cloud leaf indicate the presence of warm air ascending northward in association with WCB conditions or ascending currents intensifying at the front of a trough. This is a characteristic of the development stage in baroclinic disturbances. The boundary in water vapor imagery corresponding to the upper strong wind axis reveals trough deepening farther southward after formation.

Cyclone centers can often be identified near the start point at the western edge of a bulge as it shifts westward from its center in the formative stage, while identification from cloud patterns is difficult. Similarly, warm and cold fronts in the formative stage are determinable southward of lower clouds. This stage corresponds to the intermediate state between the formative and the development stages in the Okabayashi model.

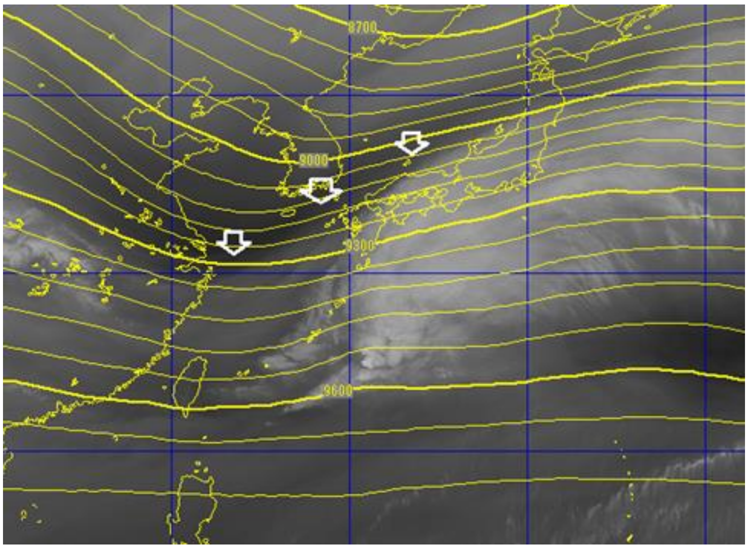

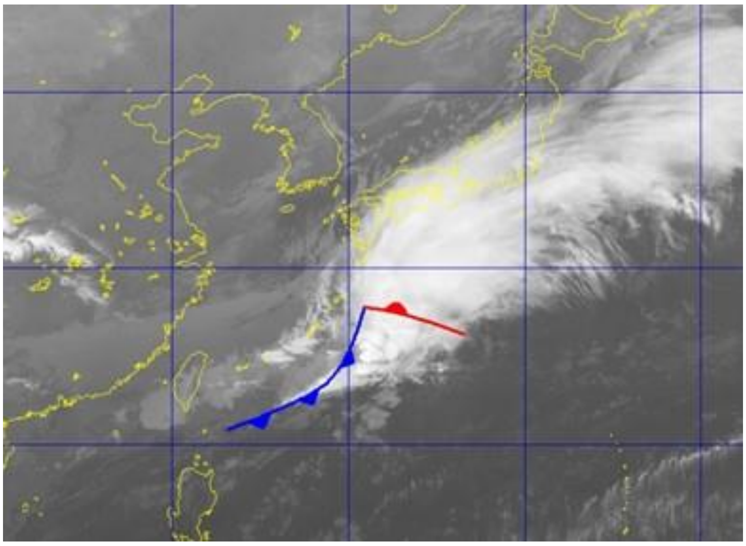

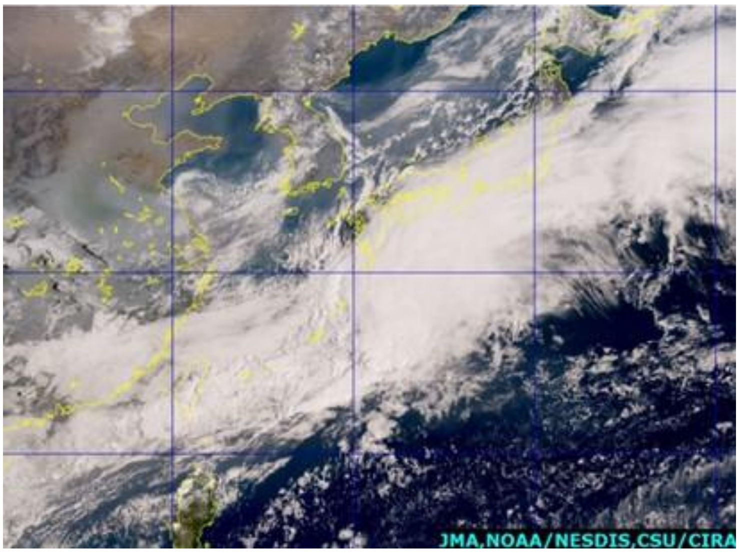

Fig. 5-2-5. Standard type in the early development stage at 00:00 UTC on 14 March 2016
Top: B10 water vapor image with 300-hPa isohypse and arrows marking the boundary;
middle: B13 infrared image: bottom: True Color Reproduction image

3. Late Development Stage (Fig. 5-2-6)

This is equivalent to the development stage in the Okabayashi model. Bulges are clearer, with streaky cloud at the rear of the cyclone indicating an inflow of cold air that forms a hook pattern. The cloud area has a meridional strike extending farther than in the early development stage. The meridional elongation of this area corresponds to the strengthened effects of cold advection at the rear of the cyclone and warm advection at its front.

The Okabayashi model poses the potential for association between the cyclonic center and the center of the cloud area at this stage. However, in this example, the center of the cyclone is farther west in the cloud area than in the early development stage, and a hook is observed at the western edge of the cloud. A cloud band is also prominent in correspondence to the cold front in association with cold inflow.

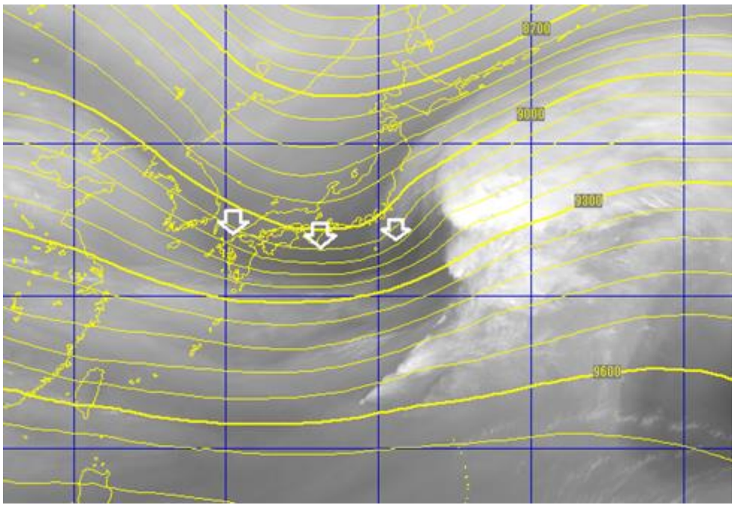

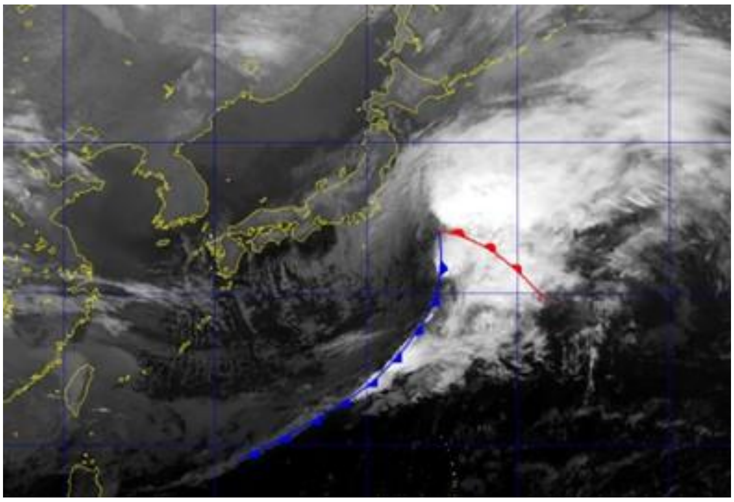

Fig. 5-2-6. Standard type, late development stage, at 18:00 UTC on 14 March 2016
Top: B10 water vapor image with 300-hPa isohypse and arrows marking the boundary;

bottom: B13 infrared image

4. Mature Stage (Fig. 5-2-7)

This is equivalent to the mature stage in the Okabayashi model, with a comma-type cloud pattern forming as a dry-air slot intrudes into the vicinity of the center. In satellite imagery, the cloud edge is distinct with a high top, and is determinable as the most developed stage. Central cyclonic pressure continues to fall, although the minimum pressure is not yet reached. Streaky cloud at the rear of the cyclone indicates intense cold-air intrusion.

The cyclone center can be determined from a lower vortex near a dry slot, with the occluded front at the western edge of a cloud area in contact with the boundary of this slot. In water vapor imagery, this is seen as a progressive darkening of a region downstream of the boundary, implying intrusion of dry air from the upper layer to the rear of the developed cyclone. Here, the occluded front is not above the cloud top on the western edge, but is farther rearward in the lower cloud area. Such patterns may arise when a dry slot surpasses a surface occluded front.

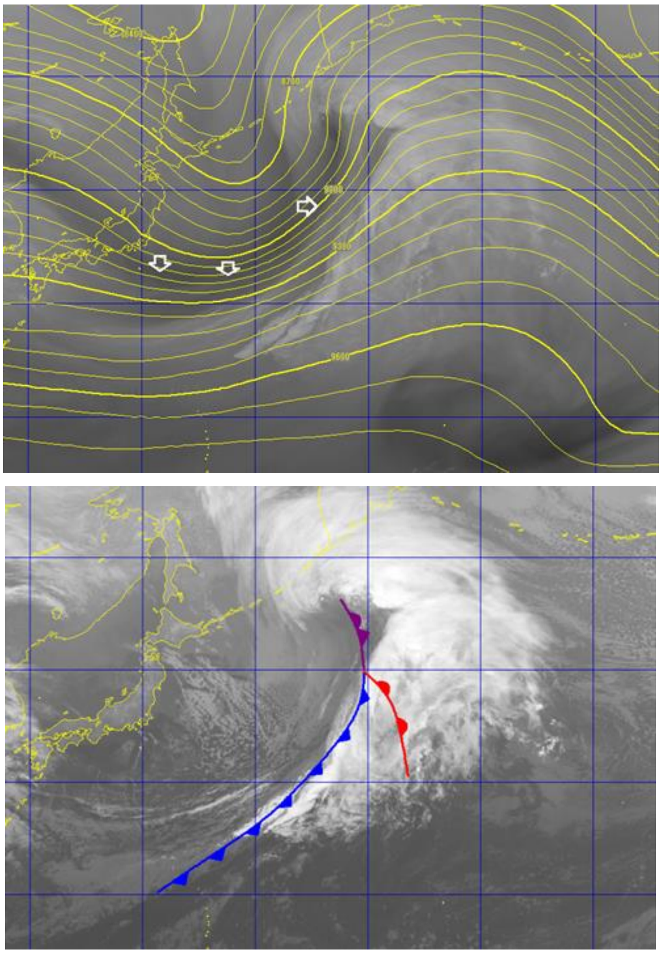

Fig. 5-2-7. Standard type, mature stage, at 12:00 UTC on 15 March 2016
Top: B10 water vapor image with 300-hPa isohypse and arrows marking the boundary;
bottom: B13 infrared image

5. Dissipation Stage (Fig. 5-2-8)

This corresponds to the occlusion stage in the Okazaki model. At the cyclonic center, convective activity decreases with lowering of the cloud top, and a lower vortex emerges. In response to cold air associated with a short-wave trough blowing from the rear of the cyclone, enhanced Cu (**E**) is seen (equivalent to the Co cloud area in the Okazaki model), and may further develop into comma cloud forms. A higher cloud-top region with active convection is seen in the vicinity of the occlusion point. The dry slot, which surpasses the surface occluded point at the mature stage, moves parallel again to this front with entwined motion around the cyclonic center.

The cloud top is lowered overall, featuring a looser edge with lower clarity as dissipation progresses. Characteristics seen in the dissipation stage include a lowering of the cloud top, particularly around the cyclonic center, and termination of darkening at the dry slot along with enhancement of the bright region. The lowest period of cyclonic central pressure in the cyclonic lifecycle is often observed after the beginning of dissipation recognizable in satellite imagery.

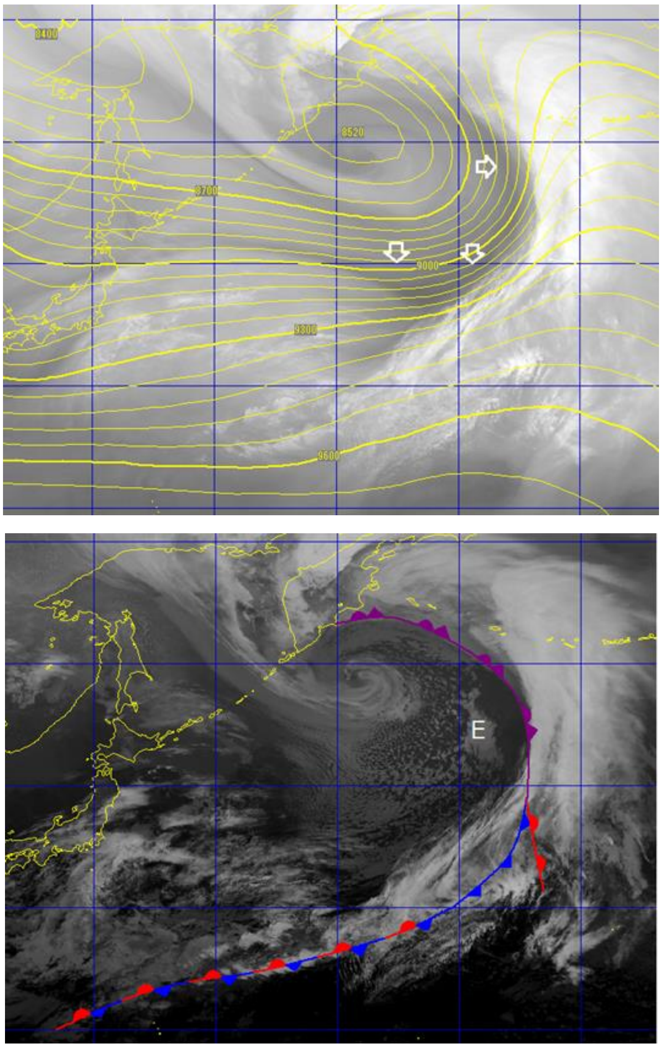

Fig. 5-2-8. Standard type, mature stage, at 12:00 UTC on 16 March 2016

Top: B10 water vapor image with 300-hPa isohypse and arrows marking the boundary;

bottom: B13 infrared image

5.2.2. Comma-type Development

Comma clouds form on the polar side of mid-latitude baroclinic zones, often during cold periods. Cyclonic conditions corresponding to comma clouds are known as polar lows, which differ from the standard type in development. Comma-cloud formation requires an updraft from positive vorticity advection in the middle layer, along with sensible and latent heat from a warm sea surface. Such clouds may emerge on a small scale in regions with weak baroclinicity, but baroclinic instability is also required for synoptic-scale cyclonic development as described below.

Reed and Blier (1986; Fig. 5-2-9) presented a comma-type cloud development model in which convective clouds emerge near positive vorticity advection during the formative stage but no structural organization is yet apparent. In the development stage, comma-type clouds form in cyclonic conditions observable at the top of the comma. Warm advection is initiated in front of the cloud area, and cold advection intensifies at its rear. During the mature stage, clouds move ahead of a long wave trough, and the tail segment acquires cold-front characteristics.

Comma clouds developing over seas east of Japan and elsewhere emerge in cold air away from major baroclinic zones. At the beginning of the formative stage, the cloud area comprises an open cell corresponding to a short-wave trough or enhanced Cu. This indicates the key roles of sensible and latent heat from the sea surface in development. The cloud area takes on comma-type characteristics as it moves to the front of the main trough.

Over the warm Sea of Japan, comma clouds tend to develop rapidly when dry air moves in from the continental area, where formation is less likely even in positive vorticity advection fields. Suzuki and Yamada (1994) reported that comma clouds take around 12 hours less to reach maturity from the formative stage than the standard type.

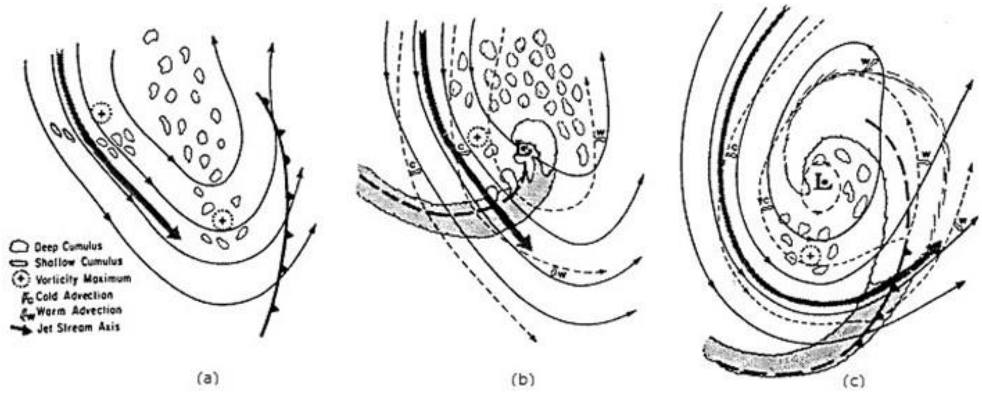

Fig. 5-2-9. Comma-cloud model (Reed and Blier, 1986)
(a) Formative stage (b) Development stage (C) Mature stage
(solid lines: 500 hPa isohypse; dashed lines: isobars above ground)

(1) Sea-area Comma Clouds

1. Formative Stage (Fig. 5-2-10)

The cloud area (B) over the Bering Sea in the figure corresponds to a well-developed cyclone, behind which cell-form convective clouds associated with cold-air advection are observed. Over the Sea of Okhotsk and the sea southeast of Kamchatka, active cell-form convective clouds are seen with an open structure in association with the cold air. The solid area **A** with upper clouds also begins to develop, representing the emergence of an as-yet unrecognizable comma cloud formation.

This area forms in association with maximum positive vorticity advection (PVAmax) in front of a short-wave trough intruding at the rear of a cold low east of Kamchatka. Cloud density at this stage is uneven, with no anticyclonic curvature at the cloud edge. The area **A** does not appear organized at this pre-cyclonic stage.

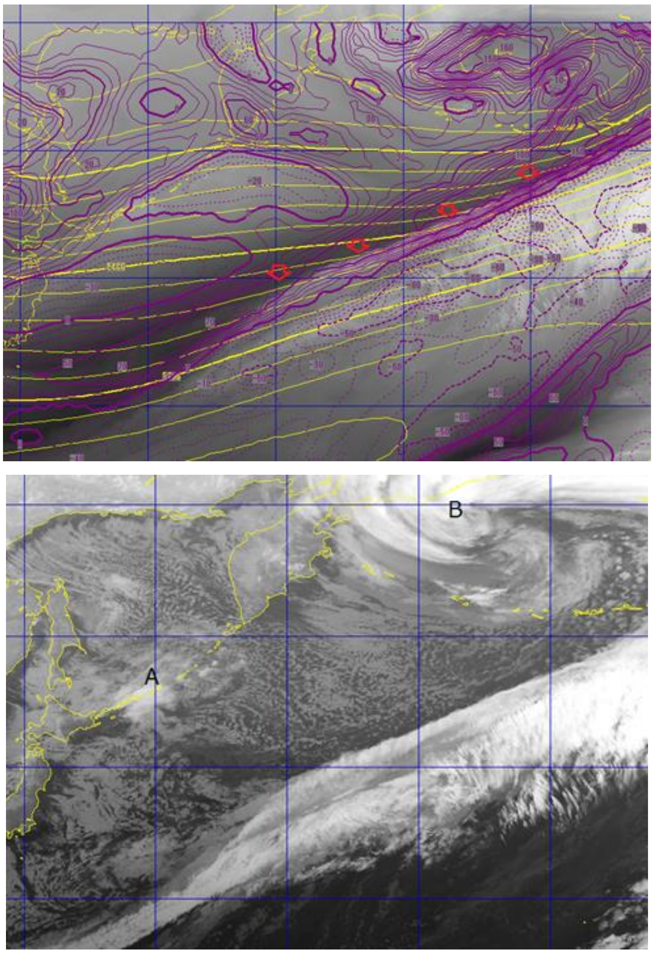

Fig. 5-2-10. Comma cloud over the sea, formative stage, at 12:00 UTC on 18 December 2015. Top: B10 water vapor image with 500-hPa isohypse and vorticity (solid line: positive; dashed line: negative); bottom: B13 infrared image with arrows marking the boundary

2. Early Development Stage (Fig. 5-2-11)

The cloud area **A** here increases both in density and top height. At its northern edge, upper cloud shows comma-shaped anticyclonic curvature. The enhanced Cu (**E**) to the west of **A** indicates the presence of a cold-air core behind the cloud area (i.e., in front of a trough associated with this air). There are fewer cell-form clouds at the front of cloud area **G**, indicating cold-air weakening. The weaker cold at the front of this area (which may alternatively be warm advection) and the presence of intense cold air at the rear are as per the Reed and Blier model.

Based on those observations, cloud area **A** is considered to have assumed a baroclinic development process. At this stage, the area began to form a comma-type shape with cyclonic conditions at its southern edge.

PVAmax intensifies after the formative stage. The comma cloud area **A** to the north of the boundary corresponds to the jet stream, manifesting at the polar side of the mid-latitude frontal zone.

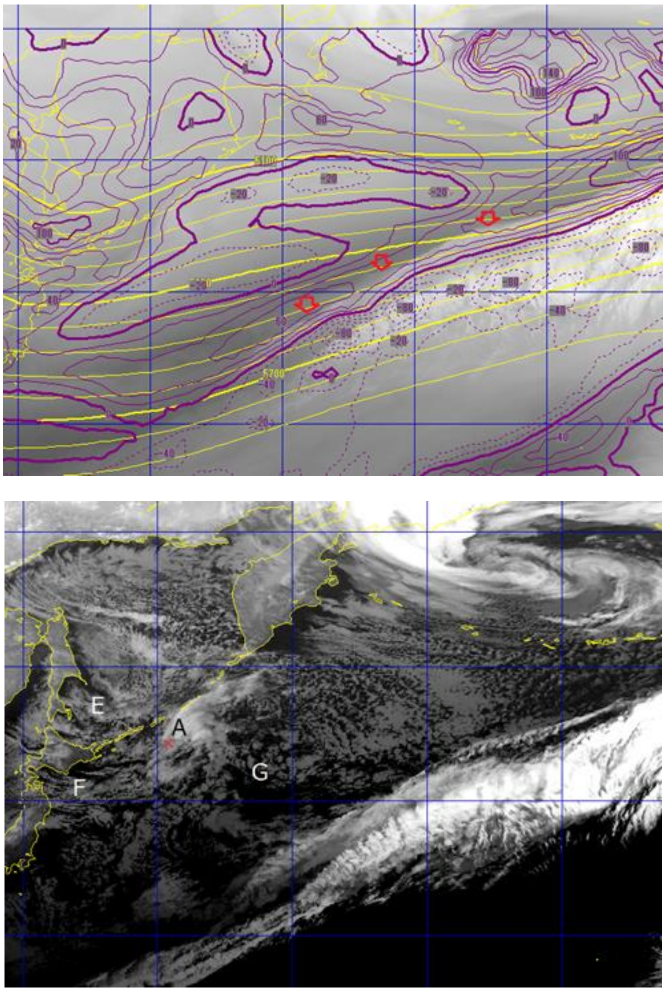

Fig. 5-2-11. Comma clouds over the sea, early development stage, at 18:00 UTC on 18 December 2015. Top: B10 water vapor image with 500-hPa isohypse and vorticity (solid line: positive; dashed line: negative); bottom: B13 infrared image

3. Late Development Stage (Fig. 5-2-12)

Anticyclonic curvature in this stage increases at the northern edge of the cloud area, creating a clearer overall comma shape with a head comprising tall clouds featuring a near-uniform top height, and a tail comprising active convective clouds. The comma shape represents an organized disturbance with PVA max values retained. The cloud line of the comma tail becomes distinct.

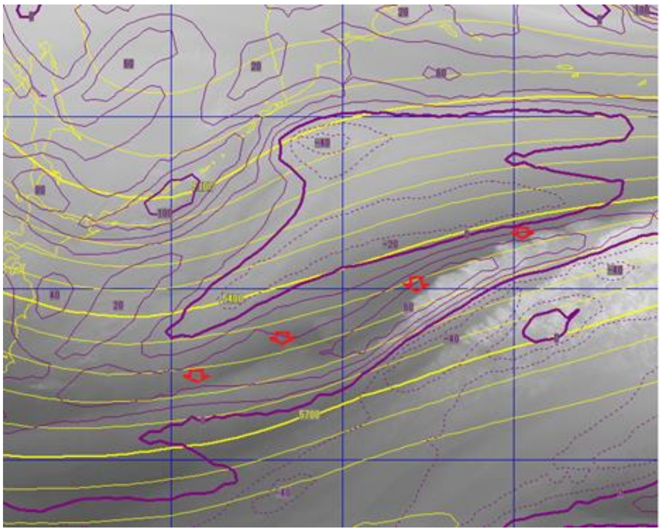

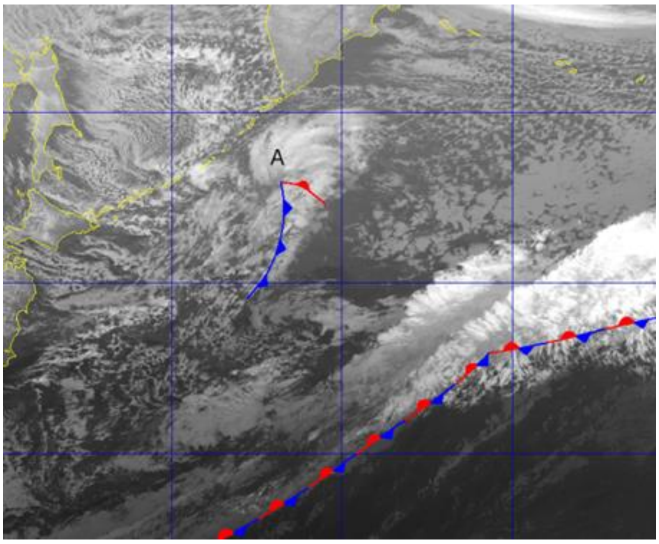

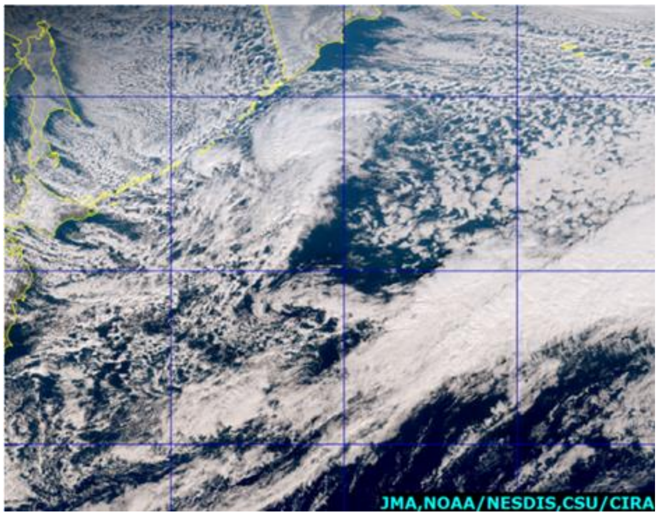
JMA,NOAA/NESDIS,CSU/CIRA

Fig. 5-2-12. Comma clouds developing over the sea, late development stage, at 00:00 UTC on 19 December 2015. Top: B10 water vapor image with 500 hPa isohypse and vorticity (solid line: positive; dashed line: negative) and arrows marking the boundary. Middle: B13 infrared image; bottom: True Color Reproduction image

4. Mature Stage (Fig. 5-2-13)

In the presence of a clear dry slot, the mature stage is reached here with the same pattern as the standard type. The cloud area measures 1,000 – 1,500 km, which is smaller than the standard type. In the figure, comma cloud development is seen in association with trough deepening around a cold low near the Kamchatka Peninsula. In contrast to the standard type, the boundary corresponding to the jet stream is still positioned south of the comma cloud. Comma-type development occurs rapidly between the initial identification of low ground pressure and maturity. It is recognized in satellite imagery as a solid cloud area before assuming cyclonic characterization.

Here, a cloud band corresponding to a stationary front is seen at 40° north latitude. Although the comma cloud and the cloud band are in close proximity, they develop individually and separately. When these areas reorganize a single mass via reciprocal influence, they are seen as an instant occlusion-type development.

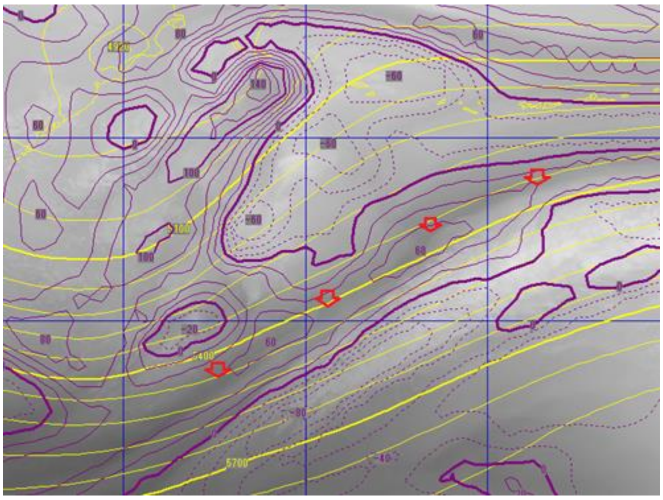

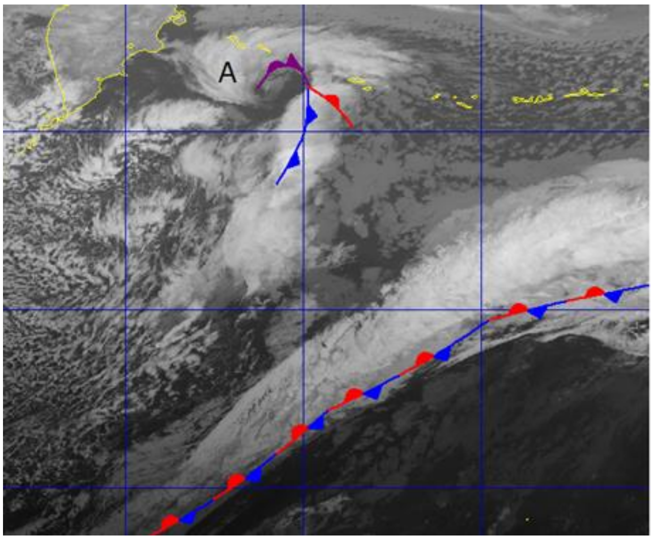

Fig. 5-2-13. Comma cloud development over the sea, mature stage, at 18:00 UTC on 19 December 2015. Top: B10 water vapor image with 500-hPa isohypse and vorticity (solid line: positive; dashed line: negative) and arrows marking the boundary.
Bottom: B13 infrared image

(2) Development of Comma Clouds Around Japan

1. Formative Stage (Fig. 5-2-14)

When the Ci area **A** approaches the Sea of Japan from the continent, the cloud area **B** containing convective clouds here rapidly develops into a Cb area over the western Sea of Japan. This Ci corresponds to an upper trough, and its movement can be tracked back to the continent. Convective clouds emerge rapidly, often taking 3 – 6 hours to develop into an organized area from a cloudless state around Japan (here, Cu moves eastward and convective cloud containing Cb (**B**) subsequently emerges 3 – 4 hours later around 15:00 UTC). The cloud area **B** is in front of a trough at 500 hPa, corresponding to an updraft based on PVAmax. As the convective cloud mass grows, it takes on an organized structure. At this point, a cyclone is identifiable in the vicinity of **x**.

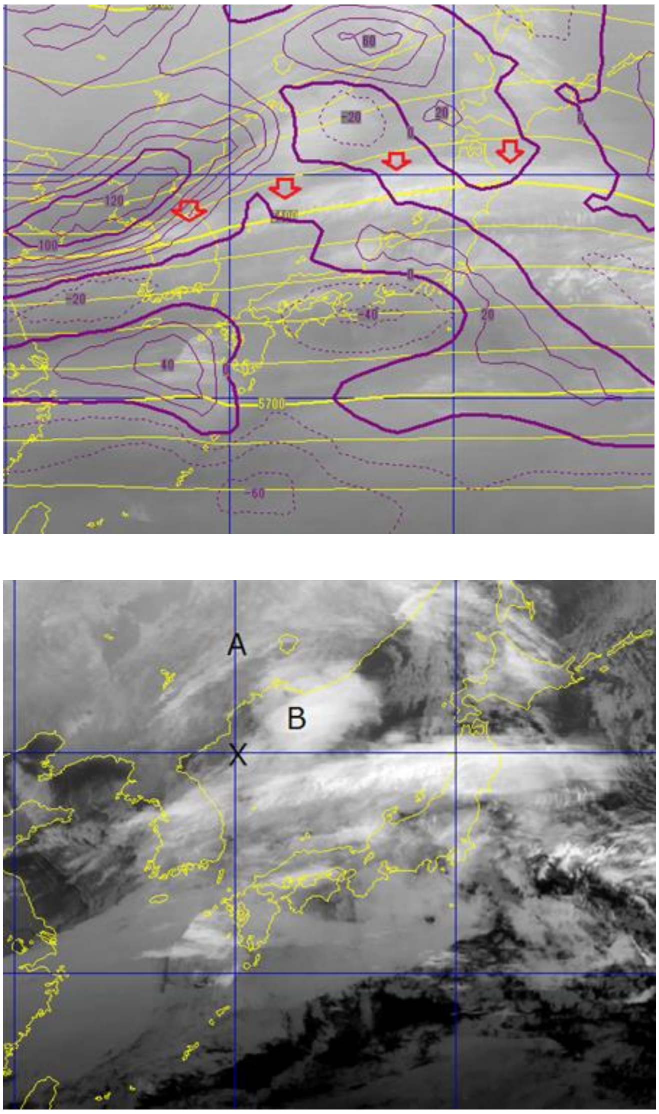

Fig. 5-2-14. Comma cloud development near Japan, formative stage, at 18:00 UTC on 15 December 2014. Top: B10 water vapor image with 500-hPa isohypse and vorticity (solid line: positive; dashed line: negative) and arrows marking the boundary.
Bottom: B13 infrared image

2. Development Stage (Fig. 5-2-15)

The cloud area here forms a comma shape with a distinct notch, an elevated top height and increased convective activity at its tail. A streaky cloud line emerges at its rear due to cold-air inflow, and the mass advances in front of the trough at 500 hPa maintaining corresponding to PVAmax.

As previously described, comma clouds near Japan characteristically develop more quickly after emergence than those developing over seas east of the country. This is attributed to cold air from the continent causing rapid instability over the warm Sea of Japan. At the comma tail, convective clouds rapidly develop to create a clear cold-front structure, raising the likelihood of phenomena such as rapid changes in wind direction, gusting winds and intense rainfall. Accordingly, satellite monitoring of these phenomena is essential.

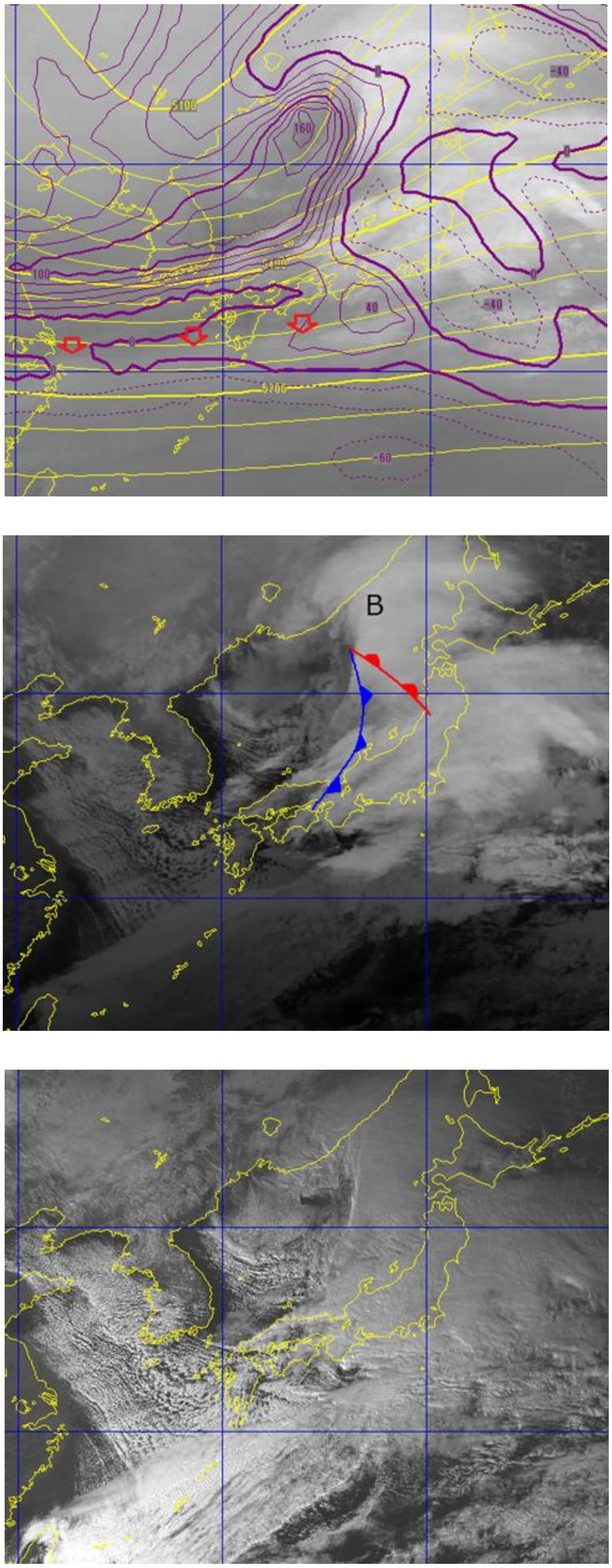

Fig. 5-2-15. Comma-cloud development near Japan, development stage, at 06:00 UTC on 16 December 2014. Top: B10 water vapor image with 500-hPa isohypse and vorticity (solid line:

positive; dashed line: negative) and arrows marking the boundary; middle: B13 infrared image; bottom: B03 visible image

3. Mature Stage (Fig. 5-2-16)

A dry slot is seen here over the sea west of Hokkaido. The cloud top is raised in the area corresponding to the comma head, indicating maturation. Comma clouds rapidly developing near Japan bring intense cold air along with streaky convective cloud at the rear of the cyclone, indicating further development. Subsequent development follows the pattern of comma clouds observed over the sea east of Japan.

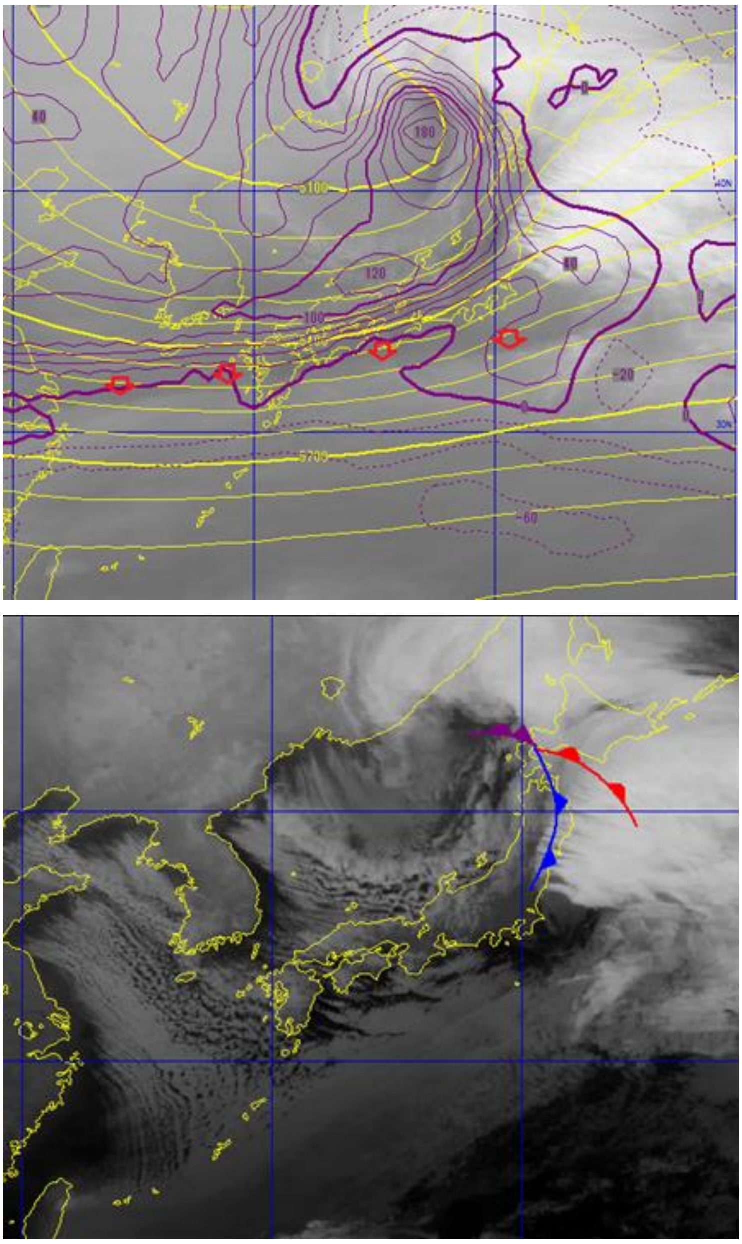

Fig. 5-2-16. Comma clouds near Japan, mature stage, at 12:00 UTC on 16 December 2014. Top: B10 water vapor image with 500-hPa isohypse and vorticity (solid line: positive; dashed line: negative) and arrows marking the boundary.
Bottom: B13 infrared image

5.2.3. Instant Occlusion-type Development

The instant-occlusion cyclone development process observed in satellite imagery indicates cloud patterns in the occluded stage resulting from comma clouds merging with a frontal cloud band. In contrast to the standard type, occluded-cloud patterns form instantly with no development stage. Figure 5-2-17 (Kitabatake, 1997) summarizes the two models proposed by Browning and Hills (1985; the BH model) and McGinnigle, Young and Bader (1988; the MYB model). The key feature of the BH model is a polar-trough conveyor belt (PTCB), which is a lower-level airflow moving poleward from a frontal cloud band. The baroclinicity of comma clouds is not seen as critical in this situation. In the MYB model, warm advection along comma clouds and updrafts associated with positive vorticity advection have critical roles, and an occlusion pattern is reached via the formation of new clouds between comma clouds and the frontal cloud band.

The MYB and BH models are more applicable to cases with and without cyclone development, respectively.

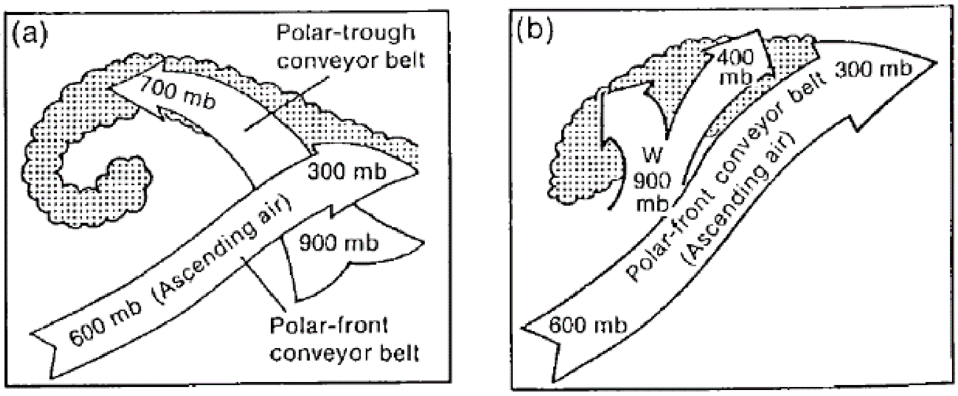

Fig. 5-2-17. Instant occlusion (Kitabatake, 1997)
(a): BH model; (b): MYB model

(1) No Further Cyclone Development (BH model)

1. Initial Stage (Fig. 5-2-18)

A cyclone corresponding to the comma-type cloud area **A** is seen east of Japan here, progressing east-northeastward. An area of upper- and middle-layer clouds **D** is observed in association with the front south of around 30° north latitude, with a southwest-northeast strike direction. The bulge observed takes on an anticyclonic curvature to the north of the cloud band upon approach.

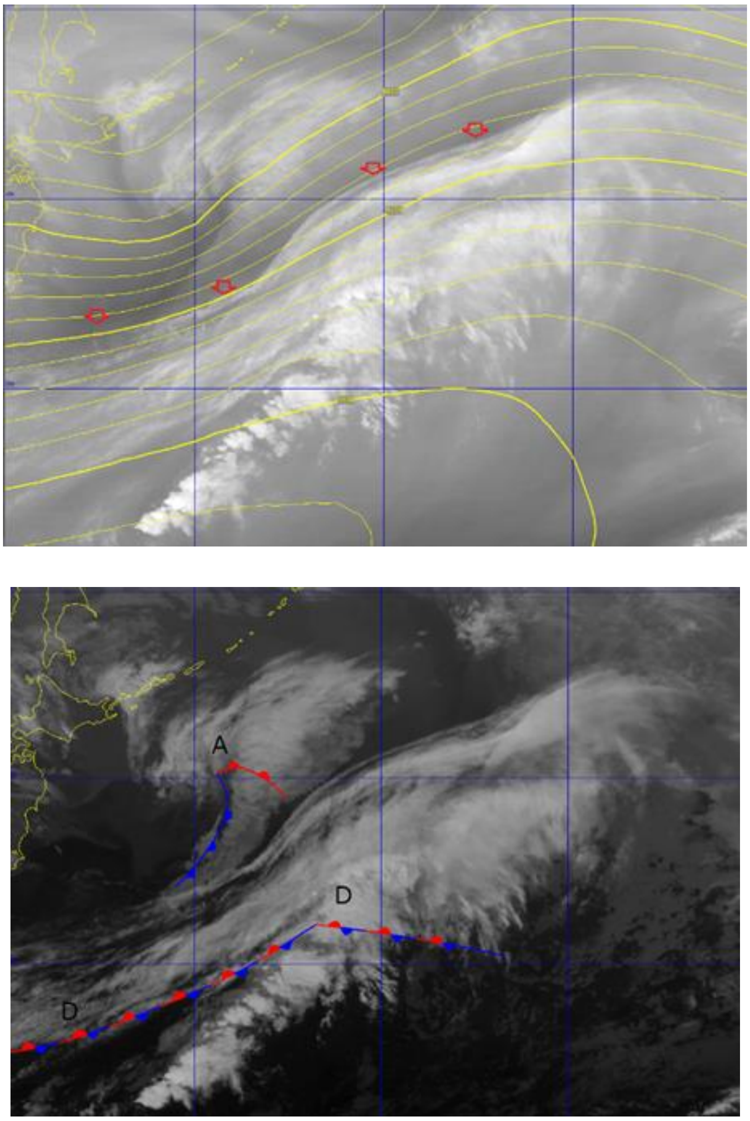

Fig. 5-2-18. Instant occlusion with no development (BH model), initial stage, at 18:00 UTC on 25 April 2011. Top: B10 water vapor image with 300-hPa isohypse and arrows marking the boundary; bottom: B13 infrared image

2. Occlusion Commencement Stage (Fig. 5-2-19)

The distance between the comma cloud **A** and the cloud band **D** here is reduced. Characteristics include a distinctive long tail with a raised top at the head of the comma cloud, increased density at the part of the band in contact with this cloud, and a heightened top in the cloud band. These characteristics represent synergetic effects between the comma and band clouds. However, the gap between the cloud band and the comma tail suggests the PTCB is insufficiently formed, and no occlusion pattern has yet developed.

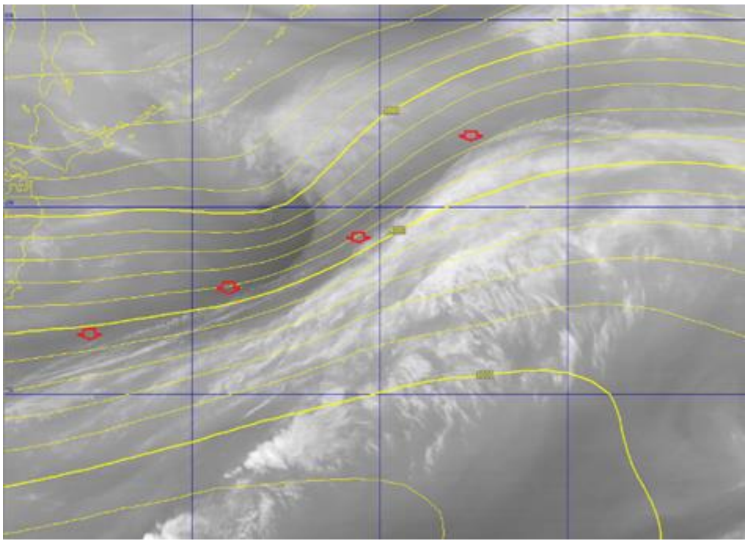

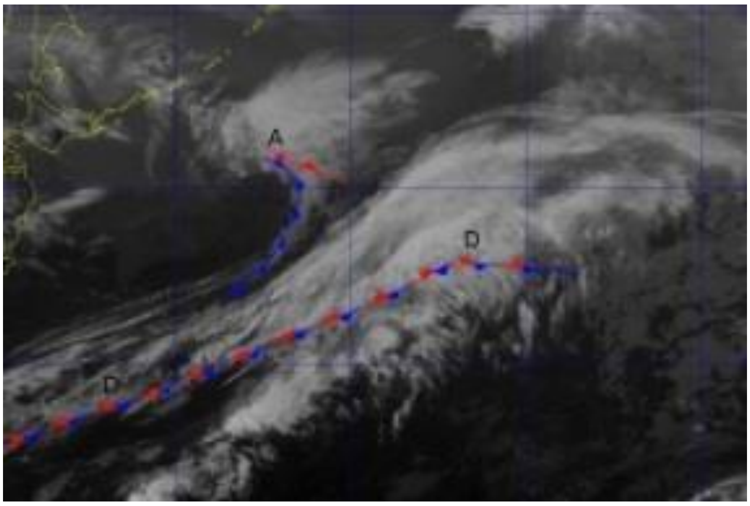

Fig. 5-2-19. Instant occlusion with no development (BH model), occlusion commencing, at 00:00 UTC on 26 April 2011. Top: B10 water vapor image with 300-hPa isohypse and arrows marking the boundary; bottom: B13 infrared image

3. Occlusion Completion Stage (Fig. 5-2-20)

The top height here is raised at the tail of the comma cloud **A** in contact with the cloud band **D**, forming an organized band with PTCB formation. In the cloud band corresponding to the frontal zone, the top rises rapidly at the part in contact with the comma cloud tail, with increased anticyclonic curvature at the northern edge. Completion of the instant occlusion is seen at this stage in satellite imagery.

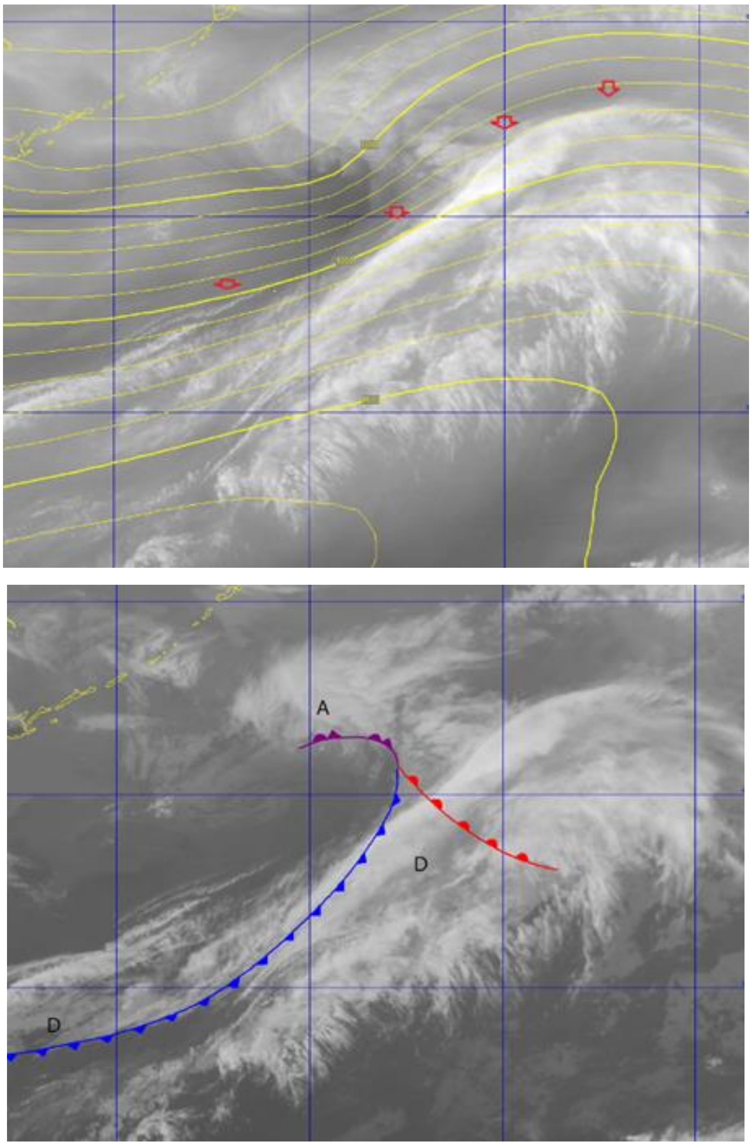

Fig. 5-2-20. Instant occlusion with no development (BH model), occlusion completed, at 06:00 UTC on 26 April 2011. Top: B10 water vapor image with 300-hPa isohypse and arrows marking the boundary; bottom: B13 infrared image

4. Dissipation Stage (Fig. 5-2-21)

The top height decreases here in the cloud band **D** corresponding to the occluded front, becoming obscure with a dissipating tendency. The cyclonic central pressure remains almost the same after the occlusion, with no further development. In the BH model, no further post-occlusion development is seen, and ready movement into the dissipation stage is observed in contrast to the output of the MYB model described below.

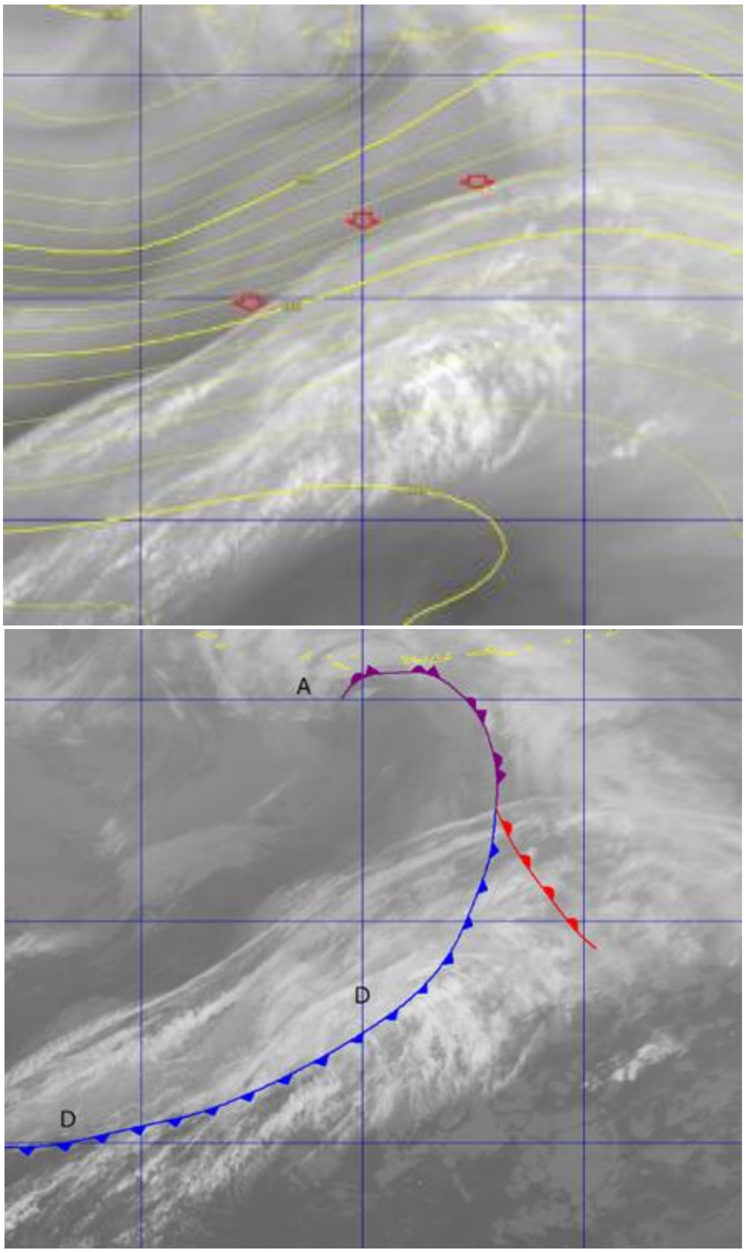

Fig. 5-2-21. Instant occlusion with no development (BH model), dissipation stage, at 00:00 UTC on 27 April 2011. Top: B10 water vapor image with 300-hPa isohypse and arrows marking the boundary; bottom: B3 infrared imagey

(2) With Cyclone Development (MYB model)

1. Initial Stage (Fig. 5-2-22)

The frontal cloud band **B-B** here extends east-northeastward over the sea south of Japan. The comma cloud formation with the obscure tail **N** is seen east of Hokkaido, advancing east-northeastward with an increasing top height. Off the Sanriku shore between the frontal cloud band and the comma cloud, the high-top cloud area **M** emerges, connecting the comma cloud in the north and the frontal cloud band in the south. A cyclone (marked with **x**) corresponding to the comma cloud and a front corresponding to the cloud band can be seen. At 850 and 700 hPa, southwestern wind is prominent with intensified warm advection off the Sanriku coast (not shown), corresponding to the development of the cloud **M** to the warm side of the comma cloud. These are typical characteristics of the MYB model.

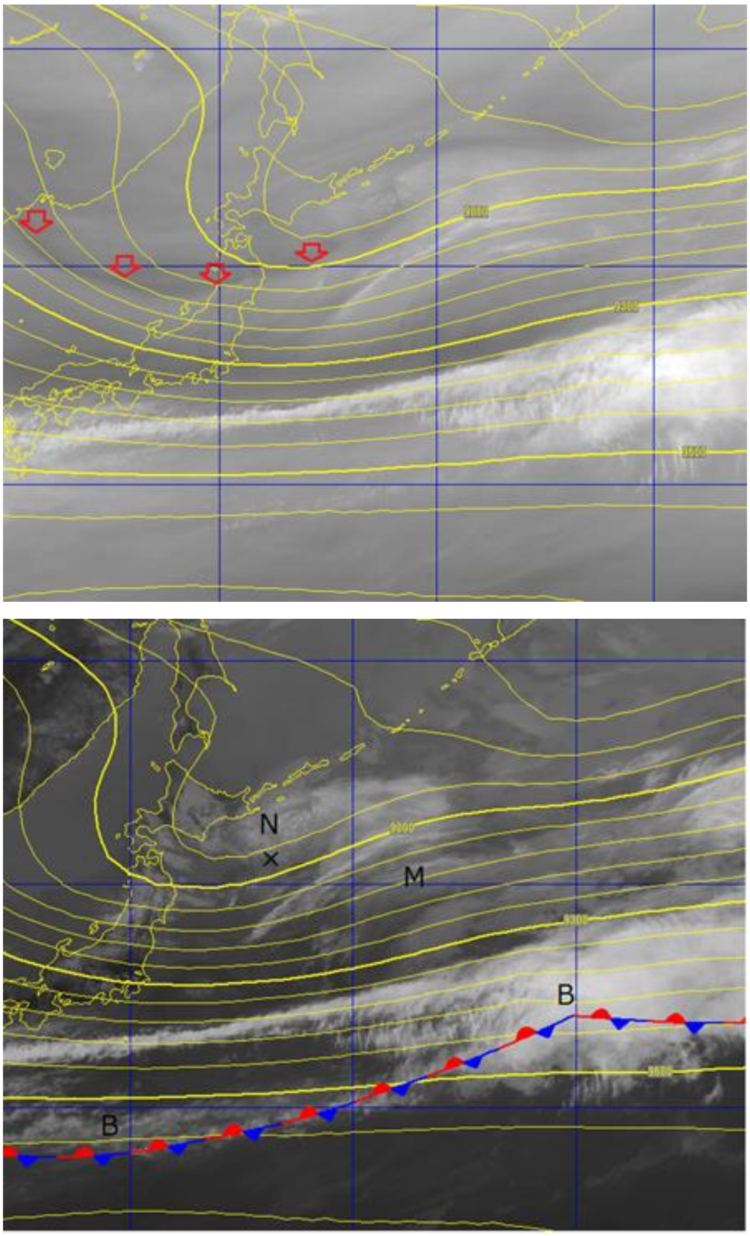

Fig. 5-2-22. Instant occlusion with development (MYB model), initial stage, at 06:00 UTC on 10 May 2015. Top: B10 water vapor image with 300-hPa isohypse and arrows marking the boundary; bottom: B13 infrared image

2. Occlusion Commencement Stage (Fig. 5-2-23)

The comma cloud **N** and the cloud area off the Sanriku coast **M** start to merge here. **N** has a higher cloud top with anticyclonic curvature at its northern edge, demonstrating development. Toward the south of **N**, the frontal cloud band top height also increases, bringing an occlusion pattern where the two cloud areas come into contact. The comma cloud and the cloud band represent cyclonic conditions with a front and a stationary front, respectively. This pre-occlusion state is indicated by the incomplete connection between the two cloud types and by the relatively minor anticyclonic curvature of the cloud band.

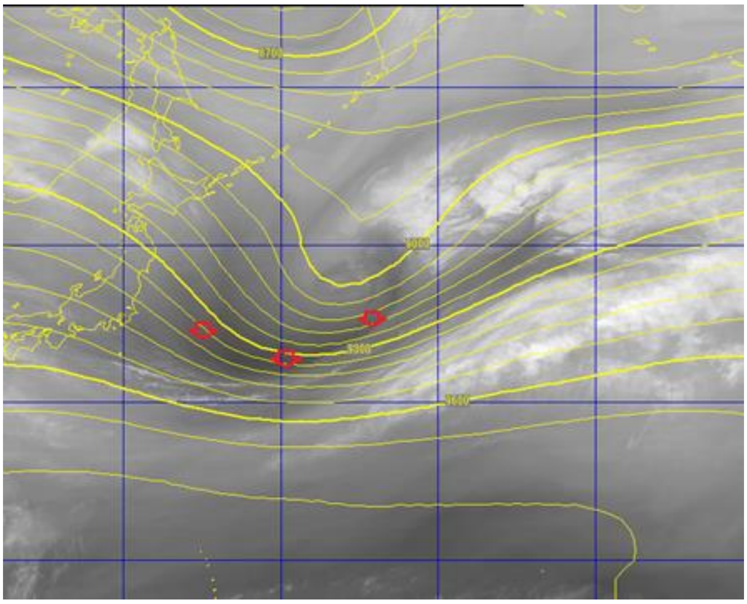

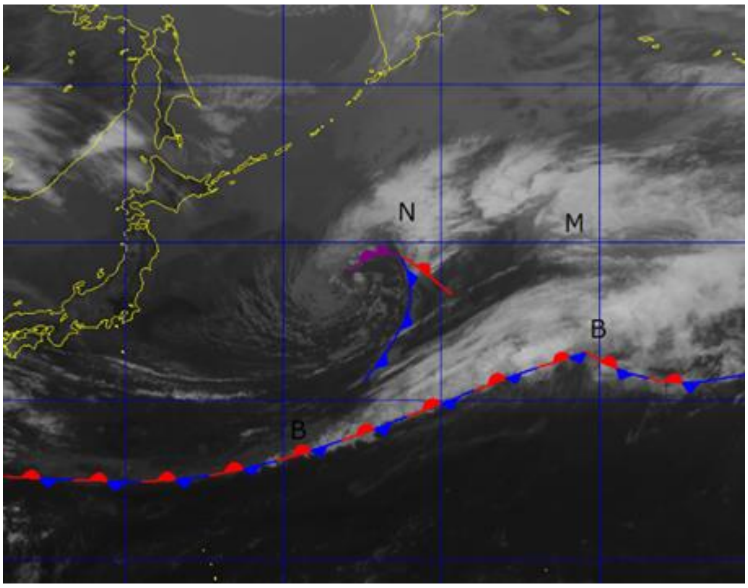

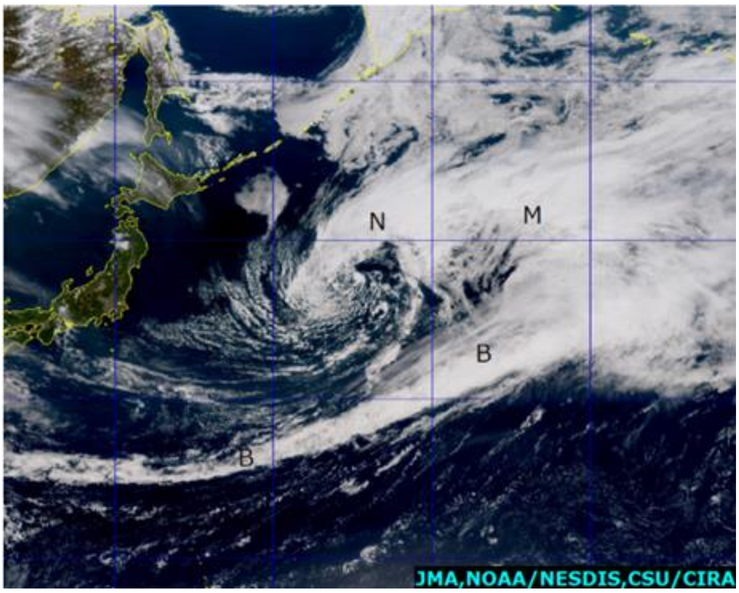

Fig. 5-2-23. Instant occlusion with development (MYB model), occlusion commenced, at 00:00 UTC on 11 May 2015. Top: B10 water vapor image with 300-hPa isohypse and arrows marking the boundary; middle: B13 infrared image; bottom: True Color Reproduction image

3. Occlusion Completion Stage (Fig. 5-2-24)

The cloud top is raised where the frontal cloud band and the comma cloud merge. The anticyclonic curvature **F-F** is distinct at the northern edge of the cloud band, and a dry slot **D** is also seen, indicating completion of the occlusion. The cyclone then follows the pattern of the standard mature stage.

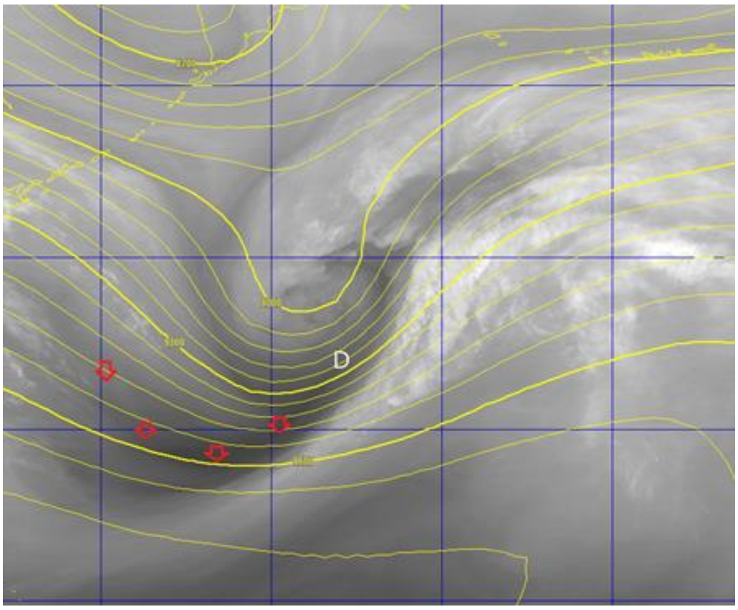

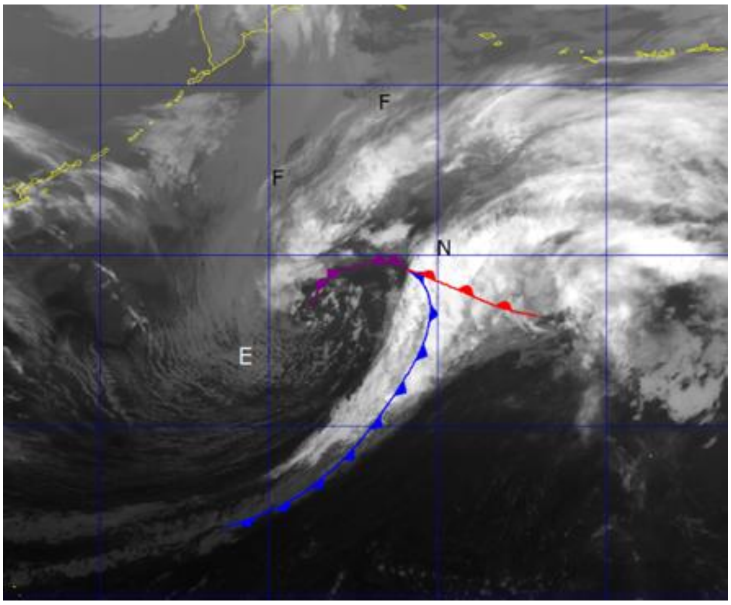

Fig. 5-2-24. Instant occlusion with development (MYB model), occlusion completed, at 12:00 UTC on 11 May 2015. Top: B10 water vapor image with 300-hPa isohypse and arrows marking the boundary; bottom: B13 infrared image

5.2.4. T-bone-type Development

The cyclonic development model presented by Shapiro and Keyser (1990; referred to here as the SK model) differs from the Bjerknes model (Fig. 5-2-25) in that a cold front does not join a warm front (i.e., frontal fracture). At the cyclonic center, cold air to the rear does not cover the surface (i.e., forming an occlusion), but a warm core remains behind (i.e., forming a warm-core seclusion). A warm front extends to the rear westward of the cyclonic center (i.e., forming a backward-arching warm front), but does not represent an occluded front.

A characteristic T-bone (i.e., T-shaped) cloud pattern, seemingly applicable to the SK model, resembling a warm occlusion is often seen in satellite imagery. A cyclone with this T-bone formation is described here for analysis in the context of the SK model, which does not explain all aspects of cyclonic development and structure. For instance, regarding backward-arching warm fronts, various discussions have been held on warm-front structures extending to the rear of cyclones. As with the warm-core seclusion period, analysis of multi-layer fronts entwined with the cyclonic center remains problematic. In contrast, satellite imagery for frontal fractures and warm core seclusions tends to match objective analysis for temperature fields and other variables.

In the SK model, in-depth analysis of mesoscale structures with insight is necessary, but weather charts and satellite imagery do not necessarily offer comprehensive details. This model may require consideration regarding applicability to weather chart analysis because of its limitations.

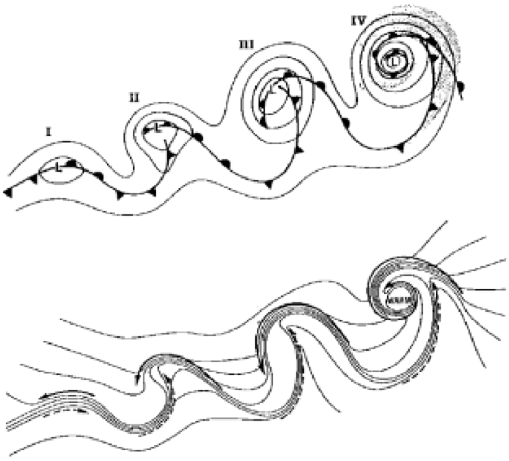

Fig. 5-2-25. T-bone models (Shapiro and Keyser, 1990)
I: incipient frontal cyclone; II: frontal fracture; III: backward-arching warm front and T-bone; IV: warm-core frontal seclusion
Top: isohypse (solid line), cloud area (dotted); bottom: temperature (solid lines), cold-air current (solid lines with arrow heads), warm-air current (dashed lines with arrow heads)

1. Initial Stage (Fig. 5-2-26)

A bulging cloud area here advances east-northeastward east of Japan with a pattern and characteristics similar to those seen the early-development stage of the standard type.

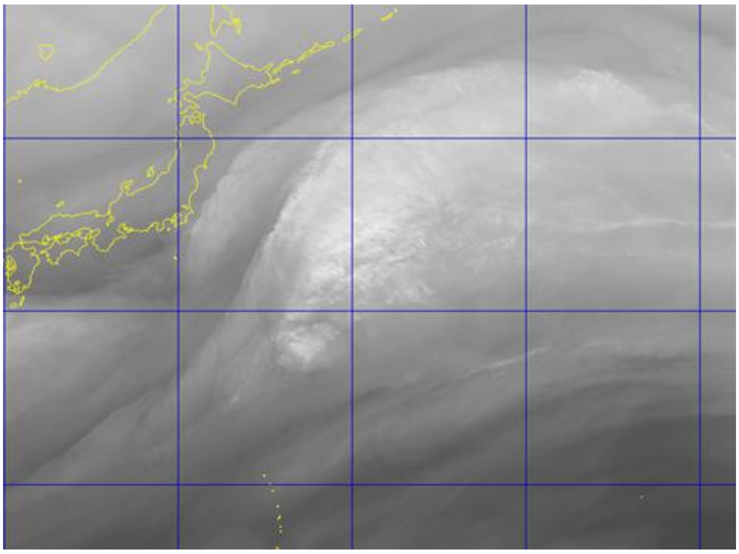

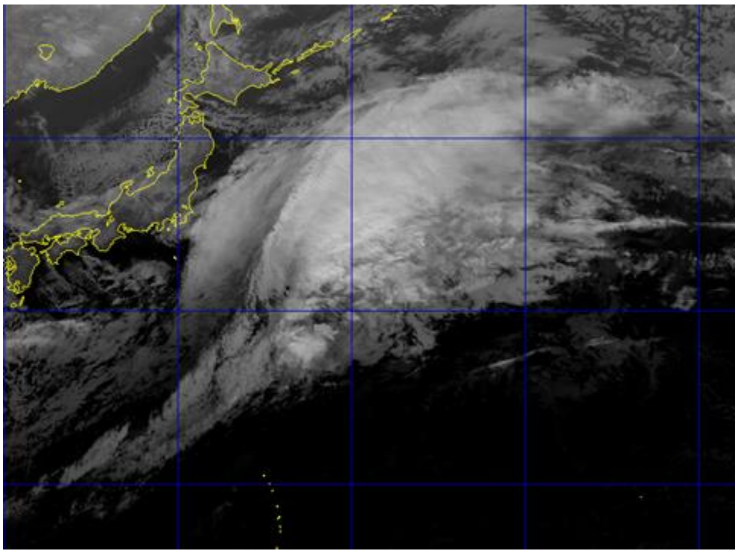

Fig. 5-2-26. T-bone development, initial stage, at 18:00 UTC on 6 February 2016
Top: B10 water vapor image; bottom: B13 infrared image

2. Frontal Fracture (Fig. 5-2-27)

The cloud area advancing east-northeastward to the east of Japan here has a further area extending east-westward, in contrast to the standard type. Anticyclonic curvature is increased at the northern edge, with a cloudless region intruding from the west. A notch (marked with arrows) begins to form, enabling determination of the cyclonic center. Although this resembles a warm occlusion pattern in the imagery, objective analysis at 850 hPa indicates no southward descent, meaning that the occlusion process has not started. A warm front is seen at the southern edge of the low-cloud area. The band **C-C** with convective clouds corresponding to the cold front extends southwestward, intersecting almost perpendicularly with the cloud area corresponding to the warm front extending longitudinally. In objective analysis at 850 hPa, cold advection intensifies at **C-C**, exhibiting a distinct cold-front structure. In contrast, the structure of the front farther north is unclear. The cold front exhibits a decreased temperature gradient at the region in contact with the warm front, as with the frontal-fracture structure in the SK model. In satellite imagery, the fractured and non-fractured parts are hard to distinguish.

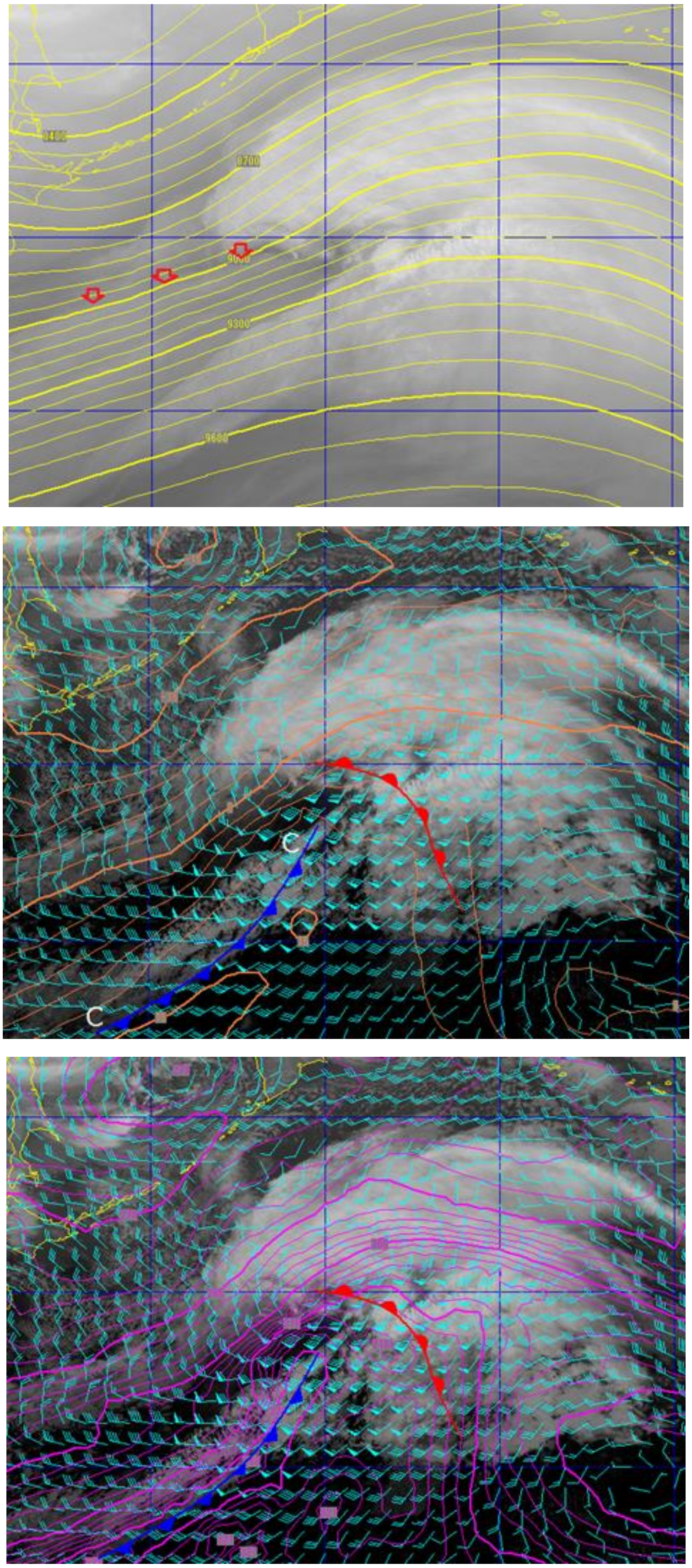

Fig. 5-2-27. T-bone development, frontal fracture, at 06:00 UTC on 7 February 2016
Top: B10 water vapor image with 300-hPa isohypse and arrows marking the boundary; middle: B13 infrared image, wind and temperature at 850 hPa; bottom: B13 infrared image,

wind and equivalent potential temperature at 850 hPa (unseen in visible image)

3. Backward-arching Warm Front (Fig. 5-2-28)

A cloud area associated with a cyclone advances eastward to the Kuril Islands here. The tall cloud area **L-M-N** relative to the warm front extends from east to west, almost perpendicularly intersecting a cloud band corresponding to the cold front extending southward, to form a clear T-bone shape. A distinct warm-front structure is visible from objective analysis at 850 hPa temperature and equivalent potential in **L-M-N**. The low-cloud vortex seen to the south near **N** in the satellite imagery indicates a nearby cyclonic center. In the SK model, the backward-arching warm front is at the southern edge of the cloud area between **M** and **N**, or at the eastern edge of the low cloud area **N-P** extending farther southward from **N**. As these areas extend around the cyclonic center anticlockwise with cold air, the structure is more of a backward-arching cold front rather than a warm one. In the SK model, the cyclonic center is seen around **M**, crossing the warm front extending from the fractured cold front. However, cyclonic centers are rarely observed in this region, more frequently appearing where lower vortices are seen (around **N** to the west of the cross point **M**).

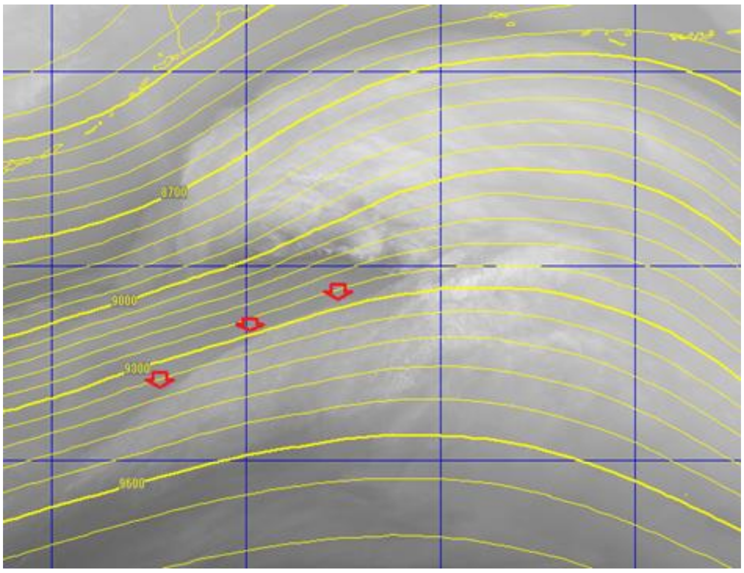

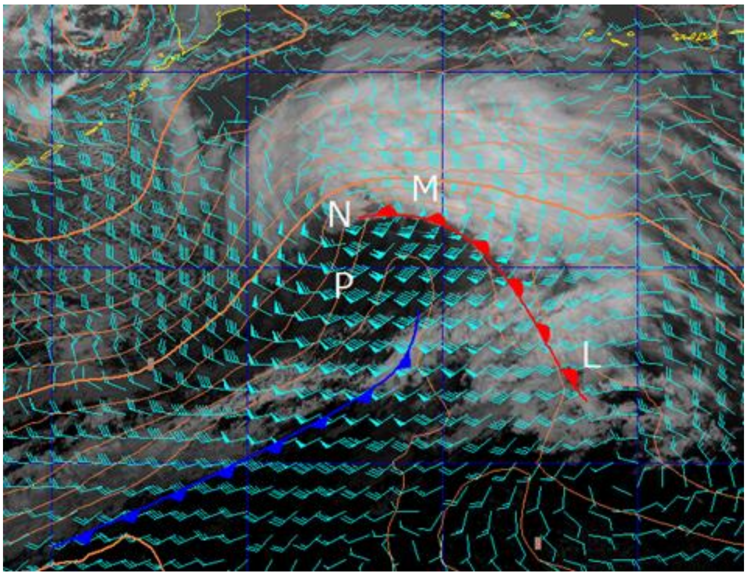

Fig. 5-2-28. Backward-arching warm front at 12:00 UTC on 7 February 2016
Top: B10 water vapor image with 300-hPa isohypse and arrows marking the boundary;
bottom: B13 infrared image, wind and temperature at 850 hPa

4. Warm-core Seclusion (Fig. 5-2-29)

In this satellite imagery, anticyclonic curvature becomes distinct at the northern and western edges of cloud areas. A low cloud vortex is also distinct here, with a dry slot around it indicating a cyclonic pattern resembling an occlusion. The cloud area starts to show meridional elongation on a course different from previous tendencies, with a cold-front cloud band extending southward across another cloud band north of a warm front to form a T-bone pattern. The low cloud vortex corresponds to the cyclonic center **L**.

In the SK model, this pattern is considered to indicate the progress of warm-core seclusion. A warm front can be identified in the figure at the edge of the cloud around the center. No clear warm core is observed at the isotherm of the 850 hPa weather map, but one can be determined from equivalent potential temperature.

Cold advection is stronger at **C** away from the center, leaving a relatively warm core around the center. In satellite imagery, a low-cloud vortex consisting of Cu and Sc represents the warm core. These clouds exhibit weak convective activity in contrast to cell-form convective clouds formed by cold-air intrusion, plausibly suggesting the presence of air relatively warmer than the surroundings.

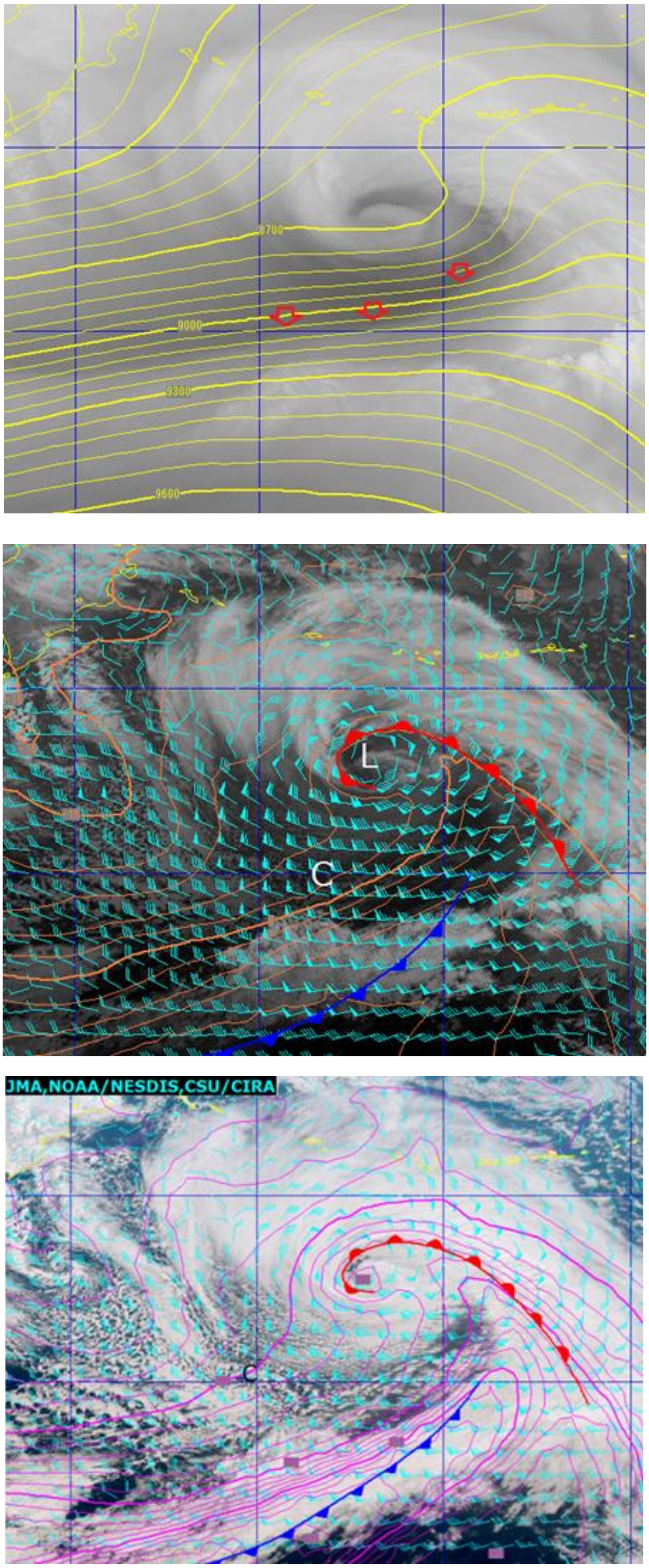

Fig. 5-2-29. Warm-core seclusion at 00:00 UTC on 8 February 2016

Top: B10 water vapor image with 300-hPa isohypse and arrows marking the boundary; middle: B13 infrared image, wind and temperature at 850 hPa; bottom: True Color Reproduction image, wind and equivalent potential temperature at 850 hPa

6. Meteorological Phenomena

6.1. Heavy Rain Associated with the Baiu Front

The Baiu front has a small horizontal temperature gradient but a large horizontal water vapor gradient, accompanied by a strong low-level jet and an intense inflow of warm wet air (known as “moist tongue”). East-west cloud bands corresponding to the front in satellite imagery are a rich source of information on such bands (widths, lengths, meridional displacement, and convective clouds within them) and convective clouds entering cloud bands (development and movement) to indicate frontal activity. Satellite imagery-based monitoring of heavy rain associated with the front is important because it enables visualization of dry intrusion, upper vortices and movement of active convective clouds.

In this section, the characteristics of satellite imagery for the Baiu front are described in relation to a case (20 – 21 June 2016) in which conditions were simultaneously affected by an upper trough and warm wet air. Rainfall exceeding as much as 100 mm per hour was recorded in the prefectures of Kumamoto and Nagasaki. In particular, precipitation of 150 mm per hour was recorded in Kosa-machi, Kumamoto, which was unprecedented locally and the fourth-highest ever in the whole of Japan at the time.

(1) Baiu Front Cloud Band and Warm Sector Convective Cloud Area

Outline

When the upper trough approaches the cloud band corresponding to the front, a bulging cloud area begins to form with anticyclonic curvature at its northern edge. In the lower layer on the warm side, a warm air mass with high specific humidity moves north toward the cloud band along the western edge of the Pacific High. Convective cloud lines can be seen among the warm air masses.

Analysis

1. Upper vortex corresponding to the trough and bulging cloud areas

As the upper trough approaches, a thick bulging cloud area begins to form as also seen in the formative and development stages of cyclones. The upper trough in water vapor imagery corresponds closely to the upper vortex.

In this case, water vapor image shows a trough axis between the Bohai Sea and the Yellow Sea (Fig. 6-1-1). Another trough in association with a dry area in the middle layer over western Kyushu is also seen. These characteristics correspond to positive vorticity maximum areas on the 500 hPa vorticity analysis chart (A and B in Fig. 6-1-2). In infrared imagery (Fig. 6-1-3), active cumulonimbus clouds are seen to the front of the trough around Kyushu. Bulging cloud expansion is also seen at the northern edge of the cloud band between western Japan and the western part of the Sea of Japan.

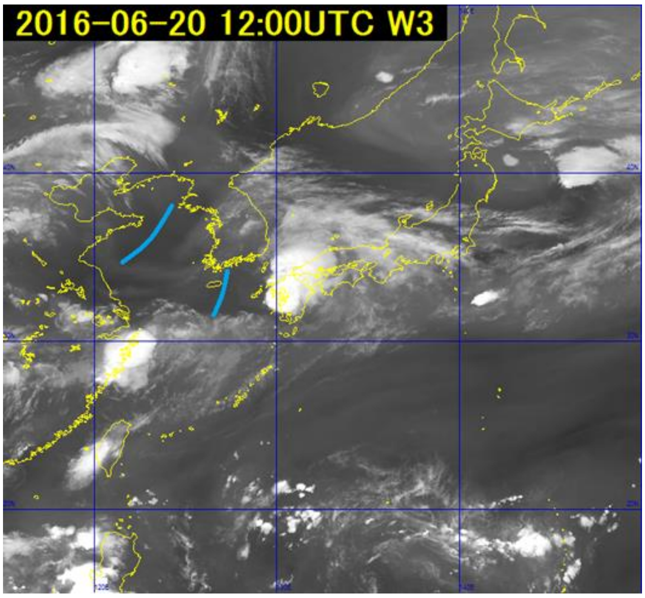

Fig. 6-1-1 B10 water vapor image for 12:00 UTC on 20 June 2016

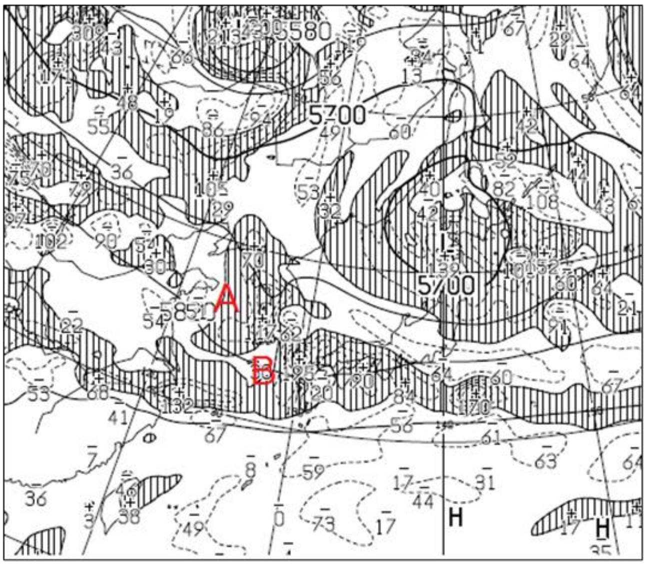

Fig. 6-1-2 500 hPa vorticity analysis chart or 12:00 UTC on 20 June 2016

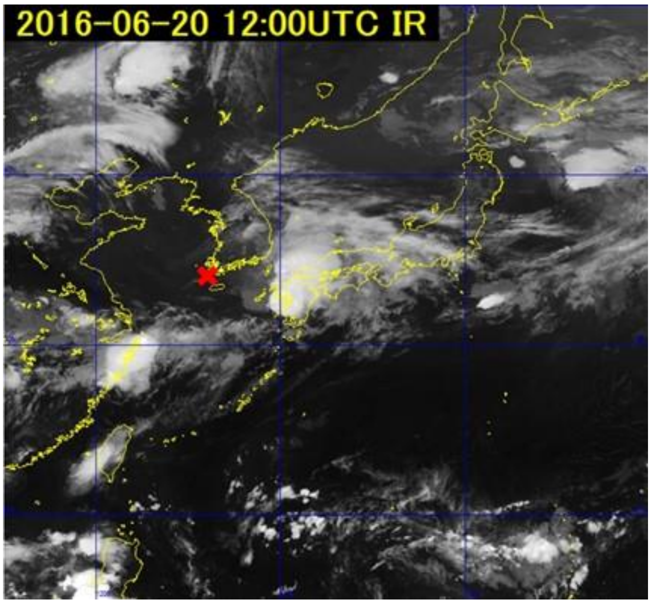

Fig. 6-1-3 B13 infrared image for 12:00 UTC on 20 June 2016
X marks the lower vortex

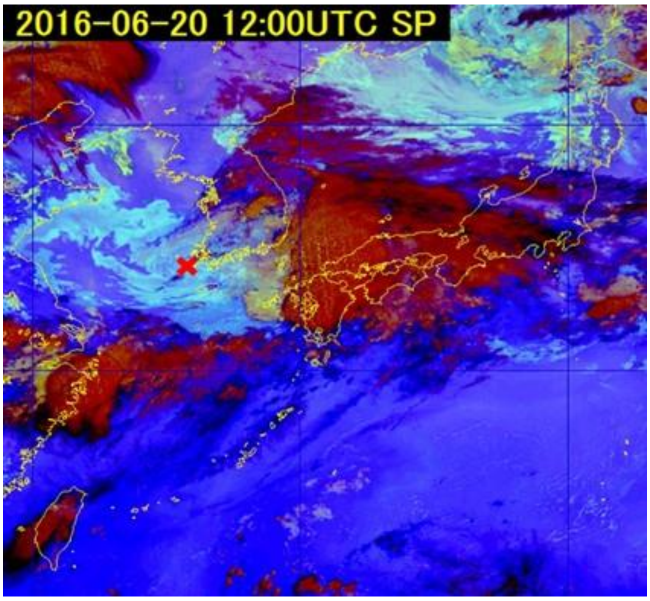

Fig. 6-1-4 Night Microphysics RGB composite image, for 12:00 UTC on 20 June 2016
X marks the lower vortex.

2. Areas of active convection near the front and in the warm sector

Active convective cloud areas and cloud lines often correspond to wind convergence areas and high equivalent-potential temperature zones in the lower layer.

In this example (Figs. 6-1-3 and 6-1-4), B13 infrared image and Night Microphysics RGB composite image reveal a lower vortex corresponding to a cyclone below the trough over the northwestern part of Jeju Island, with a front corresponding to the northern edge of the bulging Ci discussed above. The Cb area around Kyushu is associated with the eastern part of the dark region, with multiple carrot-shaped precipitation zones as seen in Fig. 6-1-5, moving slowly eastward along with the movement in the same direction of the dark region of the trough at 500 hPa as discussed above. Night Microphysics RGB composite imagery shows scattered low-level clouds moving northward toward the frontal cloud band.

Figure 6-1-6 shows Airmass RGB composite image with 925 hPa equivalent potential temperature (reddish purple) and winds (green barbs) based on JMA's mesoscale numerical weather prediction model (MSM). Here, warm moist air with high equivalent-potential temperature flowed from the southwest toward Kyushu. Northeast of the Cb area, strong velocity convergence is seen. In the same area, the horizontal gradient of equivalent potential temperature is large and winds are orthogonal to the isometric lines of equivalent potential temperature, indicating that the northeastern part of the Cb area has the largest advection. Southwestern winds of 50 kt are observed in western Kyushu, and wind profiler data from Kumamoto shows similar winds at an altitude of 500 m from around 14:00 UTC onward (figure not shown).

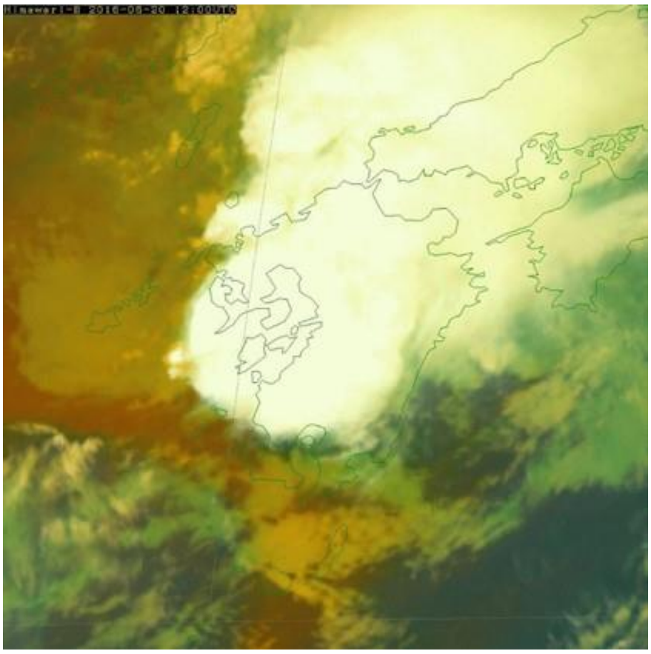

Fig. 6-1-5 Airmass RGB composite image for 12:00 UTC on 20 June 2016

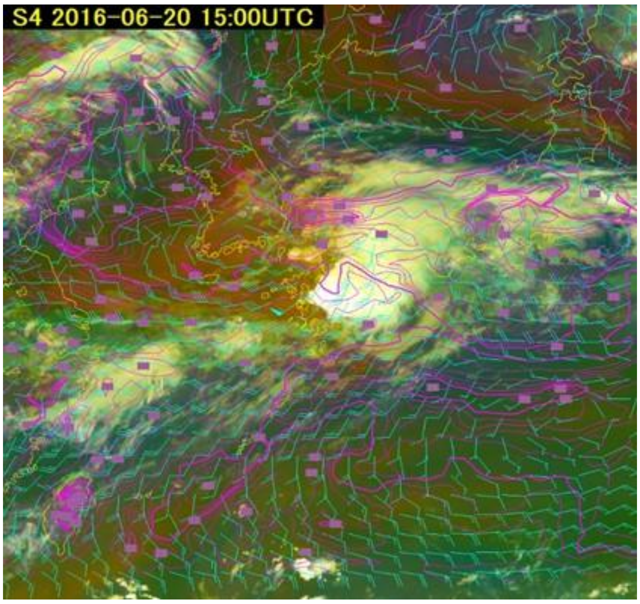

Fig. 6-1-6 Airmass RGB composite image for 15:00 UTC on 20 June 2016
925 hPa equivalent potential temperature (reddish purple) and winds (green barbs) based on MSM objective analysis with temporally corresponding initial values.

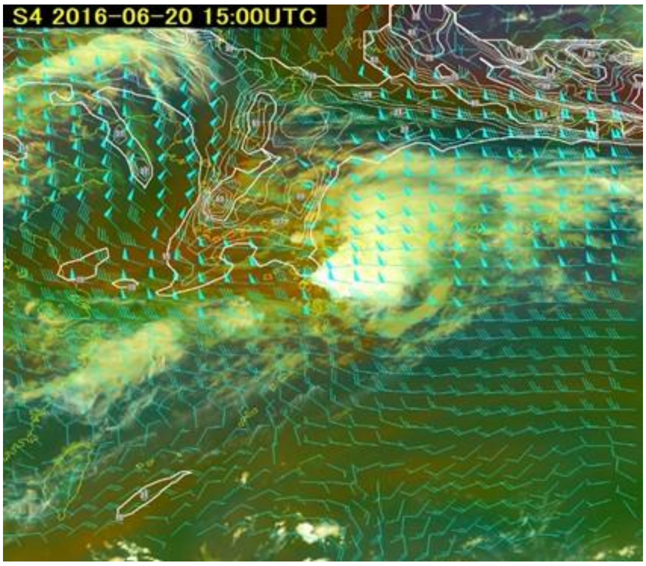

Fig. 6-1-7 Airmass RGB composite image for 15:00 UTC on 20 June 2016
250 hPa winds (green barbs) and potential vorticity at the 345 K isentropic surface (dark red) based on MSM objective analysis with temporally corresponding initial values.

3. Entrance of high potential vorticity and upper divergence

Figure 6-1-7 shows Airmass RGB composite image with potential vorticity at the 345 K isentropic surface and 250 hPa winds.

Wind distribution shows intense horizontal divergence around the Cb, as seen with the formation conditions for carrot-shaped Cb, indicating strong divergence in the upper layer. In potential vorticity distribution, a high potential-vorticity area above 1.5 PVU spreads from north to south with convective clouds ahead, as seen in the dry area of the dark region in the upper and middle layers corresponding to the brown area in Airmass RGB composite imagery. In the advection area with high potential vorticity, updraft is promoted from the middle layer to the upper layer (Japan Meteorological Agency, 2013).

As described in 2 and 3, carrot-shaped Cb areas were formed in association with strong advection near the front in the lower layer and strong divergence in the upper layer.

(2) Summary

1. Key points in relation to heavy rainfall brought by the Baiu front

A) Updraft causing convective clouds
Lower-layer convergence ahead of cyclones, intensification of equivalent potential temperature advection near the front, and orographic effects

B) Atmospheric structures promoting convective cloud development
Low-level advection of high equivalent-potential temperature, dry intrusion from the north of the front (i.e., convective instability), intrusion of cold air (i.e., latent instability), and divergence in the upper layer

C) Sufficient water vapor supply
Intrusion of air parcels with high specific humidity toward the front

D) Synoptic field conditions for maintenance of the above
Positioning of jets/troughs/cyclones, presence of tropical disturbances over the sea south of Japan, and subtropical anticyclone intensity

2. Baiu-Front characteristics relating to heavy rainfall

A) A bulging thick cloud area forms in the cloud band corresponding to the front as the upper trough approaches.

B) In areas with lower-layer convergence, convection becomes active and cloud bands corresponding to the front are formed.

C) In warm areas, convection becomes active in high equivalent-potential temperature zones in the lower layer in association with Pacific High marginal winds.

D) In areas with strong warm humid advection brought by marginal winds, convection becomes active at the southern edge of the cloud band.

References:

- Japan Meteorological Agency (2013) Weather Forecast Training Textbook (in Japanese).

6.2. Heavy Snow Associated with a Small Cyclone on the Western Coast of Hokkaido

In winter, a trough forms as a result of a relatively warm area over the sea to the west of Hokkaido surrounded by two cold anticyclones, one is above Primorye in Russia, and the other is above Sakhalin, Hokkaido, and ice on the Sea of Okhotsk. This leads to the latitudinal formation of a convergence line between the Strait of Tartary and the northern Sea of Japan associated with seasonal northwest wind and northeast winds blowing from the cold anticyclone above Sakhalin, Hokkaido, and ice on the Sea of Okhotsk. An updraft occurs along this line, and belt-form clouds emerge as a result (Fig. 6-2-1). When the upper trough and the area with maximum positive vorticity approach the belt-form clouds, updraft intensifies to bring a lower vortex containing convective clouds. A small cyclone and a bag-shaped low-pressure area are subsequently analyzed.

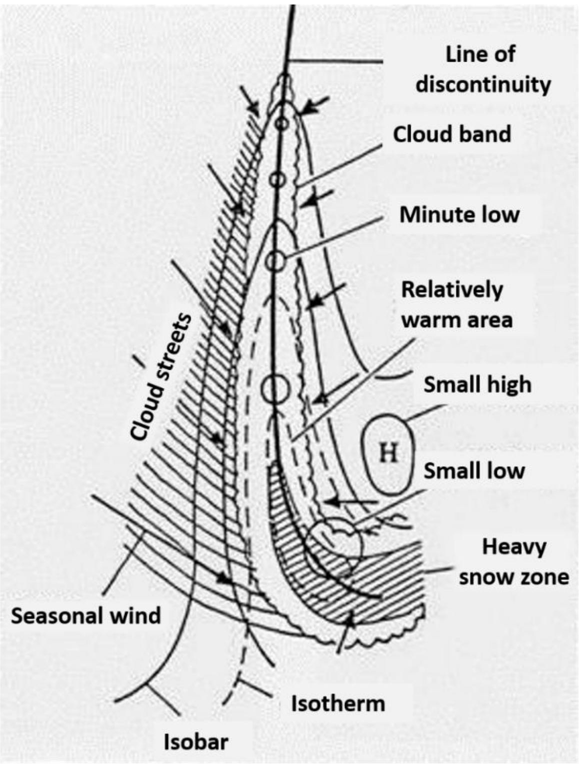

Fig. 6-2-1 Cloud bands on the western coast of Hokkaido (Okabayashi, 1972). Arrows: lower winds; thick solid line: convergence; area inside wavy line: cloud band; thin solid lines: isobars; dashed lines: ground-level isotherms.

Hokkaido Western Coast Small Lows are a type of mesoscale lower vortex. Among these are Ishikari Bay Lows, in which the vortex moves southward with winds, often bringing heavy snow to western Hokkaido. In previous research, the Sapporo District Meteorological Observatory extensively surveyed Hokkaido Western Coast Small Lows (Sapporo District Meteorological Observatory, 1989). In this study, clouds are classified into two patterns (belt or vortex form) and seven genres based on characteristics seen in satellite imagery, with the creation of a cloud formation flowchart and a worksheet for forecasting snowstorms with each cloud type. In this section, a Hokkaido Western Coast Small Low is described on the basis of satellite imagery.

(1) Characteristics Seen in Satellite Imagery

Around 14:00 UTC on 13 January 2016, two mesoscale lower vortices emerged over the northern Sea of Japan and developed rapidly off the shores of Rumoi and the Shakotan Peninsula under the influence of an upper trough moving along the polar-front jet stream. These vortices and a surrounding spiral-form Cb area subsequently moved southeastward and landed in the subprefectures of Rumoi and Shiribeshi, bringing heavy snowfall to the latter.

1 Before lower-vortex emergence

In the surface weather chart for 12:00 UTC on 13 January 2016, a cyclone was advancing eastward from the western part of the Tsugaru Strait before lower-vortex emergence (Fig. 6-2-2). In the 500 hPa upper weather chart, an upper trough with a cold-air mass below –42°C was advancing toward Primorye (Fig. 6-2-3). Infrared image shows belt-form convective clouds over the sea off western Hokkaido (Fig. 6-2-4, with a thin solid line connecting active convective clouds in the belt-form convective cloud area, forming the curve marked as **E1**).

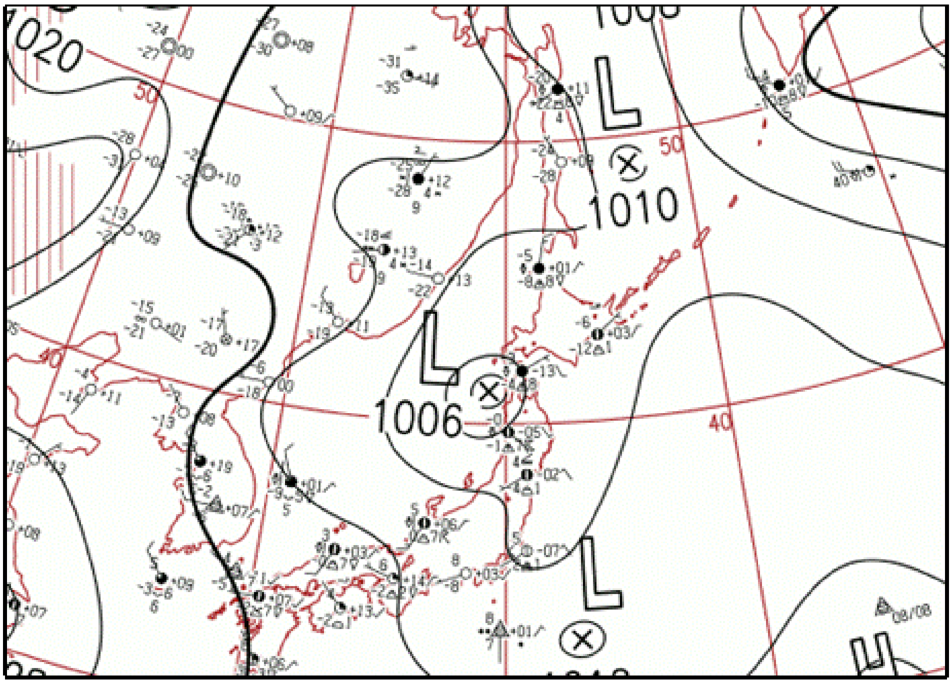

Fig. 6-2-2 Surface weather chart for 12:00 UTC on 13 January 2016

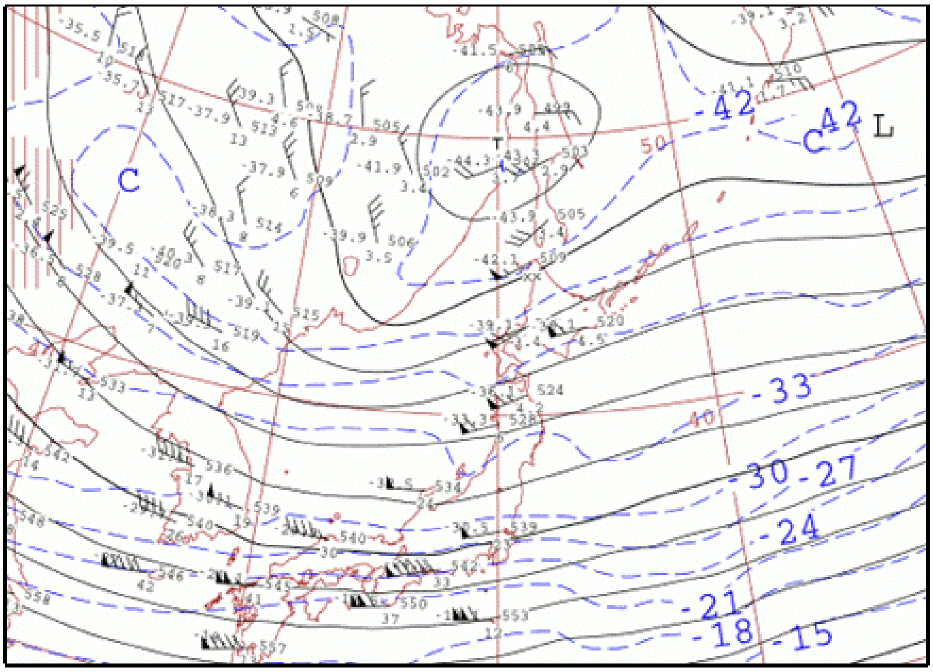

Fig. 6-2-3 500 hPa upper weather chart for 12:00 UTC on 13 January 2016

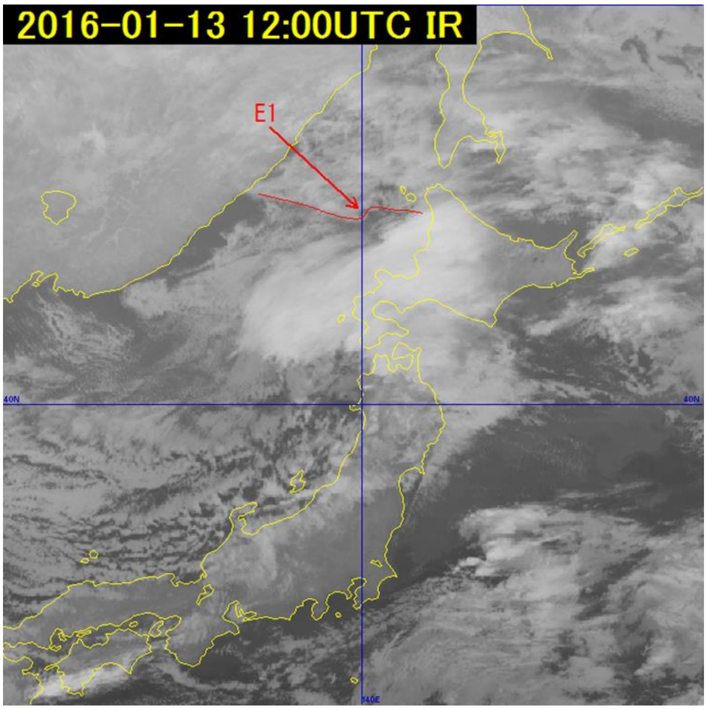

Fig. 6-2-4 B13 infrared image for 12:00 UTC on 13 January 2016

2 Lower-vortex formative stage

In the surface weather chart for 18:00 UTC on 13 January 2016, a cyclone was advancing off the coast of Hidaka, bringing the typical "west-high, east-low" pressure pattern seen in Japan in winter (Fig. 6-2-5). In infrared image, belt-form convective clouds were moving southward with increasing activity, and the curve **E1** was moving east-southeastward, overlapping with upper clouds and becoming obscure (Fig. 6-2-6). The upper trough at 500 hPa was progressing east-northeastward producing a distinct bulging cloud formation over the sea off western Hokkaido in front of the trough, along with the emergence of the mesoscale lower vortex **E2** to its west.

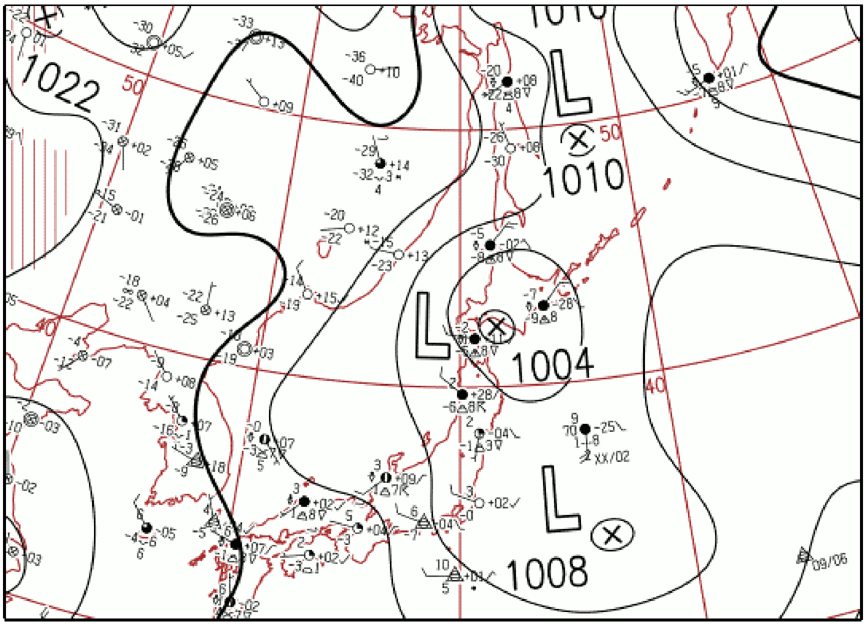

Fig. 6-2-5 Surface weather chart for 18:00 UTC on 13 January 2016

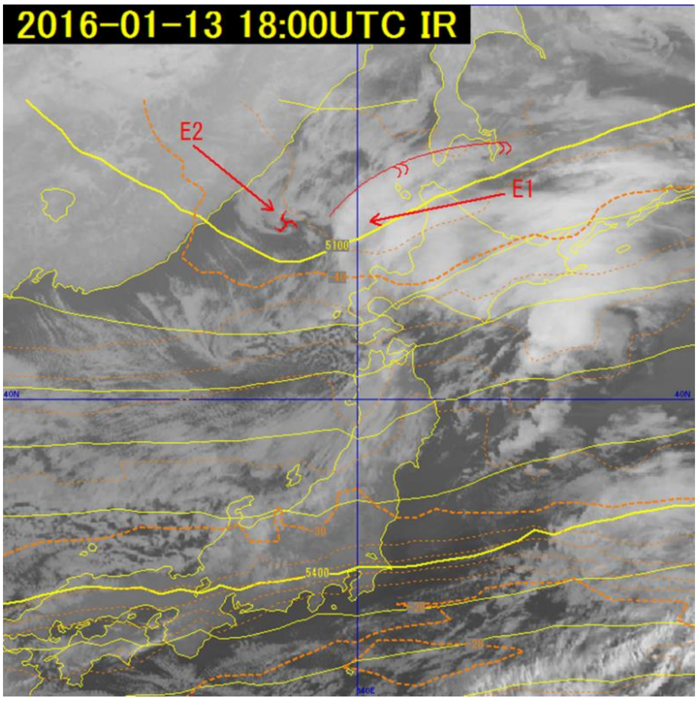

Fig. 6-2-6 B13 infrared image for 18:00 UTC on 13 January 2016, with 500 hPa geopotential heights and temperatures based on MSM objective analysis with temporally corresponding initial values

3 Lower-vortex development stage

In the infrared image for 21:00 UTC on 13 January 2016, upper clouds over the sea off western Hokkaido were advancing east-northeastward, and curve **E1** was moving onto the upper trough at 500 hPa, forming a distinctive mesoscale lower vortex off the shore of Rumoi (Fig. 6-2-7). A spiral-form Cb area was seen around the lower vortex, and radar echo intensity increased.

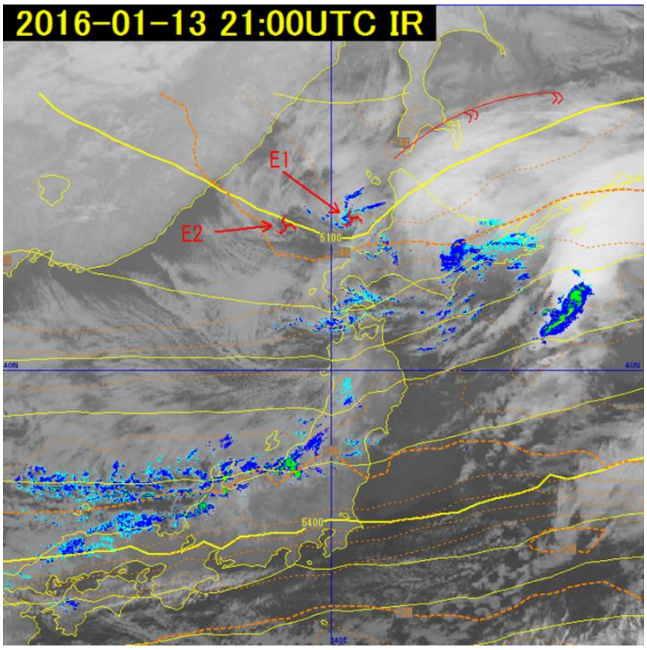

Fig. 6-2-7 B13 infrared image for 21:00 UTC on 13 January 2016, with 500 hPa geopotential heights and temperatures based on MSM objective analysis with temporally corresponding initial values and radar echoes

4 Lower-vortex mature stage

In infrared image for 00:00 UTC on 14 January 2016, the lower vortices **E1** and **E2** were accompanied by a distinct spiral-form Cb area and advancing east-southeastward while maintaining high levels of convective activity (Figs. 6-2-8, 6-2-9). **E1** is accompanied by a Cb area with a minimum brightness temperature of around –33°C and a maximum cloud top height of approximately 4,000 m, or 600 hPa (Fig. 6-2-10).

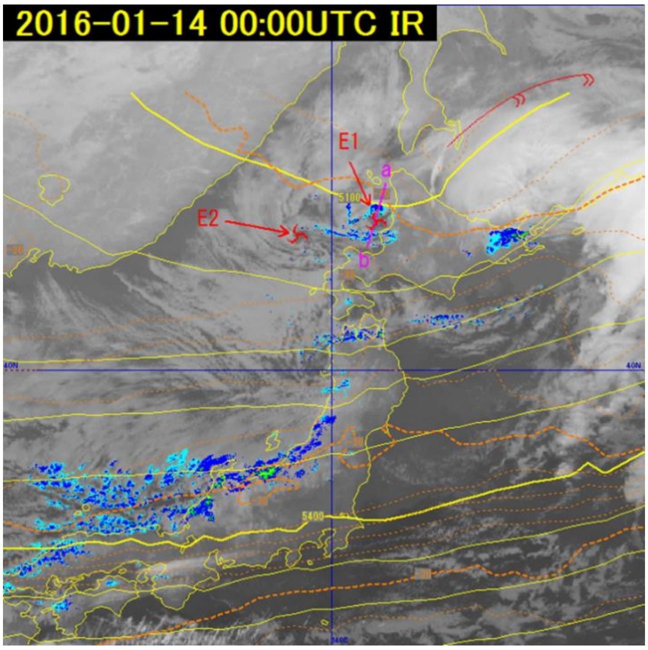

Fig. 6-2-8 B13 infrared image for 00:00 UTC on 14 January 2016, 500 hPa geopotential heights and temperatures by MSM objective analysis with temporally corresponding initial values, and radar echoes

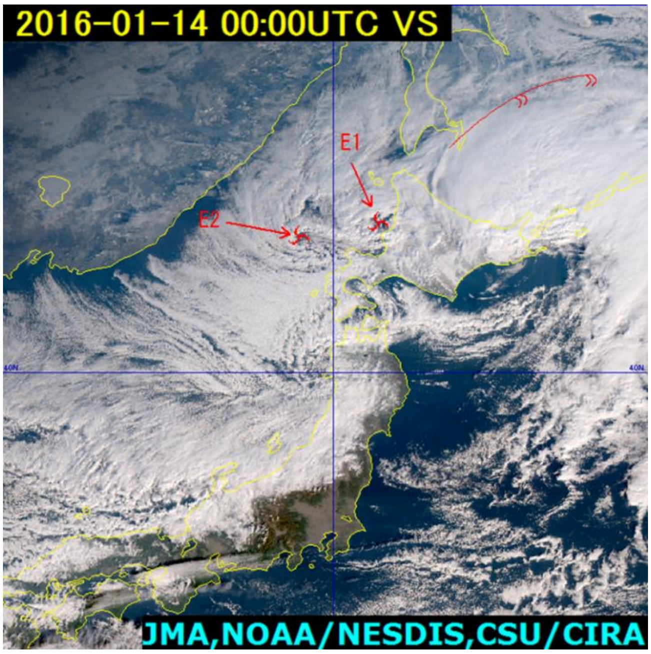

Fig. 6-2-9 True Color Reproduction image for 00:00 UTC on 14 January 2016

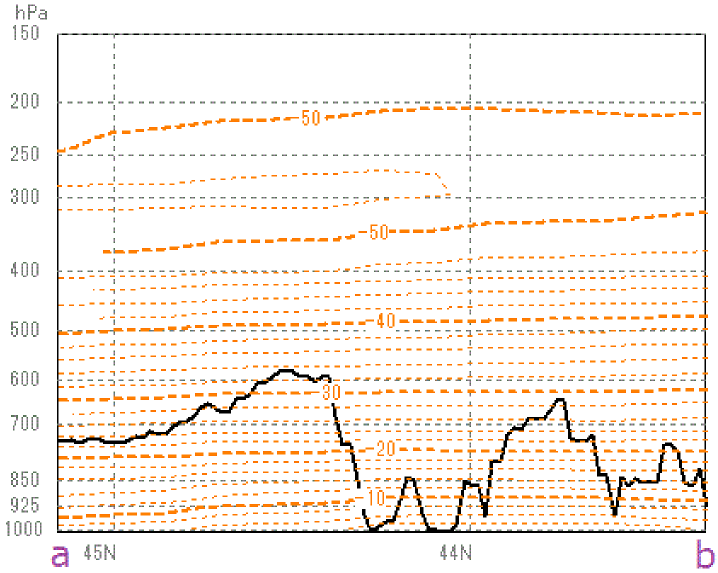

Fig. 6-2-10 Vertical cross section between a and b in Figure 6-2-8. Dashed orange lines are isotherms and the black line is cloud top height distribution. Both from MSM objective analysis with initial values at 00:00 UTC on 14 January 2016.

5 Lower-vortex dissipation stage

In the infrared image for 06:00 UTC on 14 January 2016, the lower vortex **E1** has landed near Rumoi and weakened along with its surrounding convective clouds (Fig. 6-2-11). The lower vortex **E2** has become obscure off the shore of the Shakotan Peninsula, and another mesoscale lower vortex **E3** has appeared. It is surrounded by a spiral-form Cb area, and has advanced east-southeastward and moved over an area near the Shakotan Peninsula (Fig. 6-2-12).

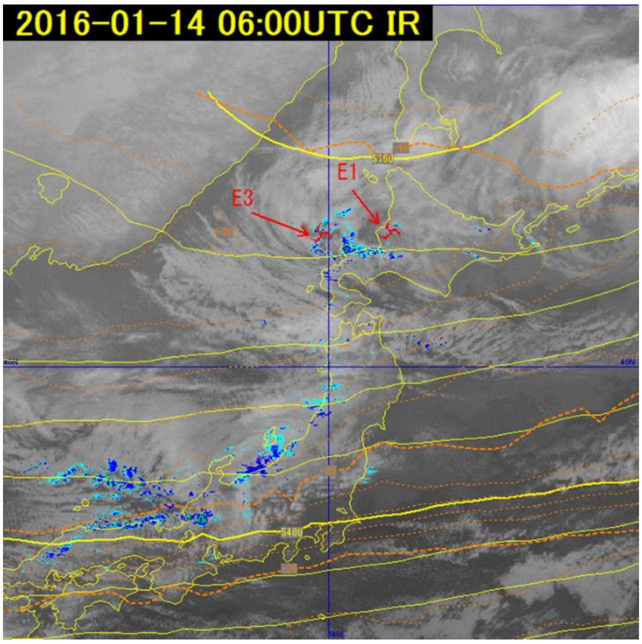

Fig. 6-2-11 B13 infrared image for 06:00 UTC on 14 January 2016, with 500 hPa

geopotential heights and temperatures based on MSM objective analysis with temporally corresponding initial values and radar echoes

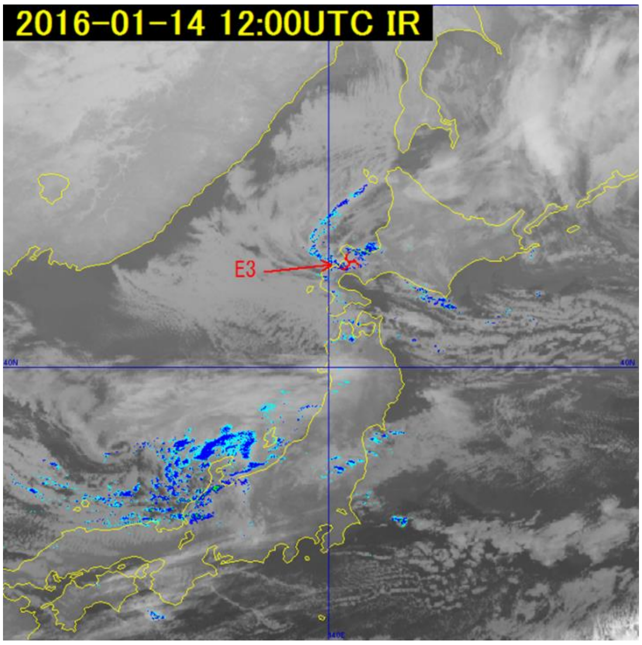

Fig. 6-2-12 B13 infrared image with radar echoes for 12:00 UTC on 14 January 2016

Figure 6-2-13 shows time-series graphs of snowfall observed by AMeDAS (JMA's Automated Meteorological Data Acquisition System consisting of automated weather stations) in Kutchan and Kimobetsu in Shiribeshi Subprefecture. At both sites, heavy snowfall was recorded approximately between 07:00 and 13:00 UTC. As in this example, mesoscale cloud vortices and cloud bands emerging over the northern Sea of Japan can bring heavy snowfall upon landing. Accordingly, it is necessary to monitor mesoscale disturbances and accompanying active convective clouds through satellite image (Fig. 6-2-14).

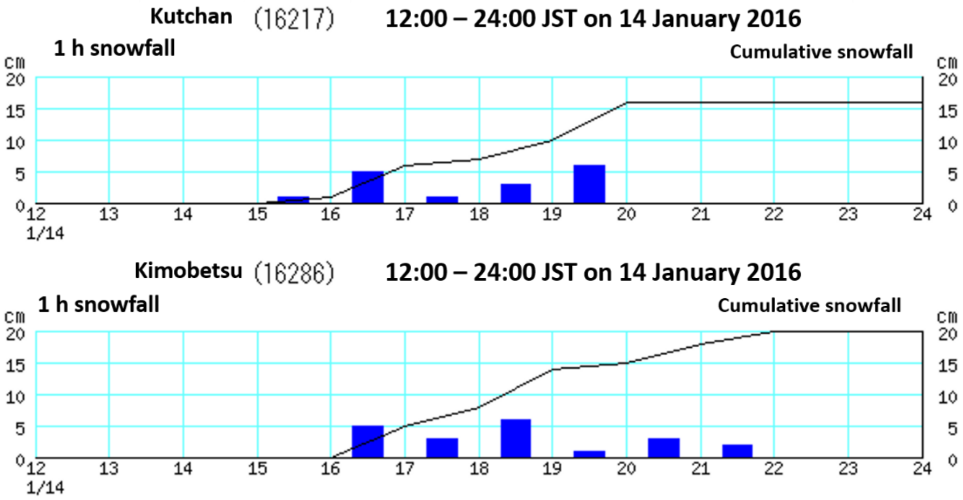

Fig. 6-2-13 Time-series graphs of snowfall observed by AMeDAS in Kutchan and Kimobetsu

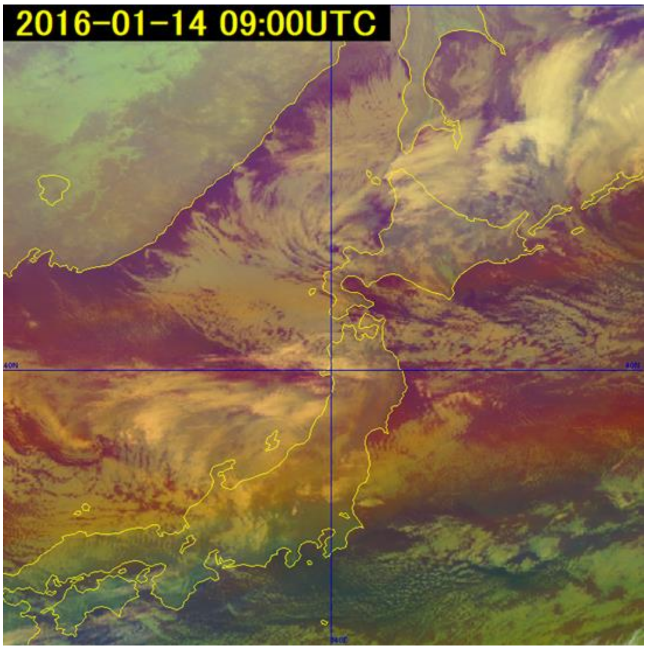

Fig. 6-2-14 Airmass RGB composite image for 09:00 UTC on 14 January 2016

(2) Typical Winter Pressure Patterns in Japan

Japan's typical winter "west-high, east-low" pressure pattern is associated with cold dry anticyclones in Siberia and cyclones in eastern Japan. Northwest seasonal winds running from high- to low-pressure areas pick up sensible heat and water vapor from the warm surface of the Sea of Japan, generating cloud streets and bringing snowfall along the mountains on the country's Sea of Japan side (known as mountain-type snowfall). However, heavy snowfall may also affect coasts and plains (plain-type snowfall). This section outlines the relationship between cloud street strikes, snowfall distribution, surface isobars and wind direction at 850 hPa.

Although a number of other elements contribute to snowfall (e.g., intensity and movement of cold-air masses at 500 hPa) focus here is placed on cloud street strikes for their visibility in satellite image.

1. Mountain-type heavy snowfall on 20 January 2016

In this event, a trough was present to the east of Hokkaido and a large zonal pressure gradient was observed over the northern Sea of Japan. The center of an upper cold-air mass with prominent lower cold advection was present over northern Japan. This pressure pattern tends to produce north-to-south cloud street strikes over the Sea of Japan, leading to strong northwest seasonal winds. Cb clouds develop on the windward side of Japan's backbone mountains, bringing heavy snow (Fig. 6-2-15). Snowfall with this pattern generally occurs from the Hokuriku region to the San'in region.

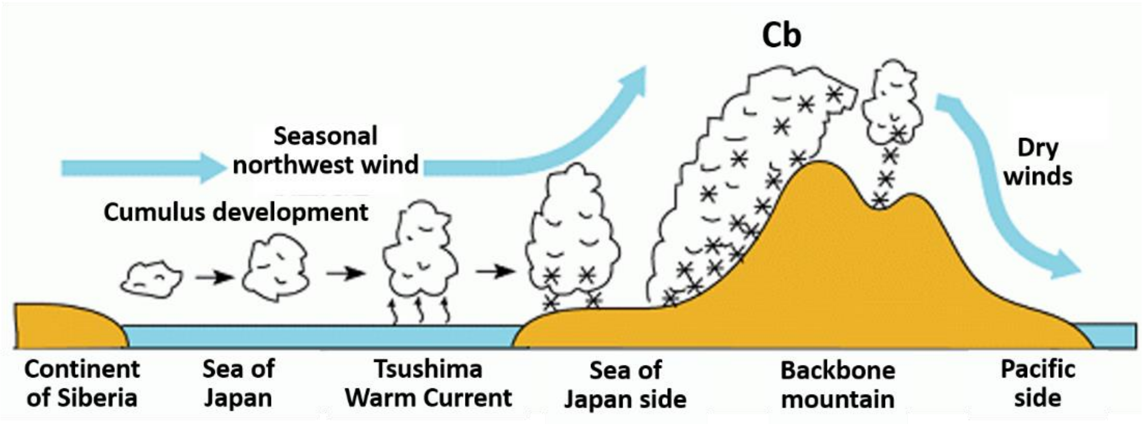

Fig. 6-2-15 Schematic drawing of mountain-type snowfall
(from the homepage of Matsue Local Meteorological Office)

A cyclone over the central Sea of Japan at 00:00 UTC on 19 January had advanced to sea areas near the Kuril Islands by 00:00 UTC on 20 January, and the zonal pressure gradient increased. Isobars around Japan became nearly meridional (Fig. 6-2-16). The cloud street strike direction generally matched the wind direction at 850 hPa (Fig. 6-2-17).

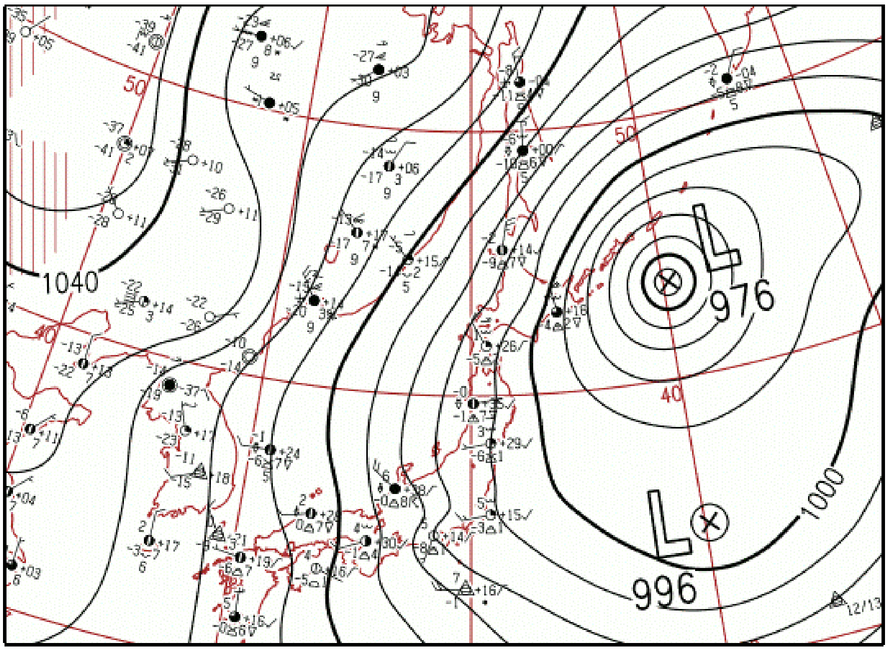

Fig. 6-2-16 Surface weather chart for 00:00 UTC on 20 January 2016

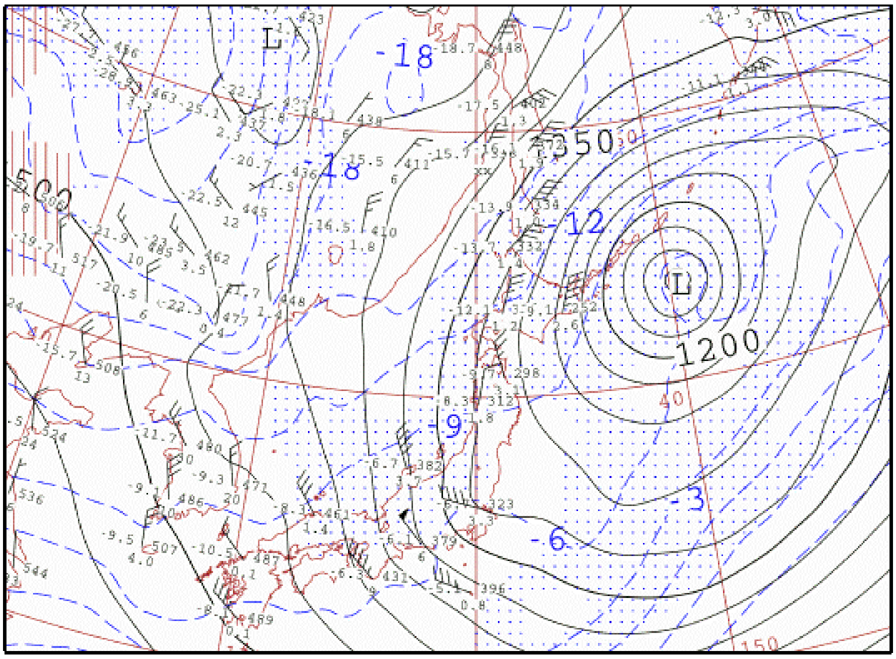

Fig. 6-2-17 850 hPa upper weather chart for 00:00 UTC on 20 January 2016

In infrared image for 00:00 UTC on 20 January, cloud streets containing Cb were observed over the Sea of Japan, and tall cloud streets that had passed over Sekigahara, the Kii Channel and the Bungo Channel were seen on the Pacific side. In the 24 hours until 15:00 UTC on 20 January, heavy snowfall of 42 cm in Sugadaira, Nagano Prefecture, and 41 cm in Kusatsu, Gunma Prefecture was recorded (Fig. 6-2-19).

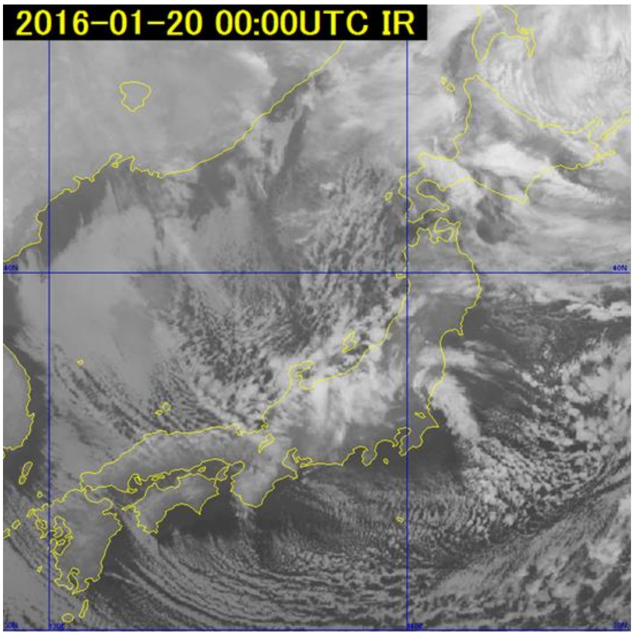

Fig. 6-2-18 B13 infrared image for 00:00 UTC on 20 January 2016

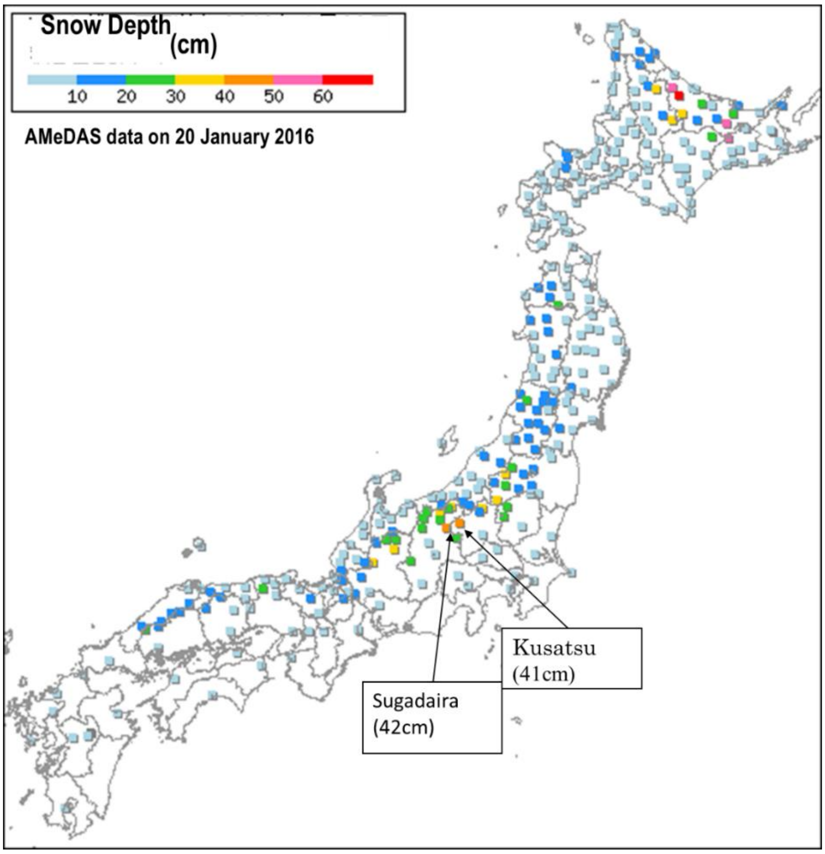

Fig. 6-2-19 Distribution of 24-hour snowfall observed by AMeDAS

2 Plain-type heavy snowfall on 16 February 2016

In this example, the center of an upper cold air mass was present over the western Sea of Japan, the zonal pressure gradient was relatively gentle over the Sea of Japan in general, and seasonal surface winds were relatively weak. With this pattern, the cloud street strike direction is often from west to east. Convective instability may increase, and minor cyclones on the ground may arise when an upper cold low moves toward the Sea of Japan. As a result, Cb clouds develop and move over Japan, and heavy snowfall is observed in coastal and plain areas (Fig. 6-2-20). Snowfall associated with this pattern generally occurs on the Sea of Japan side of the area from the Tohoku region to the Hokuriku region.

A cyclone over the northern Sea of Japan at 00:00 UTC on 15 February approached the Kuril Islands at 00:00 UTC on 16 February, and an anticyclone over the continent began expanding eastward from South China, resulting in the typical winter pressure pattern seen around Japan with a trough over the western Sea of Japan (Fig. 6-2-21). The isobars over the northern Sea of Japan struck from northwest to southeast. The pressure gradient weakened over the central and western Sea of Japan, resulting in isobars with a zonal direction.

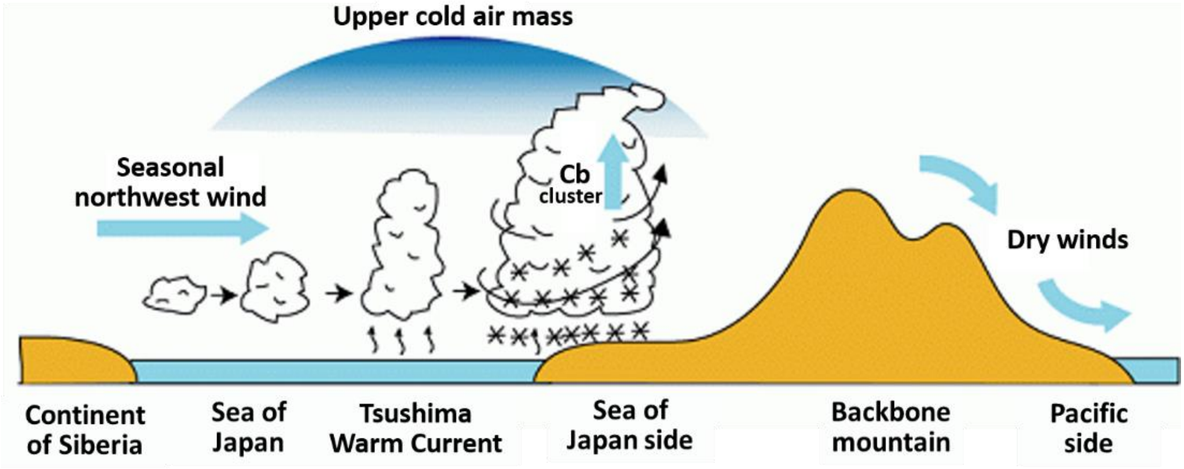

Fig. 6-2-20 Schematic drawing of plain-type snowfall
(from the homepage of Matsue Local Meteorological Office)

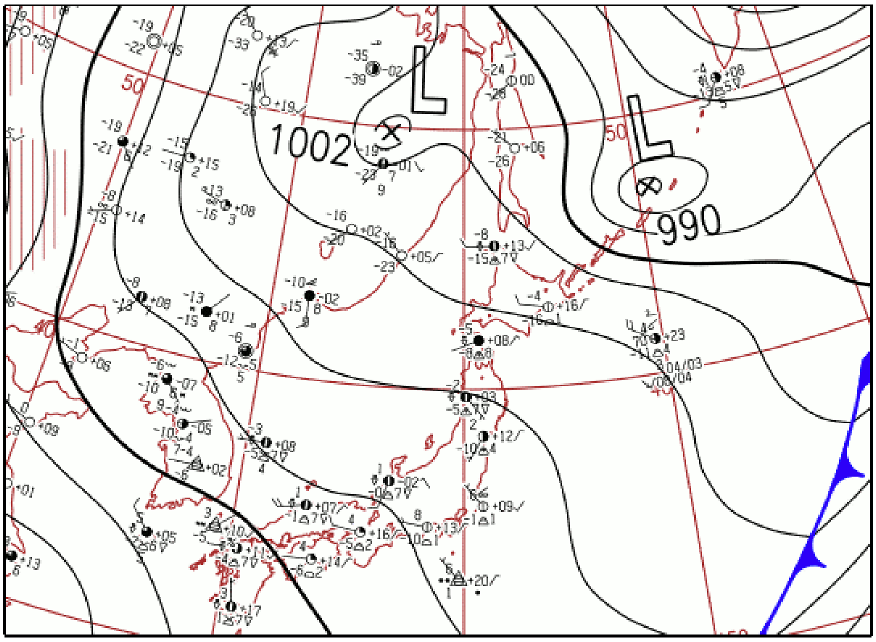

Fig. 6-2-21 Surface weather chart for 00:00 UTC on 16 February 2016

In infrared image for 00:00 UTC on 16 February, cloud streets with east-west strikes were seen over the western Sea of Japan, almost parallel to the isobars and the wind direction seen at 850 hPa (Fig. 6-2-22). Cu and some Cg were observed, and heavy snowfall occurred in overcast areas from the Noto Peninsula to the Tohoku region along the Sea of Japan.

In the 24 hours until 15:00 UTC on 16 February, heavy snowfall was observed in Oisawa, Yamagata Prefecture (35 cm) and Yashima, Akita Prefecture (32 cm) (Fig. 6-2-24).

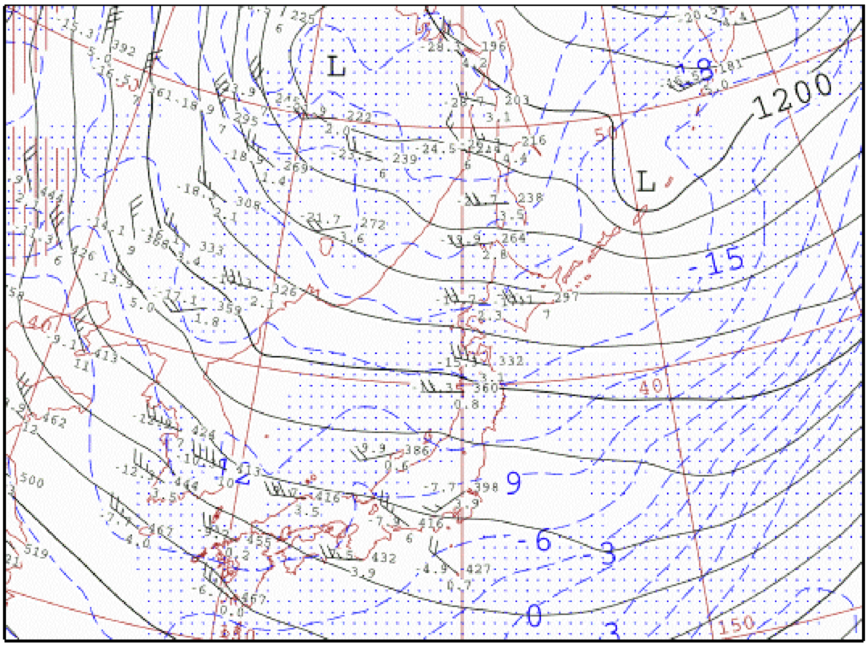

Fig. 6-2-22 850 hPa upper weather chart for 00:00 UTC 16 February 2016

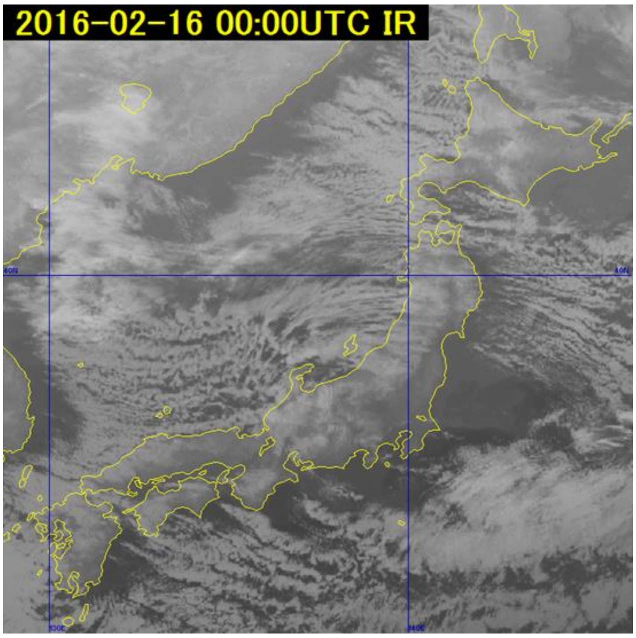

Fig. 6-2-23 B13 infrared image for 00:00 UTC 16 February 2016

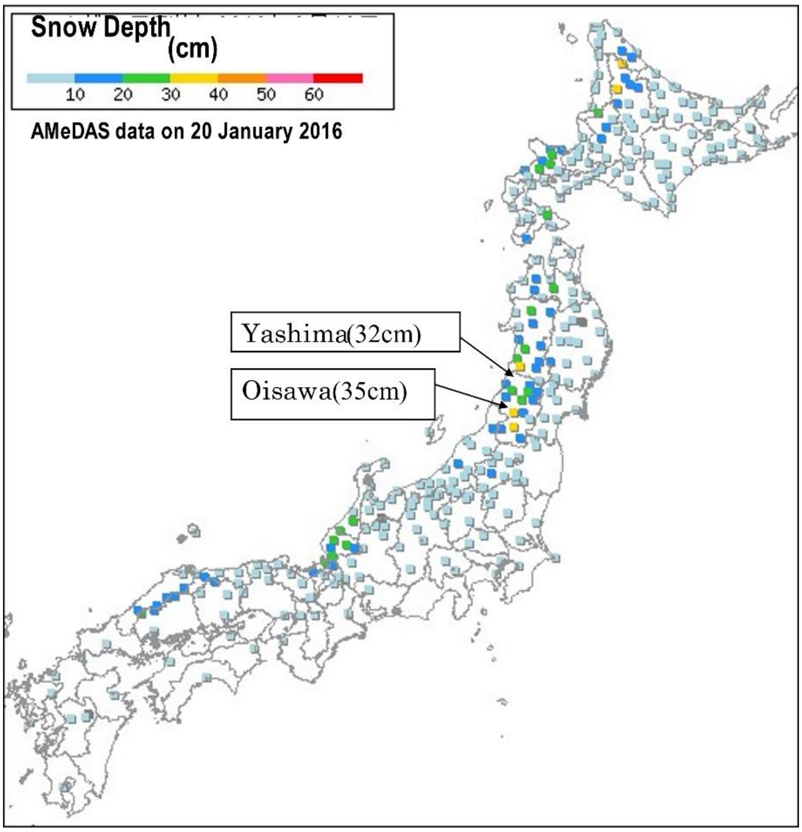

Fig. 6-2-24 Distribution of 24-hour snowfall observed by AMeDAS

References:

- Okabayashi, T. (1972) Snow Clouds seen from Satellite and their Use in Study on Snowfall, Kisyo-kenkyu Note, 113, 74-106. (In Japanese)
- Sapporo District Meteorological Observatory (1989) Study on Small Low generating around Western Coast of Hokkaido, Technical Report of Sapporo District Meteorological Observatory (Special issue 38), 137 pp. (In Japanese)

6.3. Strong Winds

Obtaining wind information from satellite data generally involves calculating motion by tracking cloud cells in successive images. In some cases, characteristic cloud patterns emerge with strong winds ("Surface wind speeds exceed 20 kt when convective cloud lines composed of cloud streets form along cold air mass blowout"; Meteorological Satellite Department, 1976), and "Wind speeds exceed 20 kt at mountain tops when lee wave clouds emerge on their lee side. The interval between associated cloud streets is proportional to the wind speed, and the interval widens as wind speed increases; Obana, 1983)".

This section presents extraction of information on lower winds based on the passage of a cold front in winter.

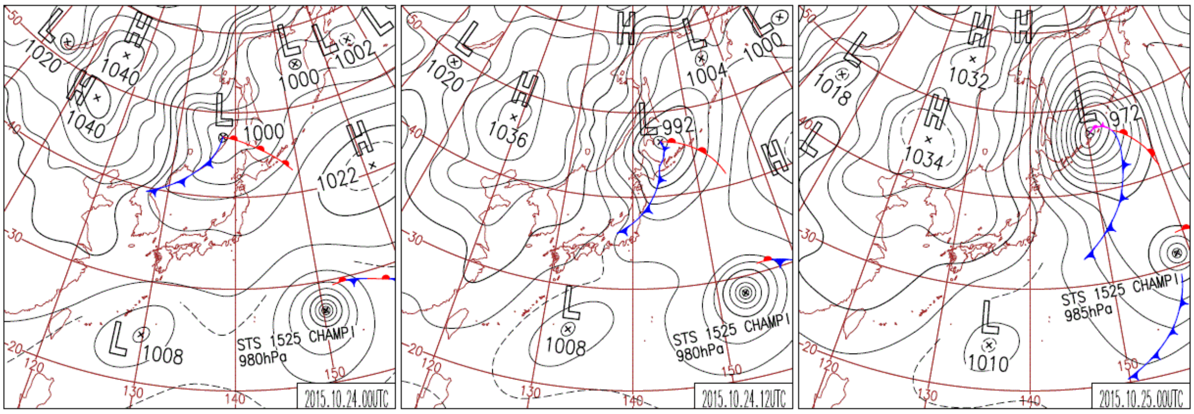

Fig. 6-3-1 Surface weather charts

Left: for 00:00 UTC on 24 October 2015, center: for 12:00 UTC on 24th, right: for 00:00 UTC on 25th

6.3.1. Strong Winds When a Cold Front Passes

Between 24 and 25 October 2015, a cyclone developed rapidly near Primorye, Russia, characterized by a central pressure reduction of 28 hPa by the time of its passage over northern Hokkaido. A winter-type pressure pattern formed around Japan, and north-northwest winds with maximum instantaneous speeds of 13.3 m/s were recorded at 02:54 UTC (11:54 JST) on 24 October in Tokyo.

(1) When the Cold Front is over the Sea of Japan

In the surface weather chart for 00:00 UTC on 24 October, a low pressure area is seen around Primorye, and the cold front is located around the northern part of the Korean Peninsula (Fig. 6-3-1). The cloud area corresponding to the cold front has not been organized, and no corresponding cloud area is seen in satellite imagery (figure not shown).

Focus here is placed on the cold front along the Sea of Japan. Figure 6-3-2 shows infrared image from nine hours after the above situation. The cloud area corresponding to the cold front is distinct, and can be inferred as an **A-B** Cb-Cu line extending from Akita Prefecture to offshore San'in. This line advanced east-southeastward or southeastward at speeds of 30 – 35 kt. Convective cloud streets accompanying the cold-air mass were as yet indistinct over the central Sea of Japan to the rear of the front, but were visible over the sea's northern part.

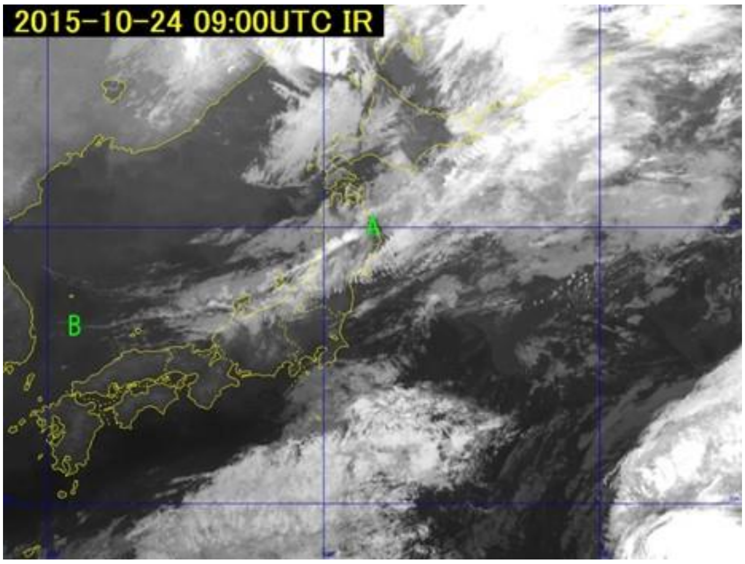

Fig. 6-3-2 B13 infrared image for 09:00 UTC on 24 October 2015

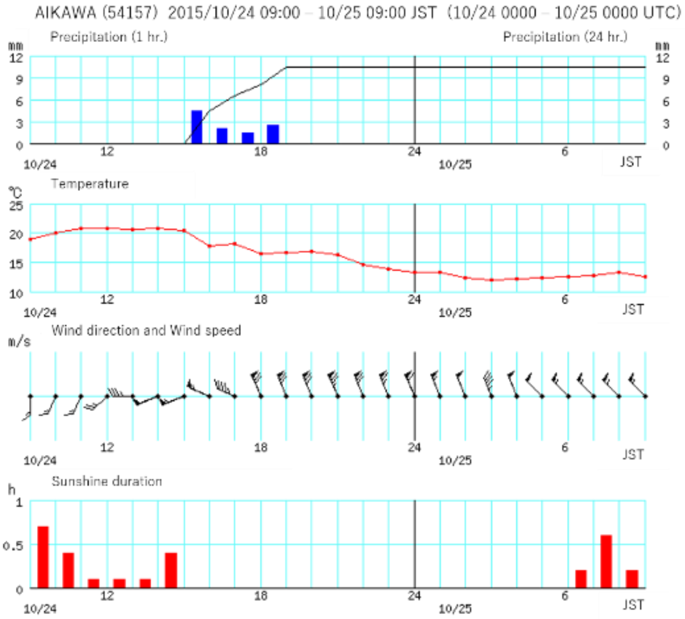

Fig. 6-3-3 Time-series graph of AMeDAS observations in Aikawa, Niigata Prefecture, between 00:00 UTC (09:00 JST) on 24 and 00:00 UTC (09:00 JST) on 25 October 2015

Strong winds with directions between west-northwest and northwest at the rear of the cold front can be inferred from the movement of the Cb-Cu line. Figure 6-3-3 shows the following:

1. The wind direction changed from west-southwest to west-northwest, and temperatures declined around 07:00 UTC (16:00 JST).
2. The wind direction changed from west-northwest to north-northwest, the wind speed increased, and the temperature declined around 09:00 UTC (18:00 JST).

The maximum instantaneous wind speed of 20.8 m/s (40 kt; north-northwest) was observed at 08:48 UTC (17:48 JST), indicating that the latter change corresponds to the Cb-Cu line in the satellite image. The maximum wind speed of 15.9 m/s (31 kt; north-northwest) was observed at 11:28 UTC (20:28 JST), which closely correlates with the movement speed (30 – 35 kt) of the **A-B** Cb-Cu line.

(2) When the Cold Front is Inland

When passing over the backbone mountains, the Cb-Cu line became obscure, making it difficult to locate the front over the inland area in satellite image. Here, the time at which the front passed over the Kanto region is estimated from time-series AMeDAS observations in Tokyo as shown in Fig. 6-3-4. A change in wind direction from west-southwest to west-northwest is seen at 12:30 UTC (21:30 JST) on 24 October. Wind speeds showed a decreasing tendency after the wind direction changed to west-northwest, but increased from 0.4 m/s (1 kt) at 13:50 UTC (22:50 JST) to 9.2 m/s (18 kt) at 15:10 UTC (00:10 JST on the 25th). The temperature showed a gradually decreasing tendency overnight, with no obvious change associated with the passage of the front. These observations suggest that the cold front passed over Tokyo at around 12:30 UTC (21:30 JST) on 24 October. In this example, there was a time lag of 2 – 3 hours until winds strengthened after the front's passage.

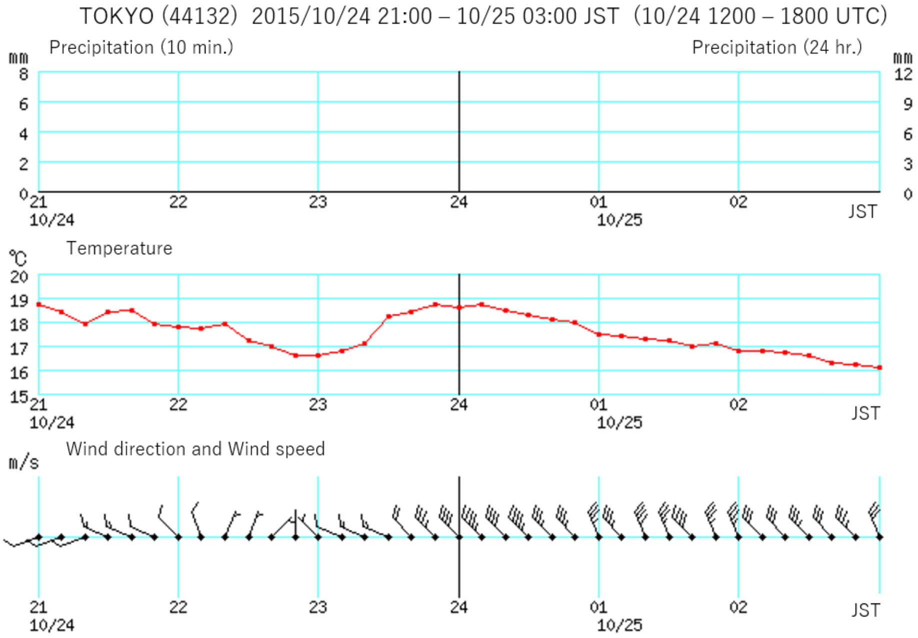

Fig. 6-3-4 Time-series graph of AMeDAS observations in Tokyo between 12:00 UTC (21:00 JST) and 18:00 UTC (03:00 JST on the next day) on 24 October 2015

The infrared image in Fig. 6-3-5 shows characteristics present just before the cold front passed. Some convective clouds over the Sea of Japan moved over land on became obscure, but others remained over the sea and were traceable. The lines for these clouds reach the area around A-B in the figure. Over the northern Sea of Japan, cloud streets accompanying the cold-air mass developed and expanded, indicating an inflow of cold air. Lee wave clouds are seen around Sado Island, Chubu and over the sea east of Japan, indicating strong winds in the upper atmosphere.

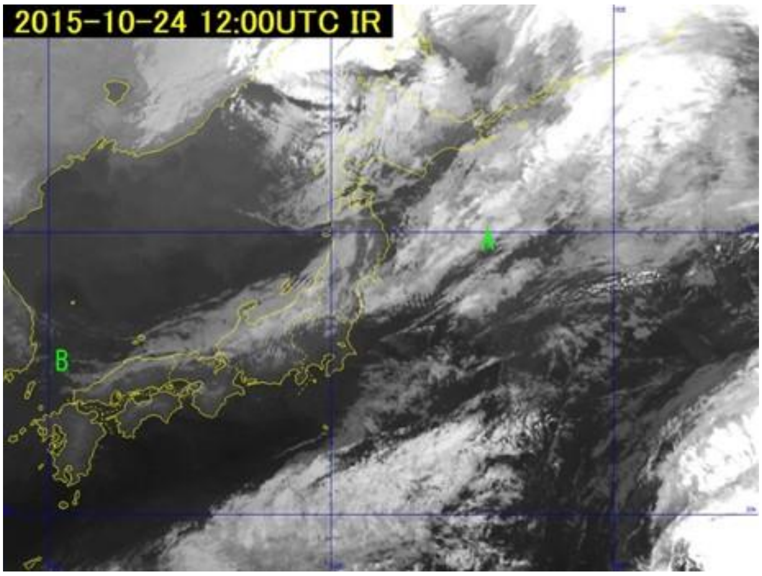

Fig. 6-3-5 B13 infrared image for 12:00 UTC on 24 October 2015

Wind speeds can be estimated from the interval between lee wave cloud lines because the two are proportional (Section 3.7 Lee Wave Clouds). In this example, the wind speed U (m/s) can be estimated using the wavelength λ (km) of the lee wave clouds emerging around Sado Island and the equation proposed by G.A. Corby (1957):

$$U = 1.7\lambda + 4.8.$$

The distance between the cloud lines in the infrared image is approximately 15 km (Fig. 6-3-6), suggesting a wind speed of 30.3 m/s (59 kt). This roughly matches the speed of 60 kt estimated from GSM data at the cloud top height (approx. 600 hPa) of the lee wave clouds in this cross-section (Fig. 6-3-7).

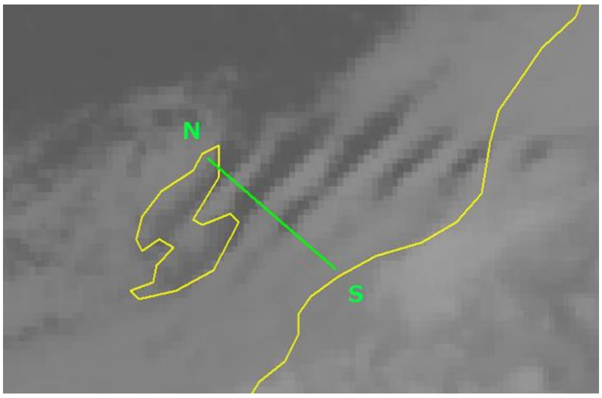

Fig. 6-3-6 B13 infrared image for 12:00 UTC on 24 October 2015

Enlarged view of the area around Sado Island. The cross-section at the green line **NS** was analyzed.

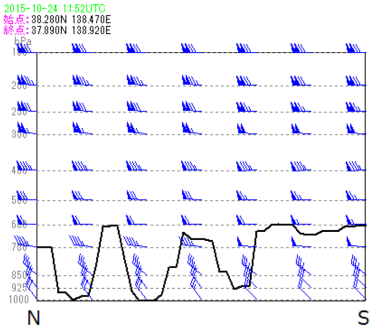

Fig. 6-3-7 Cross-section values along the line **NS** for 12:00 UTC on 24 October 2015.
Line: brightness temperature converted to pressure
Barbs: wind direction and speed (pennants: 50 kt; long barbs: 10 kt; short barbs: 5 kt). Both from GSM data

(3) When the Cold Front Passes to the Pacific

In the infrared image for 00:00 UTC on the 25th after the front passed over Japan, skies over the inland area of Kanto are clear, as commonly seen in winter, influenced by the backbone mountains (Fig. 6-3-8). Meanwhile, the Hokkaido and Tohoku regions were affected by the cold air mass and strong winds, and were covered by convective cloud streets from the Sea of Japan to the Pacific. The convective cloud cells moved at 25 – 30 kt southeastward in the area offshore of Akita on the Sea of Japan side and at 40 – 45 kt southeastward in the area offshore of Sanriku on the Pacific side. These values are in close agreement with those at 850 hPa calculated from GSM data.

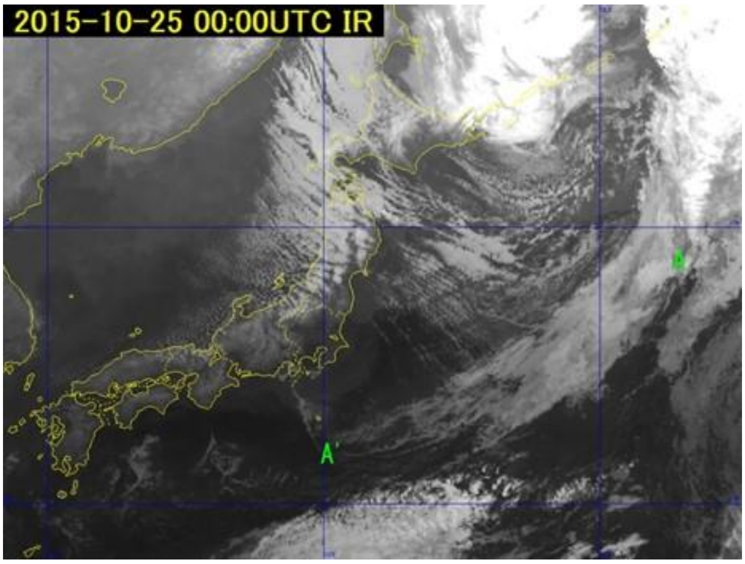

Fig. 6-3-8 B13 infrared image for 00:00 UTC on 25 October 2015
A to A' shows the position of the front from satellite imagery

6.3.2. Key points in Analyzing Strong Winds by Satellite Imagery and Its Applications

(1) Cu clouds emerging with cold-air inflow begin to form streets when the surface wind speed exceeds 20 kt. Determination of the movement of individual cells in cloud streets and analysis of low-level winds allows estimation of wind speeds over land and sea. Since cloud streets strike parallel to the wind direction over land and sea, wind direction can be estimated from that (Meteorological Satellite Department, 1976).

(2) When lee wave clouds form on the leeward side of mountain ranges, the wind speed around mountain tops is expected to exceed 20 kt. As intervals between lee wave cloud lines exhibits a linear relationship with wind speed (i.e., stronger winds equate to wider intervals), wind speed can be determined from these intervals. (Obana, 1983).

References:

- Meteorological Satellite Department (1976) Application of Meteorological Satellite Data in Analysis and Forecasting (Translation of ESSA Tech. Rep. NESC 51), Japan Meteorological Agency, 105. (In Japanese)
- Obana, R. (1983) Anomalous Clouds under orographical Influence, Analysis and application of Cloud Image from the Meteorological Satellite HIMAWARI, Meteorological Satellite Center, 251-257. (In Japanese)
- Corby, G.A. (1957) A Preliminary Study of Atmospheric Waves using Radiosonde Data, Q.J.R.Met.Soc., 83, 49-60.

6.4. Fog

6.4.1. General Characteristics of Fog

In meteorological satellite observation, it is impossible to tell whether a cloud base is on the ground (i.e., fog) or above it (i.e., cloud) because clouds are seen from outer space. Accordingly, the two phenomena are generally treated together as fog (or St) in cloud analysis using satellite imagery. The related characteristics are described here.

In infrared imagery, fog appears in dark grey. Since its cloud top is low and there is a small temperature difference from surrounding land/sea surfaces, fog identification in such imagery is challenging. The top of fog with a strong surface inversion is warmer than the surrounding fog-free surface. This is known as black fog because it appears darker than the surface.

In visible imagery, fog appears as cloud in light grey. Its top surface is smooth and even, and its top height is nearly uniform. Borders of inland fog areas often follow topography contours, making it easily identifiable in visible imagery (unless covered by thick upper or middle clouds). Fog covered by thin upper clouds can also be identified in most cases, but misidentification as rugged convective clouds may occur when covering granular upper clouds cast shadows over fog. As fog generally moves and transforms slowly, its movement and shape change can be referenced for identification.

As fog is generally less than several hundred meters thick, mountains and hills can act as obstacles and create fog-free areas on their leeward side. Based on this, wind direction can generally be estimated for such locations.

6.4.2. Daytime Fog

Figure 6-4-1 shows B03 visible image with annotation of identified fog areas for 00:00 UTC on 8 March 2016, and Fig. 6-4-2 shows Natural Color RGB composite image for the same time. In these images, veil-like white cloud areas (dashed lines in Fig. 6-4-1), which are lower-cloud with fog, are seen in the Kanto region, the prefectures of Yamanashi and Nagano, and along the coast between Kanto and offshore Sanriku. The phenomenon in northern Kanto and the prefectures of Yamanashi and Nagano is called radiation fog, produced by nighttime radiative cooling, and that along the coast between Kanto and offshore Sanriku is called advection fog, produced by warm and humid inflow. Fog in southern Kanto is a mixture of the radiation and advection types.

Radiation fog in northern Kanto and the prefectures of Yamanashi and Nagano is caused by lower nighttime surface temperatures associated with radiative cooling. It tends to follow topography in valleys and basins, with temporal expansion in the same locations. Fog rapidly dissipates in the morning as a result of solar energy.

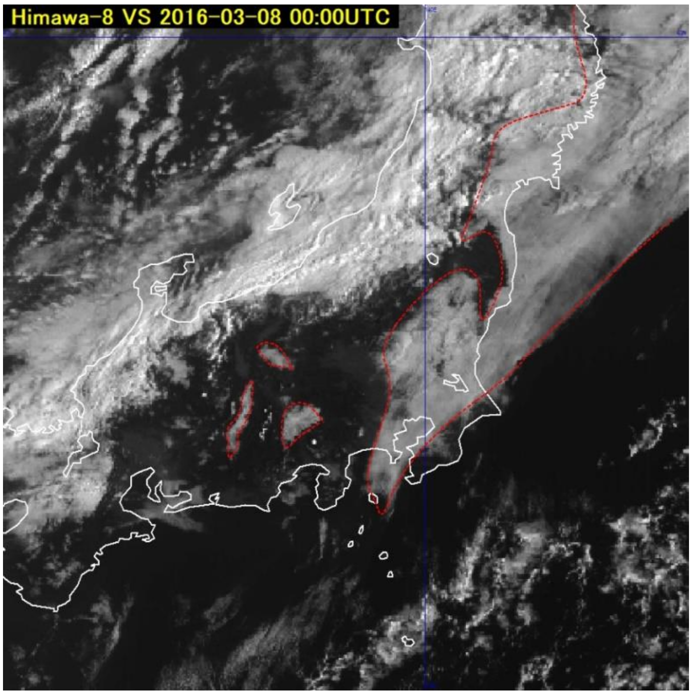

Fig. 6-4-1 B03 visible image with annotations of analyzed fog areas (red broken lines), for 00:00 UTC on 8 March 2016

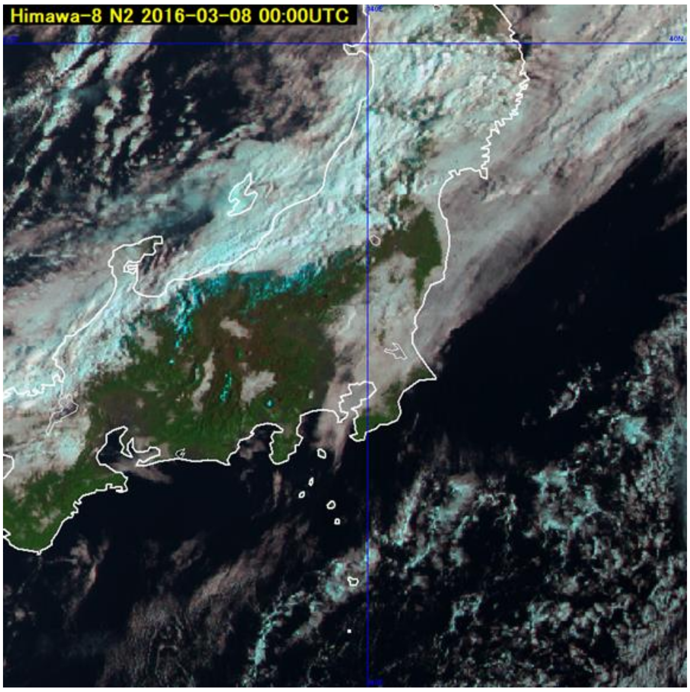

Fig. 6-4-2 Natural Color RGB composite image, at 00:00 UTC on 8 March 2016

However, advection fog over the coast between Kanto and offshore Sanriku does not rapidly dissipate after sunrise. In time-series satellite imagery, shading indicates fog moving northward. The fog in the example referenced here appears to have been caused by an inflow of warm humid air from the southwest onto the cold sea surface, causing saturation and condensation in the lower atmosphere. Figure 6-4-3 shows a surface weather chart for 00:00

UTC on 8 March 2016, Fig. 6-4-4 shows MSM numerical prediction for 925 hPa for wind and temperature, and Fig. 6-4-5 shows sea surface temperature distribution. The fog in the area from the eastern sea off Kanto to offshore Sanriku occurred where warm humid inflow from the southwest overlapped an area with low sea surface temperature.

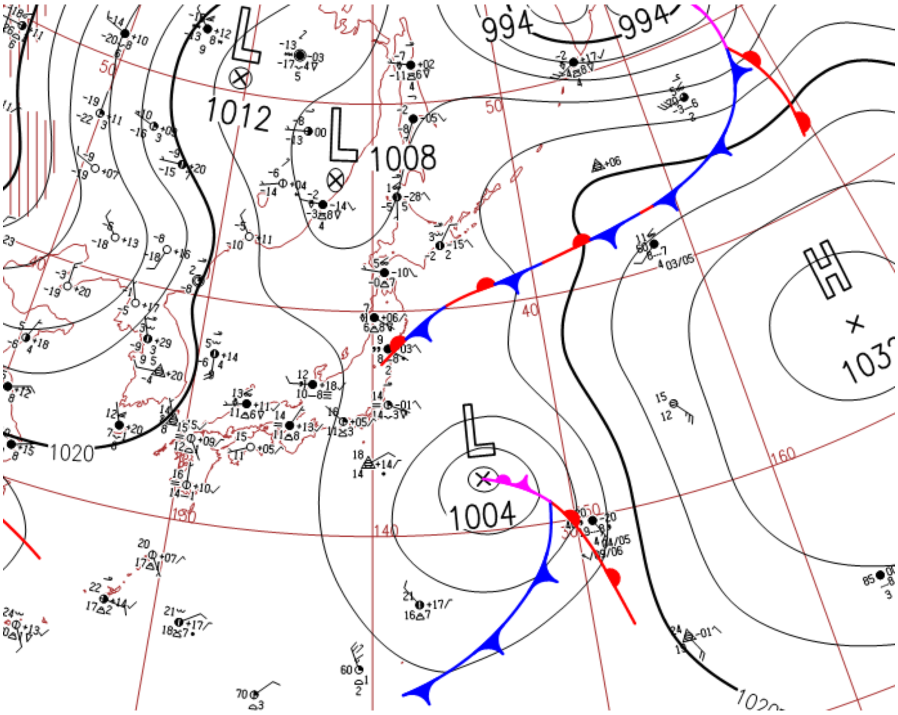

Fig. 6-4-3 Surface weather chart for 00:00 UTC on 8 March 2016

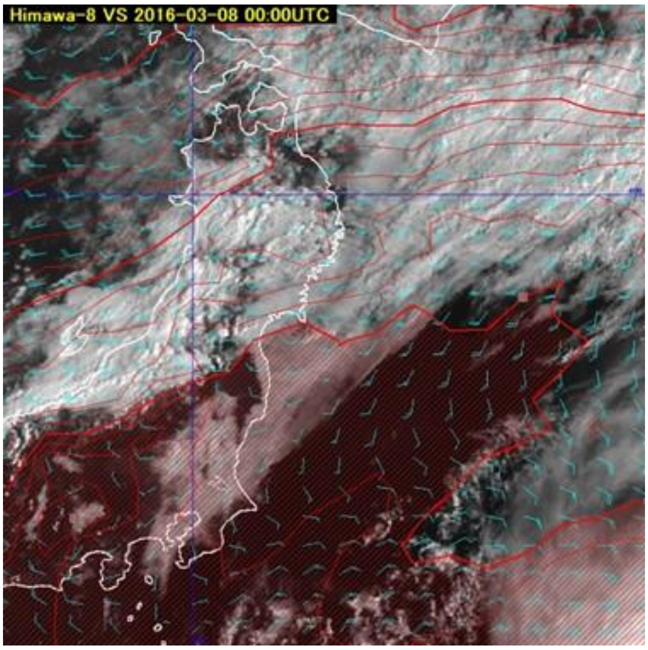

Fig. 6-4-4 B03 visible image and MSM 925 hPa numerical prediction, the area shaded in red indicates temperature above 10 ℃

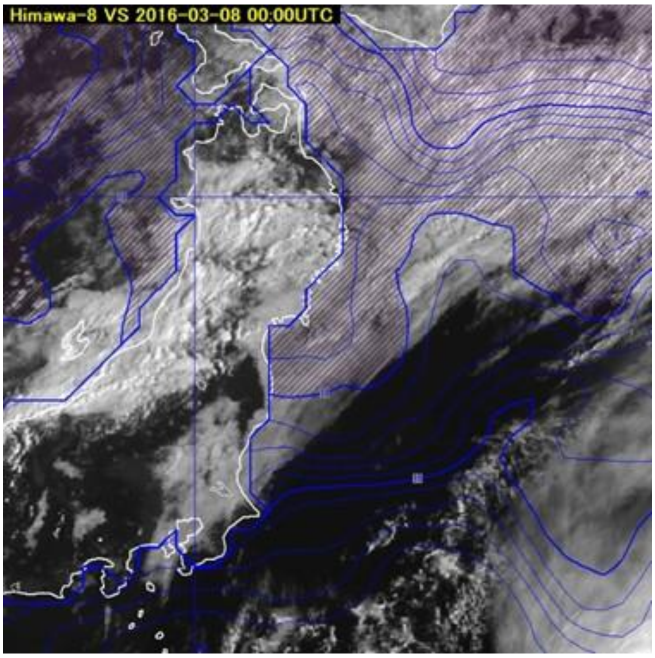

Fig. 6-4-5 B03 visible image and the sea surface temperature, the area shaded in blue indicates temperature below 10 ℃

6.4.3. Night Fog

For analysis of nighttime fog, difference images of 3.8 µm (equivalent to B07 for Himawari-8/9) and 10.8 µm (equivalent to B13 for Himawari-8/9) are generally used for Himawari-6 and 7. For Himawari-8/9, Night Microphysics RGB Composite Image provides support for fog detection.

Figure 6-4-6 shows an overlay of difference image for B07 (3.9 µm) and B13 (10.4 µm) for 21:00 UTC on 3 January 2016 and surface weather observation data for the same time. White areas are seen to be scattered over western Japan, and fog was observed in various places from surface weather data.

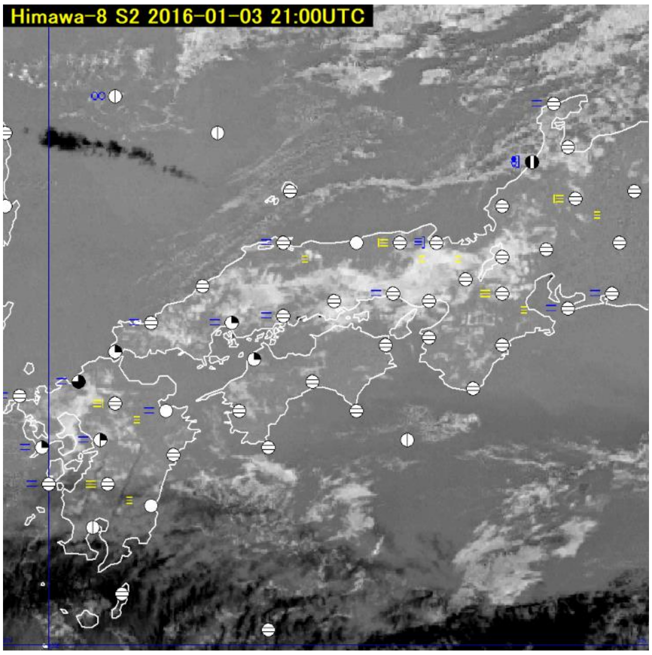

Fig. 6-4-6 The difference image of B07 and B13 of night fog emerged at various locations in western Japan, at 21:00 UTC on 3 January 2016

For comparison, Fig. 6-4-7 shows Night Microphysics RGB composite image for the same time, with pale-green areas making fog easily distinguishable. This image employs difference image of infrared B15 (12.4 µm) and B13 (10.4 µm) and of B13 and B07 (3.9µm), and B13 infrared image obtained by Himawari-8. It contains more information than difference image for B07 (3.9 µm) and B13 (10.4 µm), making it more useful for monitoring nighttime fog and lower clouds.

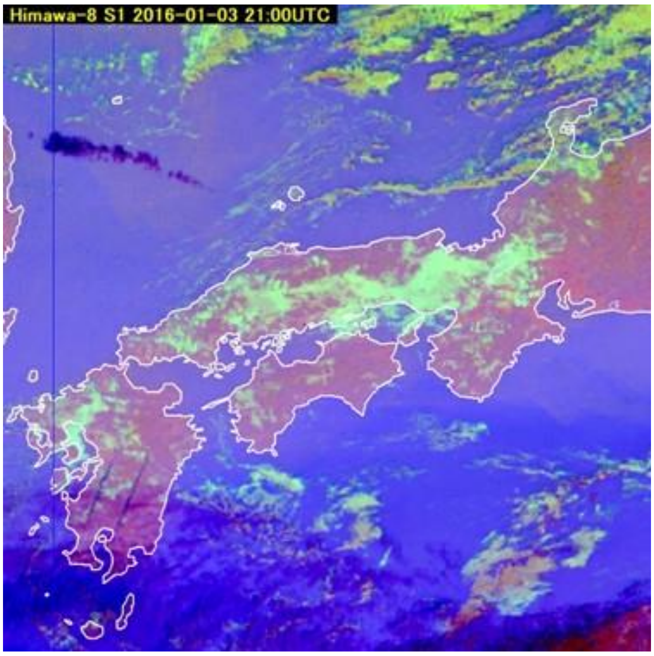

Fig. 6-4-7 Night Microphysics RGB composite image of night fog emerged at various locations

in western Japan, at 21:00 UTC on 3 January 2016

6.5. Lower Clouds

6.5.1. General Characteristics of Lower Clouds

In satellite imagery, the term ”lower clouds” refers to Cu, Sc and St types as described in Section 2.2. Less is known about lower clouds because they do not cause extreme weather conditions and are difficult to identify from infrared imagery alone (i.e., at nighttime). However, in recent years, more focus has been placed on this cloud type for their usefulness in helping to distinguish between clear and cloudy weather.

Lower clouds appear in grey or white in visible imagery and grey in infrared imagery. Convective lower clouds often form over the sea, and show up in visible imagery as large clusters of tufted or nodular cells. In infrared imagery, they appear as uniform areas with smooth surfaces and indistinct borders for individual cells due to spatial resolution limitations. Over land, stratiform lower clouds often appear as uniform areas with a smooth surface over wide regions in both visible and infrared imagery. Hasegawa (1998) reported that Cu and Sc, which have similar cloud top heights, can be discriminated by noting the faster changes in shape and gradation associated with Cu.

6.5.2. Lower Clouds over the Sea

Figure 6-5-1 presents a B03 visible image of Himawari-8 for 03:00 UTC on 21 January 2016. Lower clouds are observed over the sea, where open- and closed-cell types tend to emerge in winter. Over the sea east of Japan, open-cell Cu and Cg clouds are observed. Closed-cell clouds are also seen over the sea southeast of Hokkaido as a result of convective activity of convective cloud street weakening in correspondence with the cold-air mass. These clouds spread horizontally and changed to Sc type with a more uniform cloud top than Cu and Cg in the open-cell region with an intense cold-air mass.

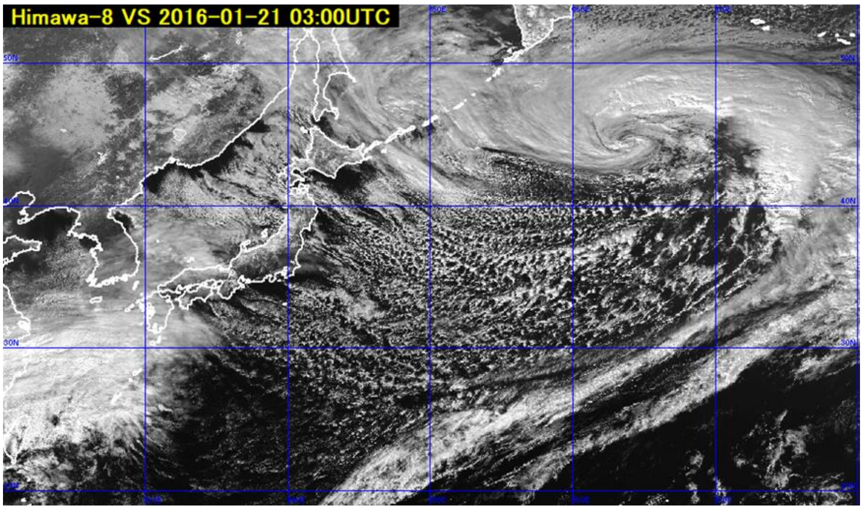

Fig. 6-5-1 B03 visible image for 03:00 UTC on 21 January 2016

6.5.3. Lower Clouds above the China Continent and the South China Sea

Figure 6-5-2 shows B03 visible image and B13 infrared image corresponding to the large-scale lower clouds over the continent and the South China Sea on 20 February 2016. The cloud areas above the continent and the East China Sea were lower St and Sc types. Lower clouds often emerge across wide areas spanning the continent and the East China Sea from winter to spring.

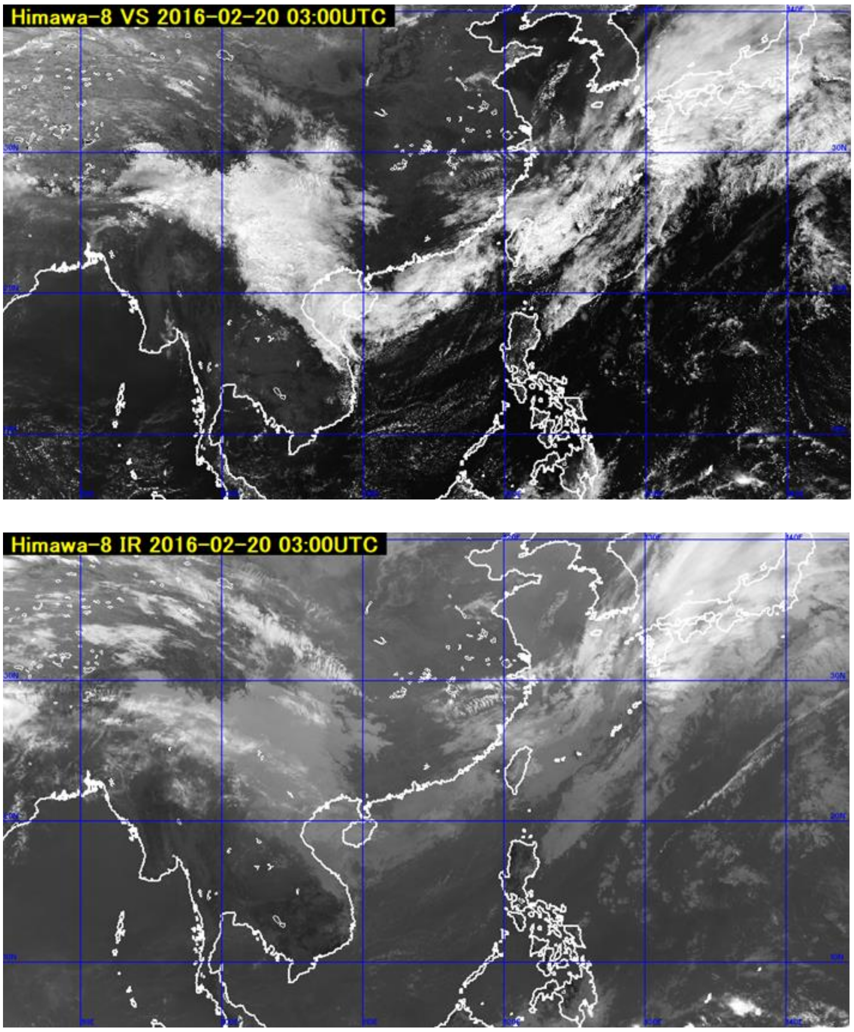

Fig. 6-5-2 B03 visible image (upper) and B13 infrared image (lower) for 03:00 UTC on 20 February 2016

6.5.4. The Distinctive Lower Clouds Seen around Japan

(1) Yamase

Yamase is a cold, wet east or northeast wind that blows over the Pacific coast of northern Japan from early to mid summer. It brings fog and St clouds that block solar radiation and sometimes cause drizzle (Fig. 6-5-3, Bokura, 1995).

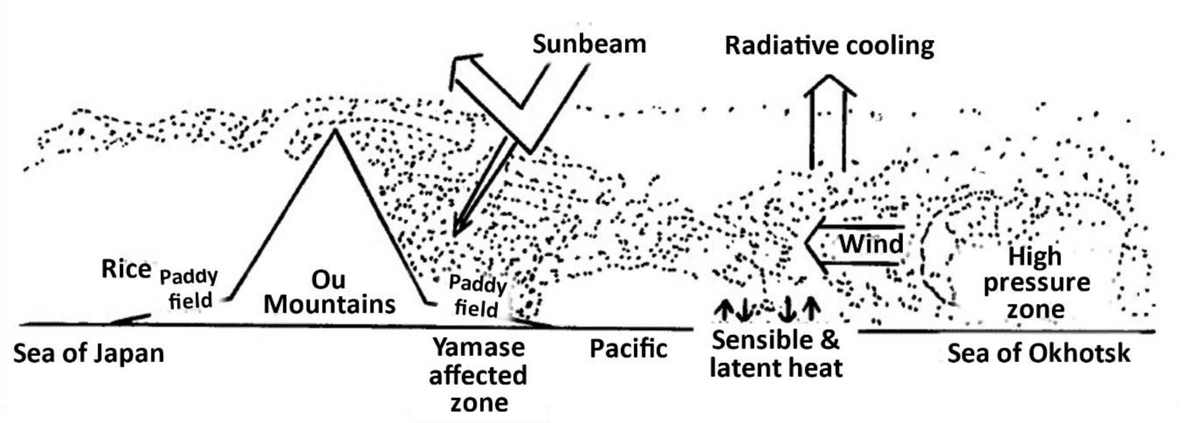

Fig. 6-5-3 Schematic drawing of Yamase (taken from Bokura, 1995)

In satellite imagery, Yamase is recognizable as St or Sc in the area from offshore Sanriku to the Pacific coast of northern and eastern Japan. Figures 6-5-4 and 6-5-5 show accompanying lower clouds. East and northeast winds from the anticyclone above the Sea of Okhotsk cover the southeastern coast of Hokkaido and the Pacific coastline of the Tohoku region with St and Sc. Lower clouds are observed from the Pacific coastlines of the Hokkaido and Tohoku regions to inland areas, while mountains prevent further spreading to the Sea of Japan side. Yamase lower clouds are observed only near the coastline rather than extending over the sea, indicating formation there. In visible imagery, clouds over land are typically brighter than those over sea.

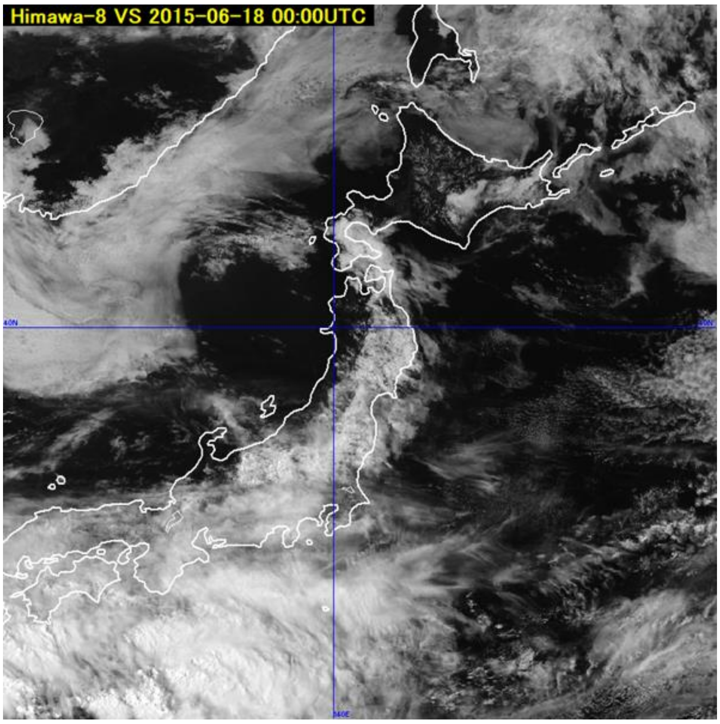

Fig. 6-5-4 B03 visible image for 00:00 UTC on 18 June 2015

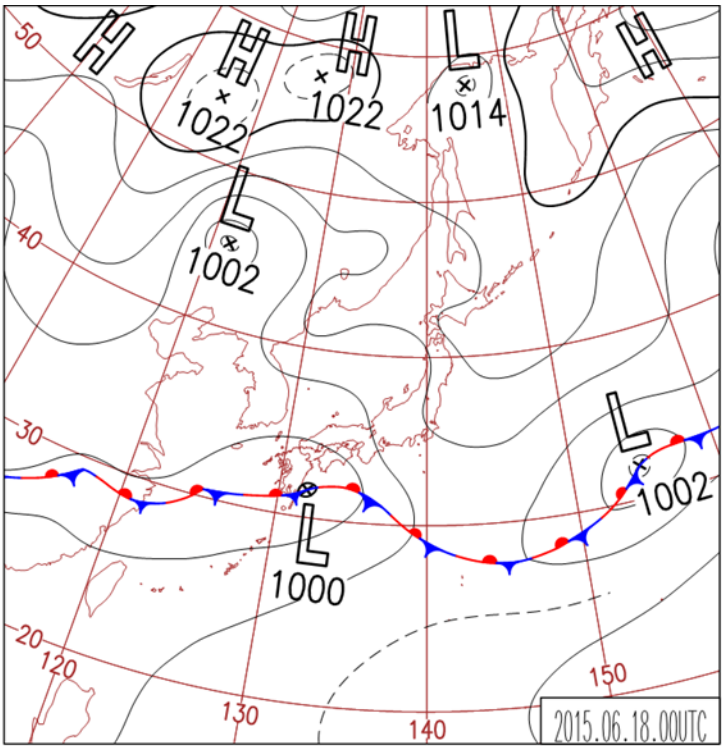

Fig. 6-5-5 Surface weather chart for 00:00 UTC on 18 June 2015

(2) The Lower Clouds along the Shear Line over the Sea South of Kanto

As the winter pressure pattern persists, flow is divided by the mountains in the Chubu region and a shear line forms over the sea south of Kanto with characteristic lower clouds around it. Suzuki and Ando (1992) defined such cloud areas as sea-cucumber or jellyfish types (Fig. 6-5-6). Cloud-area formation is closely associated with shear lines created by two air-current systems coming together around the mountain range of the Chubu region. The lines form over the sea south of Kanto in association with northeastern winds from offshore Kashima via the northern part of the mountain range and western winds from the Enshu Sea via its southern part. Convective clouds emerge along the shear line and expand northward or eastward.

Sea cucumber-type cloud areas consist of convective clouds with a long axis extending zonally along with southward expansion at the southern edge. These tend to move eastward, and have little impact on land. Figure 6-5-7 shows a B03 visible image at 03:00 UTC on 22 February 2016 when a sea cucumber-type cloud area emerged over the sea south and southeast of Kanto, and Fig. 6-5-8 shows a surface weather chart for the same time. A cloud line consisting of Cu stretches east-southeastward along its southern edge, and a cloud area consisting of Sc is seen on its northern side. This type seldom brings extreme weather over land because precipitation is often limited to the Cu line on its southern edge, the western edge of the cloud area often overlaps with the sea south of Kanto, and the air mass moves away from land.

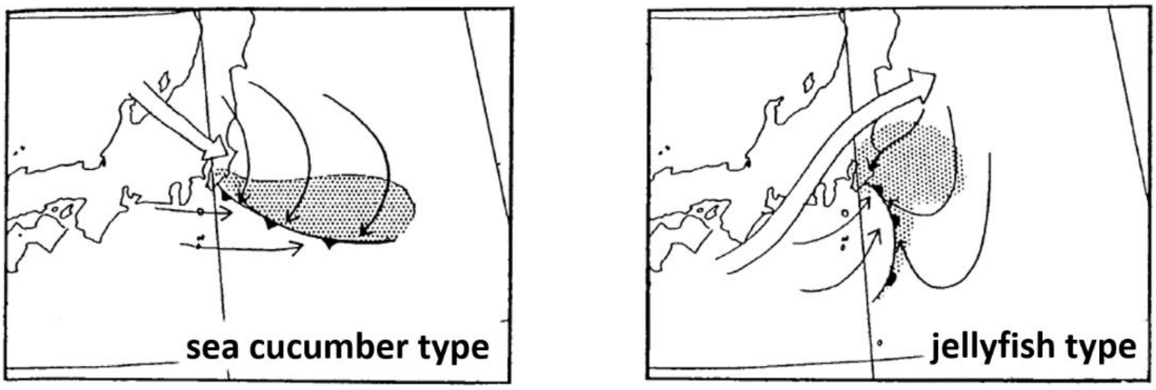

Fig. 6-5-6 Sea cucumber-type and jellyfish-type lower clouds along the shear line over the sea south of Kanto (Suzuki and Ando, 1992). Shaded areas: cloud; thin arrows: surface winds; thick open arrows: winds above the stable layer. Shear lines are indicated with front symbols.

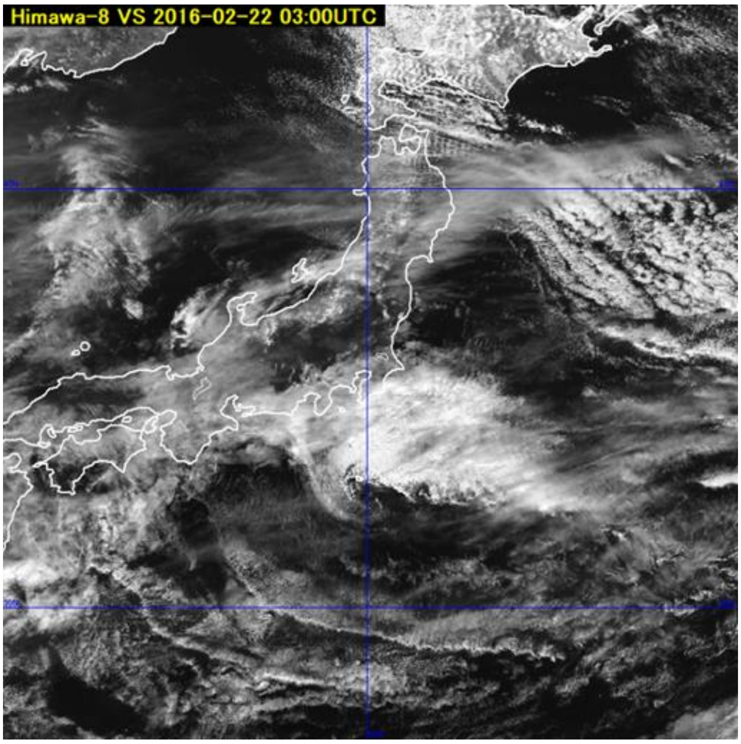

Fig. 6-5-7 B03 visible image for 03:00 UTC on 22 February 2016

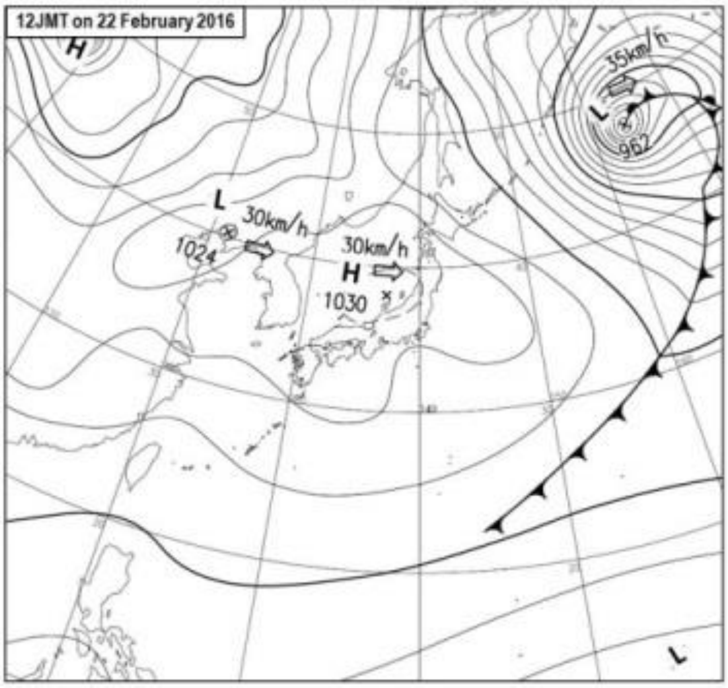

Fig. 6-5-8 Surface weather chart for 03:00 UTC on 22 February 2016

Jellyfish-type cloud areas have a long axis in the meridional direction resembling a comma, with a concave southwest end and a flared north end. These consist of lower clouds, which are often Cu, particularly on the southern and western sides. As the area develops, the northern side is composed of multi-layered clouds covered by upper and middle clouds. These tend to move northward, thereby potentially affecting the Kanto region. Figures 6-5-9 and 6-5-10 show B03 visible imagery for 03:00 UTC on 28 August 2015, when a jellyfish-type cloud area covered the Kanto region, and a surface weather chart for the same time. A Cu cloud line corresponding to a jellyfish arm extended northwest to southeast. A northern cloud area (Cu and Sc) corresponding to the jellyfish body was moving northward and expanding. This type of cloud tends to bring bad weather because precipitation is widely observed throughout its cloud area, it moves toward land, and it may be associated with upper-trough conditions and develop into a cyclone.

Sea cucumber-type cloud areas may transform into jellyfish types with the approach of an upper trough (there is no reverse transformation). Accordingly, observation of pattern developments in satellite imagery is important for forecasting.

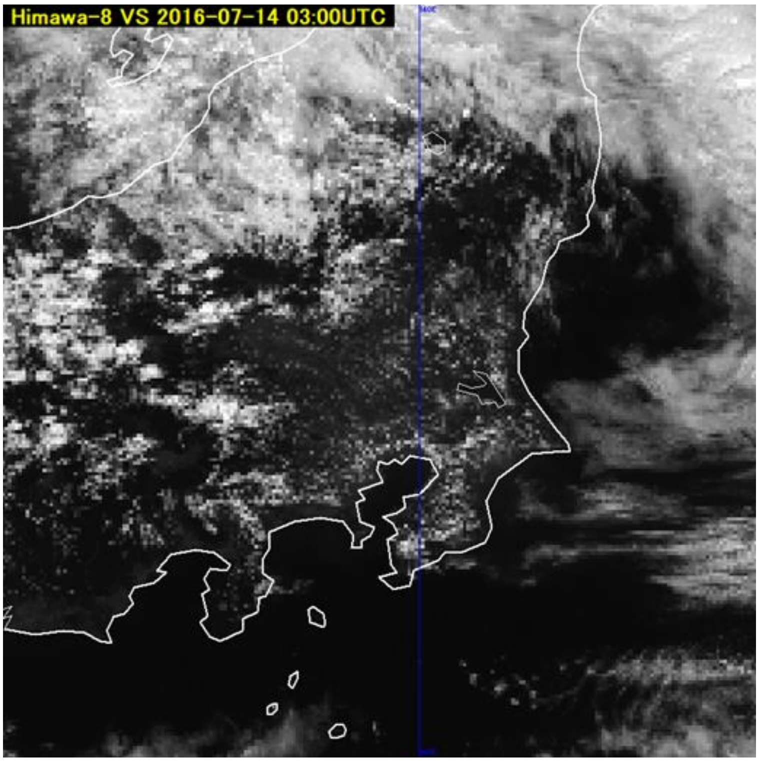

Fig. 6-5-9 B03 visible image for 03:00 UTC on 28 August 2015

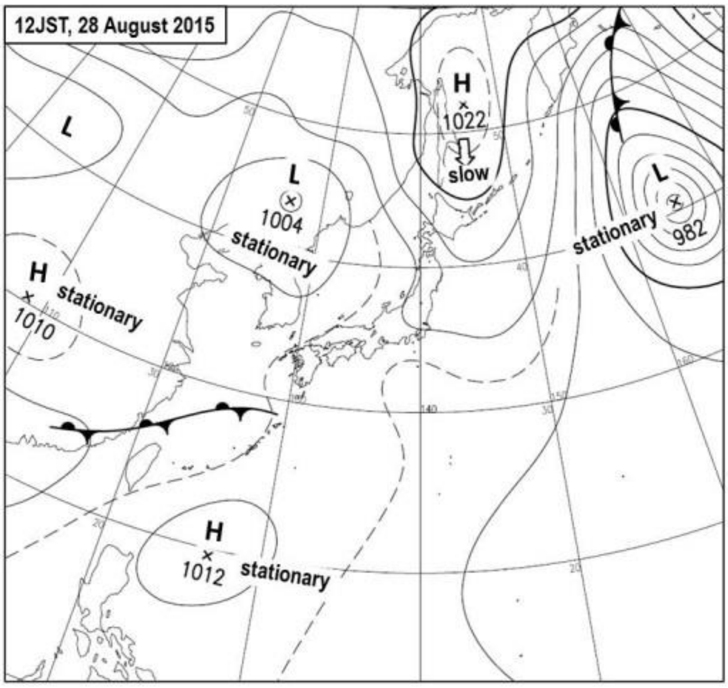

Fig. 6-5-10 Surface weather chart for 03:00 UTC on 28 August 2015

(3) Sea Breeze Front

Focus here is placed on a local-scale front that occurs at the tip of a summer sea breeze. Figure 6-5-11 shows B03 visible image, Fig. 6-5-12 shows True Color Reproduction image with prominent small Cu clouds for 03:00 UTC on 14 July 2016, and Fig. 6-5-13 shows a surface weather chart for the same time. Figure 6-5-12 clearly shows a Cu cloud line with a shape along the coast near the tip of the sea breeze slightly inland from the coast of the Kanto region.

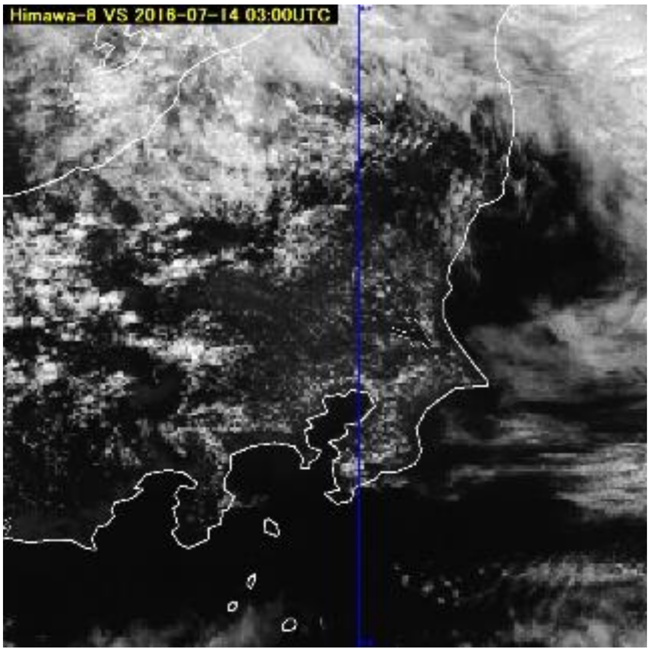

Fig. 6-5-11 B03 visible image for 03:00 UTC on 14 July 2016

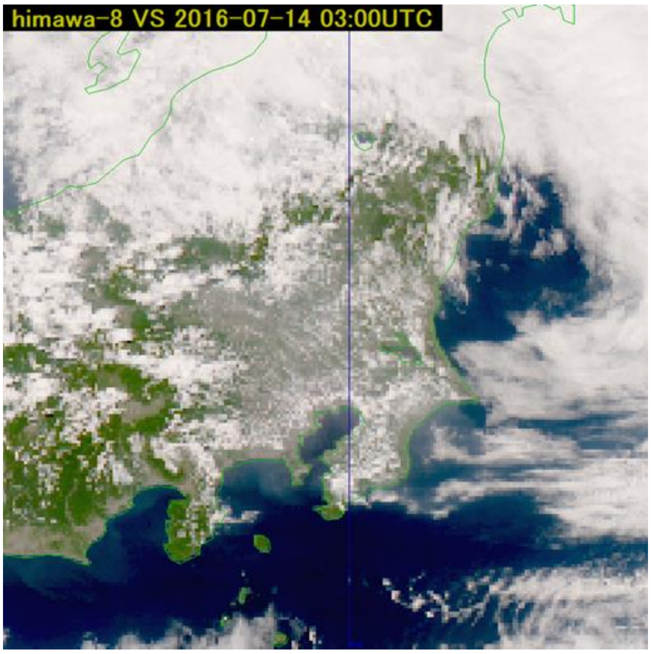

Fig. 6-5-12 True Color Reproduction image for 03:00 UTC on 14 July 2016

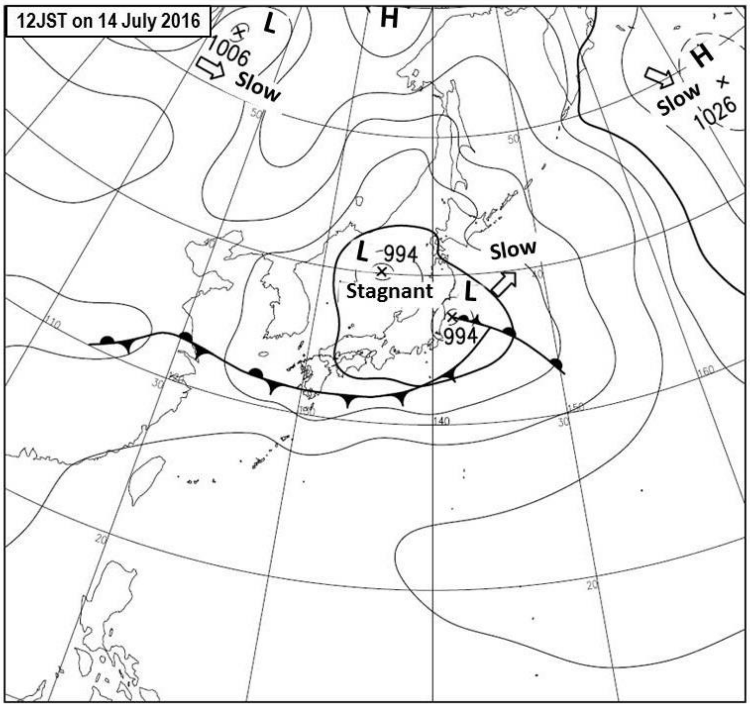

Fig. 6-5-13 Surface weather chart for 03:00 UTC on 14 July 2016

(4) Barrage Cloud Associated with Foehn

Moist air masses rising along mountain slopes become saturated, and clouds form on the windward side of the mountain. When the masses blow down on the leeward side, they dry due to adiabatic warming, and cloud dissipates (Fig. 6-5-14) in a phenomenon known as foehn. In satellite imagery, clouds appear on the windward side, and weather is fair on the leeward side. Low clouds on the windward side associated with foehn are called barrage cloud (Bader *et al.*, 1995). Figures 6-5-15 and 6-5-16 show B03 visible image and Natural Color RGB composite image for 00:00 UTC on 13 April 2016 when foehn was prominent in Toyama Prefecture. Figure 6-5-17 shows a surface weather chart for the same time.

Figures 6-5-15 and 6-5-16 show lower clouds on the Pacific side from the Kinki region to the Kanto region. These were blocked by high mountains in the Chubu region. In Fig. 6-5-16 (Natural Color RGB composite image), barrage clouds appear light blue, indicating domination by water clouds.

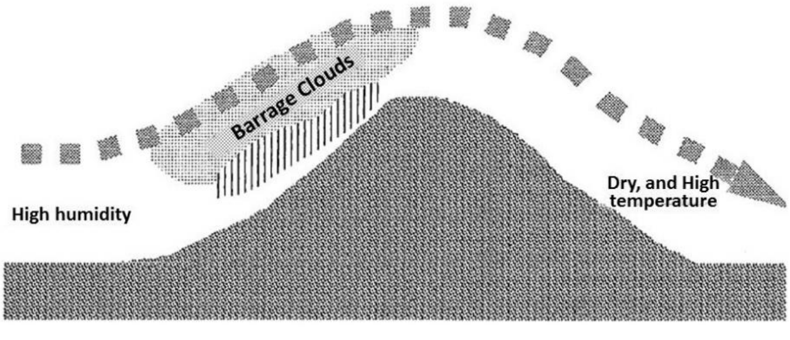

Fig. 6-5-14 Schematic diagram of foehn

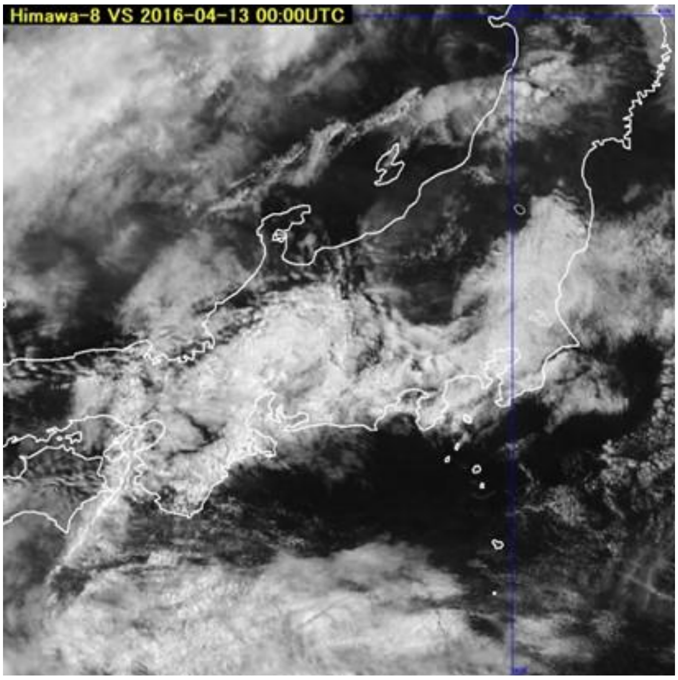

Fig. 6-5-15 B03 visible image for 00:00 UTC on 13 April 2016

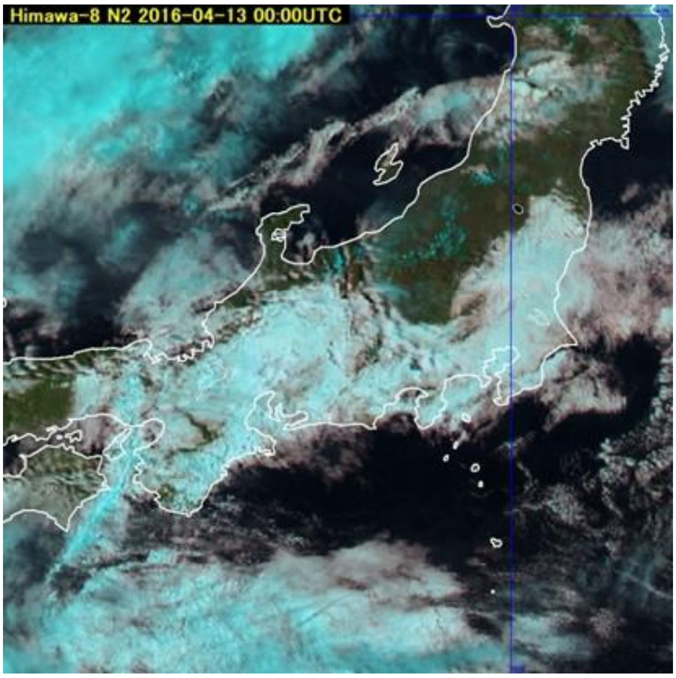

Fig. 6-5-16 Natural Color RGB composite image for 00:00 UTC on 13 April 2016

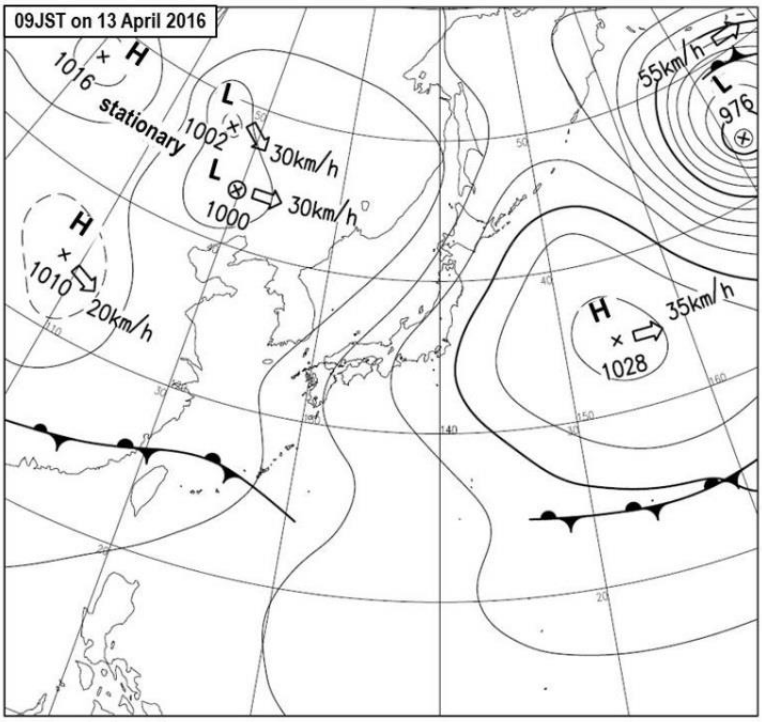

Fig. 6-5-17 Surface weather chart for 00:00 UTC on 13 April 2016

References:

- Hasegawa, Y. (1998) Features of Low Cloud and Fog on Satellite Image, Nephanalysis Case Study Reports, Meteorological Satellite Center, 1-5.
- Bokura, K. (1995) “Yamase” and Cold Summer Damage, Kisyo-kenkyu Note, 183, 15-30.
- Suzuki, K. and Y. Ando (1992) A Conceptual Model of Meso-α Scale Cloud System that Brings Local Cloudy Weather around Kanto Area, Journal of Meteorological Research, 44, 63-79.
- Bader, M. J., G. S. Forbes, J. R. Grant, R. B. E. Lilley and A. J. Waters (1995) Images in weather forecasting, Cambridge Univ. Press, 499pp.

7. Other Phenomena

7.1. Sea Ice

Sea ice around Japan is observed mainly in the Sea of Okhotsk and the Strait of Tartary. Its reflectance is similar to that of clouds, appearing in visible imagery as shades of grey – specifically light grey in the northern Sea of Okhotsk due to lower reflection relating to the area's high latitude and small solar elevation angles. As a result, sea ice areas may be mistaken for low clouds, but can easily be discriminated in animations due to its slower movement.

Figure 7-1-1 shows B03 visible image of sea ice east of Sakhalin Oblast and to the northeast of Hokkaido. This is easier to discriminate than in B13 infrared image from the same period (Fig. 7-1-2) due to lower temperature differences from the surrounding sea surface.

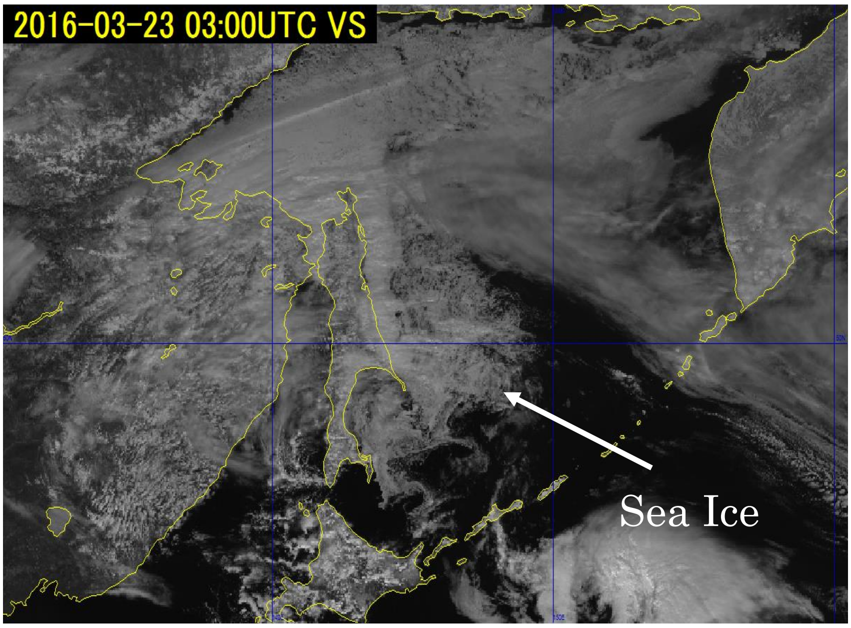

Fig. 7-1-1. B03 visible image for 03:00 UTC on 23 March 2016

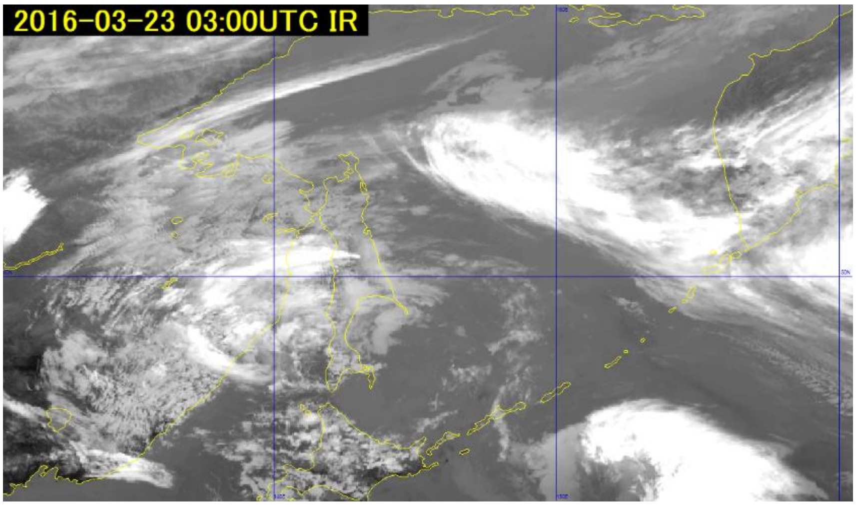

Fig. 7-1-2. B13 infrared image for 03:00 UTC on 23 March 2016

The Himawari-8 satellite Natural Color RGB composite image in Figure 7-1-3 for 05:00 UTC on 23 March 2016 shows a swirl of sea ice roughly 15 km in diameter north of the Shiretoko Peninsula, with display in cyan for easy discrimination from clouds. The vortex pattern observed is attributed to currents or wind. The swirl as a whole is too large to see from the sea or land surface, but is clear in aviation or satellite observation. Sea ice condition charts based on such imagery are issued for safety in maritime operations.

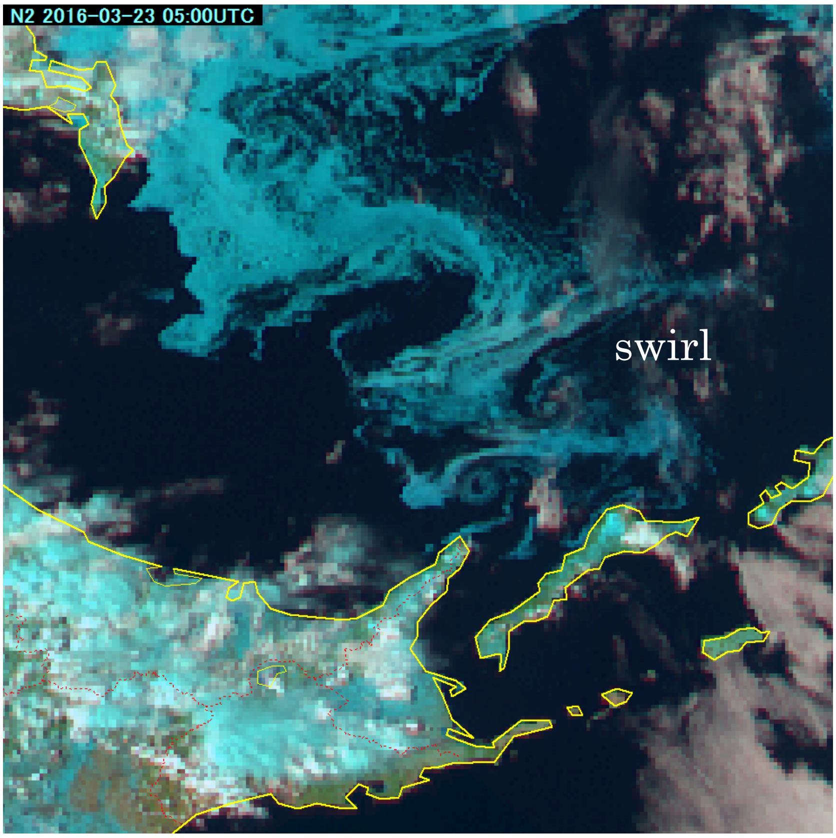

Fig. 7-1-3. Day Natural Color RGB composite image for 05:00 UTC on 23 March 2016

7.2. Snow

Snow-covered areas are displayed as white in B03 visible imagery due to high sunlight reflectance. Although identification of such areas can be challenging due to minimal temperature differences from surrounding areas, their relatively constant appearance over periods of a few days in visible imagery allows discrimination from clouds and snowfall.

Figure 7-2-1 shows B03 visible image for 19 January 2016, with mostly clear skies in the Kanto district revealing snow in white across Tokyo, Saitama, Gunma and Tochigi. Snow and clouds both appear in white, making discrimination in still imagery difficult. Discrimination is also problematic due to minimal temperature differences in the infrared imagery of Figure 7-2-2 for the same period.

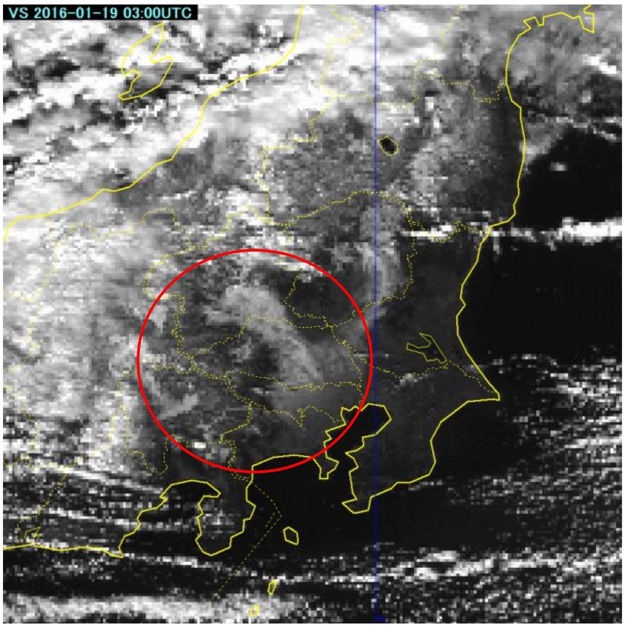

Fig. 7-2-1. Visible image for 03:00 UTC on 19 January 2016

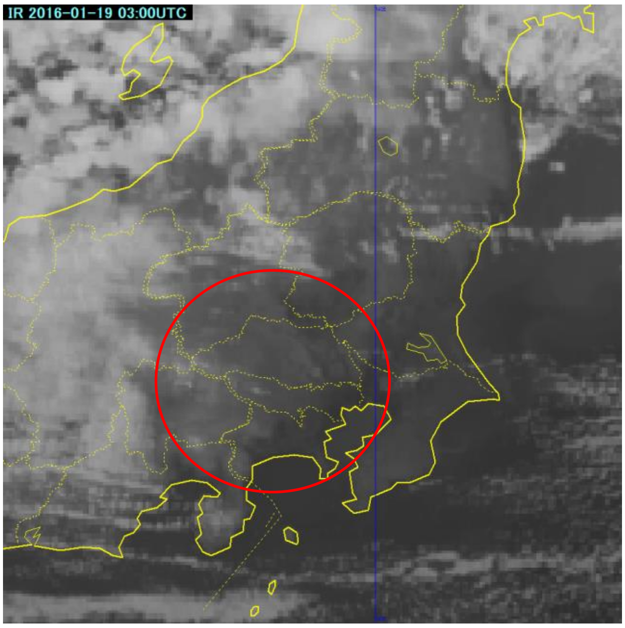

Fig. 7-2-2. Infrared image for 03:00 UTC on 19 January 2016

Figure 7-2-3 shows a Natural Color RGB composite of near-infrared and visible imagery for the same period. In the near-infrared band of B05 with an observation wavelength of 1.6 μm, the lower sunlight reflectance of ice allows discrimination from water. In Natural Color RGB composite imagery, ice crystals in upper clouds, snow areas and sea ice are all shown in cyan, enabling identification of snow areas.

Vegetation is shown in green, land surfaces in brown, and cloud/fog water particles in white.

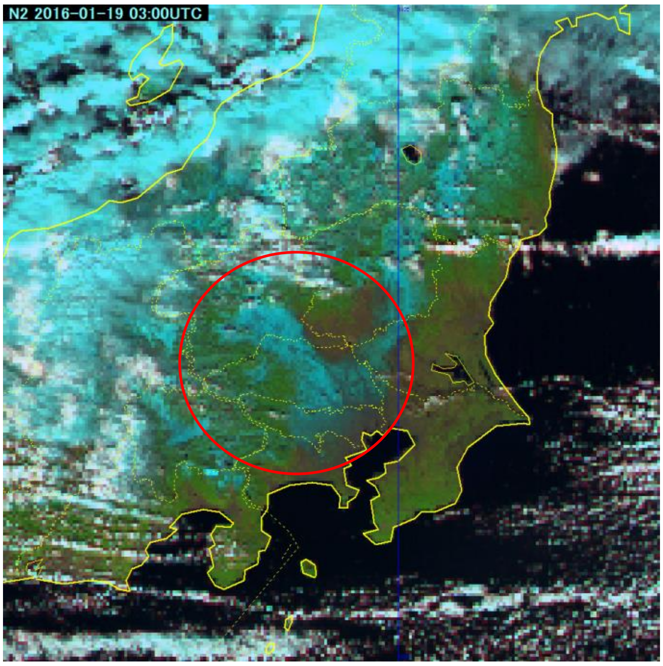

Fig. 7-2-3. Natural Color RGB composite image for 03:00 UTC on 19 January 2016

7.3. Aeolian Dust

Figures 7-3-1 – 7-3-4 show Himawari-8 image of Aeolian dust (a.k.a. yellow dust/Kosa, which is conveyed along atmospheric currents from the Gobi Desert and the Taklamakan Desert in China) whipped up by strong cyclone-related winds around the Gobi Desert for 09:30 UTC on 9 June 2015. Figure 7-3-1 is B03 visible image showing dust spiraling up in grey, whereas True Color Reproduction RGB and Natural Color RGB composite imagery shows the dust in brown (Figs. 7-3-2 and 7-3-3, respectively). Dust RGB composite imagery specifically designed for Aeolian dust monitoring shows the phenomenon in magenta, highlighting dispersive wind-related flows.

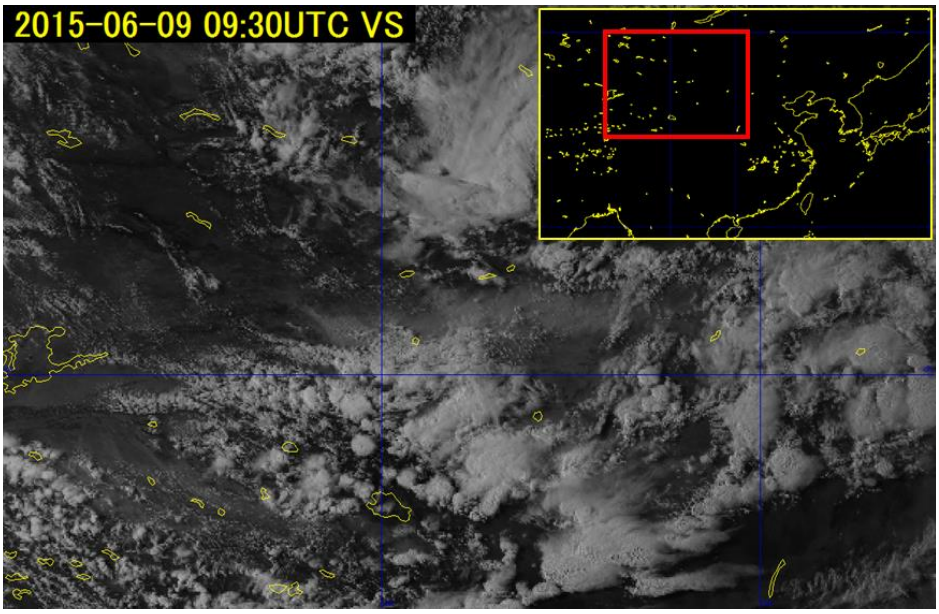

Fig. 7-3-1. B03 visible image for 09:30 UTC on 9 June 2015

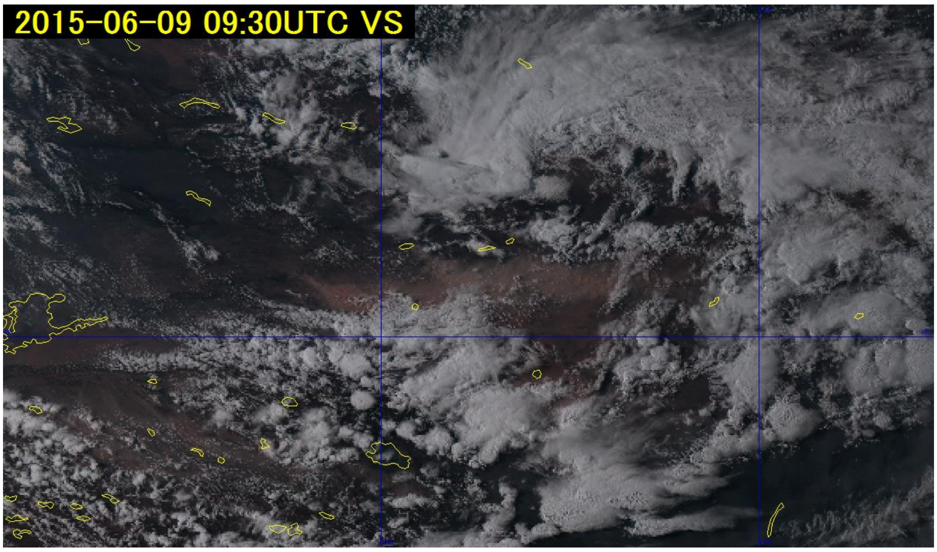

Fig. 7-3-2. True Color Reproduction RGB composite image for 09:30 UTC on 9 June 2015

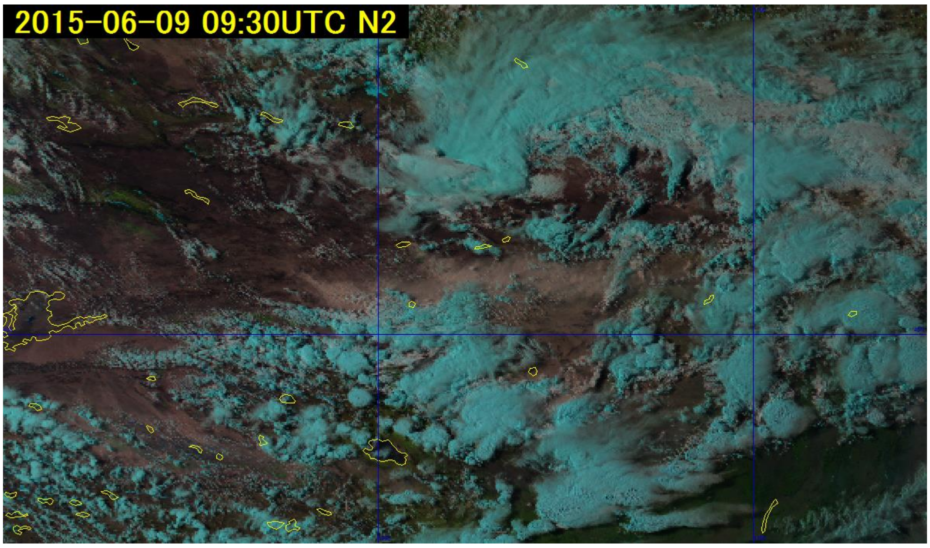

Fig. 7-3-3. Natural Color RGB composite image for 09:30 UTC on 9 June 2015

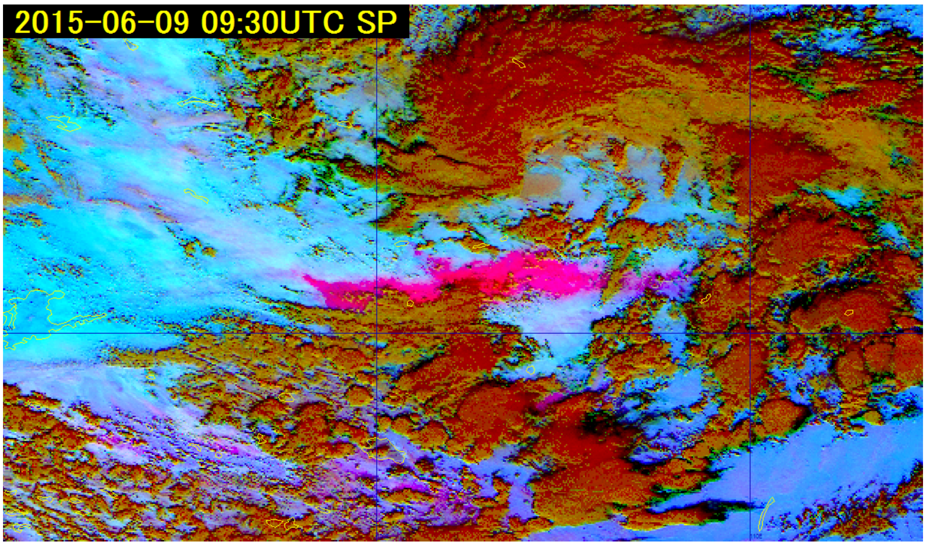

Fig. 7-3-4. Dust RGB composite image for 09:30 UTC on 9 June 2015

Figure 7-3-5 shows B03 visible image, Fig. 7-3-6 shows True Color RGB composite image, Figure 7-3-7 shows Natural Color RGB composite image, and Figure 7-3-8 shows Dust RGB composite image of Aeolian dust reaching the area around Japan for 03:00 UTC on 7 March 2016. The latter shows the dust particularly clearly in magenta.

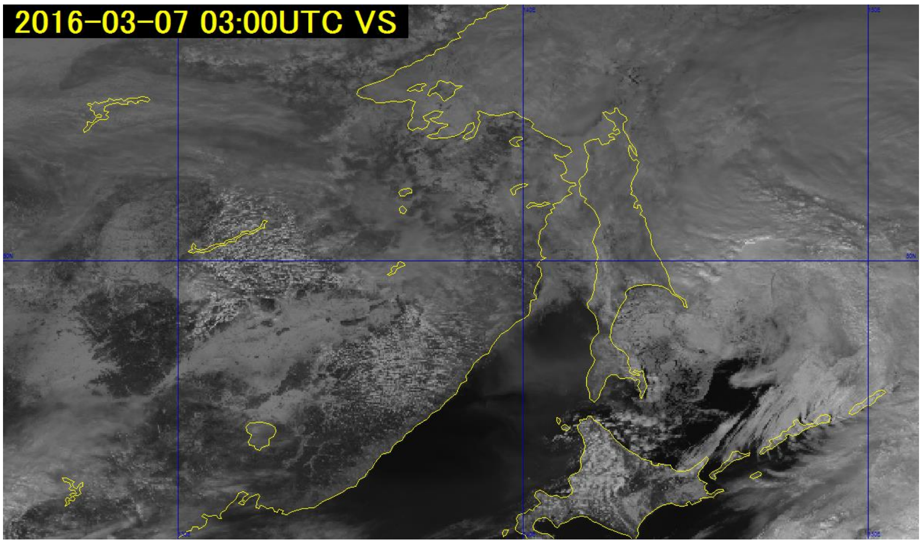

Fig. 7-3-5. B03 visible image for 03:00 UTC on 7 March 2016

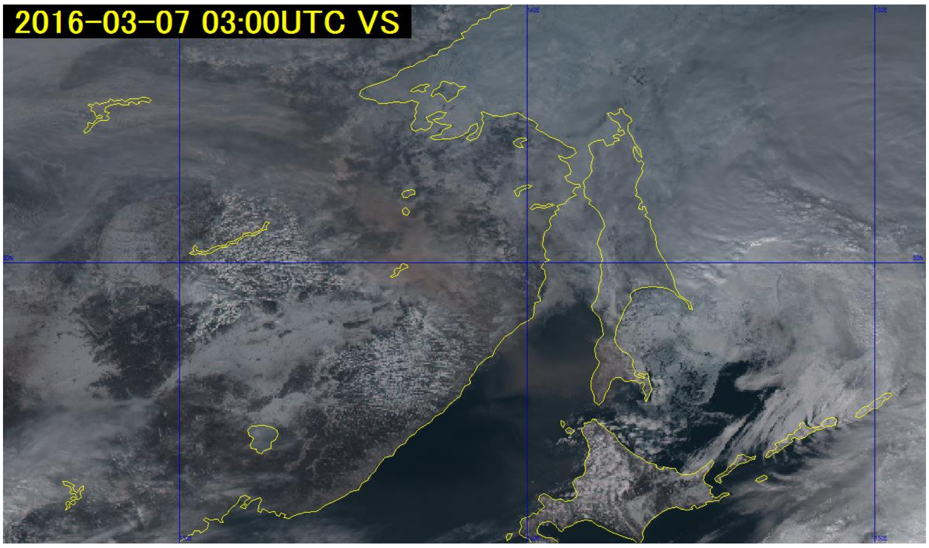

Fig. 7-3-6. True Color Reproduction RGB composite image for 03:00 UTC on 7 March 2016

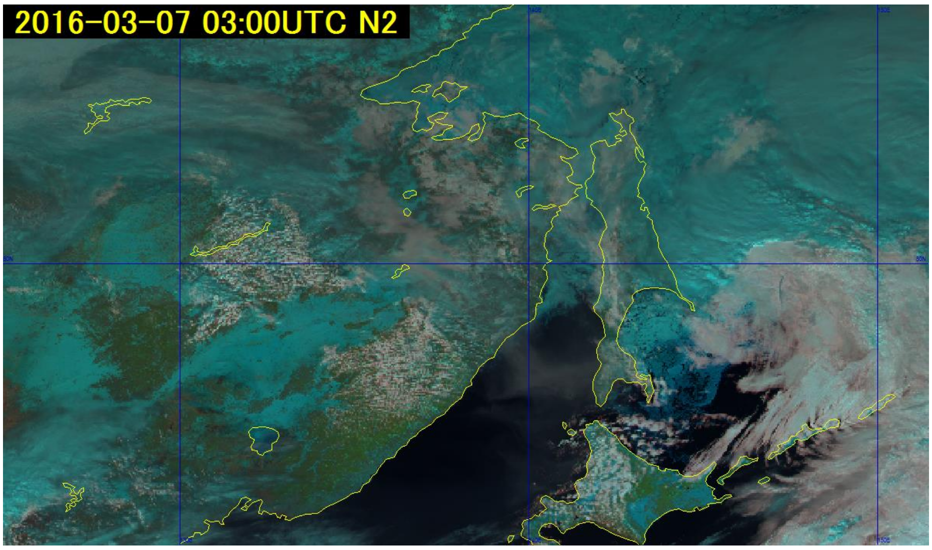

Fig. 7-3-7. Natural Color RGB composite image for 03:00 UTC on 7 March 2016

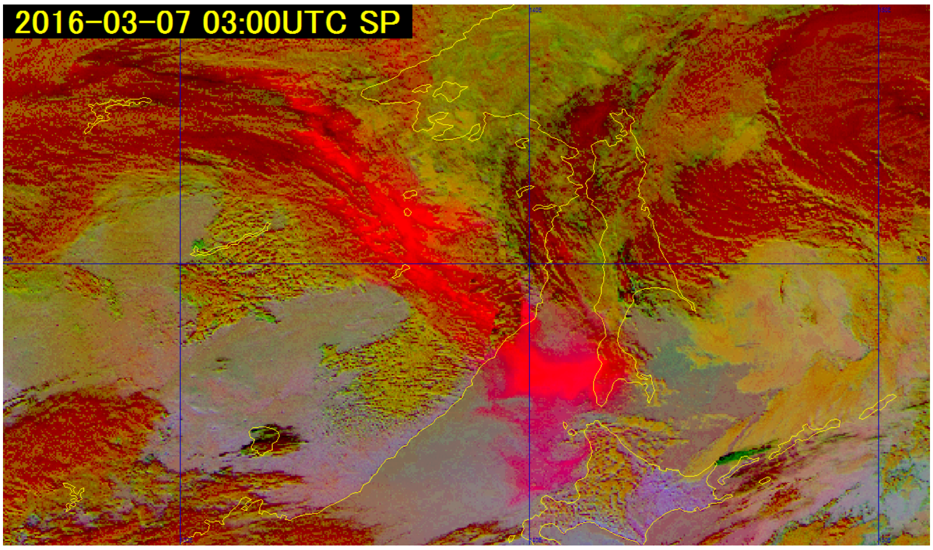

Fig. 7-3-8. Dust RGB composite image for 03:00 UTC on 7 March 2016

7.4. Volcanic Eruptions

Volcanic eruptions produce wind-dispersed plumes of potentially toxic ash and gas that can also adversely affect aviation safety, giving rise to a need for related prediction. In this context, data from several Himawari-8 satellite observation bands are analyzed to clarify volcanic ash and gas movement. Figure 7-4-1 shows True Color Reproduction image for a volcanic eruption on Kuchinoerabu Island at 02:10 UTC on 29 May 2015. While volcanic plumes are difficult to distinguish from surrounding clouds in monotone visible imagery, a visible imagery combination shows brownish plume content spreading westward and east-southeastward of the island.

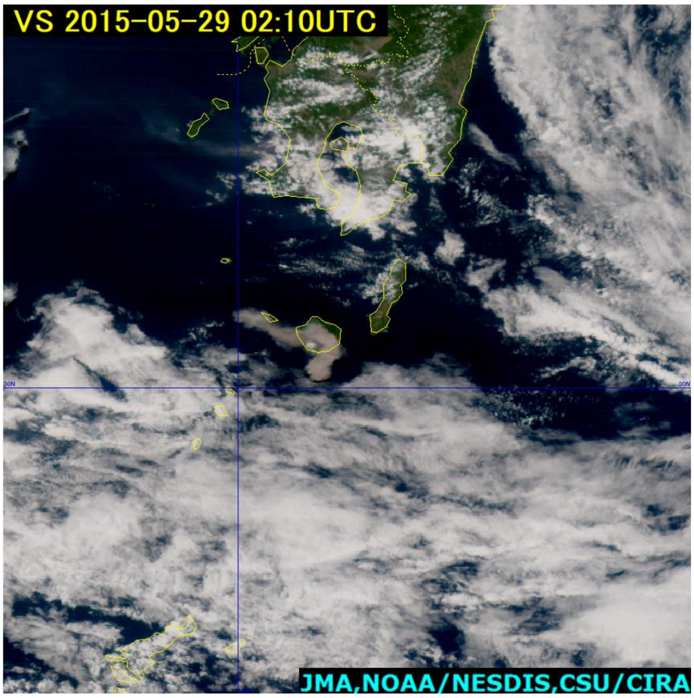

Fig. 7-4-1. B03 visible image for 09:30 UTC on 9 June 2015

Figure 7-4-2 shows Ash RGB composite image facilitating discrimination between volcanic ash and gas. It was made by combining a difference image of B13-B15 which lowers the temperature in the presence of volcanic ashes (Fig. 7-4-3) and a difference image of B13-B11 which lowers the temperature in the presence of volcanic gases (Fig. 7-4-4). The Ash RGB image shows volcanic ashes in magenta, volcanic gases in yellow-green and the overlap of the both in yellow. Following the eruption of Kuchinoerabu Island, volcanic ashes and gases were both seen.

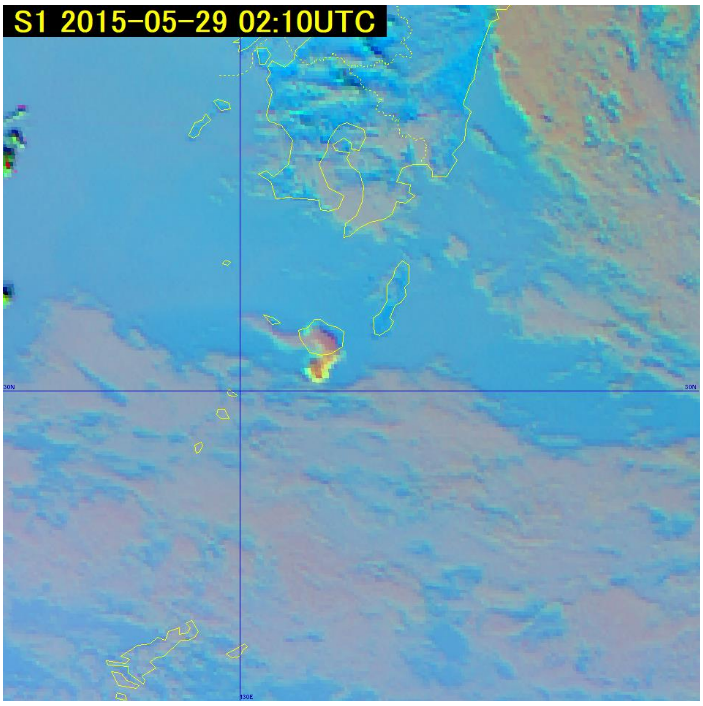

Fig. 7-4-2. Ash RGB composite image at 02:10 UTC on 29 May 2015

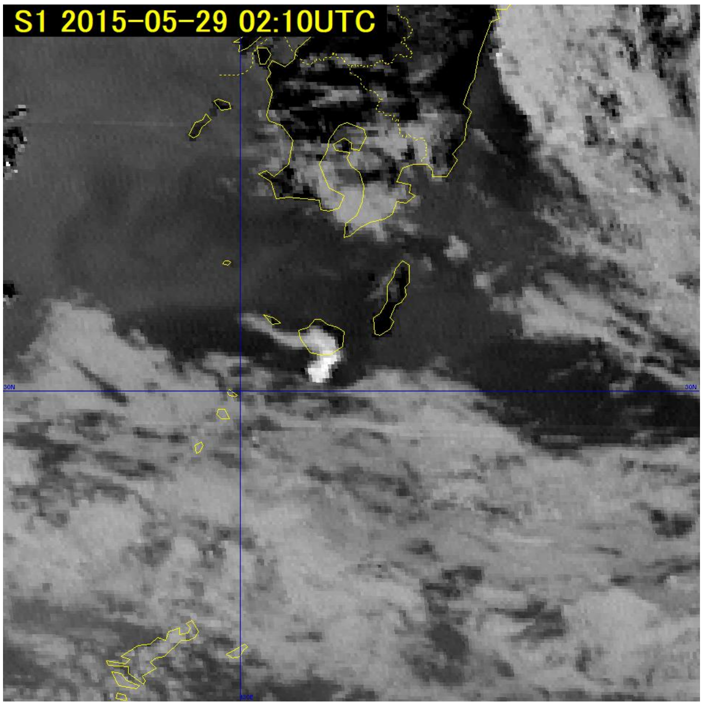

Fig. 7-4-3. Difference image of Band 15 and Band 13 at 02:10 UTC on 29 May 2015

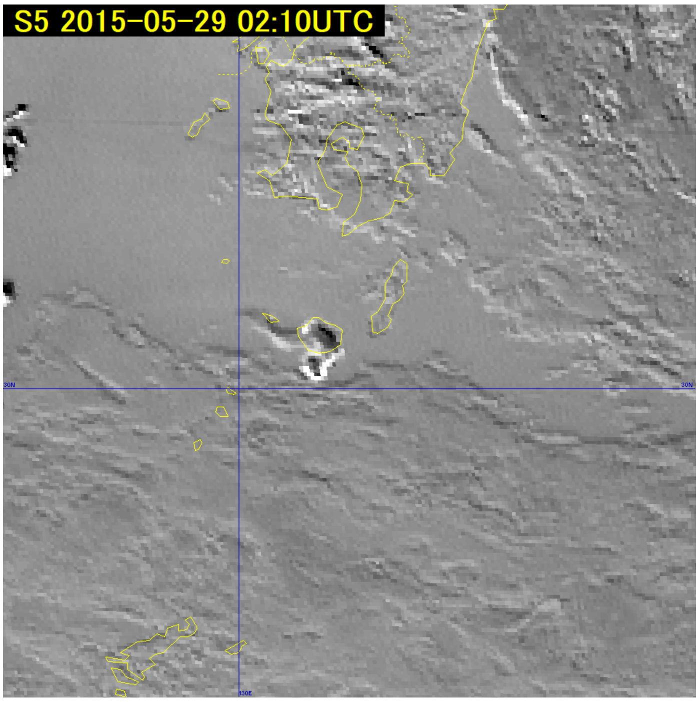

Fig. 7-4-4. Difference image of Band 13 and Band 11 at 02:10 UTC on 29 May 2015

7.5.Forest Fires and Smoke

Small-scale forest fires are difficult to identify from satellite imagery due to limited spatial resolution and observation frequency. However, the origins of larger-scale fires lasting several days can be estimated from smoke in visible imagery and hotspots in near-infrared and infrared imagery (Section 1.2: Characteristics of Each Observation Band).

Smoke from fires is often seen in visible imagery, spreading widely in a veil-like form with land and sea identifiable below, while smoke in infrared imagery cannot be seen without significant absorption. Based on these characteristics, smoke can be discriminated from clouds. The image below depicts a fire in Siberia at 07:00 on 30 April 2016. The rectangle in True Color Reproduction image contains a transparent grey area with land visible below (Fig. 7-5-1, top left), which is not seen in Band 13 image Fig. (Fig. 7-5-1, top right). Band 7 image also shows black fire hotspots (Fig. 7-5-1, bottom left), which are not observed in Band 13 image. From these observations, the grey region to the top left of Fig. 7-5-1 is assumed to be smoke capable of reaching Japan.

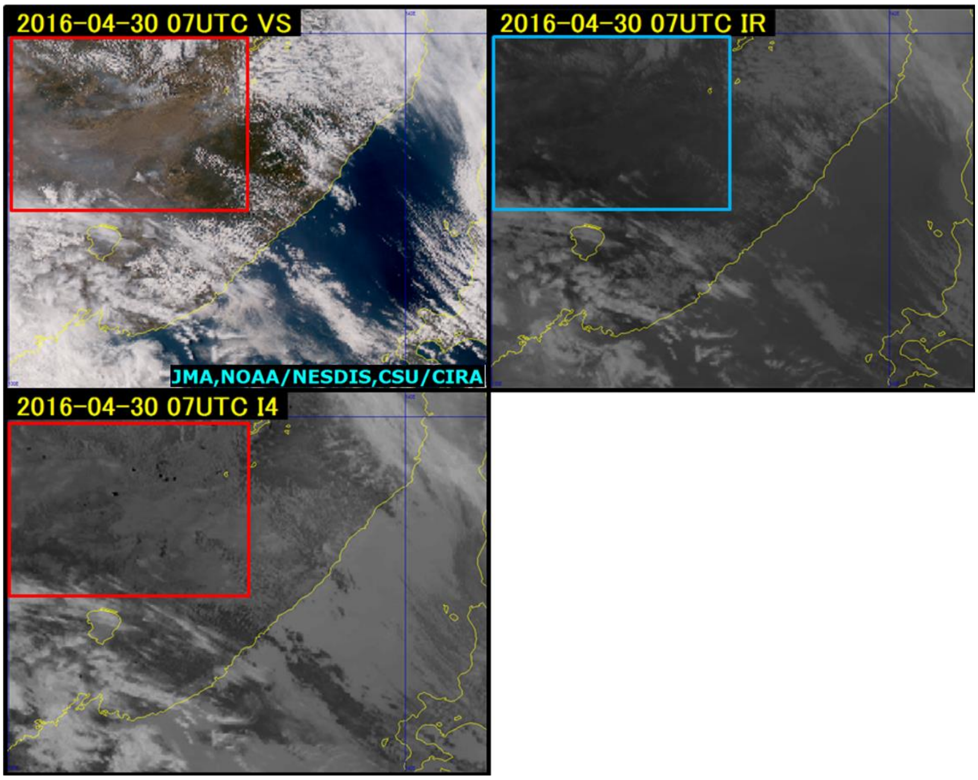

Fig. 7-5-1. Fire in Siberia at 07:00 UTC on 30 April 2016

Top left: True Color Reproduction; top right: B13 infrared; bottom left: B07 infrared

Figure 7-5-2 a from 06:00 UTC on 18 May 2016 shows a True Color Reproduction image with a white region not seen in the infrared image of Fig. 7-5-2 b. The shape/color differences from the lower clouds typically seen over the Sea of Japan suggest the presence of smoke moving from Hokkaido toward the Hokuriku and Kanto regions in correspondence with wind-direction and speed data based MSM 850-hPa analysis.

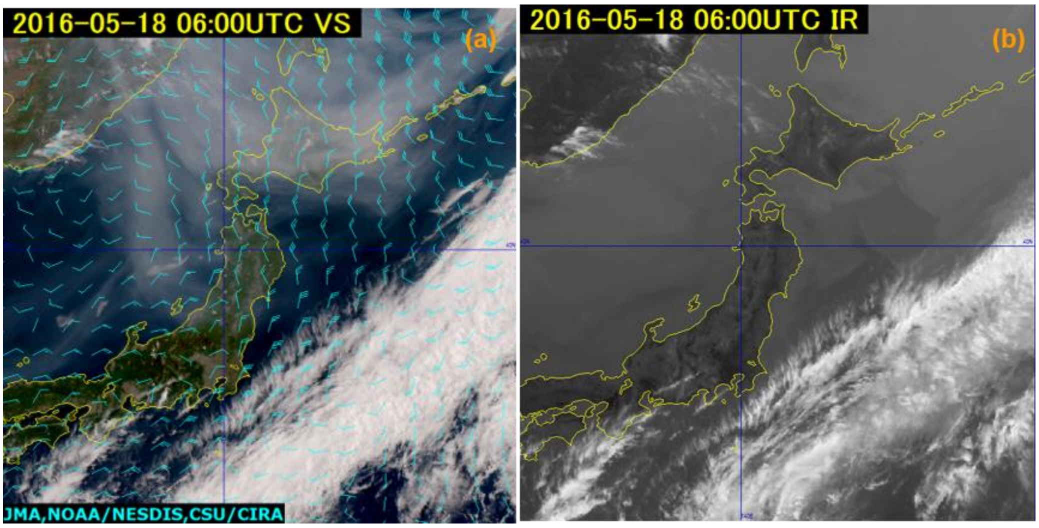

Fig. 7-5-2 Smoke from a wildfire at 06:00 UTC on 18 May 2016.
(a)True Color Reproduction image (left). (b) B13 infrared imagery (right).

Areas of burning can be determined from changes in vegetation cover. Figures 7-5-3(a)/(b) show changes relating to a fire around Lake Khanka in northeastern China. Natural Color RGB composite imagery (Fig. 7-5-3(a)) reveals a dark-brown region not seen on 14 October in northern and eastern parts of the encircled area, and many more hotspots (black dots) are seen around the lake on 25 October than on 14 October in the Band 7 imagery of Fig. 7-5-3(b). Accordingly, the region is assumed to have undergone fire damage.

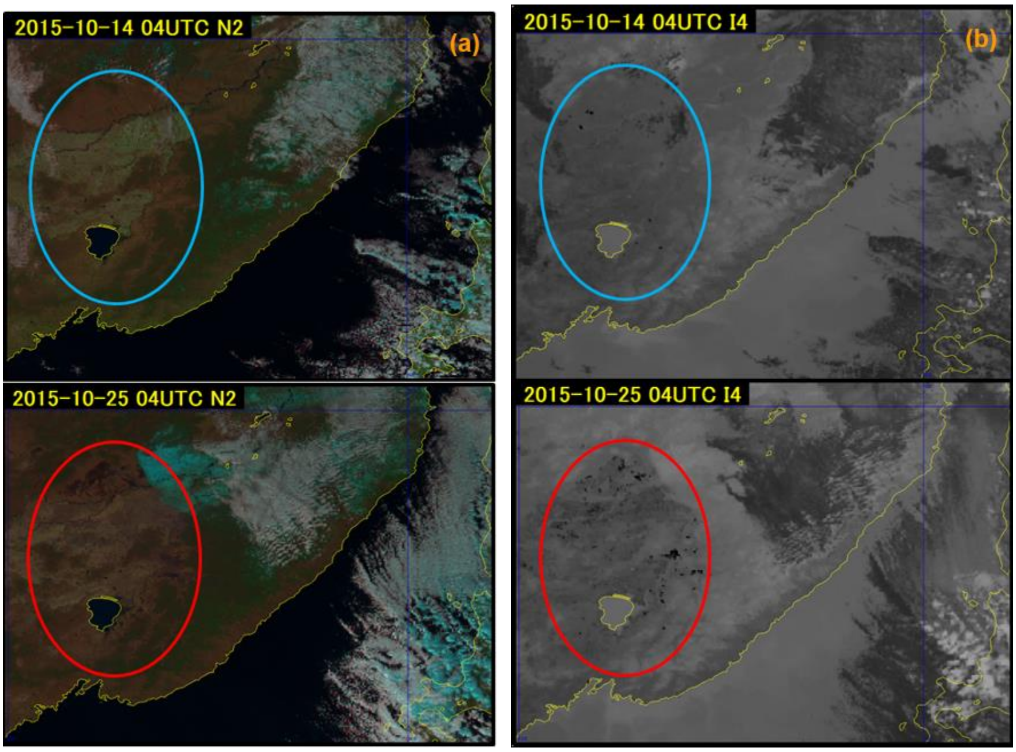

Fig. 7-5-3 Impact of wildfire around Lake Khanka.
(a) Natural Color RGB imagery (left). (b) B07 infrared imagery

Smoke from frequent major dry-season forest fires occurring in Indonesia over periods of months since the summer of 2015 is visible in satellite imagery. Figure 7-5-4(a) shows True Color Reproduction imagery revealing a thin-brown region extending from Borneo to Sumatra (not seen in the Band 13 infrared imagery of Fig. 7-5-4(b)) indicating forest fire smoke.

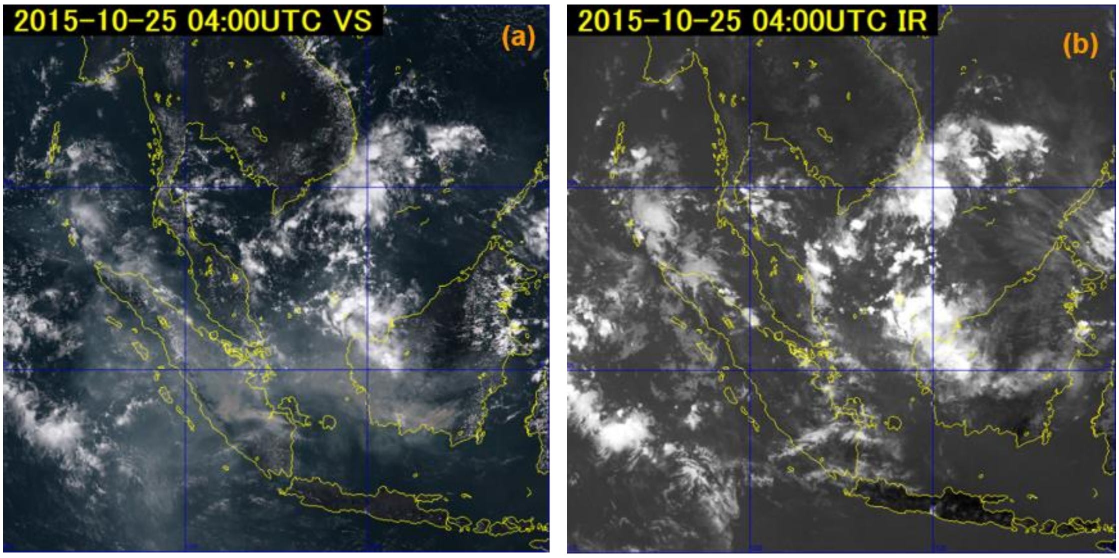

Fig. 7-5-4 Fire in Indonesia at 04:00 UTC on 25 October 2015.
(a) True Color Reproduction RGB composite image (left).
(b) B13 infrared image (right).

7.6. Sun Glint

Sun glint appears as bright reflections on the surfaces of large lakes and sea areas in visible and infrared imagery, with seasonal and temporal variations.

Its scale depends on the positions of the sun, the earth and the relevant satellite with minor latitudinal differences (up to approx. 30 km) and larger longitudinal differences (40 – 120 km). Size and reflection intensity depend on water conditions, being the smallest on relatively still sea surfaces with gentle winds and larger/darker with strong winds, thereby allowing determination of sea surface conditions.

Figure 7-6-1 shows the mechanism of sun glint on a steady sea surface acting as a mirror at Point B directly incidental to the satellite sensor, whereas the sunlight reflected at Point A is not directly incidental. Thus, the satellite sees the reflection at Point B directly and produces the brightest region of sun glint in visible imagery. Sun glint moves from east to west during the daytime in imagery. On a seasonal basis, the center moves from latitudes of 11.75° north to 11.75° south around 140° east.

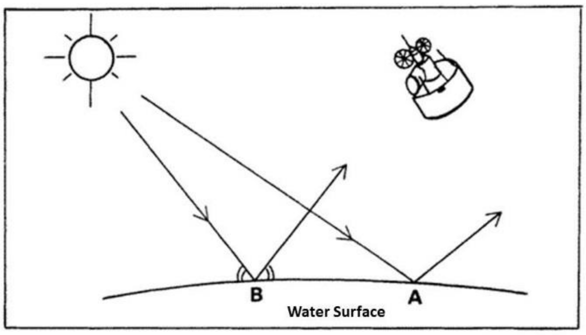

Fig. 7-6-1. Sun glint mechanism

The visible image in Fig 7-6-2 shows a bright part around 10° north latitude and 150° east longitude (arrow) representing sun glint. Small and bright glint areas like this suggest a still sea surface. From the observation time just after 10:00 JST, the sun glint is at around 150° east longitude. Figure 7-6-3 showing True Color RGB composite imagery for the same time period indicates bright sun glint over the sea surface.

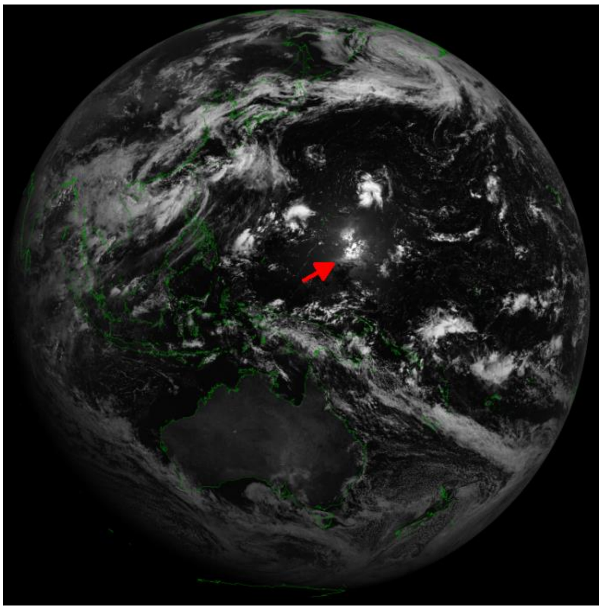

Fig. 7-6-2. Visible image for 01:20 UTC on 19 July 2015

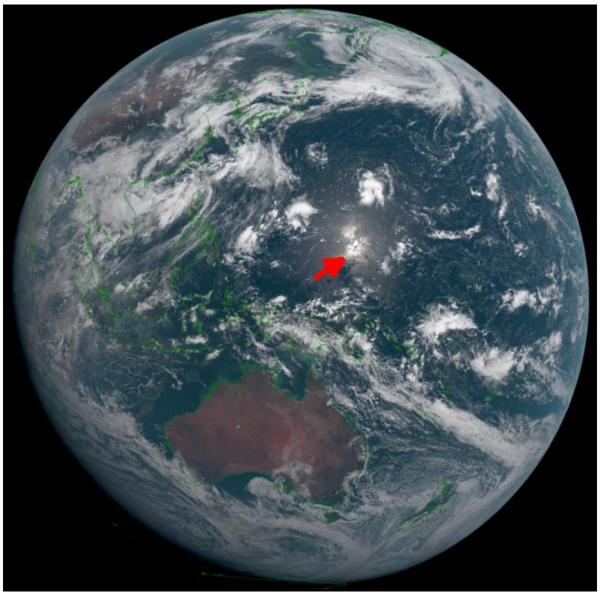

Fig. 7-6-3. True Color RGB composite image for 01:20 UTC on 19 July 2015

In December, sun glint is positioned in the Southern Hemisphere as in Fig. 7-6-4. In observation just before 09:00 JST, it is seen at 10° south latitude and 160° east longitude (arrow). Figure 7-6-5 shows True Color RGB composite image for the same time period, indicating Southern Hemisphere sun glint as in visible image.

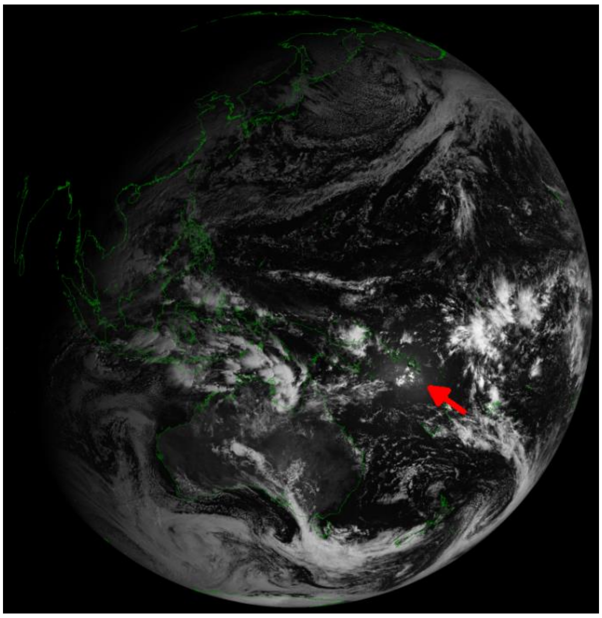

Fig. 7-6-4. Visible image for 23:40 UTC on 19 December 2015

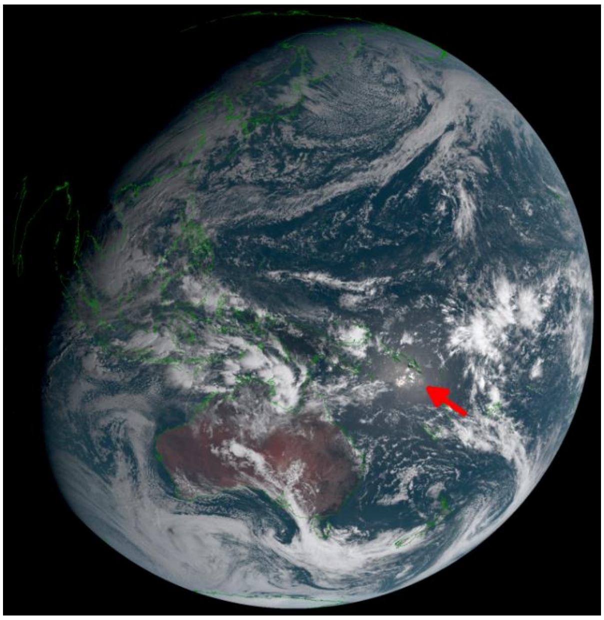

Fig. 7-6-5. True Color RGB composite image for 23:40 UTC on 19 December 2015

Reference:

- E. G. Emecen, G. Kara, F. Erdoğmuş and R. Gardashov, 2005: The Determination of Sunglint Locations on the Ocean Surface by Observation from Geostationary Satellites, TAO, Vol. 17, No. 1, 253-261., Retrieved April 1, 2024, from http://tao.cgu.org.tw/index.php/articles/archive/space-science/item/download/643_35eeb72969bfb86f14dfd41a0317dbbd

7.7. Solar Eclipses

Solar eclipses are difficult to observe at all angles of incidence because their visibility is influenced by weather conditions and location. However, geostatic meteorological satellites capture lunar shadows projected onto observation areas without fail.

True Color RGB composite imagery for 02:00 UTC on 9 March 2016 (Fig. 7-7-1) shows a black lunar shadow over the Pacific. The shadow itself and the broad cloud distribution here are much clearer than in observation from the ground surface.

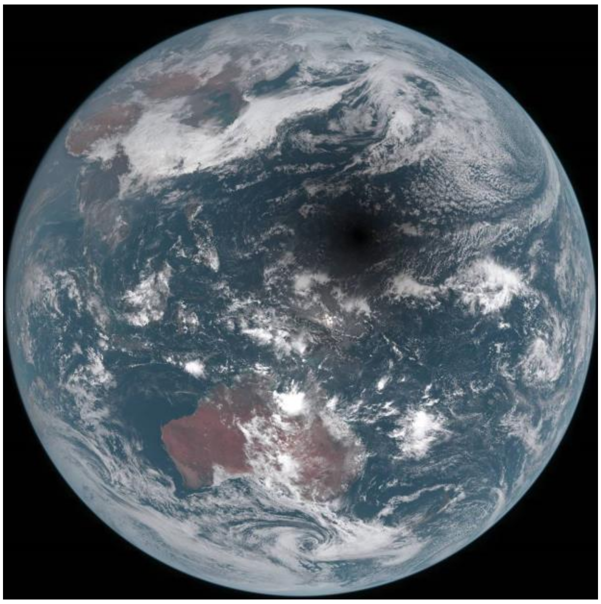

Fig. 7-7-1. True Color RGB imagery for 02:00 UTC on 9 March 2016

B03 from 0.64 μm visible imagery is enlarged in Fig. 7-7-2 a to centralize the shadow, and Fig. 7-7-2 b shows isoline reflectance. The darker center of the round shadow is clearly visible around 12° north latitude and 148° east longitude.

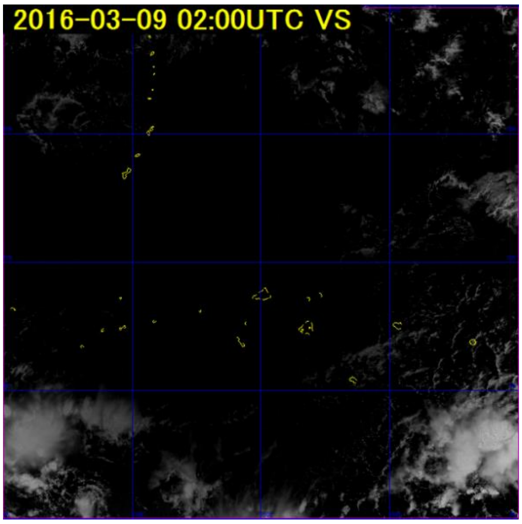

Fig. 7-7-2(a) B03 visible imagery for 02:00 UTC on 9 March 2016

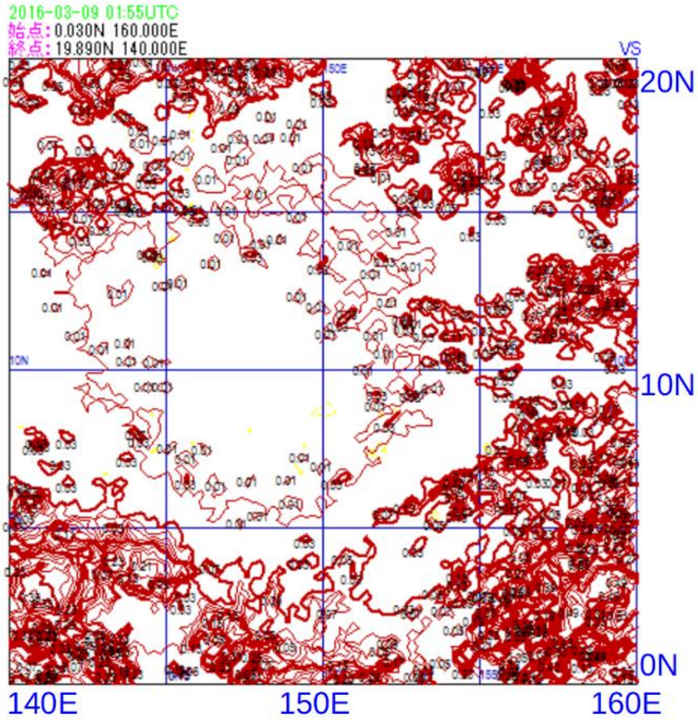

Fig. 7-7-2(b) Isoline display of Fig. 7-7-2(a) with round area of low reflectance

Figures 7-7-3(a)-(c) show enlarged Night Microphysics RGB composite imagery for the area around Borneo at the time of a solar eclipse. While Fig. 7-7-3 does not allow cloud discrimination due to the reflection of visible light over the cloud area, the imagery in b and c shows visible light being obtruded by the eclipse, enabling visualization of cloud in the same color as at nighttime. A thick cloud area associated with rainfall is seen in orange with yellow dots in region **A**, and fog and lower clouds are seen in bluish-white in region **B**.

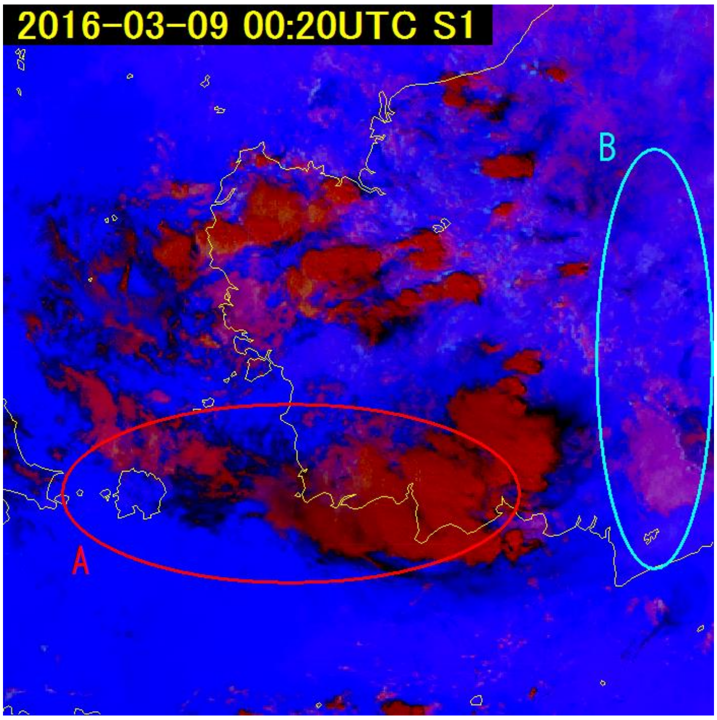

Fig. 7-7-3(a). Night Microphysics RGB composite imagery for 00:20 UTC on 9 March 2016

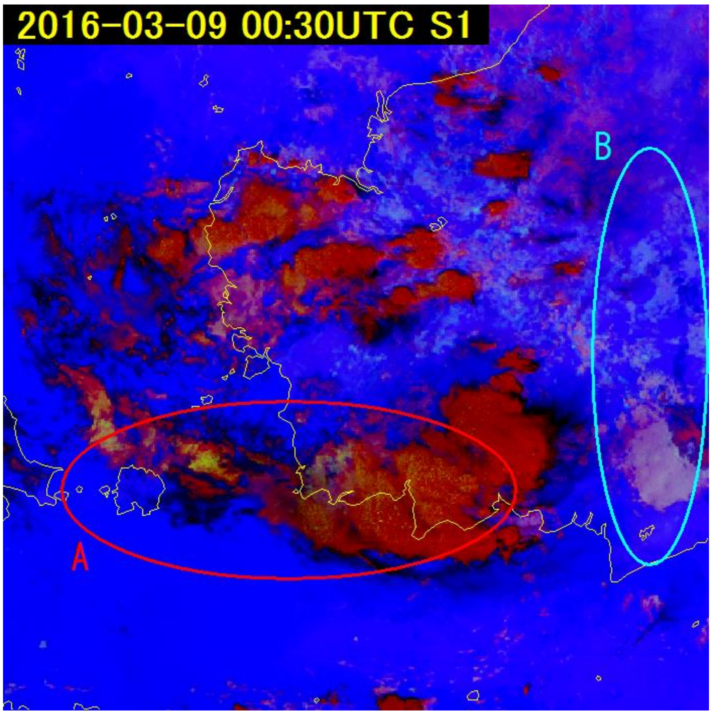

Fig. 7-7-3(b). Night Microphysics RGB composite imagery for 00:30 UTC on 9 March 2016

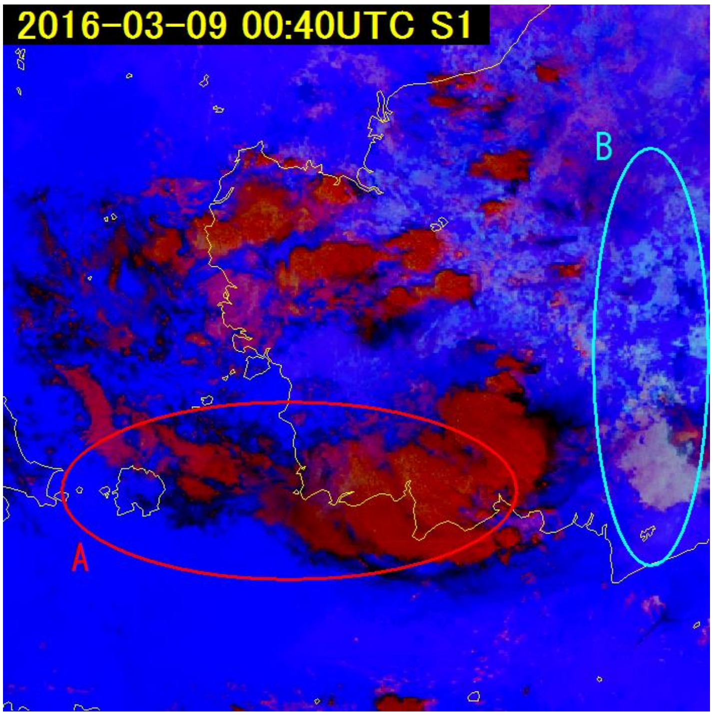

Fig. 7-7-3(c). Night Microphysics RGB composite imagery for 00:40 UTC on 9 March 2016